



Highly Resolved LES and Tests of The Effectiveness of Different URANS Models for The Computation of Challenging Natural Convection Cases

A thesis submitted to The University of Manchester for the degree
of Doctor of Philosophy in the Faculty of Engineering and Physical
Sciences

2013

Dalila Ammour

School of Mechanical, Aerospace and Civil Engineering

Contents

1	Introduction	28
1.1	Natural Convection	28
1.2	Buoyancy-driven flows	29
1.2.1	Buoyancy-driven flows in enclosures	29
1.3	Computational Fluid Dynamics	31
1.4	Turbulence and its modelling	32
1.4.1	Introduction	32
1.4.2	The phenomenon of turbulence:	32
1.4.3	Some features of turbulence	33
1.4.4	Scales of turbulence	35
1.4.5	Modelling of turbulence	36
1.5	Objectives	39
1.6	Outlines of the thesis	40
2	Literature Survey	42
2.1	Experimental investigations	42
2.1.1	Vertical tall cavities	42
2.1.2	Vertical square cavities	44
2.1.3	Other vertical cavities	46
2.2	Numerical investigations	48
2.2.1	Vertical tall cavities	48
2.2.2	Vertical square cavities	55
2.3	Tilted enclosures	56
2.3.1	Experimental investigations	56
2.3.2	Numerical investigations	58
2.4	Horizontal annular enclosures	60
2.5	Final remarks	64

3	Modelling of Turbulent Buoyancy-Driven Flows	67
3.1	Introduction	67
3.2	Navier Stokes equations in natural convection	67
3.3	Unsteady RANS modelling	68
3.3.1	The Boussinesq model	69
3.3.2	Two-equation eddy viscosity models	70
3.3.3	Second-moment closure	71
3.3.3.1	Second moment closure models	72
3.3.4	Contribution of buoyancy	72
3.4	Modelling turbulent heat fluxes	73
3.4.1	The effective viscosity approximation	73
3.4.1.1	Simple shear flows	74
3.4.1.2	Buoyancy-driven flows	74
3.4.2	The GGDH heat flux model	74
3.5	Wall treatment	76
3.5.1	The turbulent boundary layer	76
3.5.2	Role of the wall function	78
3.5.3	Wall treatment strategy	78
3.5.4	Standard wall treatment formulations	79
3.5.4.1	Single velocity-scale wall function	79
3.5.4.2	Two velocity scale wall function	80
3.5.4.3	Scalable wall function	82
3.5.5	wall functions in <i>Code_Saturne</i> 2.0	83
3.5.6	<i>Code_Saturne</i> 2.0 wall function enhancements	86
3.6	Large Eddy Simulation	86
3.6.1	Introduction	86
3.6.2	Filtering in LES	87
3.6.3	Filtered Navier-Stokes equations	89
3.6.4	The sub-grid-scale stresses	90
3.6.5	The sub-grid-scale models	91
3.6.5.1	The Smagorinsky model	91
3.6.6	Grid resolution for LES	92
3.6.7	LES initialisation	93
3.7	Final remarks	93

4	Numerical Methods	94
4.1	Introduction	94
4.2	<i>Code_Saturne</i> 2.0 solver	95
4.2.1	Features of <i>Code_Saturne</i> 2.0	96
4.3	Wall function implementation in <i>Code_Saturne</i> 2.0	98
4.3.1	Boundary conditions for the velocity ($k - \varepsilon$ model)	98
4.3.2	Boundary conditions for turbulence	99
4.4	Final remarks	100
5	URANS Computation of Flow Within 2-D Vertical and Tilted Cavities	101
5.1	2-D vertical enclosure (Betts cavity [11])	101
5.1.1	Case description	101
5.1.2	Computational mesh and numerical methods	103
5.1.3	Qualitative results	104
5.1.4	Quantitative results	106
5.1.4.1	Comparison between different standard wall functions embedded in <i>Code_Saturne</i> 2.0	106
5.1.4.2	Model validation for buoyancy-driven flows inside the vertical cavity	109
5.2	2-D tilted stable enclosure at 60°	112
5.3	2-D tilted unstable enclosure at 15°	118
5.4	Refinement of the standard one- and “two-velocity-scale wall function” in <i>Code_Saturne</i> 2.0	123
5.5	Concluding remarks	128
6	Buoyancy-Driven Flow Within the 3-D Tilted Enclosure Under Unstable Stratification	130
6.1	Introduction	130
6.2	Computational mesh and numerical methods	131
6.3	Assessment of LES resolution	133
6.4	Qualitative results	135
6.5	Quantitative results	141
6.6	Concluding remarks	160

7	Buoyancy-Driven Flow Within the 3-D Tilted Enclosure Under Stable Stratification	162
7.1	Introduction	162
7.2	Computational mesh and numerical methods	163
7.3	Assessment of LES resolution	163
7.4	Qualitative results	164
7.5	Quantitative results	168
7.6	Concluding remarks	182
8	Buoyancy-Driven Flow Within the Horizontal Annular Penetration Cavity	184
8.1	Introduction	184
8.2	Computational mesh and numerical methods	187
8.3	Assessment of LES resolution	189
8.4	Qualitative results	190
8.4.1	Time-dependent results	190
8.4.2	Time-averaged results	198
8.5	Quantitative results	201
8.6	Concluding remarks	216
9	Conclusions and Recommendations for Future Work	217
9.1	Conclusions	217
9.2	Recommendations for future work	221
A	Published papers	233
A.1	International journal paper	233
A.2	List of international conference papers	233
B	RANS models	235
B.1	Two-Equation EVMs	235
B.2	Stress transport models	244
C	Numerical methods	249
C.1	Finite Volume Method (FVM)	249
C.2	Space discretization in <i>Code_Saturne</i> 2.0	251
C.2.1	Convection schemes	252
C.2.2	Diffusion terms	253
C.2.3	Gradient reconstruction	253

C.2.3.1	Standard iterative method in <i>Code_Saturne</i> 2.0	254
C.2.3.2	Least squares method	255
C.3	Time discretization	255
C.4	Pressure-velocity coupling (pressure correction)	256
C.5	Linear system solution algorithm	257
C.6	Boundary Conditions	258
C.6.1	Inlet	259
C.6.2	Outlet	259
C.6.3	Walls	260
D	Grid sensitivity tests	261

List of Figures

1.1	Buoyancy-driven flows within different enclosures investigated in the present thesis.	30
1.2	Turbulent flow [43].	33
1.3	Turbulence energy wavenumber spectrum.	36
1.4	Schematic of comparisons between DNS, RANS and LES [43].	39
2.1	Schematic diagram of test cavity and velocity field, profiles of rms velocity fluctuations at $y/H=0.5$ [5].	46
2.2	Schematic of the flow geometries and the local number variation [1]. . .	47
2.3	Vector plot of mean velocity profiles. (a) Non-partitioned cavity (scale: 0.038 m/s/mm). (b) Partitioned cavity (scale: 0.080 m/s/mm [6]). . .	48
2.4	Convective flow patterns in the X-Y plane for $H/W=5$ ($W=22\text{mm}$) for $\theta = 90^\circ, \theta = 60^\circ$ and $\theta = 15^\circ; Ra_W = 10^4$ [51].	56
2.5	Calculated Nusselt number vs the angle of inclination α for different values of the Rayleigh number Ra_L and $A = 0.75$ [9].	57
2.6	Streamlines in the cavity at various angles of inclination [79].	58
2.7	Iso-temperature distributions and corresponding local Nusselt number at the hot wall of the undulated cavity ($Ra = 1.58 \times 10^9$ and $\phi = 90^\circ$) [7].	59
3.1	Schematic of large eddies in a turbulent boundary layer. The flow above the boundary layer has a steady velocity U ; the eddies move at randomly fluctuating velocities of the order of a tenth of U , the largest eddy size, (l) is comparable to the boundary layer thickness δ [92].	76
3.2	Velocity distribution near a solid wall.	77
3.3	General configuration of a boundary face.	79
3.4	Γ_{eff} as a function of y^+ obtained for $Pr = 1$ and $Pr_t = 1$	85
3.5	Associated transfer functions to the Fourier cut-off, top-hat and Gaussian filters.	89

5.1	Geometry of 2-D vertical cavity. Location of plot lines are indicated. . .	104
5.2	2-D computational meshes for high and low-Re modelling of the vertical cavity.	104
5.3	Temperature contours inside the vertical cavity 2.18×0.0762 . (a) $k - \varepsilon$, (b) LRR , (c) SSG , (d) $k - \omega SST$, (e) $\varphi - f$	105
5.4	Velocity magnitude contours inside the vertical cavity 2.18×0.0762 . (a) $k - \varepsilon$, (b) LRR , (c) SSG , (d) $k - \omega SST$, (e) $\varphi - f$	105
5.5	Turbulent kinetic energy contours inside the vertical cavity 2.18×0.0762 . (a) $k - \varepsilon$, (b) LRR , (c) SSG , (d) $k - \omega SST$, (e) $\varphi - f$	106
5.6	Mean temperature profiles at different locations inside the vertical cavity, comparison between different wall functions and experimental data. . .	107
5.7	Mean vertical velocity profiles at different locations inside the vertical cavity, comparison between different wall functions and experimental data.	107
5.8	Rms fluctuating vertical velocity profiles at different locations inside the vertical cavity, comparison between different wall functions and experimental data.	108
5.9	Local Nusselt number distribution along hot wall of the vertical cavity, comparison between different wall functions and the experimental data.	108
5.10	Mean temperature profiles at different locations inside the vertical cavity, comparison between RANS models and experimental data.	110
5.11	Mean vertical velocity profiles at different locations inside the vertical cavity, comparison between RANS models and experimental data. . . .	111
5.12	Rms fluctuating vertical velocity profiles at different locations inside the vertical cavity, comparison between RANS models and experimental data.	111
5.13	Local Nusselt number distribution along hot wall of the vertical cavity, comparison between RANS models and experimental data.	112
5.14	Geometry of 2-D vertical cavity. Location of plot lines are indicated. . .	114
5.15	Temperature contours inside the 60° tilted cavity. (a) $k - \varepsilon$, (b) LRR , (c) SSG , (d) $k - \omega SST$, (e) $\varphi - \alpha$	114
5.16	Velocity magnitude contours inside the 60° tilted cavity. (a) $k - \varepsilon$, (b) LRR , (c) SSG , (d) $k - \omega SST$, (e) $\varphi - \alpha$	115
5.17	Turbulent kinetic energy contours inside the 60° tilted cavity. (a) $k - \varepsilon$, (b) LRR , (c) SSG , (d) $k - \omega SST$, (e) $\varphi - \alpha$	115
5.18	Mean temperature profiles at different locations inside the 60° tilted cavity, comparison between RANS models and experimental data.	116

5.19	Mean vertical velocity profiles at different locations inside the 60° tilted cavity, comparison between RANS models and experimental data. . . .	116
5.20	Rms fluctuating vertical velocity profiles at different locations inside the 60° tilted cavity, comparison between RANS models and experimental data.	117
5.21	Local Nusselt number distribution along hot wall of the 60° tilted cavity, comparison between RANS models and experimental data.	117
5.22	Geometry of 2-D vertical cavity. Location of plot lines are indicated. . .	118
5.23	Temperature contours inside the tilted unstable cavity at 15° . (a) $k - \varepsilon$, (b) LRR , (c) SSG , (d) $k - \omega SST$, (e) $\varphi - f$	119
5.24	Velocity magnitude contours inside the tilted unstable cavity at 15° . (a) $k - \varepsilon$, (b) LRR , (c) SSG , (d) $k - \omega SST$, (e) $\varphi - f$	120
5.25	Turbulent kinetic energy contours inside the tilted unstable cavity at 15° . (a) $k - \varepsilon$, (b) LRR , (c) SSG , (d) $k - \omega SST$, (e) $\varphi - f$	120
5.26	Mean temperature profiles at different locations inside the vertical cavity, comparison between RANS models and experimental data.	121
5.27	Mean vertical velocity profiles at different locations inside the vertical cavity, comparison between RANS models and experimental data. . . .	121
5.28	Rms fluctuating vertical velocity profiles at different locations inside the vertical cavity, comparison between RANS models and experimental data.	122
5.29	Velocity vectors resulting from SSG second moment closure computation. Comparison between 2-D cavities: (a) vertical, (b) stable tilted at 60° , (c) unstable tilted at 15°	122
5.30	Mean temperature profiles at different locations inside the vertical cavity, comparison between corrected and old versions of wall functions with experimental data.	124
5.31	Mean vertical velocity profiles at different locations inside the vertical cavity, comparison between corrected and old versions of wall functions with experimental data.	125
5.32	Mean turbulent kinetic energy profiles at different locations inside the vertical cavity, comparison between corrected and old versions of wall functions with experimental data.	126
5.33	Mean dissipation rate profiles at different locations inside the vertical cavity, comparison between the corrected and old versions of wall functions with experimental data.	127

5.34	Local Nusselt number distribution along hot wall of the vertical cavity, comparison between corrected and old versions of wall functions with experimental data.	128
6.1	Geometry of 3-D cavity inclined at 15° to horizontal (unstable stratification). Location of plot lines are indicated.	131
6.2	3-D computational mesh for LES.	133
6.3	Profiles of the ratio of grid spacings to the Kolmogorov length scale at three middle planes (X/L ($Y/H = 0$ and $Z/W = 0$), Y/H ($X/L = 0$ and $Z/W = 0$), Z/W ($X/L = 0$ and $Y/H = 0$)) within the unstably stratified cavity.	134
6.4	Profiles of the ratio of the sub-grid (SGS) viscosity to the resolved turbulent viscosity at three middle planes (X/L ($Y/H = 0$ and $Z/W = 0$), Y/H ($X/L = 0$ and $Z/W = 0$), Z/W ($X/L = 0$ and $Y/H = 0$)) within the unstably stratified cavity.	135
6.5	Instantaneous temperature contours at mid-width of the unstably stratified cavity obtained from LES: (a) plane (X, Y), (b) plane (X, Z), (c) plane (Y, Z).	137
6.6	Instantaneous temperature contours at mid-width of the unstably stratified cavity obtained from $k-\varepsilon$ model: (a) plane (X, Y), (b) plane (X, Z), (c) plane (Y, Z).	137
6.7	Instantaneous temperature contours at mid-width of the unstably stratified cavity obtained from SSG model: (a) (X, Y), (b) (X, Z), (c) (Y, Z).	137
6.8	Instantaneous temperature contours at mid-width of the unstably stratified cavity obtained from SST $k-\omega$ model. Left: 1 million cell mesh, right: finer LES mesh.	138
6.9	LES results: Iso-surfaces of Q-criteria coloured by vorticity in the unstably stratified cavity.	138
6.10	LES results: instantaneous temperature contours in the unstably stratified cavity.	138
6.11	LES results: instantaneous velocity contours inside the unstably stratified cavity. Left: V velocity, right: W velocity.	139
6.12	LES results: time averaged temperature contours at three longitudinal and spanwise cross-sections of the unstably stratified cavity.	140
6.13	LES results: time averaged wall-normal (U) velocity contours at three longitudinal and spanwise sections of the unstably stratified cavity.	140

6.14	LES results: time averaged wall-parallel (V) velocity contours at three longitudinal and spanwise sections of the unstably stratified cavity. . .	140
6.15	LES results: time averaged spanwise (W) velocity contours at three longitudinal and spanwise sections of the unstably stratified cavity.	141
6.16	LES and URANS results: vector plots of velocity magnitude at the spanwise mid-section ($Y/H = 0.5$) of the unstably stratified enclosure. . . .	141
6.17	LES results: time-averaged temperature profiles at four longitudinal locations and at two spanwise sections inside the unstably stratified enclosure. Left: $Z/W = 0.5$, right: $Z/W = 0.75$	142
6.18	URANS results: time-averaged temperature profiles at four longitudinal locations on the middle spanwise section ($Z/W = 0.5$) inside the unstably stratified enclosure.	143
6.19	LES results: time-averaged U velocity profiles at five longitudinal locations inside the unstably stratified enclosure. Left: $Z/W = 0.5$, right: $Z/W = 0.75$	145
6.20	LES results: time-averaged V velocity profiles at five longitudinal sections inside the unstably stratified enclosure. Left: $Z/W = 0.5$, right: $Z/W = 0.75$	146
6.21	URANS results: time-averaged velocity profiles at five longitudinal locations and at the middle spanwise section ($Z/W = 0.5$) inside the unstably stratified enclosure. Left: U velocity, right: V velocity.	147
6.22	Comparisons between resolved and modelled k of the wall-normal rms velocity fluctuation $\sqrt{u'^2}$ at the the middle location ($Y/H = 0.5$, $Z/L = 0.5$) inside the unstably stratified cavity.	150
6.23	Time-averaged rms wall-normal velocity $\sqrt{u'u'}$ at three longitudinal locations ($Y/H = 0.1, 0.5, 0.9$) inside the 15° unstably stratified cavity. . .	150
6.24	Time-averaged rms wall-parallel velocity $\sqrt{v'v'}$ at three longitudinal locations ($Y/H = 0.1, 0.5, 0.9$) inside the 15° unstably stratified cavity. . .	151
6.25	Time-averaged rms spanwise velocity $\sqrt{w'w'}$ at three longitudinal locations ($Y/H = 0.1, 0.5, 0.9$) inside the 15° unstably stratified cavity. . . .	151
6.26	Time-averaged turbulent shear stress $\overline{u'v'}$ at three longitudinal locations ($Y/H = 0.1, 0.5, 0.9$) inside the 15° unstably stratified cavity.	151
6.27	Time-averaged rms temperature $\sqrt{t't'}$ at three three longitudinal locations ($Y/H = 0.1, 0.5, 0.9$) inside the 15° unstably stratified cavity. . . .	152
6.28	Time-averaged rms wall-normal heat flux $\overline{u't'}$ at three longitudinal locations ($Y/H = 0.1, 0.5, 0.9$) inside the 15° unstably stratified cavity. . . .	152

6.29	Time-averaged rms wall-parallel heat flux $\overline{v't'}$ at three longitudinal locations ($Y/H = 0.1, 0.5, 0.9$) inside the 15° unstably stratified cavity. . . .	152
6.30	Time-averaged rms spanwise heat flux $\overline{w't'}$ at three longitudinal locations ($Y/H = 0.1, 0.5, 0.9$) inside the 15° unstably stratified cavity.	153
6.31	Time-averaged Reynolds stresses and heat fluxes along the spanwise cross-section, at the longitudinal central location ($Y/H = 0.5$) of the 15° unstably stratified cavity.	153
6.32	Time-averaged velocity profiles along the spanwise cross-section, at three longitudinal traverses inside the unstably stratified enclosure. Left: U velocity, right: V velocity.	154
6.33	LES results: Temporal power spectrum of temperature at the monitoring points A and B inside the 15° unstable stratified cavity.	156
6.34	LES results: Temporal power spectrum of U velocity at the monitoring points A and B inside the 15° unstable stratified cavity.	156
6.35	LES results: Temporal power spectrum of V velocity at the monitoring points A and B inside the 15° unstable stratified cavity.	156
6.36	LES results: Temporal power spectrum of W velocity at the monitoring points A and B inside the 15° unstable stratified cavity.	157
6.37	URANS results: Temporal power spectrum of temperature at the monitoring point B inside the 15° unstable stratified cavity.	157
6.38	URANS results: Temporal power spectrum of V velocity at the monitoring point B inside the 15° unstable stratified cavity.	158
6.39	Profiles of time-averaged local Nusselt number at the spanwise locations $Z/W = 0.5, 0.625, 0.75$ along the heated wall of the 15° unstable cavity.	159
6.40	Profiles of time-averaged local Nusselt number at the spanwise locations $Z/W = 0.5, 0.625, 0.75$ along the cold wall of the 15° unstable cavity.	160
7.1	Geometry of 3-D cavity inclined at 15° to horizontal (stable stratification). Location of plot lines are indicated.	162
7.2	Profiles of the ratio of the SGS viscosity to the resolved turbulent viscosity at three middle planes (X/L ($Y/H = 0$ and $Z/W = 0$), Y/H ($X/L = 0$ and $Z/W = 0$), Z/W ($X/L = 0$ and $Y/H = 0$)) within the stably stratified cavity.	164
7.3	LES results: instantaneous temperature contours inside the stably stratified cavity.	166
7.4	LES results: Iso-surfaces of Q-criteria coloured by vorticity inside the stably stratified cavity.	166

7.5	LES results: time averaged temperature contours at three longitudinal and spanwise sections of the stably stratified cavity.	166
7.6	LES results: time averaged wall-normal U velocity contours at three longitudinal and spanwise sections of the stably stratified cavity.	167
7.7	LES results: time averaged wall-parallel V velocity contours at three longitudinal and spanwise sections of the stably stratified cavity.	167
7.8	LES results: time averaged spanwise (W) velocity contours at three longitudinal and spanwise sections of the stably stratified cavity.	167
7.9	LES results: vector plots of velocity magnitude at three spanwise sections of the stably stratified enclosure.	168
7.10	LES results: time-averaged temperature profiles at four longitudinal locations and at two spanwise sections inside the stably stratified enclosure. Left: $Z/W = 0.5$, right: $Z/W = 0.75$	170
7.11	URANS results: time-averaged temperature profiles at four longitudinal locations on the central spanwise section ($Z/W = 0.5$) inside the stably stratified enclosure.	171
7.12	LES results: time-averaged U velocity profiles at four longitudinal locations and at two spanwise sections inside the stably stratified enclosure. Left: $Z/W = 0.5$, right: $Z/W = 0.75$	172
7.13	LES results: time-averaged V velocity profiles at four longitudinal locations and at two spanwise sections inside the stably stratified enclosure. Left: $Z/W = 0.5$, right: $Z/W = 0.75$	173
7.14	URANS results: time-averaged velocity profiles at five longitudinal locations and at the central spanwise section ($Z/W = 0.5$) inside the stably stratified enclosure. Left: U velocity, right V velocity.	174
7.15	Time-averaged rms wall-normal velocity $\sqrt{u'u'}$ at three longitudinal locations inside the 15° stably stratified cavity.	175
7.16	Time-averaged rms wall-parallel velocity $\sqrt{v'v'}$ at three longitudinal locations inside the 15° stably stratified cavity.	175
7.17	Time-averaged rms spanwise velocity $\sqrt{w'w'}$ at three longitudinal locations inside the 15° stably stratified cavity.	176
7.18	Time-averaged shear stress $\overline{u'v'}$ at three longitudinal locations inside the 15° stably stratified cavity.	176
7.19	Time-averaged rms temperature $\sqrt{t't'}$ at three longitudinal locations inside the 15° stably stratified cavity.	176

7.20	Time-averaged rms wall-parallel heat flux $\overline{v't'}$ at three longitudinal locations inside the 15° stably stratified cavity.	177
7.21	Time-averaged Reynolds stresses and heat fluxes along the spanwise cross-section, at the longitudinal central location ($Y/H = 0.5$) of the 15° stably stratified cavity.	177
7.22	Time-averaged velocity profiles along the spanwise cross-section, at three longitudinal traverses inside the stably stratified enclosure. Left: U velocity, right: V velocity.	178
7.23	LES results: Temporal power spectrum of Temperature at the monitoring points A and B inside the 15° stable stratified cavity.	179
7.24	LES results: Temporal power spectrum of U velocity at the monitoring points A and B inside the 15° stable stratified cavity.	180
7.25	LES results: Temporal power spectrum of V velocity at the monitoring points A and B inside the 15° stable stratified cavity.	180
7.26	LES results: Temporal power spectrum of W velocity at the monitoring points A and B inside the 15° stable stratified cavity.	180
7.27	Profiles of time-averaged local Nusselt number at the spanwise locations $Z/W = 0.5, 0.625, 0.75$ along the heated wall of the 15° stably stratified cavity.	181
7.28	Profiles of time-averaged local Nusselt number at the spanwise locations $Z/W = 0.5, 0.625, 0.75$ along the cold wall of the 15° stably stratified cavity.	182
8.1	Sketch of the annular horizontal penetration cavity and its position in the AGR.	186
8.2	Geometry and boundary conditions of 3-D annular penetration cavity. Location of plot lines are indicated.	186
8.3	3-D computational mesh for LES.	188
8.4	Ratio of the grid spacing to the Kolmogorov length scale along the gap between the inner and outer cylinders $(X - h) / (H - h) = 0$, $Z/L = -0.5$	189
8.5	Ratio of the SGS turbulent viscosity to the resolved viscosity along the gap between the inner and outer cylinders $(X - h) / (H - h) = 0$, $Z/L = -0.5$	189
8.6	Instantaneous temperature contours at fully turbulent conditions and at middle cross section $X/W = 0$ (magnified view of the penetration) and three cross sections $Z/L = -0.25, -0.5, -0.75$. (a) LES, (b) SST $k - \omega$, (c) $k - \varepsilon$	191

8.7	Instantaneous axial velocity (W) contours at fully turbulent conditions and at the middle cross section $X/W = 0$ (magnified view of the penetration) and three cross sections $Z/L = -0.25, -0.5, -0.75$. (a) LES, (b) SST $k - \omega$, (c) $k - \varepsilon$	191
8.8	Instantaneous vertical velocity (V) contours at fully turbulent conditions and at the middle cross section $X/W = 0$ (magnified view of the penetration) and three cross sections $Z/L = -0.25, -0.5, -0.75$. (a) LES, (b) SST $k - \omega$, (c) $k - \varepsilon$	192
8.9	Instantaneous spanwise velocity (U) contours at fully turbulent conditions and at the middle cross section $X/W = 0$ (magnified view of the penetration) and three cross sections $Z/L = -0.25, -0.5, -0.75$. (a) LES, (b) SST $k - \omega$, (c) $k - \varepsilon$	192
8.10	LES results: vector plots of velocity magnitude at different axial sections of the penetration enclosure.	193
8.11	LES results: Iso-surfaces of Q-criteria coloured by vorticity inside the penetration enclosure.	193
8.12	LES results: streamline plots inside the penetration enclosure.	194
8.13	LES results: dimensionless T , W , V and U contours across the central (X , Y) plane ($Z/L = -0.5$) of the annular penetration at different time steps.	195
8.14	LES results: dimensionless T , W , V and U contours across the central (Y , Z) plane ($X/W = 0$) of the annular penetration at different time steps.	196
8.15	LES results: dimensionless T , W , V and U contours across the central (X , Z) plane ($Y/D = 0$) of the annular penetration at different time steps.	197
8.16	LES and URANS: Time averaged contours of dimensionless temperature T and velocity components W , V , U at the central spanwise plane of the annular penetration, obtained from: (a) LES, (b) SST $k - \omega$, (c) $k - \varepsilon$	199
8.17	LES and URANS: Time averaged contours of dimensionless temperature T and velocity components W , V , U at the central axial plane of the annular penetration, obtained from: (a) LES, (b) SST $k - \omega$, (c) $k - \varepsilon$	200
8.18	Time-averaged dimensionless temperature at angular position 0° on three locations inside the penetration ($Z/L = -0.25, -0.5, -0.75$).	203
8.19	Time-averaged dimensionless axial velocity W at angular position 0° on three locations inside the penetration ($Z/L = -0.25, -0.5, -0.75$).	204

8.20	Time-averaged dimensionless vertical velocity V at angular position 0° on three locations inside the penetration ($Z/L = -0.25, -0.5, -0.75$).	205
8.21	Time-averaged dimensionless spanwise velocity U at angular position 0° on three locations inside the penetration ($Z/L = -0.25, -0.5, -0.75$).	206
8.22	Time-averaged dimensionless temperature at angular position 270° on three locations inside the penetration ($Z/L = -0.25, -0.5, -0.75$).	207
8.23	Time-averaged dimensionless axial velocity W at angular position 270° on three locations inside the penetration ($Z/L = -0.25, -0.5, -0.75$).	208
8.24	Time-averaged dimensionless vertical velocity V at angular position 270° on three locations inside the penetration ($Z/L = -0.25, -0.5, -0.75$).	209
8.25	Time-averaged dimensionless spanwise velocity U at angular position 270° on three locations inside the penetration ($Z/L = -0.25, -0.5, -0.75$).	210
8.26	Time-averaged dimensionless temperature variance $\overline{t't'}$ at angular position 270° on three locations ($Z/L = -0.25, -0.5, -0.75$).	212
8.27	Time-averaged dimensionless Reynolds stress component $\overline{w'w'}$ at angular position 270° on three locations inside the penetration ($Z/L = -0.25, -0.5, -0.75$).	212
8.28	Time-averaged dimensionless Reynolds stress component $\overline{v'v'}$ at angular position 270° on three locations inside the penetration ($Z/L = -0.25, -0.5, -0.75$).	212
8.29	Time-averaged dimensionless Reynolds stress component $\overline{u'u'}$ at angular position 270° on three locations inside the penetration ($Z/L = -0.25, -0.5, -0.75$).	213
8.30	Time-averaged dimensionless total turbulent kinetic energy at angular position 270° on three locations inside the penetration ($Z/L = -0.25, -0.5, -0.75$).	213
8.31	Time-averaged local Nusselt number around the inner cold tube on three locations inside the penetration ($Z/L = -0.25, -0.5, -0.75$).	214
8.32	Density power spectrum of temperature T and W, V velocity components at probe location $A((X - h) / (H - h) = 0, (Y - h) / (H - h) = -0.5, Z/L = -0.5)$ inside the horizontal annular penetration.	215
C.1	Notation for the spatial discretization.	251
A.1	2-D computational meshes used for grid sensitivity tests.	262
A.2	Mean temperature profiles at three heights inside the vertical cavity. Comparison between different 2-D computational meshes.	263

A.3	Mean velocity profiles at different heights inside the vertical cavity. Comparison between different 2-D computational meshes.	263
A.4	Rms velocity fluctuation profiles at different heights inside the vertical cavity. Comparison between different 2-D computational meshes. . . .	264
A.5	Local Nusselt number distribution along heated wall of the vertical cavity. Comparison between different 2-D computational meshes.	264
A.6	Dimensionless distance (y^+) distribution along horizontal and vertical walls of the the tall cavity. Comparison between different 2-D computational meshes.	265

List of Tables

2.2	Correlations $\overline{Nu}-Ra_L$ for Aspect ratios of 0.75 and 1.5 at different angles of inclination and $10^3 < Ra < 10^8$ [9].	57
3.1	Difference between RANS averaging and LES filtering.	90
5.1	Flow properties.	102
5.2	Thermal and dynamic boundary conditions for 2-D computations. . . .	103
5.3	Parameters of 2-D coarse and fine computational meshes.	103
6.1	Thermal and dynamic boundary conditions for 3-D calculation.	131
6.2	Characteristics of LES and URANS simulations.	132
8.1	Characteristics of LES and URANS simulations.	187
A.1	Parameters of computational grids used for 2-D grid sensitivity tests. .	261

Abstract

The University of Manchester

Dalila Ammour

Doctor of Philosophy

Highly Resolved LES and Tests of The Effectiveness of Different URANS Models for The Computation of Challenging Natural Convection Cases

September 2013

In the present thesis turbulent natural convection of air within different challenging test cases are investigated numerically by means of an unstructured finite volume code, *Code_Saturne* 2.0. First, flow within both two-dimensional vertical and inclined differentially heated rectangular cavities at 60° and 15° to the horizontal for an aspect ratio of $H/L = 28.6$ and Rayleigh number of 0.86×10^6 is computed using several high and low-Re models. Here the effectiveness of the RANS models in *Code_Saturne* is assessed through comparisons with a range of available experimental data. After some tests of thermal field inside vertical cavity, the “two-velocity-scale wall function” is chosen to be used with high-Re models. In both vertical and inclined cases the overall flow pattern appears similar, with a single circulation cell, and a boundary layer at the wall. The levels of turbulence energy are generally slightly lower in the inclined case. Most models give a reasonable prediction of measured Nusselt number, with the two low-Re approaches generally being closer to the data than the schemes employing wall functions. For the 15° inclined cavity, a multi cellular motion is shown by the high-Re models. Nevertheless, all the model predictions disagree with experimental data due to the presence in real flow of 3-D unsteady structures as found in Benard convection problems. These cannot, definitely, be reproduced using a 2-D geometry. Both highly resolved LES and unsteady RANS computations are then conducted, for turbulent natural convection of air inside 15° unstably and stably stratified cavities. In accordance with recent experimental data, the LES computations for both enclosures returned three-dimensional time-averaged flow fields. In the case of the unstably stratified enclosure, the flow is highly unsteady with coherent turbulent structures in the core of the enclosure. Results of LES computations show close agreement with the measured data. Subsequent comparisons of different URANS schemes with the present LES are used in order to explore to what extent these models are able to reproduce the large-scale unsteady flow structures. All URANS schemes have been found to be able to reproduce the 3-D unsteady flow features present in the 15° unstable cavity. However, the low-Re model tested as well as requiring a high resolution near-wall grid, also needed a finer grid in the core region than the high-Re models, thus making it computationally very expensive. Flow within the 15° stable cavity also shows some 3-D features, although it is significantly less unsteady, and the URANS models tested here have been less successful in reproducing this flow pattern. Finally, natural convection of CO_2 inside a horizontal annular penetration enclosure, which can be found in AGR’s, has been performed using a highly resolved LES and a set of RANS models. The Rayleigh number is 1.5×10^9 . RANS models agree with the present LES on the fact that the flow is unsteady and there are large-scale oscillations present which decrease in amplitude as one moves from the open towards the closed end of the annular enclosure. Overall heat transfer and thermal quantitative and dynamic results show that RANS schemes are in close agreement with the current LES data except some discrepancies shown by the high-Re model which can be returned to the limitation of the simple wall function used to predict such complex flow.

Declaration

No portion of the work referred to in the thesis has been submitted in support of an application for another degree or qualification of this or any other university or other institute of learning.

Copyright statement

- I.** The author of this thesis (including any appendices and/or schedules to this thesis) owns certain copyright or related rights in it (the “Copyright”) and s/he has given The University of Manchester certain rights to use such Copyright, including for administrative purposes.
- II.** Copies of this thesis, either in full or in extracts and whether in hard or electronic copy, may be made only in accordance with the Copyright, Designs and Patents Act 1988 (as amended) and regulations issued under it or, where appropriate, in accordance with licensing agreements which the University has from time to time. This page must form part of any such copies made.
- III.** The ownership of certain Copyright, patents, designs, trade marks and other intellectual property (the “Intellectual Property”) and any reproductions of copyright works in the thesis, for example graphs and tables (“Reproductions”), which may be described in this thesis, may not be owned by the author and may be owned by third parties. Such Intellectual Property and Reproductions cannot and must not be made available for use without the prior written permission of the owner(s) of the relevant Intellectual Property and/or Reproductions.
- IV.** Further information on the conditions under which disclosure, publication and commercialization of this thesis, the Copyright and any Intellectual Property and/or Reproductions described in it may take place is available in the University IP Policy (see <http://documents.manchester.ac.uk/DocuInfo.aspx?DocID=487>), in any relevant Thesis restriction declarations deposited in the University Library, The University Library’s regulations (see <http://www.manchester.ac.uk/library/aboutus/regulations>) and in The University’s policy on Presentation of Theses.

Acknowledgments

One of the joys of completion is to look over the journey past and remember people who have helped and supported me along this long but fulfilling road.

Foremost, I would like to express my sincere gratitude to my advisors Prof. Hector Iacovides and Dr. Tim Craft for their guidance, their patience, and their immense knowledge. Their support helped me during my research and writing of this report.

Besides my advisors, I would like to thank Prof. Dominique Laurence for his valuable encouragement and advices. I am grateful to Dr. Rob Prosser for his insightful comments during the past examinations which helped me improve the quality of my work.

I gratefully acknowledge the financial support from EDF energy (Barnwood).

My sincere thanks goes to Dr. Juan Uribe, Dr. Yacine Addad, Dr. Flavien Billard, and Dr. Stefano Rolfo for their help. My thanks also goes to the EDF team for their guidance to familiarise with the numerical code. I would like to thank the staff of the University of Manchester especially Mrs. Pat Shepherd for her help and kindness.

I thank my fellow office mates and my friends in Manchester and abroad for their great company and support.

And last, but not least, I would not have contemplated this road if not for my parents, who instilled within me a love of creative pursuits, science and language, all of which finds a place in this thesis. I would like to thank my family, my parents and my grand mother, for their love, comprehension, patience and their precious prayers.

Dedicate to my dear parents...

Nomenclature

Acronyms

AGR	Advanced Gas Reactors
CDS	Central Differencing Scheme
CFD	Computational Fluid Dynamic
CV	Control Volume
DNS	Direct Numerical Simulation
EVM	Eddy-Viscosity Model
GGDH	Generalized Gradient Diffusion Hypothesis
LES	Large Eddy Simulation
LRR	Launder, Reece and Rodi model
RANS	Reynolds Averaged Navier-Stokes
RMS	Root Mean Square
RSM	Reynolds Stress Model
SGS	Sub-Grid-Scale
SOLU	Second Order Linear Upwind
SSG	Speziale, Sarkar and Gatski
SST	Shear Stress Transport
UDS	Upwind Differencing Scheme
URANS	Unsteady Reynolds Averaged Navier-Stokes

Greek symbols

β	Thermal expansion coefficient
δ	Thickness of the boundary layer
η	Kolmogorov length scale
Γ	Molecular thermal diffusion
Γ_{eff}	Effective thermal diffusion
κ	Von Kármán constant
μ	Molecular dynamic viscosity
μ_t	Turbulent dynamic viscosity
ν	Kinematic viscosity
ν_t	Turbulent kinematic viscosity
ν_{SGS}	Sub-grid-scale eddy viscosity
ω	Dissipation rate per unit of turbulent kinetic energy
Ω_{ij}	Vorticity tensor
$\bar{\varepsilon}$	Average dissipation rate of turbulent kinetic energy k
ϕ_{ij}	Pressure strain-rate of Reynolds stresses
ρ	Density
τ_{ij}	Viscous stress
θ	angular position
Δ	Filter width
ε	Dissipation rate of turbulent kinetic energy k
ε_{ij}	Dissipation rate of Reynolds stress component

Latin symbols

\mathcal{P}_k	Production of turbulent kinetic energy
-----------------	--

$\overline{\mathcal{P}_k}$	Average production of turbulent kinetic energy
$\overline{u'_i t'}$	Turbulent scalar flux
$\overline{u'_i u'_j}$	Reynolds stress tensor
$\overline{U}, \overline{V}, \overline{W}$	Filtered velocity components
\underline{n}	Unit vector in the direction normal to the wall
g	Acceleration due to gravity
G_{ij}	Buoyant production of Reynolds stress $\overline{u'_i u'_j}$
G_k	Buoyant production of turbulent kinetic energy
Gr	Local Grashof number
k	Turbulent kinetic energy
l	Turbulent length scale
l_m	Characteristic length scale
Nu	Local Nusselt number
P	Pressure
Pr	Molecular Prandtl number
Pr_t	Turbulent Prandtl number
Ra	Local Rayleigh number
Re	Reynolds number
Ri	Richardson number
S	Strain rate invariant ($S = \sqrt{2S_{ij}S_{ij}}$)
S_{ij}	Strain tensor
T	Temperature
t	Time
u'_i	fuctuating velocity component

U, V, W	Mean velocity components
U_τ	Friction velocity
U_k	Friction velocity based on k ($U_k = C_\mu^{1/4} \sqrt{k}$)
x, y, z	Cartesian coordinates directions
y^+	Dimensionless distance to the wall ($y_k^+ = \frac{y U_k}{\nu}, y^+ = \frac{y U_\tau}{\nu}$)
y_ν	Viscous sublayer thickness
y_P	Distance from the near-wall node to the wall

Chapter 1

Introduction

1.1 Natural Convection

Convection is defined as the transport of mass and energy by potential gradients and by bulk fluid motion. Where the fluid flow arises from an external agent, the process is generally called forced convection. In contrast, fluid motion can also be induced by body forces such as gravitational, centrifugal, or Coriolis forces, and this process is generally called natural convection. Our attention will be focussed on natural convection where the flow results from an interaction of the density difference with the gravitational (or some other body force) field and is therefore inevitably linked with, and dependent on, the temperature and/or concentration fields. The main characteristics of most natural convection flows include: the absence of externally imposed velocity scales and the convection currents been generated due to the body forces acting on a fluid in which there is a density gradient. The density gradient is, in turn, often generated by temperature differences and the buoyancy force is due to gravity.

There are two main scenarios often encountered in the context of natural convection. In the first, a density gradient exists in a fluid in a direction that is parallel to and aligned with the gravity vector, whilst in the second the gradient is aligned but in the opposite direction to gravity. Such situations lead to “stable” or “unstable” density stratification of the fluid. In a stable stratification, less dense fluid is at the top and more dense fluid at the bottom. In the absence of other effects, convection will be absent, and the heat transfer problem can be treated as one of conduction. In an unstable stratification, in which less dense fluid is at the bottom, and more dense fluid at the top, provided the density gradient is sufficiently large, convection will start spontaneously and significant mixing of the fluid will occur.

1.2 Buoyancy-driven flows

Buoyancy effects occur, in principle, in any variable-density flow in a gravitational field. The importance of the buoyancy increases with density gradient and it is characterised by the size of the Richardson number, the simplest form of which is:

$$Ri = \frac{\Delta\rho}{\rho} \frac{gh}{u^2}, \quad (1.1)$$

where $\Delta\rho$ is the density difference that occurs over a typical (usually vertical) length scale h in a flow of velocity u . As this Richardson number, in Equation (1.1), tends to zero, so does the importance of buoyancy. Flows created entirely by buoyancy forces are referred to as buoyancy-driven flows. The range of buoyant flows that can occur in nature and in engineering practice is large and has been extensively considered. Natural convection flows occur generally in atmospheric and oceanic circulation, electric machinery, nuclear reactor cooling systems, heated or cooled enclosures, electronic power supplies, and so forth.

1.2.1 Buoyancy-driven flows in enclosures

Natural convection flows in enclosures are good examples of complicated flow types. These flows have a number of technical applications, including ventilation in buildings, cooling of electronic equipments, solar collectors, energy storage systems and cooling of nuclear reactors.

Over the past years, convection phenomena induced by body forces have been the subject of extensive research efforts. Internal problems such as the flow and heat transfer between parallel plates or in fluid-filled cavities are considerably more complex than the external forced or even mixed convection problems. Thus far, external problems have received a great deal of attention while relatively little has been done about internal ones. For confined natural convection problems, the boundary layers and core are closely coupled to each other and this coupling presents the main source of difficulty in obtaining analytical solutions to internal problems. In order to elucidate some important physical flow features, and industrial applications, of the natural convection in enclosures, Figure 1.1 shows the ensemble of test cases considered in the present thesis. First, the flow within two dimensional vertical tall-cavities is examined in order to test the different wall functions embedded in In-house and Open source CFD code *Code_Saturne* 2.0. The cavities are then tilted at 60° under stable stratification and

15° under unstable stratification in order to see the influence of the angle of inclination.

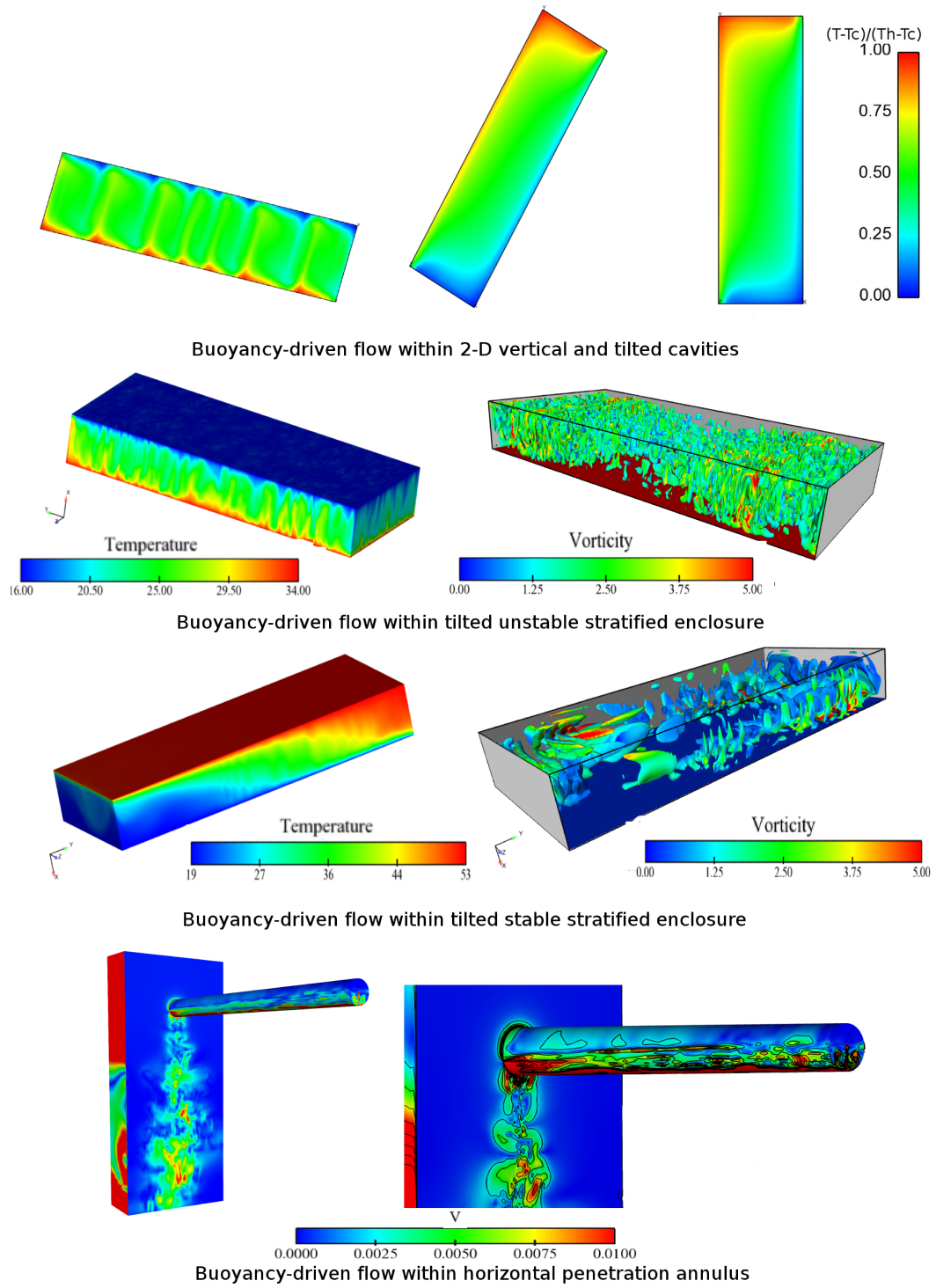


Figure 1.1: Buoyancy-driven flows within different enclosures investigated in the present thesis.

The second set of cases tested here are three-dimensional stable and unstable stratified tilted enclosures at 15° to the horizontal. LES and URANS techniques are used here and recent experimental data set is available for validation. A final industrial test case is considered, representing a horizontal annular penetration enclosure which can be found in the AGR's (Advanced Gas Cooled Reactors).

1.3 Computational Fluid Dynamics

Computational fluid dynamics is one of the tools (in addition to experimental and theoretical methods) available to solve fluid-dynamic problems, being the numerical approximation to the solution of mathematical models of fluid flow and heat transfer. With the advent of modern computers, computational fluid dynamics evolved from potential-flow and boundary-layer methods to more complex configurations. It is now used in diverse fields, including engineering, physics, chemistry, meteorology, and geology. The crucial elements of computational fluid dynamics are discretization, grid generation and coordinate transformation, solution of the coupled algebraic equations, turbulence modeling, and visualization.

Numerical solution of partial differential equations requires representing the continuous nature of the equations in a discrete form. Discretization of the equations consists of a process where the domain is subdivided into cells or elements (that is, grid generation) and the equations are expressed in discrete form at each point in the grid by using finite difference, finite volume, or finite element methods. The finite difference method requires a structured grid arrangement (that is, an organized set of points formed by the intersections of the lines of a boundary-conforming curvilinear coordinate system), while the finite element and finite volume methods are more flexible and can be formulated to use both structured and unstructured grids (that is, a collection of triangular, or other shaped, elements or a random distribution of points).

There are a variety of approaches for resolving the phenomena of fluid turbulence. The Reynolds-averaged Navier-Stokes (RANS) equations are derived by decomposing the velocity into mean and fluctuating components. An alternative is large-eddy simulation, which solves the Navier-Stokes equations in conjunction with a sub-grid turbulence model. The most direct approach to solving turbulent flows is direct numerical simulation, which solves the Navier-Stokes equations on a mesh that is fine enough to resolve all length scales in the turbulent flow. Unfortunately, direct numerical simulation is limited to simple geometries and low-Reynolds-number flows because of the limited capacity of even the most sophisticated supercomputers.

The final step is to visualize the results of the simulation. Visualization software permits generation of velocity vectors, pressure and velocity contours, streamline generation, calculation of secondary quantities (such as vorticity), and animation of unsteady calculations. Despite the sophisticated hardware, visualization of three-dimensional and unsteady flows is still particularly difficult. Moreover, many advanced visualization techniques tend to be qualitative, and the most valuable visualization often consists of simple x-y plots comparing the numerical solution to theory or experimental data.

Computational fluid dynamics has wide applicability in such areas as aerodynamics, hydraulics, environmental fluid dynamics, and atmospheric and oceanic dynamics, with length and time scales of the physical processes ranging from millimeters and seconds to kilometers and years. Vehicle aerodynamics and hydrodynamics, which have provided much of the impetus in the development of computational fluid dynamics, are primarily concerned with the flow around aircraft, automobiles, and ships. Nowadays, further applications include cooling of nuclear reactors and heat exchangers.

1.4 Turbulence and its modelling

1.4.1 Introduction

Turbulence is a phenomenon that occurs frequently in nature; it has, therefore, been the subject of study for several centuries. In 1510, Leonardo Da Vinci accompanied a drawing of the vortices shed behind a blunt obstacle with the following observation:

“Observe the motion of the water surface, which resembles that of hair, that has two motions: one due to the weight of the shaft, the other to the shape of the curls; thus, water has eddying motions, one part of which is due to the principal current, the other to the random and reverse motion”.

1.4.2 The phenomenon of turbulence:

Turbulence causes the appearance in the flow of eddies with a wide range of length and time scales that interact in a dynamically complex way (Figure 1.2). Turbulence is commonly encountered in almost all flows of practical engineering and environmental relevance:

- In most internal flows such as pipes and conduits, heat exchangers and other thermal and chemical equipment, pumps, compressors, turbines, internal combustion (IC) engines, hydraulic machinery and equipments, in building space...etc

- In most external flows such as around and in wakes of aircraft, ships, trains and road vehicles...etc
- In Earth's atmosphere (also on and around other planets) in winds at high and low altitudes (atmospheric boundary layer).
- In natural convection flows, rivers, lakes and oceans.

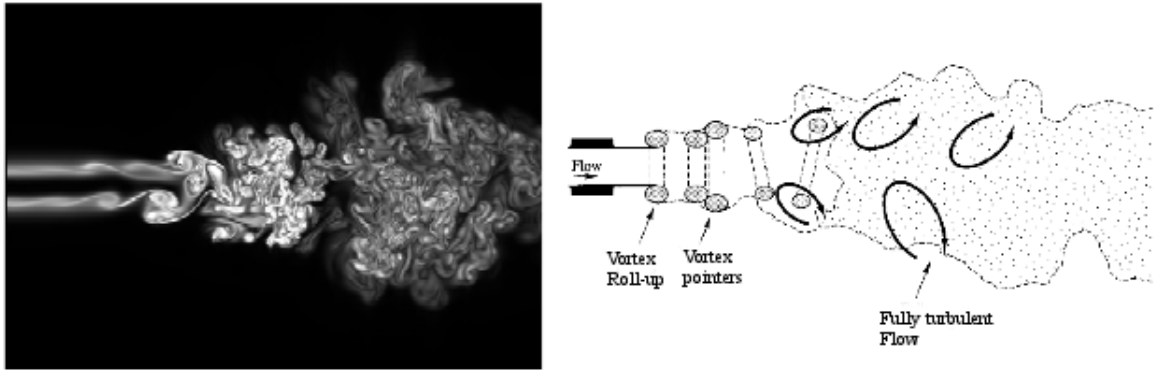


Figure 1.2: Turbulent flow [43].

Although turbulence is ubiquitous and a part of our daily life, there is no clear definition of turbulence. One can state that turbulence denotes a state of fluid flow in which all properties (velocity, pressure, density, temperature,...) fluctuate continuously in an irregular, disorderly, non-repeating manner.

Other definitions and statements on turbulence can be found in the literature.

1.4.3 Some features of turbulence

Turbulence is, by its nature, an irregular, disorderly, non-stationary, three-dimensional, highly non-linear, irreversible, stochastic phenomenon. Here are some interesting features of turbulence:

- Randomness which means disorder and non-repeatability.
- Vorticity: high concentration and high intensity of vorticity (rotation of fluid element, $\vec{\omega} = \vec{\nabla} \times \vec{v}$), the dynamics of which involves vortex stretching, elongation, spinning, breakup, coalescing and pairing, all playing important roles in turbulence interactions.

- Nonlinearity and three-dimensionality are basic features of turbulence, both originating in vorticity production due to vortex self stretching. This is a three-dimensional phenomenon which creates and maintains the turbulence vorticity.
- Continuity of eddy structure which is reflected in a continuous spectrum of fluctuations over a range of frequencies, i.e. a spectrum of eddies of varying size. Here an “eddy” means a vaguely identifiable fluid structure in swirling motion, revealed by flow visualisation and associated with a Fourier component of a particular frequency or wave length (“cellular pattern”).
- Energy cascade, irreversibility and dissipation: this presumes a continuous vortex stretching and a consequent one-directional transfer of energy towards smaller eddies until finally dissipated into heat by viscosity. Hence, turbulence cannot maintain itself and will decay rapidly if the source of its generation (a supply of energy) disappears.
- Intermittency: turbulence can interact with non-turbulent fluid flow, can appear intermittently in time at certain locations, or can occupy only parts of the flow domain. Its appearance in time and space is characterised by an intermittency factor.
- High diffusivity: fluctuations stretch and distort the fluid elements containing a lump of property inhomogeneity (hot spots of heat, species, momentum, vorticity) until the increase in surface area and in property gradient enables molecular effects to act efficiently, thus far enhancing, by several orders of magnitude, the mixing and transport of momentum, heat and species. The consequences of this are intensive spreading, mixing and transporting of momentum, heat and species.
- Local isotropy of turbulence structure: Large eddies keep memory of their origin and retain the imposed directional orientation. Cascade vortex stretching damps the transmission of information on the turbulence origin towards the smaller motion and, if the Reynolds number is sufficiently high, small scale motions lose their orientational preference and become statistically isotropic (Kolmogorov). This local isotropy (localised in spectral space to the high wave numbers) is also a very fortunate property of turbulence; it allows the neglect of viscosity in analysing and computing turbulence. If the source of turbulence is eliminated, the whole spectrum of turbulent motion tends to become isotropic (“isotropic turbulence”). In most cases turbulence is non-isotropic and inhomogeneous.

1.4.4 Scales of turbulence

Turbulence and its interactions are characterised by turbulence time- and length scales (or velocity scales). Different interactions are governed by different scales (eddies of different sizes and life-times). Turbulence generation and its transport (diffusion) are associated with large eddies, while the viscous dissipation occurs at the smallest turbulence scales. Large eddies in a shear layer or in an enclosure can grow until they fill the layer or the entire flow domain, hence the largest length scale can be related to the characteristic flow dimension. Large eddies are mostly responsible for transport of momentum, heat and species (diffusion length scale), and generation of turbulence in shear layers occurs due to the mean flow deformation and its interaction with the most energetic eddies (energy containing eddies which are close in size to the largest eddies). Through the process of their generation large eddies extract energy from the mean motion. These energy containing eddies are large in size though not the very largest (which are usually weak, with lower energy content) and they are most efficient in extracting energy from the mean motion. However, they also control the amount of energy which they give away to the smaller eddies (the start of the cascade process), which will ultimately be dissipated by viscosity (around the Kolmogorov scale). We denote the rate of dissipation of turbulent kinetic energy by ε . Hence, we can define the time and length scales of energy containing eddies in terms of the total content of turbulence kinetic energy k and its dissipation rate ε , i.e as $f(k, \varepsilon)$. Dimensional analysis yields time and length scales respectively

$$\tau = \frac{k}{\varepsilon}, \quad (1.2)$$

$$l_T = \frac{k^{3/2}}{\varepsilon}, \quad (1.3)$$

The velocity scale of turbulence is denoted by u_T , It is defined as:

$$u_T = K^{1/2} \quad (1.4)$$

where $K = \frac{1}{2} \overline{u'_i u'_j}$ is the mean kinetic energy in the turbulence.

One can summarise, in Figure 1.3, the three main sets of scales in a turbulent flow (there may be more if other physical phenomena take part); these are:

- the large scale, based on the problem domain geometry,

- the Taylor microscale, which is an intermediate scale, basically corresponding to Kolmogorov's inertial subrange, and
- the Kolmogorov (or dissipation) scale which is the smallest of turbulence scales.

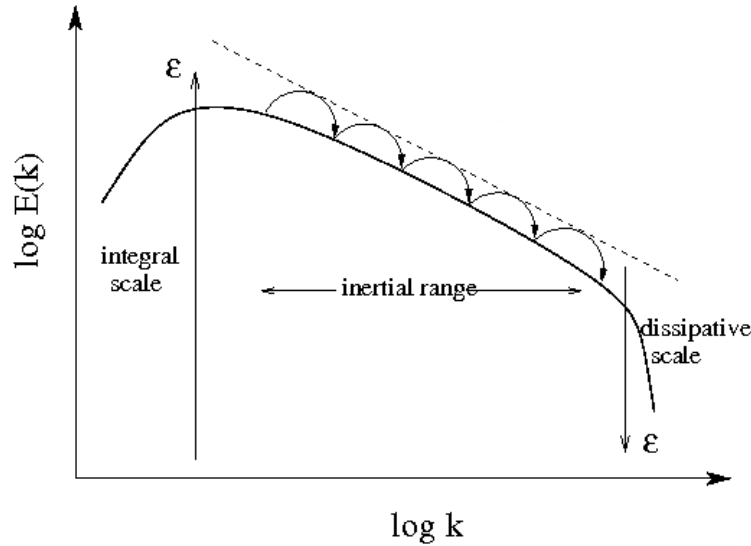


Figure 1.3: Turbulence energy wavenumber spectrum.

1.4.5 Modelling of turbulence

Over 100 years after 'Osborne Reynolds' experiments, turbulence is still one of the outstanding problems in applied mechanics. No useful analytical solutions of turbulent flows of engineering interest are available, although statistical theories of turbulence have provided good understanding of the scaling laws in various flow regimes. Experimental studies have also given insight in the understanding of the structure of turbulent flows. Flow visualisation has been particularly useful in the identification of the coherent eddies that are responsible for most of the energy production, especially in regions of high shear. Measurement techniques have progressed significantly: it is now possible to obtain single-point measurements of velocity and velocity gradient components using Laser-Doppler velocimetry or multiple wire anemometers, or velocity distributions in a plane, through Particle-Image or Particle-Tracking Velocimetry. Some empirical correlations for certain flows have been obtained, and can be used in some situations.

A widely-used approach to analysing turbulent flows is via Reynolds decomposition, in which averaging operation permits to decompose any quantity f into its mean part,

\bar{f} , and a fluctuating part, $f'(x, t) = f(x, t) - \bar{f}(x)$. The long-time average \bar{f} is defined as:

$$\bar{f}(x) = \lim_{T \rightarrow \infty} \frac{1}{T} \int_t^{t+T} f(x, t) dt, \quad (1.5)$$

where T is a time interval much longer than all the time scales of the turbulent flow.

If the flow is unsteady, time averaging cannot be used and it has to be replaced with ensemble averaging. The concept of this is to imagine a set of flows in which all of the variables that can be controlled (energy, boundary conditions etc.) are identical but the initial conditions are generated randomly. This will give flows that differ considerably from one another. An average over a large set of such flows is an ensemble average; In mathematical form written as:

$$\bar{f}(x, t) = \frac{1}{N} \sum_{n=1}^N f_n(x, t) dt, \quad (1.6)$$

If the averaging operation (1.5) is applied to the equations of motion, one obtains the well-known Reynolds-averaged Navier-Stokes equations (RANS), that describe the evolution of the mean quantities. RANS equations are represented in Chapter 3. The effect of turbulent fluctuations appears in a Reynolds stress term that must be modelled to close the system. A very wide range of models for the Reynolds stresses is available, ranging from simple, algebraic models, to $k - \varepsilon$ models, to full or algebraic Reynolds stress closures. The solution of the RANS equations is now used in engineering applications to predict the flow in fairly complex configurations. This approach, however, suffers from one principal shortcoming, the fact that the model for the Reynolds stresses must represent a very wide range of scales. While the small scales tend to depend only on viscosity, and may be somewhat universal, the large ones are affected very strongly by the boundary conditions (consider, for instance, the difference between the spanwise rollers present in mixing layers and wakes and the elongated streamwise vortices that are found in the near-wall region of a turbulent boundary layer). Thus, it does not seem possible, or at least may be a significant challenge, to model the effect of the large scales of turbulence in the same way in flows that are very different.

The direct numerical simulation (DNS) of turbulence is, in principle, the most straightforward approach to the solution of turbulent flows. In DNS, the governing Navier-Stokes equations are discretized and solved numerically. If the mesh and time step are fine enough to resolve even the smallest scales of motion, and the scheme is designed to minimise the numerical dispersion and dissipation errors, one can obtain an

accurate three-dimensional, time-dependent solution of the governing equations completely free of modeling assumptions, and in which the only errors are those introduced by the numerical approximation. DNS makes it possible to compute and visualise any quantity of interest, including some that are difficult or impossible to measure experimentally, and to study the spatial relationships between quantities of interest (for instance, vorticity and energy production), to obtain insight on the detailed kinematics and dynamics of turbulent eddies. DNS has been a very useful tool, over the past ten years, for the study of transitional and turbulent flow physics, but it also has some limitations. First, the use of highly accurate and high-order schemes is desirable to limit dispersion and dissipation errors; these schemes (spectral methods, for example) tend to have little flexibility in handling complex geometries and general boundary conditions. Secondly, to resolve all scales of motion, one requires a number of grid points in the three directions proportional to the $9/4$ power of the turbulent Reynolds number, Re_t , and the cost of the computation scales like $Re^{3/4}$. For these reasons, DNS has largely been limited to simple geometries (flat plate boundary layers, homogeneous flows) at low Reynolds numbers, and its application to engineering-type problems within the next decade appears unlikely.

Large-eddy simulation (LES) is a technique intermediate between the direct simulation of turbulent flows and the solution of the Reynolds-averaged equations. In LES, the contribution of the large, energy-carrying structures to momentum and energy transfer is computed exactly, and only the effect of the smallest scales of turbulence is modelled. Since the small scales tend to be more homogeneous and universal, and less affected by the boundary conditions than the large ones, there is hope that their models can be simple and require fewer adjustments when applied to different flows than similar models for the RANS equations. The attention in the present work is focussed on highly resolved LES computations of buoyancy-driven flows.

The extent of modelling for certain CFD approaches is illustrated in figure 1.4. It is clearly seen that models solving the Navier Stokes equations (DNS or LES) have the ability to provide better results. However they have a demand of much greater computer power than those models applying RANS methods.

One can summarise the modelling requirements of the above approaches as follows:

- DNS requires no modelling, but it demands resolution from the large scales all the way through the beginning of the dissipation scales.
- LES requires modelling of part of the inertial subrange and the dissipation scales. The amount of required modelling is set by the amount of resolution that can be

afforded.

- RANS requires modelling of everything from the integral scales into the dissipation range.

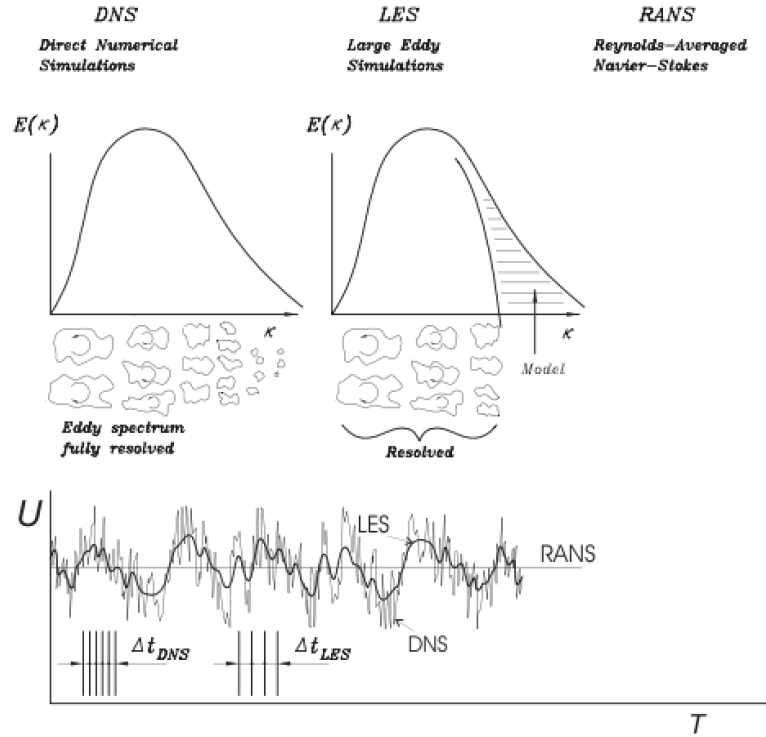


Figure 1.4: Schematic of comparisons between DNS, RANS and LES [43].

1.5 Objectives

Buoyant flows occur in a variety of engineering cooling systems including ventilation in buildings, cooling of electronic equipments, thermal design of furnaces, energy storage systems and cooling of nuclear reactors. It is therefore essential to have reliable and efficient numerical simulation models. Buoyant flows, even in simple geometries, tend to be physically complex, which poses severe challenges to RANS turbulence models used widely by industry. The principal objective of this research is to employ the Large Eddy Simulation (LES) method to produce accurate simulations of buoyancy-driven flows in complex internal systems found in engineering applications, both to examine

the flow physics, and to provide data for use in testing and validating RANS modelling approaches. As a first pair of test cases, 2-D buoyancy driven flow within differentially heated vertical and inclined enclosures at 60° and 15° to the horizontal have been computed using Unsteady RANS modelling approaches. The aim of this stage is to test the performance of different high- and low-Reynolds number turbulence models embedded in *Code_Saturne* 2.0, together with the different wall function treatments available.

3-D LES and URANS computations of the flow within a 15° inclined cavity under both unstable and stable stratifications have then been conducted. Finally, a more complicated test case is considered here, the horizontal penetration enclosure, which can be found in the AGR's. Measured data are not available for this case, so a highly resolved LES and URANS techniques have both been used to investigate the flow pattern in such a geometry.

In these latter cases the results from the URANS approaches are compared with the LES data, to allow conclusions to be drawn on the model's performance for a range of buoyancy-driven flows.

1.6 Outlines of the thesis

The work presented here is organised as follows: after a detailed introduction presented in this Chapter, which includes introductory definitions of natural convection, buoyancy-driven flows, CFD and turbulence, together with its scales and modelling approaches, Chapter 2 contains a detailed literature survey of previous investigations carried out by researchers on buoyancy-driven flows inside different geometries, including both experimental and numerical studies.

Chapter 3 gives details of the governing equations and modelling procedures and physical models used for the present computations, with particular attention given to the URANS models and wall functions implemented in *Code_Saturne* 2.0. Details of the LES filtering and modelling are also given here. Specific forms of particular turbulence models employed are given in Appendix B.

The Finite Volume Method, which is widely applied as a discretization strategy in CFD codes, will be presented in Chapter 4, together with details of the particular numerical discretization and solution treatments employed in *Code_Saturne* 2.0.

Chapter 5 includes a description, results and discussion of the numerical simulation of 2-D vertical and inclined cavities using different RANS models embedded in *Code_Saturne* 2.0. Models tested include high-Reynolds number $k - \epsilon$ and Reynolds

stress transport models, with different wall function treatments, and low-Reynolds number models such as the SST $k - \omega$ scheme and elliptic blending models including the $\varphi - f$ and newer $\varphi - \alpha$ schemes.

Chapter 6 considers the computations of flow within 3-D enclosures tilted at 15° at the horizontal under unstable stratification, using a high resolution LES and URANS models. The corresponding case at 15° with stable stratification is covered in Chapter 7.

In Chapter 8, LES and URANS computations of buoyancy-driven flow in the industrial test case of a horizontal annular penetration will be considered. Detailed qualitative and quantitative results, including comparisons between URANS and LES predictions will be presented.

Finally, Chapter 9 includes conclusions together with suggestions for future work.

Chapter 2

Literature Survey

2.1 Experimental investigations

2.1.1 Vertical tall cavities

Warner [89] investigated experimentally turbulent natural convection in air flow at low pressure along a vertical heated flat plate, for Rayleigh numbers up to 10^{12} . Extensive measurements of the temperature field indicated a good similarity in the temperature profile when compared on the basis of the natural coordinate. The use of a power law temperature profiles was shown to be undesirable for the case of turbulent natural convection. Except at the wall itself, the turbulent mean temperature profile was well represented in natural coordinates by a laminar profile over a great portion of the thermal layer. The primary effect of increased distance along the plate upon the temperature profiles appeared to be a thickening of the thermal layer, with all profiles taking the same basic form for moderate distances from the wall.

Measurement data on temperature fields and heat flux is extensive, ranging from well-known experiments of Mac Gregor and Emery [63] who investigated the flow and heat transfer in a vertical two dimensional enclosure with the height-to-width ratio, H/W , greater than unity, to the large models of domestic rooms investigated by Yguel [93]. However, the low velocities involved were difficult to measure, as hot wire probes generated their own local convection and were insensitive to the flow reversals present in the flow.

Yin et al. [94] investigated experimentally natural convection in an air layer contained in a rectangular cavity having side walls at different temperatures and for various aspect ratios ranging from 4.9 to 78.8. The Grashof number based on layer thickness ranged from 1.5×10^3 to 7.0×10^6 . The measured temperature profile shapes were

found to be relatively independent of the temperature difference between the two vertical plates for each aspect ratio. Temperature inversions, believed to be caused by a high rate of tangential convection of heat relative to the horizontal transport, were observed in several test conditions.

Despite the widespread occurrence of natural convection in enclosed regions, the availability of good quality experimental data involving both temperature and velocity fields is still very limited. Cheesewright and Ziai [18], Bowles and Cheesewright [14] and Cheesewright and King [17] carried out experimental investigations on two-dimensional buoyant cavity flows. They studied rectangular cavities to produce experimental data for validation of two-dimensional computer codes. The working fluid was air and the Rayleigh number developed, based on the cavity height, was 10^{10} . They produced a large amount of measurements of mean and fluctuation values of velocity and temperature in the cavity. LDA and thermocouples were employed to carry out measurements of velocity and temperature, respectively. They observed that the flow near the hot and cold walls was not symmetric to each other. Also they reported relaminarisation on the floor wall and then transition to turbulence at 20% of the way up the hot wall. The measurements of velocity fluctuations showed a reduction at the bottom of the cavity, which confirmed the relaminarisation phenomena. Mergui et al. [20] investigated a nearly square cavity. The flow was only transitional, with a stratified quiescent flow in the core even at a Rayleigh number based on cavity width, W , of $Ra = 2.3 \times 10^9$.

Dafa'Alla and Betts [29] and Tian et al. [82] investigated the flow in a simple rectangular cavity, with opposing vertical walls held at different temperatures. The existence of turbulence within such a cavity depends on the aspect ratio ($A = \frac{H}{W}$) and Rayleigh number. In the first of the above studies, the aspect ratio was 28.6 and $Ra = 10^6$, and the flow in the core region was fully turbulent with rms turbulence levels over half the maximum mean vertical velocity. Most experimental work was undertaken to provide data under idealised thermal boundary conditions, such as constant heat flux active walls and adiabatic or perfectly conducting passive ones. Dafa'Alla and Betts [29] attempted to impose a constant heat flux on the hot wall, with an isothermal cold wall and all other walls were insulated. They encountered particular difficulties at the junction between the electrically heated hot plate and the nominally adiabatic top and bottom walls. These problems are typical of all attempts to reproduce idealised boundary conditions. Although the results of Ince and Launder [52] in modelling these flows computationally were encouraging to the turbulence modellers, the uncertainty in boundary layer definition in regions of rapidly changing temperature gradient (e.g, at one end of the nominally adiabatic top and bottom surfaces) meant that one did not

know whether the relatively minor differences between the experiment and the computation should be attributed to the turbulence model or problems with the experiment. The apparatus of Dafa'Alla and Betts [29] was rebuilt to ensure well-defined, readily measurable, and smooth varying temperatures within the boundary walls. Conduction within the walls became part of the problem, but there was a clear unambiguous specification. Moreover, the flow was controlled to be two-dimensional over most of the enclosure volume.

Betts and Bokhari [11] designed an experiment to overcome the difficulties which were discussed previously and to provide an appropriate benchmark for modellers. They investigated the natural convection of air in a tall differentially heated rectangular cavity of 2.18m high by 0.076m wide by 0.52m in depth. The experiments were performed with temperature differentials between the vertical plates of 19.6°C and 39.9°C , giving Rayleigh numbers based on the cavity width of 0.86×10^6 and 1.43×10^6 . Under these conditions, the flow in the core of the cavity is fully turbulent and property variations with temperature were comparatively small. Mean and turbulent temperature and velocity variations within the cavity were measured, together with heat fluxes and turbulent shear stresses. The temperature and flow fields were found to be closely two-dimensional, except near to the front and back walls, and anti-symmetric across the diagonal of the cavity. The provision of partially conducting top and bottom walls successfully overcame the problems associated with trying to achieve an adiabatic surface there. The differing thermal stratification between the flow across the top and bottom, which plagued previous investigations, was also overcome.

2.1.2 Vertical square cavities

Kirkpatrick and Bohn [57] experimentally studied natural convection at high Rayleigh numbers in a cubical enclosure with various thermal boundary conditions. All of the experiments were variations of the heating-from-below case. Their results indicated that the heated floor promoted mixing in the enclosure and reduced the thermal stratification. By increasing the Rayleigh number, the thermal stratification decreased at the core of the cavity and then changed suddenly at $Ra \approx 0.65 \times 10^{10}$. The thermal stratification was also not symmetric about the centre-line.

Tian and Karayiannis [82] conducted an experimental study of low level turbulent natural convection in an air filled vertical square cavity. The dimensions of the cavity were $0.75\text{m} \times 0.75\text{m} \times 1.5\text{m}$, reported to give two-dimensional flow. The hot and cold walls of the cavity were isothermal at 50°C and 10°C , respectively, giving a Rayleigh number of 1.58×10^9 . The temperature and velocity distributions were nearly anti-

symmetrical, with fairly good agreement in velocity and temperature profiles at mid-height near the vertical hot and cold walls. Slight differences were found at mid-width. It was concluded that the flow was limited to a narrow strip along the walls where the velocity and temperature changed sharply. In the vertical boundary layer, the velocity reached its maximum value between the buoyant sub-layer and the outer layer and decreased to negative values at the outer edge of the boundary. The negative values were the result of four vortices, two forming in each of the hot top and cold bottom corners. The flow in the cavity core was stationary and stratified.

Ampofo and Karayiannis [5] carried out an experimental study of low-level turbulent natural convection in an air filled vertical square cavity, figure 2.1. they used the same rig and set-up as Tian & Karayiannis [82]. The local velocity and temperature were simultaneously measured at different locations in the cavity and both mean and fluctuation quantities were presented together with the local and average Nusselt numbers, the wall shear stress as well as the turbulent kinetic energy and the dissipation rate of the temperature variance. It was concluded that for this kind of cavity, the inner boundary layer along the isothermal walls was less than 7% of the outer boundary layer thickness. Also, the viscous layer, which was next to the isothermal walls, was about 3mm thick (60% of the inner layer) whilst the conductive layer was 2mm thick. The turbulent quantities were almost negligible in the conductive layer, which confirmed that the heat transfer in this region was by pure conduction. The local Nusselt number reached a maximum at the bottom of the hot wall and at the top of the cold wall because of a thinner thermal boundary there. They showed also that at the bottom of the hot wall (and top of the cold wall) the turbulent heat flux was effectively zero. The absence of a turbulent heat flux in these regions suggested that the lower part of the hot wall (and upper part of the cold wall) boundary layer had many of the characteristics of a laminar flow. In general, the horizontal turbulent heat flux was one order of magnitude smaller than the vertical turbulent heat flux.

Valencia et al. [86] reported experimental measurements and numerical simulations of natural convection in a cubical cavity heated from below and cooled from above at turbulent Rayleigh numbers using water as a convective fluid ($Pr = 6.0$). Direct numerical simulations (DNS) were carried out, assuming the Boussinesq approximation, using a second-order finite volume code ($10^7 \leq Ra \leq 10^8$), and taking into consideration heat conduction through the sidewalls. The particle image velocimetry technique was used to measure the velocity field at Rayleigh numbers equal to 10^7 , 7×10^7 and 10^8 . There was general agreement between the predicted time averaged local velocities and those experimentally measured.

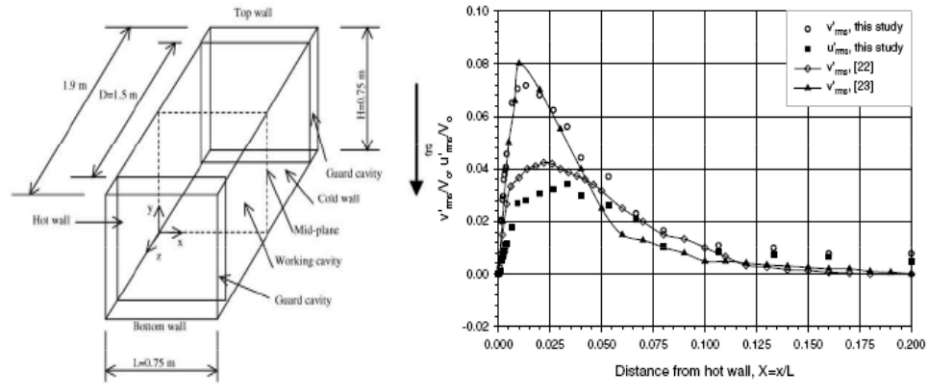


Figure 2.1: Schematic diagram of test cavity and velocity field, profiles of rms velocity fluctuations at $y/H=0.5$ [5].

2.1.3 Other vertical cavities

The effects of backward-facing and forward-facing steps on turbulent natural convection along a vertical heated flat plate, figure 2.2, were examined experimentally by Abu-Mulaweh [1]. Laser-Doppler velocimetry and cold wire anemometry were used to, respectively, measure simultaneously the time-mean turbulent velocity and temperature distributions and their turbulent fluctuation intensities. The experiment was carried out for a step (backward-facing and forward-facing) height of 22mm and a temperature difference between the heated walls and the free stream (ambient air) of $30^{\circ}C$. Results reveal that the maximum local Nusselt number occurred in the vicinity of the reattachment region. For the backward facing step this maximum was approximately twice that found on a flat plate under similar flow and thermal conditions, whilst for the forward-facing step it was two and a half times the flat plate value.

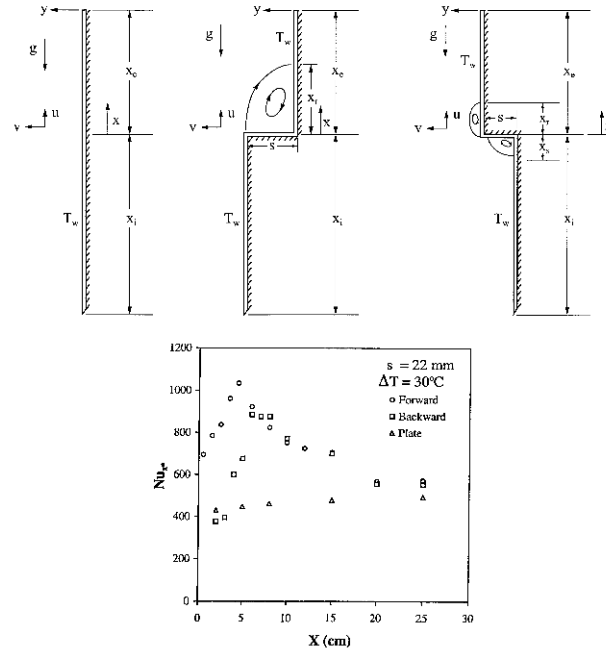


Figure 2.2: Schematic of the flow geometries and the local number variation [1].

Ampofo [6] studied experimentally turbulent natural convection of air in non-partitioned and partitioned cavities with differentially heated vertical and conducting horizontal walls, figure 2.3. The dimensions of the cavity, which were 0.75 m high, 0.75 m wide and 1.5 m deep, resulted in two-dimensional flow in the mid-plane of the cavity. The hot and cold walls of the cavity were isothermal at 50 and 10°C, respectively, giving a Rayleigh number of 1.58×10^9 . Five partitions of a higher thermal conductivity material than that of the cavity wall were installed on the hot wall. The partitions were 150mm long, 3mm thick and covered the depth of the cavity. The local velocity and temperature were systematically measured at different locations in the cavity using a laser Doppler anemometer and a micro-diameter thermocouple. Both mean and fluctuation quantities were presented. The most important conclusion from this study was the effect of the partitions on the heat transfer rates along the hot wall. The local average Nusselt number was obtained and indicated that partitions of this length tended to reduce the heat transfer rates along the hot wall compared with similar cavities without partitions. The velocity, temperature and the turbulence results obtained in the partitioned cavity differed substantially from the corresponding results in the non-partitioned cavity with the same dimensions and under the same experimental conditions. Due to the high heat transfer input from the hot partitioned wall, all the flow and thermal field quantities obtained in the cold wall boundary layer of the partitioned cavity had higher peaks and

thicker boundary layer structure than the corresponding values in the non-partitioned cavity.

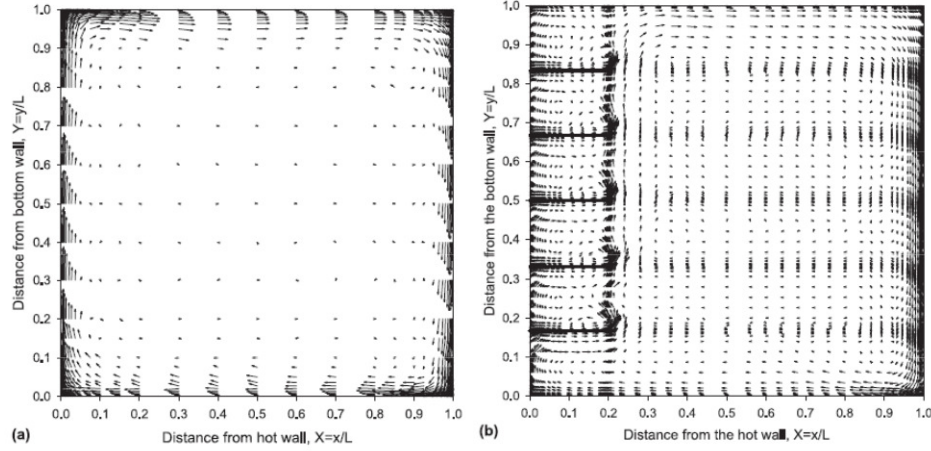


Figure 2.3: Vector plot of mean velocity profiles. (a) Non-partitioned cavity (scale: 0.038 m/s/mm). (b) Partitioned cavity (scale: 0.080 m/s/mm [6]).

2.2 Numerical investigations

2.2.1 Vertical tall cavities

William and Capp [41] analyzed the turbulent natural convection boundary layer next to a heated vertical surface by classical scaling arguments. It was shown that the fully developed turbulent boundary layer must be treated in two parts: an outer region consisting of most of the boundary layer in which viscous and conduction terms were negligible and an inner region in which the mean convection terms were negligible. The inner layer was identified as a constant heat flux layer. An overlap region, which was called the buoyant sublayer, was shown to exist at high Rayleigh number values. In this region the temperature and the velocity were dependent on the cube root of distance from the wall. Regions of linear variation of velocity and temperature existed next to the wall and they were termed the conductive and thermo-viscous sublayers. Heat transfer and friction laws were derived for the fully developed boundary layer.

Evren-Selamet et al. [39] conducted a numerical study on natural convection in a vertical slot with a narrow upper section. The fluid (air) in the slot was initially at a uniform temperature and motionless. The top and bottom were insulated. The left

wall was subjected to a step change in temperature, while the right wall was kept at the initial temperature. The resulting flow patterns and heat transfer for different Rayleigh numbers were numerically studied by a projection method involving a Godunov-type discretization for convective terms. Transient solutions of the equations of momentum and energy have been obtained. The Godunov discretization of the convective terms was shown to provide an accurate representation of the flow and temperature fields in buoyancy-driven flows. The numerical results were in good agreement with available predictions obtained by other investigators. The study demonstrated the existence of different flow regimes, which changed from conduction-dominated to convection-dominated as the Rayleigh number was increased. It was concluded that the laminar solution at high Rayleigh numbers, greater than 10^6 , showed a thermal stratification in the core which was almost independent of the Rayleigh number and seemed to vanish totally for infinitely large Rayleigh number. Differences between the turbulence model predictions were largest for quantities that are determined in the inner layer of the vertical boundary layer, the wall heat transfer and the wall shear stress. Differences in the prediction of the vertical velocity maximum, the turbulent viscosity maximum, the horizontal velocity at half the cavity width and the thermal stratification in the core were small. Differences between the model predictions were larger for water than for air.

Peeters and Henkes [74] investigated numerically the turbulent natural convection boundary layer for air along a heated vertical plate with an algebraic (ASM) and fully differential (RSM) Reynolds-stress model. Sensitivity tests on the RSM constants showed which constants dominated the mean-flow prediction, and which constants only affected turbulence quantities. Modifications were employed to improve predictions of the near-wall turbulence. RSM calculations of the turbulence quantities agreed well with available experimental data. ASM results were poorer, but in qualitative agreement with experiments. They concluded that, in natural-convection boundary layers, the local-equilibrium assumption had only limited applicability. Furthermore, the eddy-viscosity concept used in the $k - \varepsilon$ model (KEM) was also tested. The KEM gave good mean-flow results, but for a good prediction of the detailed turbulence structure the RSM was needed.

Ince and Launder [52] studied numerically turbulent natural convection in a cavity of 5:1 aspect ratio, in which the heated and cooled surfaces (long sides) were vertical. An extended form of $k - \varepsilon$ eddy viscosity model was adopted, which had earlier been employed to study the same flow assuming two-dimensional (2-D) motion with perfectly insulated end walls. They considered the three-dimensional (3-D) behavior and allowed

realistic heat losses through the nominally adiabatic surfaces. The study explored the extent to which failures of earlier predictions of the cavity flows of Cheesewright and co-workers [14, 18, 17] could be attributed to the fact that these studies did not account for heat losses from nominally adiabatic surfaces, or for 3-D effects. It was, indeed, found that accounting for both these factors led to much closer agreement with experiment than hitherto. Indeed, they found there was a significant rise in Nusselt number very close to the side walls associated with the appreciable down flow induced by heat leakage through the side wall. The Nusselt numbers at the cold wall were appreciably low, simply because 20% of the heat entering the cavity through the heated wall left through the insulated surfaces. Comparing 3-D with 2-D computations, the temperature profiles were similar in the lower half of the cavity, although near the top of the cavity the core fluid in the 2-D computations became significantly warmer.

Hanjalić [44] studied numerically the flow pattern and the temperature field in empty and partitioned, two-dimensional (2D), rectangular enclosures at Rayleigh numbers $10^{10} \sim 10^{12}$, using an extended algebraic model for turbulent heat transport $\overline{\theta u_i}$. The geometries considered, with partial, downward-extending and full adiabatic and conductive vertical partitions, imitate neighbouring rooms in real buildings with a doorway in between. Two closure levels were applied: three- and four-equation models, $k - \varepsilon - \overline{\theta^2}$ and $k - \varepsilon - \overline{\theta^2} - \varepsilon_\theta$, both incorporating low-Reynolds number modifications, which allowed integration up to the wall and, in principle, prediction of turbulence transition. The computations confirmed earlier experimental findings that in this range of Rayleigh numbers, the flow became turbulent, but the turbulence remained confined to only some regions of the enclosure. Noticeable improvements in capturing details of the turbulent field, particularly at transitional Rayleigh numbers, were achieved with the algebraic model for turbulent heat transport $\overline{\theta u_i}$, with both the three- and four-equation models, as compared with employing the eddy diffusivity hypothesis. It was concluded that for all cases, the applied model gave plausible mean temperature and velocity fields. For enclosures filled with air at higher Rayleigh numbers the computations in undivided and partitioned 2-D enclosures reproduced a persistent turbulence in some parts of the enclosures. The low-Re $k - \varepsilon$ model reproduced a turbulent regime erratically and only at substantially higher Ra numbers. The algebraic flux model proved capable of generating and maintaining the mechanical and thermal turbulence. In cases with side heating and cooling, the turbulence was found in regions adjacent to the non-adiabatic walls, influencing substantially the averaged heat transfer across the enclosure. In all cases considered, the computations yielded strong variations of the Nusselt number along the non-adiabatic walls, with a sudden increase at the onset of turbulence transition, the

location of which depended on the Ra number.

Dol [34] used results of direct numerical simulation (DNS) of turbulent natural convection between two differentially heated infinite vertical plates for $Ra = 5.4 \times 10^5$ to assess models of various terms in the transport equations for the turbulent heat-flux vector $\overline{\theta u_i}$ and the temperature variance $\overline{\theta^2}$. He also presented results of the computation of natural convection in a tall cavity. The hypotheses used to truncate a differential model into algebraic forms were examined, together with a fully differential and a four-equation $k - \varepsilon - \overline{\theta^2} - \varepsilon_{\theta\theta}$ algebraic models. Computations yielded acceptable agreement with experimental and DNS data. It was concluded that a term-by-term comparison of the transport equations for the turbulent heat flux and the temperature variance led to the conclusion that most models of individual terms poorly reproduced the DNS of the corresponding terms in the exact equations. Dol also mentioned that none of the algebraic expressions reproduced the heat-flux components, this was caused by mutual compensation of errors in modelling individual terms.

Versteegh [88] performed Direct Numerical Simulation (DNS) of natural convection flow in an infinite, differentially heated, vertical channel at four Rayleigh numbers varying from 5.4×10^5 to 5.0×10^6 for $Pr = 0.709$. He focussed their attention on the turbulent Reynolds-stresses, heat fluxes and variance and their budgets. He interpreted the budgets in terms of the physical processes that determine this flow. In addition, he calculated the stresses and budgets based on the structures found from linear stability analysis of the laminar solution of this problem. The latter budgets were compared with the budgets for fully developed turbulent flow, in order to estimate the influence of the large scale coherent structures on the budgets. He found that in the near-wall region, the shear production of turbulence was negative. The turbulent budgets showed that the flow can be divided into a near wall region, where diffusive transport balances dissipation, and an outer region, where (pressure) production balances dissipation. Only in the region near the velocity maximum did advective transport became important. For the turbulent case, the large temperature fluctuations near the velocity maximum, combined with the high Rayleigh number, induced forces that destroyed the original flow pattern.

Liu & Wen [62] developed a new buoyancy-modified turbulence model on the basis of the four-equation model, $k - \varepsilon - \overline{\theta^2} - \varepsilon_{\theta}$, of Hanjalić [44]. The strong anisotropy of Reynolds stresses due to buoyancy effects in the vertical boundary layers was considered by inclusion of a newly devised “return-to-isotropy” concept in the pressure-strain correlation. The wall-reflection functions were also modified. The new model was tested in buoyancy-driven cavity flows. It demonstrated significant improvements in captur-

ing the non-isotropy of Reynolds-stresses and turbulent heat flux in vertical boundary layers. It was concluded the model was capable of predicting the lateral extent of the turbulent boundary layer near the vertical wall. Significant improvement was achieved on the predictions of velocity fluctuations for the region near the vertical walls.

Peng [75] investigated numerically a turbulent natural convection flow ($Ra = 1.58 \times 10^9$) in a confined cavity with two differentially heated side walls by means of Large Eddy Simulation (LES). The mean flow in the cavity was characterized by stable thermal stratification and a relatively low turbulence level. Good agreements were found when comparing with measurements. Nevertheless, there were some discrepancies in the prediction of turbulence statistics, particularly in the outer region of the near-wall flow where the boundary layer interacts with the recirculating core region. In the viscous/conductive sublayer of the boundary layer close to the heated/cooled vertical walls the flow tended to form streak-like structures, which did not however appear in the near-wall flow along the horizontal top and bottom walls.

Hanjalić [45] reviewed some specific modelling issues related to buoyant flows in the context of one-point closures. The inadequacy of isotropic eddy-diffusivity models was discussed first, followed by the rationale of the second-moment modelling and its term-by-term scrutiny based on Direct Numerical Simulations (DNS) data. Algebraic models based on a rational truncation of the differential second-moment closure were proposed.

Tieszen et al. [83] compared results from two-dimensional calculations using the $\overline{v^2} - f$ and a $k - \varepsilon$ model with data for two geometries, the vertical flat plate and the 5:1 height: width box with constant temperature hot and cold side walls. The results showed that the $\overline{v^2} - f$ model was at least as good as the $k - \varepsilon$ model with a two-layer wall treatment. The $\overline{v^2} - f$ model gave good prediction for the vertical flat plate data without changes. However, in the hot-wall, cold-wall, box it had a delayed transition with respect to the data and significantly under-predicted the heat transfer. With the addition of the GGDH for modelling the heat flux, the overall heat transfer comparisons improved.

Corcione [26] studied numerically steady laminar natural convection in air-filled 2-D rectangular enclosures heated from below and cooled from above for a wide variety of thermal boundary conditions at the sidewalls. A specifically developed numerical model based on the SIMPLER algorithm was used for the solution of the mass, momentum and energy transfer governing equations. Simulations were performed for several values of both the width-to-height aspect ratio of the enclosure in the range between 0.66 and 8, and the Rayleigh number based on the cavity height in the range between 10^3

and 10^6 . The temperature distributions and the heat transfer rates were analyzed. In particular, with reference to the typical configuration where the sidewalls are adiabatic, it was found that the heat transfer effectiveness of the bottom wall increased (or slightly decreased) as each adiabatic sidewall was replaced by a cooled (or a heated) sidewall. An opposite behavior was observed for the top wall. The heat transfer rate results obtained were expressed through dimensionless correlation-equations. Once the Rayleigh number was assigned, for all the thermal configurations investigated, the heat transfer rates from the top and bottom walls tended asymptotically to the same value (typical of horizontal air layers) as the cavity aspect ratio increased. The local heat fluxes from the top and bottom walls were strictly dependent on the thermal boundary conditions assumed at both sidewalls.

Hsieh [49] investigated numerically turbulent natural convection in enclosures with differentially heated vertical walls. Low-Reynolds-number turbulence models were adopted. He showed that when the turbulence level in the core region of the cavity was low, most low-Re models, particular those showing good performance for bypass transitional flows, tended to relaminarise the flow and, as a consequence, significantly under-predicted the near-wall turbulence intensities and boundary-layer thickness. He also tested an unsteady RANS approach, employing a low-Re $k - \varepsilon$ model, and the predicted flow field was found to be effectively relaminarised. To overcome this difficulty, likely caused by the low-Re functions in the ε -equation, the two-layer approach was attempted, in which the near-wall lengthscale was prescribed algebraically using the one-equation $k-l$ model of Wolfshtein (1969). The two-layer approach combined with a quadratic stress-strain relation gave overall the best performance in terms of mean velocities, temperature and turbulence quantities.

Choi et al. [21] carried out a numerical study of natural convection in a rectangular cavity with a low-Re differential stress and flux model. The turbulence model considered in the study is that developed by Peeters and Henkes [74] and further refined by Dol and Hanjalić [35]. This model was applied to the prediction of natural convection in a rectangular cavity, together with the two-layer model, the shear stress transport model and the time-scale bounded $\overline{v^2} - f$ model, all with an algebraic heat flux model. It was shown that the low-Reynolds number differential stress and flux model predicted well the mean velocity and temperature, the rms vertical velocity fluctuations, the Reynolds shear stress, the horizontal turbulent heat flux, the local Nusselt number and the wall shear stress, but slightly under-predicted the vertical turbulent heat flux. The performance of the $\overline{v^2} - f$ model was comparable to that of the low-Reynolds number differential stress and flux model except for an overprediction of the horizontal turbulent

heat flux. The two layer model predicted poorly the mean vertical velocity component and under-predicted the wall shear stress and the local Nusselt number. The shear stress transport model predicted well the mean velocity, but the general performance of the shear stress transport model was nearly the same as that of the two-layer model, under-predicting the local Nusselt number and the turbulent quantities.

Snoussi et al. [80] studied numerically natural convection flow resulting from the combined buoyancy effects of thermal and mass diffusion in a cavity with differentially heated side walls with different aspect ratios ranging from 1 to 4. The water on the left hot wall of the cavity was vaporized from the liquid-vapor interface. The vapor moved through the air and condensed at the cooled right wall. The Finite Element Method (FEM) was used and the full vorticity transport equation, together with the stream function, and concentration and energy equations, were solved. This numerical approach allowed them to analyse the complex natural convection flow situations arising in the cavity, and appeared to be sufficiently versatile to permit computation of other effects such as inclination of glazing cavities.

Aksouh and Mataoui [4] predicted numerically natural convection of air in an enclosed tall differentially heated rectangular cavity of $0.076m \times 2.18m \times 0.52m$. Two differential temperatures between the vertical plates, respectively 19.6°C and 39.9°C , corresponding to the low and higher Rayleigh numbers of 0.86×10^6 and 1.43×10^6 were considered. The closure of the motion equations was achieved by two statistical turbulence models coupled with wall functions: the energy dissipation $k - \varepsilon$ model and the RNG model to improve the effects of low Reynolds numbers, particularly in the viscous sublayer near the wall. The numerical solution of the RANS equations was performed through a finite volume method based on a second order upwind space discretization and a pressure-velocity PISO algorithm. It was found that comparison between the two models showed that the predictions of the RNG model were in better agreement with experimental data than those of the standard $k - \varepsilon$ model for flow at low Rayleigh number. The discrepancy between the two models was especially observed close to the wall. The increase of the temperature difference between the hot and the cold wall generated an increase of the turbulence intensity in the flow. This increase was more significant near the wall. However, the velocity magnitude and streamline contours showed that in addition to the primary flow, which moved between the active walls, a secondary flow with weak velocity amplitude was also present. This secondary flow started only in the core region of the cavity, and moved fluid along the spanwise axis.

Trias et al. [85] investigated numerically a set of 2-D and 3-D Direct Numerical Simulations (DNS) in a differentially heated air-filled cavity of aspect ratio 4 with

adiabatic horizontal walls giving Rayleigh numbers, based on the cavity height, of 6.4×10^8 , 2×10^9 and 10^{10} , and Prandtl number of air $Pr = 0.71$. Significant differences were observed between 2-D and 3-D results. The numerical algorithm and the methodology used to verify the code and the simulations were presented. The main features of the flow, including the time-averaged flow structure, the power spectra and probability density distributions of a set of selected monitoring points, the turbulent statistics, the global kinetic energy balances and the internal waves motion phenomenon were all presented and discussed.

2.2.2 Vertical square cavities

Markatos and Pericleous [66] presented a computational method which they used to obtain solutions of the buoyancy-driven, turbulent flow and heat transfer in a square cavity with differentially heated side walls. A series of Rayleigh numbers, ranging from 10^3 to 10^{16} were investigated numerically. Donor-cell differencing was used and mesh-refinement tests were performed for all considered Rayleigh numbers. They tested a two-equation model of turbulence ($k - \varepsilon$) for Rayleigh numbers greater than 10^6 , that included gravity~density gradient interactions. They concluded that the use of the $k - \varepsilon$ model indicated that, despite its well-known deficiencies in terms of physical realism, it led to a reasonable prediction of the overall flow structure of the considered problems.

Henkes et al. [47] calculated numerically the laminar and turbulent natural-convection flow in a two-dimensional square cavity heated from the vertical side up to a Rayleigh number of 10^{14} for air and up to 10^{15} for water. Three different turbulence models were compared: the standard $\kappa - \varepsilon$ model with logarithmic wall functions and the low-Reynolds-number models of Chien [19], and Jones and Launder [53]. The position of the laminar-turbulent transition in the vertical boundary layer was found to strongly depend on the turbulence model used. Moreover, multiple solutions for the transition position could occur for a fixed Rayleigh number on the same numerical grid. The thermal stratification in the core of the cavity broke up when the flow became turbulent. Comparison of the averaged wall-heat transfer with experiments for the hot vertical plate and for tall vertical cavities showed that the standard $\kappa - \varepsilon$ model gave a too high prediction, whereas the low-Reynolds-number models were reasonably close to the experiment. Below a critical Rayleigh number (Ra_{cr}), the solution was laminar everywhere. Increasing the Prandtl number increased the critical Rayleigh number Ra_{cr} .

2.3 Tilted enclosures

2.3.1 Experimental investigations

The natural convection motion and heat transfer rates in an inclined rectangular air layer, in which two opposing isothermal rigid-boundaries were kept at different temperatures, were investigated experimentally by Inaba [51] for various angles of inclination from $0 - 180^\circ$, figure 2.4, various aspect ratios, $\frac{H}{W} = 5 - 83$, and Rayleigh numbers $Ra_w = 1.2 \times 10^3 - 2 \times 10^6$. Flow and heat transfer behaviours in these inclined air layers were investigated by flow visualisations and measurements of temperature profiles and heat transfer through the air layer. Three types of flow patterns in the laminar flow regime were recognised, depending on the inclination angle θ . For $\theta \leq 30^\circ$, there existed mainly multi cellular flows (Rayleigh Benard convection). For $\theta = 30^\circ \sim 60^\circ$, convoluted flows (spiral flows) with their axes directed to up slope were recognised in the inclined air layer. For $\theta = 60^\circ \sim 150^\circ$, a unicellular flow (boundary layer flow) existed in the inclined air layer. For small aspect ratios ($\frac{H}{W} = 10 - 29$), the change of Nusselt number Nu_w with inclination angle θ became complex because of the difference of flow patterns. The Nu_w values were maximum between $15^\circ \sim 60^\circ$, and decreased steeply with increasing θ .

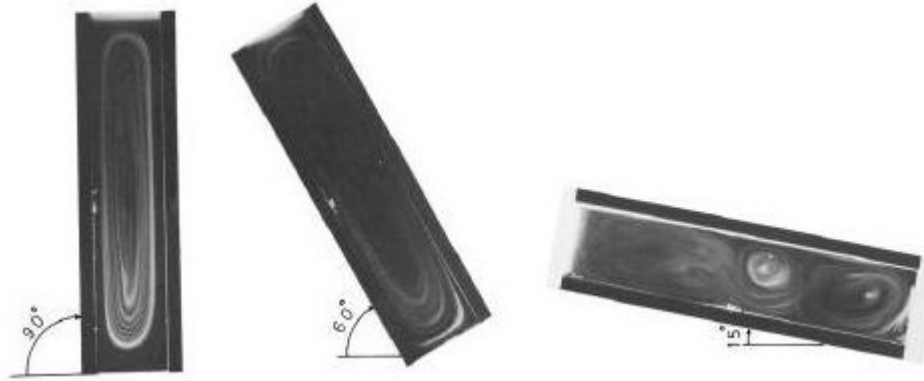
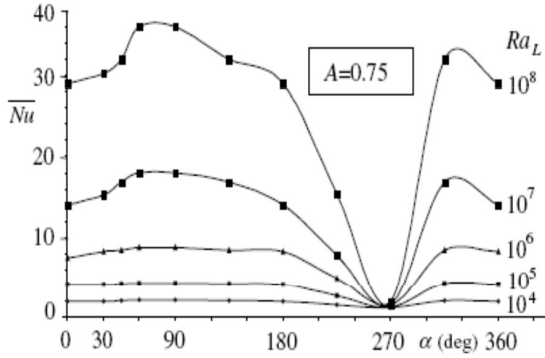


Figure 2.4: Convective flow patterns in the X-Y plane for $H/W=5$ ($W=22\text{mm}$) for $\theta = 90^\circ, \theta = 60^\circ$ and $\theta = 15^\circ; Ra_w = 10^4$ [51].

Steady-state natural convection taking place in rectangular cavities filled with air was studied both experimentally and numerically by Baïri et al. [9]. The active walls, hot and cold, of the cavity were maintained isothermal at temperatures T_H and T_C , respectively, and the other walls were adiabatic. Different angles of inclination

α of the cavity from 0° to 360° were considered, including the significant configurations corresponding to inclinations of 0° (vertical active walls), 90° (hot wall down, Rayleigh–Bénard convection) and 270° (hot wall up, pure conductive mode). Two aspect ratios $A = L/H = 0.75$ and 1.5 were investigated, L being the distance between the active walls and H the height of the cavity. The numerical study was carried out by means of the finite volume method and provided thermal and dynamic maps of the fluid for several geometrical configurations obtained while varying α , A and $\Delta T = T_H - T_C$. The range of the Rayleigh number, Ra_L , extended from 10 to 10^8 (see Figure figure 2.5). The convective exchanges computed by the RNG- $k - \varepsilon$ turbulence model were, for most of the treated cases, close to those obtained experimentally. The overall differences were relatively small, with an average discrepancy between calculations and measurements of about 6%, corresponding to the expected uncertainty of the model and measurements. The authors provided new correlations of the type $\overline{Nu}_L - Ra_L$ which were useful for the sizing of structures based on this type of cavity (Table 2.2).



$\alpha(deg)$	Correlation
0, 30, 360	$\overline{Nu}_L = 0.147Ra_L^{0.287}$
45, 135, 315	$\overline{Nu}_L = 0.130Ra_L^{0.305}$
60, 90	$\overline{Nu}_L = 0.133Ra_L^{0.304}$
270	$\overline{Nu}_L = 0.058Ra_L^{0.058}$

Figure 2.5: Calculated Nusselt number vs the angle of inclination α for different values of the Rayleigh number Ra_L and $A = 0.75$ [9].

Table 2.2: Correlations $\overline{Nu} - Ra_L$ for Aspect ratios of 0.75 and 1.5 at different angles of inclination and $10^3 < Ra < 10^8$ [9].

Recently, Cooper et al. [25] performed a set of experiments in which They focused on the effects of angle of inclination on buoyancy-driven flows inside tall, rectangular, differentially heated cavities. They considered a rectangular cavity with an aspect ratio of 28.6, with its two long sides maintained at different temperatures and the other walls are all thermally insulated. The Rayleigh numbers, based on the temperature difference and spacing on the long sides, were $Ra = 0.86 \times 10^6$ and 1.43×10^6 , the working fluid was air. Laser Doppler anemometry was used for the velocity and thermocouple traverses for the thermal fields. Results were presented for both inclined cavities at 60° to the

horizontal with the heated surface the upper one and at 15° with the heated surface being the lower one. For the latter case, additional data were presented for a Rayleigh number of $Ra = 1.54 \times 10^6$. Cooper et al. [25] observed that for moderate angles of inclination, under stable temperature stratification, the flow was two-dimensional and the effects of the angle of inclination were primarily confined to the fluctuating fields. For large angles of inclination, with unstable temperature stratification, a set of four longitudinal vortices were formed over the entire width of the cavity, which made the dynamic field three-dimensional. The enhanced mixing at 15° led to uniform temperature in the cavity core and thus only minor deviations from two-dimensionality in the thermal field. A modest rise in Rayleigh number did not affect the mean motion, but caused an increase in the normalised turbulence intensities, which in turn led to a more uniform temperature within the cavity core and a practically two dimensional thermal field. In this experiemnt the authors estimated the relative uncertainties as: 6% in the Rayleigh number, 20% in the Nusselt number and 3% in buoyancy velocity.

2.3.2 Numerical investigations

Sharif & Liu [79] studied numerically turbulent natural convection at a moderately high Rayleigh number (4.9×10^{10}) in a two- dimensional side-heated square cavity at various angles of inclination, Figure 2.6.

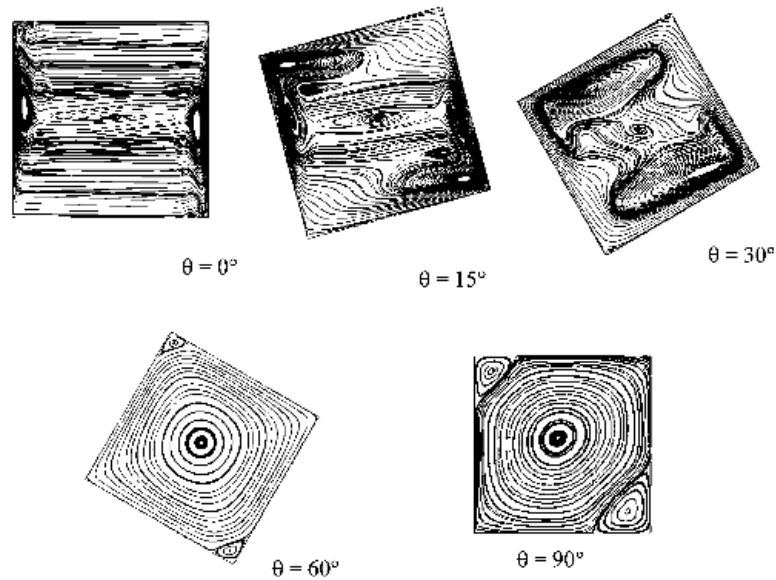


Figure 2.6: Streamlines in the cavity at various angles of inclination [79].

The $k - \omega$ and $k - \varepsilon$ models were evaluated against experimental measurements. The performance of the Wilcox $k - \omega$ model was found to be superior in capturing the flow physics such as the strong streamline curvature in the corner regions. The Lam and Bremhorst $k - \varepsilon$ model was not capable of predicting these features but provided reasonable predictions away from the corners. None of these models, however, was capable of predicting the boundary-layer transition from laminar to turbulent. In order to study the effect of the inclination of the square cavity on the heat transfer and flow patterns, computations were then performed using the Wilcox $k - \omega$ model [90] for a range of inclination angles from 0° through 90° , keeping other parameters fixed. The computed flow patterns, isotherms, convection strengths, variation of the local Nusselt numbers along the heated walls, and the average Nusselt number for various inclination angles of the square cavity were reported. It was noticed that the flow fields and heat transfer characteristics became significantly different for inclinations greater than 45° .

Aounallah et al. [7] investigated numerically turbulent natural convection of air flow in a confined and wavy cavity with two differentially heated side walls for Rayleigh number ranging from 1.58×10^9 to 10^{12} . The authors tested different RANS models, together with what they termed a “coarse DNS”. The aim was to study the effect of the inclination angle and the amplitude of the undulation on turbulent heat transfer. They showed the influence of the undulation of the cavity and its orientation. The trend of the local heat transfer was wavy with different frequencies for each undulation, Figure 2.7.

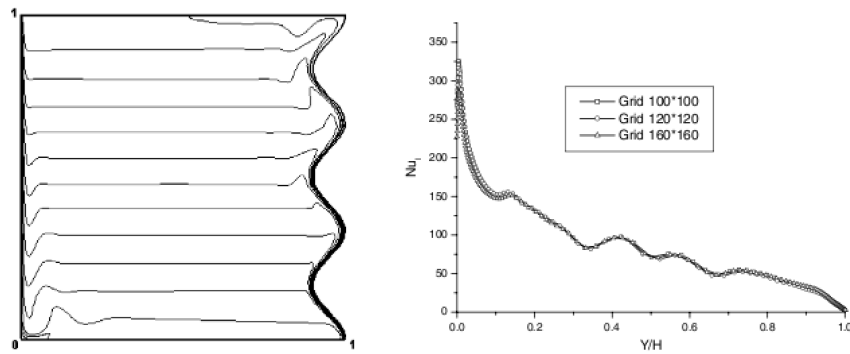


Figure 2.7: Iso-temperature distributions and corresponding local Nusselt number at the hot wall of the undulated cavity ($Ra = 1.58 \times 10^9$ and $\phi = 90^\circ$) [7].

The turbulence caused an increase in the convective heat transfer on the wavy wall

surface compared to the square cavity for high Rayleigh numbers. They proposed a correlation of the mean Nusselt number as a function of Rayleigh number for Rayleigh numbers between 10^9 – 10^{12} .

Addad et al. [3] carried out an LES and RANS of natural convection in a “shallow” cavity with a heated ceiling and cooled floor. The rectangular cavity aspect ratio was $1/29$, with its longest axis forming a small angle of 5° or less with the horizontal axis. The Rayleigh number was 4.16×10^8 . The strong temperature gradient at the floor or ceiling resulted in a laminar layer, while on the other side of the velocity peak turbulence was able to develop, and in the central layer the flow was found to be again strongly stratified. They concluded that RANS models reproduced Nusselt numbers very well because there was only very weak turbulence and most of the heat was transferred by a laminar convective mode rather than any turbulence effect.

Cooper et al. [24] investigated numerically flow in a rectangular cavity with an aspect ratio of 28.6, with its two long sides maintained at different temperatures and the two short end-walls thermally insulated. The Rayleigh number, based on the temperature difference and spacing on the long sides, was 0.86×10^6 and the working fluid was air (Prandtl number 0.71). The dimensions of the cavity were $2.18m \times 0.52m \times 0.0762m$. This study focussed on the effects of angle of inclination. Results were presented for a cavity inclined at 60° and at 5° angles of inclination, with the hot surface being the upper one for both angles. A number of strategies were employed for the modelling of near-wall turbulence, including the analytical wall function (AWF of Craft et al. [27]) and also for the modelling of the turbulent stresses and heat fluxes. They found that the AWF approach resulted in reliable flow and thermal predictions, while the prediction of temperature fluctuations improved with the introduction of second-moment closures. For tall differentially heated cavities with either vertical heated walls or inclined at moderate angles to the vertical, the $k - \varepsilon$ model predictions were in close agreement with measurements. The LRR model displayed some deficiencies, with the linear version over-estimating velocity peaks at mid-height and the more elaborate non-linear model over-estimating the turbulent mixing near the end walls. The present study has begun by examining these cases using several RANS models implemented in *Code_Saturne* 2.0 and the LES approach.

2.4 Horizontal annular enclosures

The subject of buoyancy-driven flow inside a two dimensional horizontal annulus has attracted great attention from researchers in both experimental and computational

fields.

Castrejon and Spalding [15] performed an experimental and a numerical study of the transient free-convection flow in an annulus between two concentric horizontal cylinders, the inner one of which was heated. In the experiment, photographs were taken, and successive positions of plume of heated fluid were observed. For the numerical study, an implicit finite-domain solution procedure embedded in the PHOENIX code was used to solve a closed system of four coupled differential equations. The numerical solution procedure afforded considerable insight into both general patterns. The authors found a fairly good agreement between predictions and experimental measurements. However, the numerical model failed to predict the transition to random motion which occurred towards the end of the observation period.

Kumar [58] studied numerically natural convection of gases in a horizontal annulus, where the inner cylinder was heated by the application of a constant heat flux and the outer cylinder was isothermally cooled. For different diameter ratios of $1.2 - 10$ and a wide range of Rayleigh numbers of $10^5 - 3 \times 10^6$, he presented detailed results of temperature, velocity and heat transfer. His results showed a crescent-shaped eddy dominated for the small diameter ratio, and a kidney-shaped flow pattern appeared for the large diameter ratio. He also observed that the inner wall temperature was a function of diameter ratio and Rayleigh number. He concluded that an increase in Rayleigh number increased the heat transfer rate and most of the heat was rejected within 20° from the top line of symmetry on the outer cylinder for small diameter ratios. The heat rejection became more uniform around the outer cylinder as the diameter ratio increased.

McLeod et al. [67] investigated experimentally heat transfer by natural convection of Helium between horizontal isothermal concentric cylinders at cryogenic temperatures. Overall heat transfer rates, profiles of time-averaged temperature, and temperature fluctuations were measured for Rayleigh numbers of $8 \times 10^6 - 2 \times 10^9$ and for thermal expansion numbers of $0.25 - 1$. Time-averaged temperature profiles of the annulus gas were qualitatively shown. It was concluded that by increasing the thermal expansion number, for a constant Rayleigh number, more developed turbulence existed at a given annulus location. They also showed that changing the expansion parameter did not have any effect on the overall heat transfer rate.

Large Eddy Simulation based on sub-grid modelling of natural convection in concentric horizontal annuli with a heated inner and cooled outer cylinder were conducted by Miki et al. [69]. The Rayleigh number used was 1.18×10^9 . They presented results of time-averaged temperature. The authors found reasonable agreement comparing with

the experimental data. They concluded that the additional terms associated with the sub-grid scale model in LES dissipated energy at high wave numbers, and the amount of dissipation depended strongly on the Smagorinsky constant C_s .

Ho et al. [48] conducted a numerical study supplemented with experiments of flow visualization and halo-graphic interferometric measurements, concerning the buoyancy induced fluid flow and heat transfer between two horizontal, differentially heated cylinders inside a circular, air filled enclosure subjected to external convection. The Rayleigh numbers considered were between 10^4 and 10^7 , and the inclination angles of the enclosure were 30° , 60° and 90° . The external convection at the circular enclosure wall was found to further promote buoyant convection flow and it enhanced heat transfer between cylinders. The effects of varying the Rayleigh number, the orientation angle of the enclosure and the gap width between the cylinders in the presence of external convection were found to be similar to those observed in an adiabatic enclosure.

Desai and Vafai [32] studied numerically turbulent buoyancy-driven flow in an annulus bounded by concentric, horizontal cylinders and adiabatic end walls. They used in their simulation a wall function approach coupled with the standard $k - \varepsilon$ model to solve time-averaged equations of fluid motion and heat transfer. The Rayleigh number used ranged from 10^6 to 10^9 . Contours of turbulent kinetic energy and turbulent viscosity were presented, the latter contours indicated that the highest turbulence intensities were found in the upper portion of the annulus and in the region near the inner cylinder where boundary layer separation occurred. Heat transfer rates were found to be higher than those in the laminar regime. Their results showed a decrease in heat transfer rates from the inner and outer cylinder with an increase of the gap width. They also investigated the effects of Prandtl number. The turbulent viscosity was found to decrease for fluids with higher Prandtl number. A three dimensional domain was also employed to study the effect of the end walls on the natural convection process. It was observed that the Nusselt number decreased at the end walls because of the more prominent damping effect of the end walls at high Rayleigh numbers.

Desai and Vafai [33] carried out an experimental and numerical study of natural convection in an open ended horizontal annular cavity. In the experimental study, smoke flow visualization using laser-induced lighting was used in order to understand the flow field around the open end of the cavity. A known heat flux was applied to each component of the cavity (inner cylinder, inner cylinder tip, outer cylinder and walls) and local surfaces temperature measurements were made to determine heat transfer characteristics of the convective flow. In the numerical investigation, a finite element analysis was applied to solve time-averaged-steady-state equations of fluid motion and

heat transfer. The Rayleigh number considered ranged from 1.3×10^9 to 5.1×10^9 . The flow field results indicated the strong influence of the open end on the flow field within the cavity. The bulk flows were characterized by the suction of cold fluid into the lower portions of the cavity and ejection of the hot fluid as a buoyant jet from the top of the cavity. Interactions between the inner and the outer flow fields were responsible for enhancing heat transfer rates from the open ended cavities.

Natural convection in horizontal concentric and eccentric annuli with heated inner cylinder was studied by Kenjeres and Hanjalić [56] using several variants of single-point closure models at the eddy diffusivity and algebraic flux level. They found that the application of an algebraic model for turbulent heat flux $\overline{\theta u_j}$ derived from the differential transport equation and closed with low-Reynolds number forms of transport equations for the kinetic energy, k , its dissipation rate ε , and temperature variance $\overline{\theta^2}$, reproduced well the experimental data for mean and turbulence properties and heat transfer over a range of Rayleigh numbers. It was concluded that turbulence persisted only in a narrow plume above the heated inner cylinder with laminar flow in the rest of the annuli. They found that the application of the extended algebraic turbulence models proved to be crucial for predicting the flow pattern and wall heat transfer at transitional Rayleigh numbers.

Chakir et al. [16] studied numerically the natural convection of gases (mixture of SF6 and N2) in a horizontal annulus. The study represented a thermal analysis of high voltage power gas insulated transmission lines. The considered Rayleigh number was ranging from 10^5 to 10^{10} . It was found that the maximum temperature deviation was 15%. The Nusselt number showed a high dependency on the Rayleigh number. The increase of heat convection for high Rayleigh numbers occurred mainly in the middle part of the cylinder and at the top of the outer one. The temperature in the centre of the annulus became constant for cases with higher turbulence levels. The temperature gradient was higher in the wall boundary layers than outside them.

Padilla and Silveiraneto [73] carried out three-dimensional large eddy simulation of natural convection in a horizontal annulus using Smagorinsky's dynamic sub-grid model. The onset of transition to turbulence and turbulent regimes were analyzed. It was found that as the Rayleigh number increased, the flow became fully irregular and chaotic when a turbulent regime was reached. The flow dynamic characteristics and the plume transition were captured and results returned good agreement with available experimental data.

Addad et al. [2] carried out a numerical simulation of natural convection between concentric cylinders using RANS and LES approaches on three geometries. The first

two were a single inner cylinder at gap-based Rayleigh numbers of 1.18×10^9 and 2.38×10^{10} and ratio of outer-to-inner cylinder diameters $R_o/R_i = 4.87$ and 3.37 . the third test case was a cylinder with three inner tubes. It was concluded that the flow patterns in the latter case were more complex than the one internal concentric cylinder cases. The two-equation RANS models used were found to be less satisfactory than in the concentric annular with single inner tubes test cases while second moment closure results were closer to LES predictions.

Omranian [72] recently started simulating the flow in a horizontal annular penetration cavity with a cooled central cylinder using a high-Reynolds-number $k - \varepsilon$ model with the analytical wall function approach within the in-house computer code STREAM. The resulting computations showed that within the penetration the flow became unsteady. Because of the absence of any measured validation data for the latter test case, a major aim for the present study is to perform a highly resolved Large Eddy Simulation, in order to provide full and accurate data of the thermal and dynamic fields of the flow in the penetration, and the rate of heat transfer to/from the central tube, and to determine how far the flow can be driven inside the penetration. A further aim is to test the ability of RANS models available in the *Code_Saturne* 2.0 software to predict this type of flow.

2.5 Final remarks

The review of previous experimental and numerical investigations helped us to understand the physics of turbulent buoyant flows and allowed us to know the performance of some turbulence models to predict turbulent buoyancy-driven flows within different configurations including rectangular, square and cylindrical enclosures. Interesting results have been concluded from the previous reviewed investigations within vertical and tilted enclosures. When configurations in which the length in the direction of the body force is large compared to the width, thermal instabilities could be encountered when the heating is from below. The character of the core velocity and temperature distribution for natural convection at large Rayleigh number in an enclosure depends on the imposed thermal conditions. The relatively few existing experiments have shown that under different conditions, different core configurations can be obtained. In square cavities, the velocity maximum occurs near the hot and cold walls, and reduces to almost zero in the core region. It was concluded that laminar flow is located in the core and turbulent flow near both hot and cold walls. Several turbulence models have been tested for the investigation of natural convection in enclosures ranging from sim-

ple high-Reynolds-number models to more complicated low-Reynolds-number models. New models have also been developed for buoyant flows. In general, RANS models showed reasonable performance for predicting buoyant flows within vertical and tilted enclosures. It was concluded from the literature survey that low-Re models (like $\overline{v^2} - f$ model of Durbin [38]) showed better performance than high-Re models (like $k - \varepsilon$ model of Jones and Launder [54]). Turbulence models were very promising when they were used with advanced approaches for modelling heat fluxes, GGDH of Daly and Harlow [30], the algebraic buoyancy-modified $k - \varepsilon - \overline{\theta^2} - \varepsilon_\theta$ model of Hanjalić [44] and others. High-Re models, including $k - \varepsilon$ and RSM models gave good results when used with an advanced analytical wall function of Craft et al. [27]. As mentioned above, few researchers studied buoyant flows inside tilted cavities. In the first part of the present thesis one was interested in investigating the influence of different angles of inclination on the dynamic of buoyant flows. Buoyancy-driven flow inside tilted cavities (Betts cavity [11]) under both unstable and stable stratification were computed. One of the aims was to test the effectiveness of the unsteady RANS approach (URANS) for modelling such flows, a range of RANS models embedded in *Code_Saturne* 2.0 have been used to identify which of these models is suitable for predicting buoyancy-driven flow inside the cavity. Highly resolved LES has been used to provide accurate data for validation purpose.

Previous investigations of buoyant flow inside 2-D and 3-D annular enclosures have also been reviewed here. It has been concluded that the heat transfer is dependent on the Rayleigh number and a significant increase in Rayleigh number inside the horizontal annular enclosures enhances the heat transfer. Inside 3-D closed annular cylinders the overall heat transfer decreases at the end walls because of the prominent damping effect of the walls. Eddy-viscosity-models showed less satisfactory results for the horizontal annulus unless they are used in conjunction with an advanced wall function like the analytical wall function. The application of advanced algebraic models show their ability to predict the correct heat transfer within the enclosure. The final test case in the present thesis is a pure industrial test case, the penetration annular cavity which plays a major role in the cooling systems of the Advanced Gas Cooled Reactors (AGRs). Flow within the penetration annular enclosure is a complex buoyant flow and therefore it is considered as a challenging industrial application. The aim beneath this computation is to satisfy the industrial needs by providing an LES accurate data of the thermal and dynamic fields of the flow in the penetration, and the rate of heat transfer to/from the central tube, and to determine how far the flow can be driven by buoyancy force inside the penetration. Some initial URANS simulations have been conducted in order

to determine appropriate boundary conditions and to provide an initial qualitative and quantitative view of the flow patterns found in the problem with the absence of any measured validation data.

Chapter 3

Modelling of Turbulent Buoyancy-Driven Flows

3.1 Introduction

Turbulence modelling comprises the various strategies developed for predicting mean flow quantities and averaging solutions to the Navier-Stokes equations. The most popular approaches in this regard seek to close the RANS (Reynolds Averaged Navier-Stokes) equations.

Ultimately the capabilities of RANS models, no matter how complex, remain limited, and alternative modelling approaches continue to be sought. The most popular of these is LES, in which the “filtered” Navier-Stokes equations are solved with the aid of simplified models for small-scale phenomena, called sub-grid scale stress models. Such methods reduce the dependence on modelling at the cost of greater computer resources.

Both RANS and LES approaches have been used in the present work. This Chapter will start by outlining the RANS modelling and near-wall treatments adopted, and then describe the LES modelling approaches.

3.2 Navier Stokes equations in natural convection

The incompressible Navier-Stokes and temperature equations in natural convection cases can be written as:

$$\rho \frac{\partial u_i}{\partial x_i} = 0, \tag{3.1}$$

$$\rho \frac{\partial u_i}{\partial t} + u_j \rho \frac{\partial u_i}{\partial x_j} = -\frac{\partial P}{\partial x_i} + \frac{\partial}{\partial x_j} \left(\mu \frac{\partial u_i}{\partial x_j} \right) + \rho g_i, \quad (3.2)$$

$$\rho \frac{\partial T}{\partial t} + u_j \rho \frac{\partial T}{\partial x_j} = \frac{\partial}{\partial x_j} \left(\frac{\mu}{Pr} \frac{\partial T}{\partial x_j} \right), \quad (3.3)$$

where \underline{g} is the gravity vector.

In the present thesis the Boussinesq approximation is used, which treats density as a constant value in all solved equations, except for the buoyancy term in the momentum equation:

$$(\rho - \rho_0) \underline{g} \approx -\rho_0 \beta (T - T_0) \underline{g}, \quad (3.4)$$

where β is the thermal expansion coefficient, defined as:

$$\beta = -\frac{1}{\rho_0} \frac{\partial \rho}{\partial T}, \quad (3.5)$$

The density in the final term of Equation 3.2 is then written, after re-arrangement, as:

$$\rho = \rho_0 (1 - \beta (T - T_0)), \quad (3.6)$$

where ρ_0 and T_0 are the reference density and the reference temperature respectively. This approximation is accurate as long as changes in actual density are small, specifically, the Boussinesq model is valid when $\beta (T - T_0) \leq 1$.

3.3 Unsteady RANS modelling

In unsteady RANS computations, ensemble averaged forms of the Navier-Stokes equations are solved, in which second-moment correlations between velocity and temperature fluctuations, u' and t' , appear. These computations are all performed in a time-dependent framework (URANS), implying that certain low-frequency scales in time can be resolved in the calculation. Flow field thermal and dynamic quantities can then be interpreted as being the sum of three contributing terms: the time averaged term, and

the fluctuating part which consists of both the modelled and resolved time-dependent terms f' and f'' . The quantity f in URANS is defined as:

$$f(x, t) = \bar{f}(x) + f'(x, t) + f''(x, t), \quad (3.7)$$

The incompressible Reynolds-Averaged-Navier-Stokes equations in natural convection cases with Boussinesq approximation can be written as:

$$\rho_0 \frac{\partial U_i}{\partial x_i} = 0, \quad (3.8)$$

$$\rho_0 \frac{\partial U_i}{\partial t} + U_j \rho_0 \frac{\partial U_i}{\partial x_j} = -\frac{\partial P}{\partial x_i} + \frac{\partial}{\partial x_j} \left(\mu \frac{\partial U_i}{\partial x_j} - \rho_0 \overline{u'_i u'_j} \right) + \rho_0 \beta (T - T_0) g_i, \quad (3.9)$$

The Reynolds-averaged temperature equation can be written as:

$$\rho_0 \frac{\partial T}{\partial t} + U_j \rho_0 \frac{\partial T}{\partial x_j} = \frac{\partial}{\partial x_j} \left(\frac{\mu}{Pr} \frac{\partial T}{\partial x_j} - \rho_0 \overline{u'_j T'} \right), \quad (3.10)$$

In order to close the system, models must be introduced for the Reynolds stresses and turbulent heat fluxes. The forms tested in the present work are detailed below.

3.3.1 The Boussinesq model

The most common approach to eddy-viscosity modelling is known as the Boussinesq approximation. The Boussinesq approximation assumes that the Reynolds-stress-tensor is proportional to the mean-flow strain tensor, i.e.,

$$\overline{u'_i u'_j} = \frac{2}{3} k \delta_{ij} - \nu_t S_{ij}, \quad (3.11)$$

where the mean rate-of-strain tensor S_{ij} is given by,

$$S_{ij} = \frac{1}{2} \left(\frac{\partial U_i}{\partial x_j} + \frac{\partial U_j}{\partial x_i} \right), \quad (3.12)$$

In this relationship, the constant of proportionality is the eddy viscosity, ν_t . It is

important to note here that the eddy viscosity is not a property of the fluid, like the molecular viscosity, but a property of the flow field and hence will vary in time throughout the flow domain.

Before the Boussinesq approximation can be applied, one needs to find a model for the eddy viscosity. The three main types of eddy viscosity models are algebraic (or zero-equation models), one-equation models and two-equation models. Algebraic models use an algebraic specification for the eddy viscosity that is related to the mean flow and geometric properties. One-equation models solve a single partial differential equation (PDE) that is used to evaluate the eddy viscosity, whereas two-equation models solve two PDEs. The latter models will be discussed in the following section.

The Boussinesq approximation has been criticised as a major limitation of eddy-viscosity models. This is because it assumes that the Reynolds-stress-tensor is isotropic, i.e., its axes align with the mean-strain tensor. However, in many flow situations anisotropy effects cannot be neglected and a full second-order closure is necessary.

3.3.2 Two-equation eddy viscosity models

The eddy viscosity relates the Reynolds stresses to the mean strains via a turbulent, or eddy, viscosity ν_t :

$$\overline{u'_i u'_j} = \left(\frac{2}{3}\right) k \delta_{ij} - \nu_t \left(\frac{\partial U_i}{\partial x_j} + \frac{\partial U_j}{\partial x_i} \right), \quad (3.13)$$

One of the most widely-used eddy-viscosity models available in *Code_Saturne* 2.0 is the $k - \varepsilon$ model of Jones and Launder [53]. Two transport equations are solved, for turbulent kinetic energy, k , and its dissipation rate, ε , and details such as coefficient values are given in Appendix B. This $k - \varepsilon$ model is a high-Reynolds-number model, not accounting for any near-wall viscous effects, and so is used with wall functions.

In addition to the above high-Re model, a number of low-Re schemes, designed to resolve the flow across the near-wall viscous layer, have also been tested in the present work. The first of these is the *SST* shear stress transport model of Menter [68], which combines the above $k - \varepsilon$ model with a $k - \omega$ model formulation of Wilcox [90] in the near-wall region using empirical functions based on the distance from the wall to switch between the two. Details of this scheme are given in Menter [68] (also detailed in Appendix B).

The other two low-Reynolds-number eddy viscosity models employed here are based on the elliptic-relaxation approach of Durbin [38] (this model is detailed in Appendix

B). Called $\overline{v^2}-f$ and $\varphi - f$ respectively, the $\overline{v^2}/k-f$ model was proposed by Hanjalić et al. [46] and, independently, by Laurence et al. [61]. They aimed to improve the robustness by solving a transport equation for the ratio $\varphi = \overline{v^2}/k$ instead of $\overline{v^2}$ in the $\overline{v^2}-f$ model of Durbin [38], and the model is also based on solving an elliptic equation for a function f that appears in the modelled equations.

The second elliptic relaxation approach tested here, the $\varphi - \alpha$ scheme, was devised by Laurence et al. [61] and Billard [13] to be more stable than the $v^2/k-f$ model, and solves a modelled transport equation for $\varphi = \overline{v^2}/k$, and an elliptic equation for a switching function α (which takes the value 0 at walls and relaxes towards 1 further away). Details of the latter model are also presented in Appendix B.

3.3.3 Second-moment closure

One weakness of the eddy viscosity models is that the stresses respond instantly to changes in the mean strain. The route chosen for testing more advanced forms in this work is stress transport models which solve modelled transport equations for each stress component. The Reynolds stress tensor is likely to be anisotropic in flows where rapid changes in mean strain rate exist. In the following situations the Boussinesq approximation may fail [92]:

- Flows with sudden changes in mean strain rate.
- Flows over curved surfaces.
- Flows in ducts with secondary motions.
- Flow in rotating fluids (swirling flows).
- Three dimensional flows.
- Flows with boundary layer separation.

One method for dealing with anisotropic turbulence flow is to discard the Boussinesq approximation and use a nonlinear relationship between the Reynolds stress tensor and the mean strain tensor ([74], [72]). Second-order closures go one step further and account for anisotropy by modelling the actual transport equations for each individual component of the Reynolds stress tensor.

3.3.3.1 Second moment closure models

The Reynolds stress equations are a system of six equations, one for each independent component of the Reynolds-stress-tensor. The second-order correlations are now the dependent variables and the new unknowns involve third-order correlations as well as correlations involving gradients of the fluctuating velocities and pressure. Second moment closure models close the Reynolds-stress equation by replacing the unknowns with coefficients and algebraic expressions that are based upon mean flow properties. The advantage of second-moment closure models over eddy-viscosity models is that the Reynolds stress tensor is not treated as an isotropic tensor.

Two stress transport models embedded in *Code_Saturne* 2.0 have been tested here, namely the LRR scheme of Launder-Reece-Rodi [60], and the slightly more complex SSG formulation of Speziale-Sarker-Gatski [81]. Both of these are high-Reynolds-number models, and are therefore applied in conjunction with wall function (Details of stress transport models are presented in Appendix B).

3.3.4 Contribution of buoyancy

When a non-zero gravity field and temperature gradient are present simultaneously, the two-equation EVMs in *Code_Saturne* 2.0 take account of this extra source of turbulence generation (or destruction) via additional contributions to both the k and ε equations. The generic transport equations for the $k - \varepsilon$ scheme are presented as:

$$\frac{\partial k}{\partial t} + U_j \frac{\partial k}{\partial x_j} = \frac{\partial}{\partial x_j} \left[(\nu + \nu_t / \sigma_k) \frac{\partial k}{\partial x_j} \right] + P_k - \varepsilon, \quad (3.14)$$

$$\frac{\partial \varepsilon}{\partial t} + U_j \frac{\partial \varepsilon}{\partial x_j} = \frac{\partial}{\partial x_j} \left[(\nu + \nu_t / \sigma_\varepsilon) \frac{\partial \varepsilon}{\partial x_j} \right] + C_{\varepsilon 1} \frac{\varepsilon}{k} P_k - C_{\varepsilon 2} \frac{\varepsilon^2}{k}, \quad (3.15)$$

the total production of k is defined as:

$$P_k = -\overline{u'_i u'_j} \frac{\partial U_i}{\partial x_j} + G_b, \quad (3.16)$$

where the generation of turbulence due to buoyancy is given by

$$G_b = -\beta g_i \overline{u'_j t'}, \quad (3.17)$$

where β is the thermal expansion coefficient, and g_i is the gravitational acceleration component in the i direction.

The generic stress equations are presented as follows:

$$\frac{\partial}{\partial t} (\overline{u'_i u'_j}) + \frac{\partial}{\partial x_k} (U_k \overline{u'_i u'_j}) = D_{T,ij} + D_{L,ij} + P_{ij} + G_{ij} + \phi_{ij} - \varepsilon_{ij} + F_{ij} + S_{user}, \quad (3.18)$$

For the stress transport models, the total production P is defined as

$$\overline{P_{ij}} = - \left(\overline{u'_i u'_k} \frac{\partial U_j}{\partial x_k} + \overline{u'_j u'_k} \frac{\partial U_i}{\partial x_k} \right) + G_{ij}, \quad (3.19)$$

with

$$G_{ij} = -\beta \left(\overline{g_i u'_j t'} + \overline{g_j u'_i t'} \right), \quad (3.20)$$

3.4 Modelling turbulent heat fluxes

To solve the energy equation, and close the buoyancy generation and related terms in the dynamic field in buoyancy-affected flows, one needs to approximate the turbulent heat fluxes $\overline{u'_j t'}$ (the last term in the energy equation (3.10)).

3.4.1 The effective viscosity approximation

Extending the ideas of the Boussinsq approximation, Equation (3.11), to the turbulent heat fluxes, one might approximate these by:

$$\overline{u'_j t'} = -\alpha_t \frac{\partial T}{\partial x_j}, \quad (3.21)$$

where the eddy diffusivity α_t is taken as $\alpha_t = \nu_t / Pr_t$, and Pr_t is the turbulent Prandtl number. In practice, Pr_t is usually taken as a constant of around 0.9 for wall-bounded flows. In free shear layers a slightly lower value (around 0.6) is often more appropriate.

With the above eddy-diffusivity model, the turbulent heat fluxes are related directly to the corresponding temperature gradients.

3.4.1.1 Simple shear flows

Considering “1” and “2” the streamwise and the cross-stream directions respectively, with $U(y)$ and $T(y)$. In a simple shear horizontal flow, with the temperature gradient across the shear layer, the eddy-diffusivity model gives:

$$\overline{u_1' t'} = -(\nu_t / Pr_t) \frac{\partial T}{\partial x_1}, \quad (3.22)$$

$$\overline{u_2' t'} = -(\nu_t / Pr_t) \frac{\partial T}{\partial x_2}, \quad (3.23)$$

3.4.1.2 Buoyancy-driven flows

For buoyancy affected flows, there exist two general stratification patterns: the unstable and the stable stratifications. Considering a horizontal flow where the gravitational force and the temperature gradient are aligned. Using the eddy-diffusivity model for $\overline{u_j' t'}$, for the stably stratified buoyant flows, the buoyancy production is defined as:

$$G_b = -\beta g_j \overline{u_j' t'} = -\beta g_j (\nu_t / Pr_t) \frac{\partial T}{\partial x_j}, \quad (3.24)$$

If the temperature gradient $\partial T / \partial x_j$ is negative, the gravity g is negative, so the buoyancy production G_b is positive (unstable stratification).

In case of a vertical buoyant flow, where the gravitational force and the temperature gradient are not aligned, one still has Equation (3.24), however the temperature gradient is now rather small (the dominant temperature gradient is normal to the wall), and consequently the buoyancy production is also small.

3.4.2 The GGDH heat flux model

An improved turbulent heat flux model was suggested by Daly and Harlow [30], known as the generalised gradient diffusion hypothesis (GGDH). The form of the GGDH model is expressed as:

$$\overline{u'_i t'} = -C_T \frac{k}{\varepsilon} \overline{u'_i u'_j} \frac{\partial T}{\partial x_j}, \quad (3.25)$$

where the constant C_T takes the value of 0.3.

Again Considering “1” and “2” the streamwise and the cross-stream directions respectively, with $U(y)$ and $T(y)$. In the simple shear flows considered earlier, the heat flux expressions are now evaluated as:

$$\overline{u'_1 t'} = -C_T \frac{k}{\varepsilon} \overline{u'_1 u'_j} \frac{\partial T}{\partial x_j}, \quad (3.26)$$

$$\overline{u'_2 t'} = -C_T \frac{k}{\varepsilon} \overline{u'^2_j} \frac{\partial T}{\partial x_j}, \quad (3.27)$$

If using the linear EVM formulation for the stresses the heat flux expressions become

$$\overline{u'_1 t'} = -C_T \frac{k}{\varepsilon} \nu_t \frac{\partial U}{\partial x_j} \frac{\partial T}{\partial x_1}, \quad (3.28)$$

$$\overline{u'_2 t'} = - (2/3) C_T \frac{k^2}{\varepsilon} \frac{\partial T}{\partial x_2}, \quad (3.29)$$

The GGDH model is known for its ability to give a better representation of the turbulent heat fluxes than the effective viscosity approximation [72]. For the prediction of buoyancy-driven flows within the present test cases the effective diffusivity approximation is used and it shows acceptable results for some particular test cases, for example in certain unstable stratifications. The GGDH model is not used here because at the time, when the present results were obtained and later, the GGDH model or other more complex algebraic models were not embedded in the distributed versions of *Code_Saturne* 2.0 and their implementation would need reasonably extensive validation tests, so they have not been applied in the present thesis.

3.5 Wall treatment

3.5.1 The turbulent boundary layer

Figure 3.1 shows a schematic of the large-scale motions in a turbulent boundary layer. The size of the largest eddies is limited by the presence of the wall. Typically for boundary layer flows,

$$l = \kappa y, \quad (3.30)$$

where l is the length scale of the turbulent eddies, κ is the Von Kármán constant, $\kappa = 0.41$, and y is the distance from the wall. Very close to the wall, Equation (3.30) does not hold. Molecular viscosity begins to affect the nature of the turbulent fluctuations and damps the motion of the turbulent eddies.

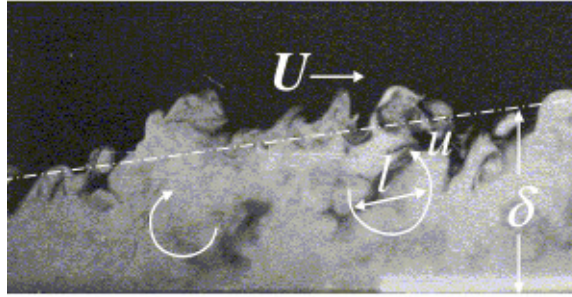


Figure 3.1: Schematic of large eddies in a turbulent boundary layer. The flow above the boundary layer has a steady velocity U ; the eddies move at randomly fluctuating velocities of the order of a tenth of U , the largest eddy size, (l) is comparable to the boundary layer thickness δ [92].

The Log-Law of the wall for the tangential velocity (Figure 3.2) is presented as follows:

$$U^+ = \frac{1}{\kappa} \ln y^+ + B, \quad (3.31)$$

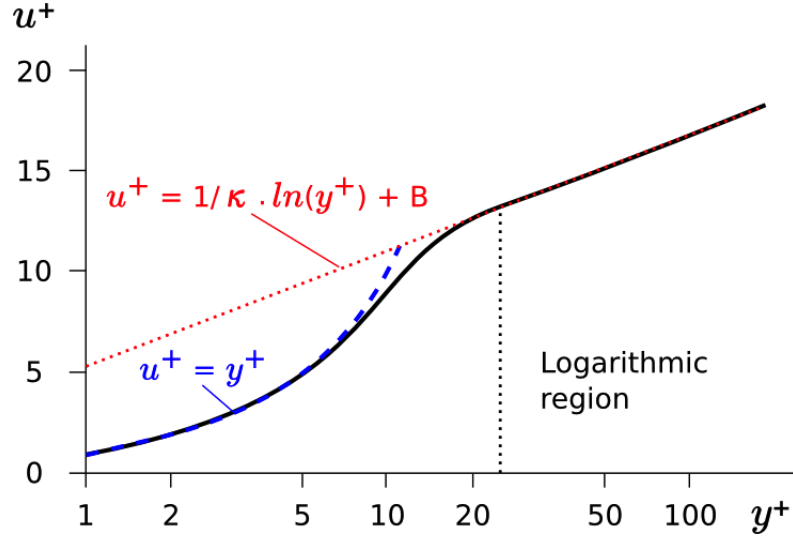


Figure 3.2: Velocity distribution near a solid wall.

where U^+ is the dimensionless velocity and y^+ is the normal dimensionless distance to the wall. These are defined as:

$$U^+ = \frac{U}{U_\tau}, \quad (3.32)$$

$$y^+ = \frac{U_\tau y}{\nu}, \quad (3.33)$$

where the friction velocity, $U_\tau = \sqrt{\tau_w/\rho}$, and $\tau_w = \mu \frac{\partial U}{\partial y} |_w$ is the shear stress at the wall. Coles and Hirst [23] found estimates of κ and B from correlation with a number of attached, incompressible boundary layer experiments. The values are:

$$\kappa = 0.41, \quad B = 5.0 \sim 5.2, \quad (3.34)$$

Experiments have shown that the near-wall region can be divided up into four layers:

- In the inner layer, called the viscous sub-layer where molecular viscosity plays a dominant role in momentum transport.
- The buffer layer where both molecular and turbulent effects are present.

- The log-law region, the length-scale does grow linearly with wall distance, is where one gets the log law.
- Beyond this, in the outer layer, called the defect layer, turbulence plays the dominant role in momentum transport. In this region molecular viscosity is negligible.

In typical high-Reynolds-number flows, the buffer region starts at y^+ values less than 30 and the viscous sub-layer at values less than 5.

3.5.2 Role of the wall function

The importance of the law of the wall in the present work is that it provides an explicit formula for the mean turbulent velocity profile near a solid boundary. With this in hand, it is not necessary to employ the fine meshing required to capture the scales near the wall. Instead, one can use the log-law formula to provide a boundary condition for the velocity at the outer edge of the buffer layer, or even further from the wall, thus allowing a coarse near-wall mesh to be employed. This significantly reduces the required amount of total arithmetic for simulating wall-bounded flows and is widely used both in RANS methods and in LES.

The above log-law is valid only for equilibrium boundary layer flows, and so implies a loss of accuracy when applied to more complex flows involving separation or other non-equilibrium features. There have been more advanced treatments developed to address some of these weaknesses (e.g. AWF of Craft et al. [27]), but these have not been employed in the current work. The sections below outline the approaches on which the present modelling has been based.

3.5.3 Wall treatment strategy

The typical strategy of employing a wall function involves:

1. The use of relatively large near-wall control volumes (so the near-wall cell node lies in the fully turbulent flow region).
2. Calculation of wall shear-stress and appropriate generation and dissipation rates of turbulent kinetic energy for the near-wall control volume.
3. Modification of the discretized transport equations for wall-parallel momentum and turbulent kinetic energy or Reynolds stresses over near-wall control volumes, using the above wall shear stress and cell-averaged generation/dissipation rates.
4. Numerical solution of resulting discretized equations.

3.5.4 Standard wall treatment formulations

One considers the general configuration of a boundary face as shown in Figure 3.3:

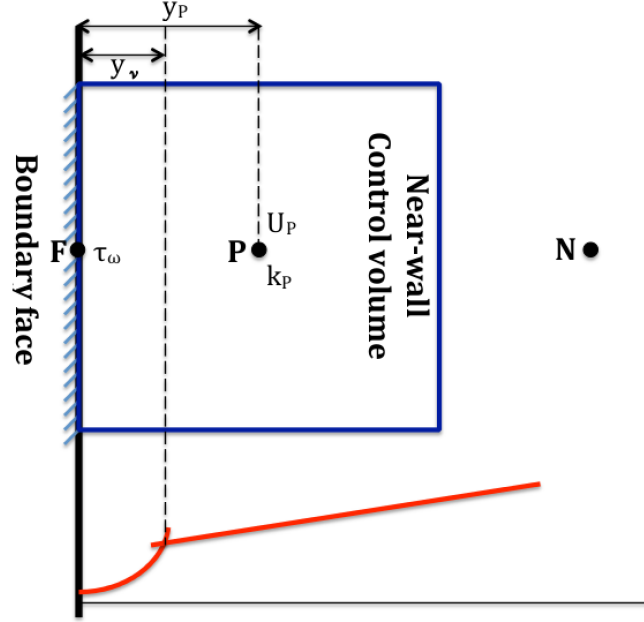


Figure 3.3: General configuration of a boundary face.

F denotes the centre of the boundary face, and P is the centre of the near-wall control volume.

3.5.4.1 Single velocity-scale wall function

Using the log-law of Equation 3.31, applying it at a near-wall node leads to Equation 3.35, from which one can obtain the wall shear stress:

$$\frac{U_P}{(\tau_w/\rho)^{1/2}} = \frac{1}{\kappa} \ln \left[E y \frac{(\tau_w/\rho)^{1/2}}{\nu} \right] = U^+ = \frac{1}{\kappa} \ln y^+ + B \equiv U^+ = \frac{1}{\kappa} \ln E y^+, \quad (3.35)$$

where $\kappa = 0.41$ and $E = 8.4$ is a roughness parameter usually taken as a constant determining the thickness of the viscous sublayer.

The temperature variation is represented as:

$$T^+ = \frac{\rho C_p \sqrt{\tau_w / \rho} (T_P - T_w)}{\dot{q}_w''} = \frac{1}{\tilde{\kappa}} \ln y^+ + B \equiv \frac{1}{\tilde{\kappa}} \ln \tilde{E} y^+, \quad (3.36)$$

where C_p is the specific heat capacity, T_w and \dot{q}_w'' are, respectively, temperature and heat flux to the wall from the fluid, $\tilde{\kappa}$ is the thermal Von Kármán constant (usually taken to be 0.38), and $\tilde{E} \simeq 9$ (for smooth walls).

After rearrangement, the heat transfer rate in terms of the distance of the wall-adjacent control volume, y_P , and the temperature, T_P is represented as

$$\dot{q}_w'' = \frac{\tilde{\kappa} \rho C_p \sqrt{\tau_w / \rho} (T_P - T_w)}{\ln \tilde{E} y^+}, \quad (3.37)$$

3.5.4.2 Two velocity scale wall function

The above form of the wall function has been used successfully to compute heat transfer rates in many attached flows. However, an unfortunate weakness of this approach is that, if the wall shear stress should fall to zero, so also does the wall heat transfer rate (see the book of Hanjalić and Launder [43]). The heat transfer coefficients are close to maximum at stagnation points, then the equation could give highly inaccurate results. There have therefore been several refined versions of wall functions proposed where attempts have been made to develop forms applicable over a wider range of flow conditions. The best known and the most widely used form is that due to Jones and Launder [53], where essentially the wall friction velocity $\sqrt{\tau_w / \rho}$ is replaced by the square root of the near-wall turbulence energy, k . The law of the wall for velocity and temperature is thus reformulated as

$$U^* \equiv \frac{U_P k_P^{1/2}}{(\tau_w / \rho)} = \frac{1}{C_\mu^{1/4} \kappa} \ln \left(\frac{E C_\mu^{1/4} k_P^{1/2} y}{\nu} \right) = \frac{1}{\kappa^*} \ln E^* y^*, \quad (3.38)$$

$$T^* = \frac{\rho C_p k_P^{1/2} (T - T_w)}{\dot{q}_w''} = \frac{1}{C_\mu^{1/4} \tilde{\kappa}} \ln \frac{\tilde{E} C_\mu^{1/4} k_P^{1/2} y}{\nu} = \frac{1}{\tilde{\kappa}^*} \ln \tilde{E}^* y^*, \quad (3.39)$$

where $\kappa^* \equiv \kappa C_\mu^{1/4}$ and $\tilde{\kappa}^* \equiv \tilde{\kappa} C_\mu^{1/4}$, $E^* = E C_\mu^{1/4}$ and $\tilde{E}^* = \tilde{E} C_\mu^{1/4}$, $y^* \equiv k^{1/2} y / \nu = (k^{1/2} / U_\tau) y^+$.

Assuming the above formulae are valid at the near-wall control volume results in the wall shear stress being given as:

$$\tau_\omega = \frac{\kappa^* U_P k_P^{1/2}}{\ln E^* y^*}, \quad (3.40)$$

Rearranging Equation 3.39, one obtains the following expression linking the wall heat flux to the wall and near-wall nodal temperatures:

$$\dot{q}_\omega'' = \frac{\widetilde{\kappa^*} \rho C_p k_P^{1/2} (T_P - T_\omega)}{\ln \widetilde{E^*} y^*}, \quad (3.41)$$

The advantage of the above approach for impinging and reattaching flows is that the heat transfer is non-zero, and is typically of around the correct magnitude for such flow situations.

In order to use the above form one needs to define k_P , and this is usually obtained by solving the k transport equation over each near-wall cell. However, since generation and dissipation terms will vary considerably across the cell, simply using the discretization approach of evaluating them at the cell centre may not be sufficiently accurate.

An approach taken in some solvers, including the code used for the present thesis (*Code_Saturne* 2.0), is to base the generation rate on a turbulent shear stress that is assumed to be constant over the cell (and hence equal to the wall shear stress) and mean velocity gradient obtained by differentiating the logarithmic velocity profile. This leads to:

$$P_{k,P} = \frac{\tau_\omega^2}{\rho^2 \kappa^* k_P^{1/2} y_P}, \quad (3.42)$$

The above formulations do not fully account for the strong variation of production and dissipation rates over the near-wall region. To account for this, one approach is to estimate cell-averaged values of P_k and ε , that can then be used in the discretized k transport equation.

One such approach was proposed by Chieng and Launder [20], the approach is based on building approximations for the variation of generation and dissipation rates over the near-wall cell. One assumes the turbulent shear stress is zero within the viscous sublayer, and then equal to the wall shear stress beyond that, whilst the mean velocity gradient outside the viscous sublayer is obtained from differentiating the log-law. The

mean turbulence energy generation rate over the near-wall control volume, $\overline{P_k}$, is then approximated as:

$$\overline{P_k} = \frac{1}{y_n} \int_{y_\nu}^{y_n} \frac{(\tau_\omega/\rho)^2}{\kappa^* k_P^{1/2} y} dy = \frac{(\tau_\omega/\rho)^2}{\kappa^* k_P^{1/2} y_n} \ln \left(\frac{y_n}{y_\nu} \right), \quad (3.43)$$

where y_n is the distance of the near-wall node centre to the wall, and y_ν is the distance of the edge of the viscous sub-layer to the wall.

The wall value of the dissipation rate may be evaluated, according to Jones and Launder [53], as:

$$\varepsilon_\omega = \lim_{y \rightarrow 0} \frac{2 \nu k}{y^2} = \nu \frac{\partial^2 k}{\partial y^2}, \quad (3.44)$$

The value of k at the edge of the viscous layer is taken as that at the near-wall node, the dissipation within the sublayer is then assumed to be uniform, equals to:

$$\varepsilon_\nu = \frac{2 \nu k_P}{y_\nu^2}, \quad (3.45)$$

The dissipation rate can then be estimated by assuming a linearly increasing length-scale across the cell, so that at the centre of the near-wall control volume one has:

$$\varepsilon_P = \frac{k_P^{3/2}}{C_l y_P}, \quad (3.46)$$

where $C_l = \kappa^*/C_\mu = \kappa/C_\mu^{3/4} \approx 2.5$.

Thus the spatially averaged dissipation rate over the near-wall control volume is expressed as:

$$\bar{\varepsilon} = \frac{1}{y_n} \left[\int_0^{y_\nu} \frac{2 \nu k_P}{y_\nu^2} dy + \int_{y_\nu}^{y_n} \frac{k^{3/2}}{C_l y} dy \right] = \frac{1}{y_n} \left[\frac{2 \nu k_P}{y_\nu^2} + \frac{k^{3/2}}{C_l y} \ln \left(\frac{y_n}{y_\nu} \right) \right], \quad (3.47)$$

3.5.4.3 Scalable wall function

The scalable wall function approach of Grotjans and Menter[42] is based on limiting the minimum value of y^+ so the value of the velocity gradient at the first cell will be the same as if it was on the edge of the viscous sublayer. A new value of y^+ is then

calculated, denoted by y_b^+ , using the friction velocity U_k :

$$y_b^+ = \max\left(\frac{U_k y}{\nu}, y_{lim}^+\right) \quad \text{with} \quad y_{lim}^+ = 11.06, \quad (3.48)$$

The wall-shear stress over the wall boundary face can be computed as:

$$\tau_{wall} = \rho U_\tau U_k, \quad (3.49)$$

In this procedure the wall can be seen as the limit of the logarithmic layer. When the grid is fine ($y^+ < y_{lim}^+$), the relation between U_τ and U becomes linear, that is:

$$U = \alpha U_\tau, \quad (3.50)$$

The friction velocity U_τ is obtained, using the log law, as a function of y_b^+ :

$$U_\tau = \frac{U}{\frac{1}{\kappa} \ln(y_b^+) + C}, \quad (3.51)$$

One obtains:

$$\alpha = \frac{1}{\kappa} \log(11.06) + 5 = 10.86, \quad (3.52)$$

The advantage of this procedure is that predictions are less sensitive to the location of near-wall nodes.

3.5.5 wall functions in *Code_Saturne 2.0*

In *Code_Saturne 2.0*, like in any other CFD solver, the high-Reynolds number approach is based on the use of wall functions to bridge the viscous sublayer and determine the shear stress. There exist three simple wall function formulations in the official version of the code, including the single-velocity-scale, two-velocity-scale and scalable wall functions described in the previous section. wall functions in *Code_Saturne 2.0* are all base on the log-law assumption.

In *Code_Saturne 2.0*, the transport equation for turbulent kinetic energy k is solved (or, for the components of the normal stresses if a second moment closure is used). The rate of production at the centre of the near-wall control volume, P , is calculated as:

$$P_k = |\tau_\omega| \frac{C_\mu^{1/4} k_P^{1/2}}{\kappa y_P}, \quad (3.53)$$

The momentum and enthalpy equations (for uniform wall temperature) in the wall-

normal direction are reduced to (the pressure gradient is neglected):

$$\tau_\omega = \mu \frac{\partial U}{\partial y} - \overline{\rho u'_i u'_j}, \quad (3.54)$$

and

$$\frac{\mu_t}{Pr_t} \frac{\partial T}{\partial y} - \overline{\rho u'_j t'} = \frac{q_\omega}{C_p}, \quad (3.55)$$

where C_P is the specific heat capacity of the fluid, and Pr_t is the turbulent Prandtl number.

As mentioned earlier, the heat fluxes in *Code_Saturne* 2.0 are modelled using the effective viscosity approximation:

$$\overline{\rho u'_j t'} = -\frac{\mu_t}{Pr_t} \frac{\partial T}{\partial y}, \quad (3.56)$$

By integrating Equation (3.55) and introducing the following normalised values:

$$T^+ = \frac{(T - T_\omega) C_p U_\tau}{q_\omega}, \quad y^+ = \frac{y U_\tau}{\nu}, \quad (3.57)$$

one obtains:

$$\frac{1}{Pr} \frac{dT^+}{dy^+} - \frac{\overline{\rho u'_j t'}}{q_\omega} = 1, \quad (3.58)$$

Considering Equation (3.56), the relation (3.58) can be re-written as:

$$\left(\frac{1}{Pr} \frac{dT^+}{dy^+} - \frac{1}{\sigma_t} \frac{\mu_t}{\mu} \right) \frac{dT^+}{dy^+} = 1, \quad (3.59)$$

or

$$\Gamma_{eff} \frac{dT^+}{dy^+} = 1, \quad (3.60)$$

A 3-layer model is used to approximate the variation of Γ_{eff} over the near-wall cell.

$$\left\{ \begin{array}{ll} \Gamma_{eff} = 1/Pr, & y^+ < y_1^+, \\ \Gamma_{eff} = 1/Pr + a_1 (y^+)^3 / Pr_t, & y_1^+ \leq y^+ < y_2^+, \\ \Gamma_{eff} = \kappa y^+ / Pr_t, & y_2^+ \leq y^+, \end{array} \right. \quad (3.61)$$

the values of y_1^+ and y_2^+ are obtained by calculating the intersection points of the three formulations used in the above expression for Γ_{eff} (see figure 3.4).

By integrating Equation (3.58) and using the same assumption above, one obtains:

$$\left\{ \begin{array}{ll} T^+ = Pr y^+, & y^+ < y_1^+, \\ T^+ = a_2 - \sigma_t / a_1 (y^+)^2, & y_1^+ \leq y^+ < y_2^+, \\ T^+ = Pr_t / \kappa \ln(y^+) + a_3, & y_2^+ \leq y^+, \end{array} \right. \quad (3.62)$$

where: $a_1 = \frac{Pr_t}{1000}$, $a_2 = 15Pr^{2/3}$, $a_3 = 15Pr^{2/3} - Pr_t / 2\kappa (1 + \ln(1000\kappa / Pr_t))$.

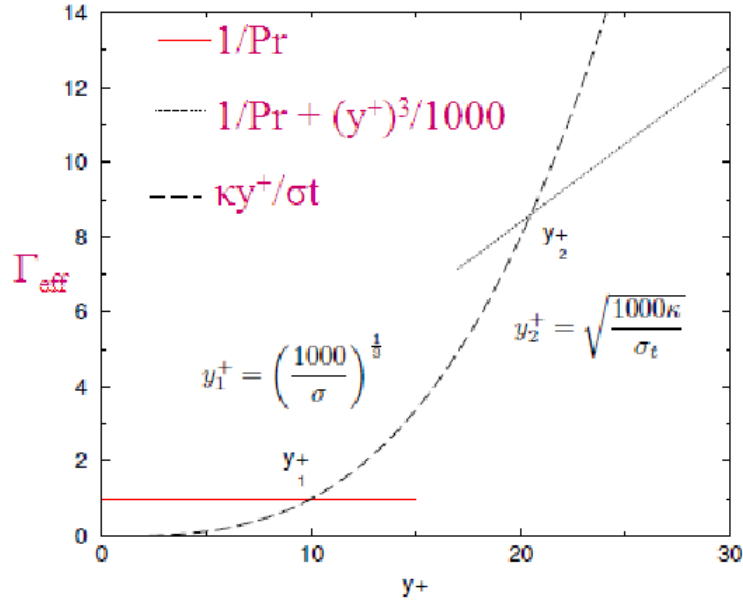


Figure 3.4: Γ_{eff} as a function of y^+ obtained for $Pr = 1$ and $Pr_t = 1$.

An exploration of some further refinements to the wall function embedded in *Code_Saturne* 2.0 has been undertaken in the present thesis, and details of these enhancements are given below.

3.5.6 *Code_Saturne* 2.0 wall function enhancements

In the original *Code_Saturne* 2.0 implementation a Neumann boundary condition for ε was imposed at the near wall node. The value of ε was obtained from the expression:

$$\varepsilon_P = \frac{4yU_k^5\rho^2}{\kappa\mu^2(y^+)^2}, \quad (3.63)$$

In the present thesis this has been modified to a Dirichlet boundary condition, to be consistent with the epsilon variation implied by Equation 3.46, to the following:

$$\varepsilon_P = \frac{k_P^{3/2}C_\mu^{3/4}}{\kappa y_P}, \quad (3.64)$$

The results of introducing these modifications will be shown in Chapter 5.

3.6 Large Eddy Simulation

3.6.1 Introduction

In a turbulent flow, it is observed that there are many different length scales. These length scales are representative of eddy scales in the motion. It is believed that the large scales receive the energy from the main flow, and subsequently deliver it via smaller scales to the smallest scales where it is dissipated. This phenomenon is called the cascade process.

The idea of LES comes from the hypothesis that the small scales, regardless of the type of flow and boundary conditions, show an isotropic behaviour. So if the large scales are resolved, it is sufficient to use a fairly simple model for the small scales which are called the sub-grid scales or SGS. In order to get reasonably good accuracy, the grid should be fine enough to ensure the cut-off (the wavenumber representing the smallest resolved scales) takes place within the inertial sub-range, but that at least a portion of that sub-range is actually resolved. According to Kaltenbach et al. [55], an LES simulation based on spectral methods over a moderate Reynolds number range will produce reliable results if the near wall grid spacings based on wall units are of the order of $\Delta x^+ = 100$ for streamwise direction, $\Delta y^+ = 1$ in the cross stream direction and $\Delta z^+ = 30$ in the spanwise direction. The extent of the grid in the spanwise direction should be such that the two point correlations of all important parameters in this direction reach to the zero.

There are four conceptual steps in LES:

- A filtering operation is defined to decompose the velocity $U(x, t)$ into the sum of a filtered (or resolved) component $\bar{U}(x, t)$ and a residual (or sub-grid-scale, SGS) component $u_{SGS}(x, t)$.
- The filtered velocity field $\bar{U}(x, t)$, which is three-dimensional and time-dependent, represents the motion of the large eddies.
- The equations for the evolution of the filtered velocity are derived from the Navier-Stokes equations. These equations are of a standard form, with the momentum equation containing the residual-stress tensor that arises from the residual motions.
- Closure is obtained by modelling the residual-stress tensor, most simply by an eddy-viscosity model.

The filtering in LES should, ideally, only remove the small scales, leaving the larger, energy-containing ones resolved. Near a wall, this has significant resolution implications, since the turbulence scales become smaller, due to near-wall effects, and so a very fine grid and small time step are required if one is to resolve a significant proportion of the turbulent motions here.

3.6.2 Filtering in LES

It is essential to define the quantities to be computed precisely. A velocity field that contains only the large scale components of the total field is needed. This is best produced by filtering the velocity field; in this approach, the large or resolved scale field is the one to be simulated. In the definitions below the fields will be treated as one-dimensional, but the generalisation, to three dimensions is straight forward. The filtered velocity is defined by:

$$\bar{U}_i(x) = \int G(x, x') u_i(x') dx', \quad (3.65)$$

where $G(x, x')$, the filter kernel, is a localised function. Filter kernels which have been applied in LES include a Gaussian, a box filter and a cutoff (a filter which eliminates all Fourier coefficients belonging to wave-numbers above a cutoff). Every filter has a length scale associated with it, Δ . Roughly, eddies of size larger than Δ are considered as the large eddies while those smaller than Δ are deemed to be the small eddies, whose effect will be modelled.

The LES filter is defined by the filter function $G(y)$ which must satisfy the condition

$$\int_{-\infty}^{+\infty} G(y) dy = 1, \quad (3.66)$$

For a flow variable ϕ , the filtered and “fluctuating” components $\bar{\phi}$ and ϕ' , respectively, are defined as

$$\bar{\phi} = \phi \star G = \int_{R^3} \phi(y) G(y-x) dy, \quad \phi' = \phi - \bar{\phi}, \quad (3.67)$$

where R denotes the set of real numbers and \star denotes the convolution operator.

There are many types of filter functions G used in the LES community. The most common are “box” (or “top-hat”) filter, the Gaussian filter, and Fourier sharp cut-off filter, all illustrated in Figure 3.5.

The box filter

The “box” filter function is given by

$$G(y) = \begin{cases} 0, & |y| > \Delta/2 \\ 1/V, & |y| < \Delta/2 \end{cases}, \quad (3.68)$$

where Δ is the characteristic filter length, and V is the filter volume, defined as Δ^3 .

Gaussian filter

The Gaussian filter function is given by

$$G(y) = \sqrt{A/\pi} \cdot e^{-Ay^2}, \quad (3.69)$$

where the constant A is commonly chosen to be $A = 6/\Delta^2$.

Fourier cut-off filter

Finally, the wave cut-off filter is defined in Fourier space. For this filter, all wave numbers above a cut-off number, k_c , are modelled, while all wave numbers below are resolved:

$$\hat{G}(y) = \begin{cases} 1, & k \leq k_c \\ 0, & k > k_c \end{cases}, \quad (3.70)$$

To illustrate the difference between the filters defined above they are applied to a test function, and the spectra of the filtered variables are shown in Figure 3.5. The top hat and Gaussian filters give similar results; in particular, they both smooth the large-scale fluctuations as well as the small-scale ones, unlike the Fourier cutoff, which only affects the scales below the cutoff wave number.

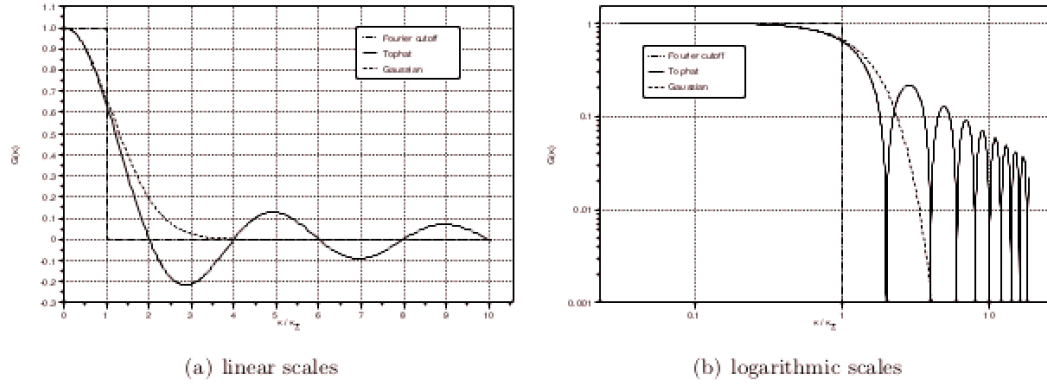


Figure 3.5: Associated transfer functions to the Fourier cut-off, top-hat and Gaussian filters.

3.6.3 Filtered Navier-Stokes equations

If the filtering operation (3.79) is applied to the governing Equations (3.1), (3.2) and (3.3), one obtains the filtered equations of motion. Following the introduction of the Boussinesq approximation for the buoyancy effect, they can be represented as:

$$\rho_0 \frac{\partial (\overline{U}_i)}{\partial x_i} = 0, \quad (3.71)$$

$$\rho \frac{\partial (\overline{U}_i)}{\partial t} + \frac{\partial}{\partial x_j} (\rho_0 \overline{U}_i \overline{U}_j) = -\frac{\partial \overline{P}}{\partial x_i} + \mu \frac{\partial}{\partial x_j} \left(\frac{\partial \overline{U}_i}{\partial x_j} + \frac{\partial \overline{U}_j}{\partial x_i} \right) - \rho_0 \frac{\partial \tau_{SGS,ij}}{\partial x_j} - \rho_0 (\overline{T} - T_0) g_i, \quad (3.72)$$

$$\rho_0 \frac{\partial \bar{T}}{\partial t} + \frac{\partial}{\partial x_j} (\rho_0 \bar{U}_j \bar{T}) = \frac{\partial}{\partial x_j} \left(\frac{\mu}{Pr} \frac{\partial \bar{T}}{\partial x_j} \right) - \rho_0 \frac{\partial h_{SGS,j}}{\partial x_j}, \quad (3.73)$$

The above filtering of the equations in space leads to unknown sub-grid-scale (SGS) stresses and heat fluxes in the filtered equations. They are defined in section 3.6.4 and modelled in section 3.6.5.

It should be noted that LES filtering is quite different from RANS averaging. The fundamental differences are summarised in the Table 3.1.

RANS	LES
$\overline{\phi'} = 0$	$\overline{\phi'} \neq 0$
$\frac{\partial \overline{\phi}}{\partial x_i} = \overline{\frac{\partial \phi}{\partial x_i}}$	$\frac{\partial \overline{\phi}}{\partial x_i} \neq \overline{\frac{\partial \phi}{\partial x_i}}$
$\overline{\overline{\phi}} = \overline{\phi}$	$\overline{\overline{\phi}} \neq \overline{\phi}$

Table 3.1: Difference between RANS averaging and LES filtering.

3.6.4 The sub-grid-scale stresses

The nonlinear term in Equation (3.72), can be decomposed (using the sub-grid-scale velocity $U_i(x, t) = \bar{U}_i(x, t) + u_i(x, t)$), and the SGS stresses written as:

$$\tau_{SGS,ij} = \overline{U_i U_j} - \bar{U}_i \bar{U}_j = \left(\overline{\bar{U}_i \bar{U}_j} + \overline{\bar{U}_i u_j} + \overline{\bar{U}_j u_i} + \overline{u_i u_j} \right) - \bar{U}_i \bar{U}_j, \quad (3.74)$$

$$\tau_{SGS,ij} = L_{ij} + C_{ij} + R_{ij}, \quad (3.75)$$

where

- $L_{ij} = \left(\overline{\bar{U}_i \bar{U}_j} - \bar{U}_i \bar{U}_j \right)$ is called the Leonard tensor, and represents interactions among the large scales.
- $C_{ij} = \left(\overline{\bar{U}_i u_j} + \overline{\bar{U}_j u_i} \right)$ is the Cross stress which represents the interactions between large and small scales.
- $R_{ij} = \overline{u_i u_j}$ is the Reynolds stress which reflects the interactions between sub-grid scales.

The Leonard tensor has only the resolved scales in it, so one can say the Leonard stress represents the interaction between the large scales and is responsible for transferring the energy to the unresolved small scales. This process is known as Outscatter.

The Cross stress tensor has a cross product of filtered and unfiltered fields in it, this means it has two known terms and two unknowns, but as a whole it an unknown quantity and needs to be modelled. It represents interactions between resolved and unresolved scales, and is hence responsible for the transferring of energy from large to small scales, or vice-versa (back scatter).

Finally the Reynolds stress involves only unresolved scales, and has to be modelled. This term is responsible for the transfer of energy from small scales to the large ones. This reverse flow phenomenon of energy is known as the backscatter.

The models used to approximate the SGS Reynolds Stress are called sub-grid-scale (SGS) or sub-filter-scale models.

3.6.5 The sub-grid-scale models

3.6.5.1 The Smagorinsky model

In coarse LES, the dissipative scales of motion are resolved poorly. The main role of the sub-grid-scale model is, therefore, to remove energy from the resolved scales, mimicking the drain that is associated with the energy cascade. Most sub-grid-scale models and heat fluxes are eddy-viscosity models of the forms:

$$\tau_{SGS,ij} = -2\nu_t \overline{S_{ij}} + \frac{\delta_{ij}}{3} \tau_{kk}, \quad (3.76)$$

$$h_{SGS,j} = -\frac{\nu_t}{Pr_t} \frac{\partial \overline{T}}{\partial x_j}, \quad (3.77)$$

where Pr_t is the SGS Prandtl number. In the LES literature, a broad range of values has been proposed for this parameter, from 0.25 to 0.9 (see for example Ciofalo [22]).

The Smagorinsky sub-grid-scale model is used in the present LES computations, in which the sub-grid eddy-viscosity is modelled as:

$$\nu_t = (C_s f_{vd} \Delta)^2 |\overline{S}|, \quad (3.78)$$

with $|\overline{S}| = \left(2\overline{S_{ij}}\overline{S_{ij}}\right)^{1/2}$, where $\overline{S_{ij}} = \left(\partial\overline{U_i}/\partial x_j + \partial\overline{U_j}/\partial x_i\right)/2$ is the strain rate tensor. f_{vd} is the Van Driest damping function [37]. Δ is the grid size (for anisotropic grids, the

cube root of the cell volume is usually employed, mentioned below in the next section). $C_s = \sqrt{C}$ is the Smagorinsky constant, the value of the coefficient C can be determined from isotropic turbulence decay; if the cutoff is in the middle of a long inertial subrange, the Smagorinsky constant takes values between 0.18 and 0.23 (and $C \simeq 0.032$ —0.053) (see Ferziger and Peric [40]). In the presence of shear, near solid boundaries or in transitional flows, however, it has been found that it must be decreased. This has been accomplished by various types of ad hoc corrections such as Van Driest damping [37] or intermittency functions.

The widely-used form being that of VanDriest [37] in which the length scale Δ is multiplied by the damping function f_{vd} :

$$\Delta \rightarrow \Delta f_{vd} \equiv \Delta \left(1 - \exp\left(-y^+/A^+\right)\right), \quad (3.79)$$

Here $y^+ = yu_\tau/\nu$ is the standard non-dimensional distance from the wall, and $A^+ = 25$ is the Van Driest constant.

3.6.6 Grid resolution for LES

The quality of LES computation mostly relies on the scale separation between scales of turbulence captured and the ones modelled, which is related to the grid resolution. A quantitative measure of the turbulence resolution, introduced by Pope [76], depends on the resolved turbulent kinetic energy, k , and the SGS turbulent kinetic energy, k_{SGS} , defined as:

$$\bar{k} = \frac{1}{2} \left(\overline{U U} \right), \quad (3.80)$$

$$k_{SGS} = \frac{1}{2} \left(\overline{UU} - \overline{U} \overline{U} \right), \quad (3.81)$$

one considers R the resolution criterion, defined as:

$$R = \frac{k_{SGS}}{k_{SGS} + \bar{k}}, \quad (3.82)$$

R varies between 0 (equivalent to DNS where no model is needed) and 1. In the present LES computations, the resolution criterion R takes a very small value close to zero. This is achieved by employing a very fine mesh which can assure the resolution of not just large length scales but also many of the smallest dissipative ones.

One set of guidelines to estimate grid spacing quality for near-wall LES is to consider

the non-dimensional cell size (in wall units). For a grid with grid-spacings of Δx , Δy and Δz in the x , y and z directions respectively, the lengthscale in the SGS model is here taken as:

$$\Delta = (\Delta x, \Delta y, \Delta z)^{1/3}, \quad (3.83)$$

where κ is the Von Karman constant which takes the value of 0.41, and n is the distance to the nearest wall. In the present thesis, it is believed that, for a good resolution, the grid has been designed to respect the constraints: $\Delta x^+ \ll 40$, $\Delta y^+ \ll 1$ and $\Delta z^+ \ll 20$.

3.6.7 LES initialisation

When running an LES computation of a given test case it is important to initialise with turbulence at the start of a time dependent solution process. This is achieved by starting an LES simulation from a converged unsteady RANS simulation of the same test case. The mean profiles of the velocity from the RANS computation are those of a turbulent flow, and they can consequently allow the LES solution to develop more rapidly than if initialised from some other, more arbitrary field.

3.7 Final remarks

The RANS and LES governing equations have been exposed in the present Chapter, and the turbulence and near-wall models used in this thesis have been described. Full details of the schemes, including closure coefficients are given in Appendix B. The modelling strategies described in this Chapter will be used to compute buoyancy driven flow inside different enclosures ranging from 2-D vertical and tilted cavities to 3-D inclined cavities under different stratifications, and finally an industrial test case in Chapters 5 to 8, making comparison to recent experimental data, where available.

Chapter 4

Numerical Methods

4.1 Introduction

This chapter describes the numerical methods and solution processes used in the present work to generate approximate solutions to the flow equations described in the previous Chapter 3.

The most fundamental consideration in CFD is how one treats a continuous fluid flow with a computer. The most widely used general method is to discretize the spatial domain into small cells to form a volume mesh, and then apply suitable algorithms to approximate the governing equations of motion on these cells. For all such CFD approaches, the same basic procedure is followed:

- **Pre-processing:** This consists of the input of a flow problem to a CFD program, typically by means of an operator-friendly interface or Fortran programming, and the subsequent transformation of this input into a form suitable for use by the solver. The activities at the pre-processing stage involve:
 1. Definition of the geometry and regions of interest: the computational domain,
 2. The volume occupied by the fluid is divided into discrete cells (the mesh). Standard meshes are typically constructed in either a structured or unstructured arrangement, using one or more type of cell elements. The most commonly known types of elements in 3D are: the tetrahedron, the pyramid, the prism and the hexahedron. *Code_Saturne* 2.0 can handle many types of cells, including a number of formats generated from packages such as SALOME SMES, I-DEAS Nx, GMSH, Gambit (used in the present thesis), Simail, Harpoon, ICEM-CFD, Star-CCM+. The meshes used in the present thesis are structured (conforming), and

composed of hexahedral elements. For 2-D simulations, different structured uniform and non-uniform coarse grids have been made to be used with high-Reynolds number models; a structured non-uniform fine grid has been built to be used with low-Reynolds number models. For 3-D simulations, structured, non-uniform grids have been used.

3. Selection of the physical phenomena that need to be modelled.
 4. Specification of the appropriate boundary condition types to be applied (denoted by names or colours).
- **Solver:** Assembling discretized equations and solving them. The solver considered here is the unstructured finite volume code called *Code_Saturne* 2.0.
 - **Post-processing:** As in pre-processing a huge amount of development work has recently took place in the post-processing field. Owing to the increased popularity of engineering workstations, many of which have outstanding graphics capability, the leading CFD packages are now equipped with versatile data visualisation tools. These include: domain geometry and grid display, vector plots, line and shaded contour plots, particle tracking, view manipulation (translation, rotation, scaling, etc.), colour postscript output.

4.2 *Code_Saturne* 2.0 solver

At Electricity De France (EDF), development of in-house codes has been a strategic choice for more than thirteen years. In particular, for problems requiring local three-dimensional analyses with refined flow modelling, specific effort had been put into in-house “general purpose CFD codes” such as N3S-EF [CHA 92] and ESTET-ASTRID [MAT 92]. N3S-EF, an unstructured finite element code, could tackle complex geometries, while ESTET-ASTRID, a structured finite volume code, provided refined physical modelling. In 1996, EDF initiated a program to unify the potentials of these two products within the same software, *Code_Saturne* 2.0. In addition to making available to users the most advanced capabilities of these two complementary products, it was also a convenient way to benefit from the recent advances in design, software development, programming and meshing techniques, numerical schemes and physical modelling.

Code_Saturne 2.0 is an unstructured finite-volume, open source code (www.Code-Saturne.org). It solves the Navier-Stokes equations for 2D, 2D-axisymmetric and 3D flows, steady or unsteady, laminar or turbulent, incompressible or weakly dilatable,

isothermal or not, with scalars transport if required. Several turbulence models are available, from Reynolds-Averaged models (a. k. a. RANS models) to Large-Eddy Simulation models. In addition, a number of specific physical models are also available as "modules": gas, coal and heavy-fuel oil combustion, semi-transparent radiative transfer, particle-tracking with Lagrangian modelling, Joule effect, electric arcs, weakly compressible flows, atmospheric flows, rotor/stator interaction for hydraulic machines.

4.2.1 Features of *Code_Saturne* 2.0

- **Discretization**

Code_Saturne 2.0 is based on a co-located Finite Volume approach that handles meshes with any type of cell (tetrahedral, hexahedral, prismatic, pyramidal, polyhedral...) and any type of grid structure (unstructured, block structured, hybrid, conforming or non-conforming...). The code can solve flows in steady or unsteady mode. It uses a theta scheme for the time discretization.

- **Velocity-pressure coupling:** *Code_Saturne* 2.0 uses a fractional step method, similar to SIMPLEC. Rhie & Chow interpolation is used when solving the pressure to avoid spurious oscillations. The main steps involved are:

1. Velocity prediction: Solve the momentum equation with an explicit pressure gradient and obtain a predicted velocity
2. Pressure correction: Use the continuity equation to enforce mass conservation
3. Update velocity field

After the velocity has been updated, the resolution of turbulent variables and scalars is done according to their time scheme.

- **Linear system resolution:** *Code_Saturne* 2.0 has different ways of solving the linear system:

1. Jacobi (default for velocity, temperature, turbulent variables, passive scalars).
2. Algebraic multigrid (default for Poisson equation).
3. Conjugate gradient (default for Poisson equation).

4. Stabilised bi-conjugate gradient (BI-CGSTAB) (optional).
- **Convective scheme:** Different schemes for convective terms are available in *Code_Saturne* 2.0:
 1. First order upwind Scheme.
 2. Second order centred scheme.
 3. Second order Linear Upwind (SOLU) Scheme.

A slope test is activated by default for second order schemes to switch from second order to first order upwind in case of overshoots.

- **Gradient calculation:** In *Code_Saturne* 2.0 several options are available:
 1. Iterative reconstruction of the non-orthogonalities (initialisation by zero or based on the least-square method).
 2. Least squares method (with a standard, extended or partial extended neighbourhood).

These features will be detailed in the next section.

- **User routines:** The following principal routines are used in the present thesis:
 1. `usclim.f90`: this routine allows the user to define particular boundary conditions (inlet, outlet, walls, symmetries or other non standard boundary conditions) on the boundary faces and modify them if needed for particular cases.
 2. `usini1.f90`: this routine allows the user to define all the physical properties and parameters needed for running the calculation including the physical properties, the number of time-steps, averaging...etc
 3. `usphyv.f90`: this routine allows the user to specify variable physical properties, such as density.
 4. `usproj.f90`: this routine is called at the end of each time step and has access to the whole set of variables of the code. It is therefore useful for performing user-specific post-processing.

Other routines exist in *Code_Saturne* 2.0, each one having a specific role. The user can make modifications, depending on the case studied and the models used or models to be modified.

Details of the finite volume method, space and time discretization schemes and other numerical methods in *Code_Saturne* 2.0 are shown in Appendix C.

4.3 Wall function implementation in *Code_Saturne* 2.0

4.3.1 Boundary conditions for the velocity ($k - \varepsilon$ model)

One considers the boundary face as shown in Figure 3.3. The default approach for treating walls when using High-Re RANS models for turbulent flows in *Code_Saturne* 2.0 is to employ the two-velocity-scale logarithmic wall function, described above in Section 3.5.4.2. Using this approach to account for physical phenomena related to the wall layer, it is necessary to modify the wall boundary conditions described above, to approximate the wall shear stress. The tangential stress can be written, (in a way that introduces the turbulent viscosity), as:

$$\tau_\omega = \rho_P U_\tau U_k = \frac{U_\tau}{\kappa y_P} \rho_P \kappa y_P U_k = \frac{U_\tau}{\kappa y_P} \mu_t^{ml}, \quad (4.1)$$

where U_k is the friction velocity at the wall obtained from the turbulent kinetic energy. For the two-velocity-scale model, U_k and U_τ are defined as:

$$U_k = C_\mu^{1/2} k_P^{1/4} \quad (4.2)$$

$$\begin{cases} \frac{U_P}{U_\tau} = \frac{1}{\kappa} \ln(y_k^+) + 5.2 & \text{for } y_k^+ > y_\nu^+ \\ \frac{U_P}{U_\tau} = y_k^+ & \text{for } y_k^+ \leq y_\nu^+ \end{cases}, \quad (4.3)$$

with $C_\mu = 0.09$ and $\kappa = 0.42$. y_k^+ represents a dimensionless wall distance, $y_k^+ = U_k y_P / \nu$ (ν is the molecular kinematic viscosity taken at the centre of the boundary cell). y_ν^+ is the dimensionless limit distance which separates the viscous sublayer from the logarithmic region. Its value is $1/\kappa$, by default, and 10.88 in LES.

The turbulent viscosity in Equation (4.1) is modelled using a mixing-length approximation as: $\mu_t^{ml} = \rho_P \kappa y_P U_k$.

The velocity gradient at the cell face is computed in the code as:

$$(\mu_I + \mu_{t,I}) \frac{\partial U}{\partial n} = (\mu_N + \mu_{t,N}) \frac{(U_F - U_P)}{y_P}, \quad (4.4)$$

Using Equations 4.1 and 4.4, one obtains the value of the velocity at the face U_F :

$$U_F = U_P - \frac{y_N}{\mu_P + \mu_{t,P}} \tau_\omega = U_P - \frac{U_k}{\kappa (\mu_P + \mu_{t,P})} \max(\mu_t^{ml} - \mu_{t,P}), \quad (4.5)$$

An approximation made in *Code_Saturne* 2.0 is to impose a zero normal velocity at the wall, and use Equation 4.5, projected onto the plane parallel to the wall:

$$U_F = U_{\tau,P} - \frac{U_k}{\kappa (\mu_P + \mu_{t,P})} \max(\mu_t^{ml} - \mu_{t,P}), \quad (4.6)$$

In cells where the value obtained for y^+ is lower than y_ν^+ , a no-slip condition is applied.

The wall boundary condition for the wall-parallel velocity when using the $k - \varepsilon$ model is thus summarised as:

$$\begin{cases} U_F = v_F & y^+ \leq y_\nu^+ \\ U_F = v_F + \left[U_{\tau,P} - \frac{U^*}{\kappa (\mu_P + \mu_{t,P})} \max(\mu_t^{ml} - \mu_{t,P}) \right] & \text{Otherwise} \end{cases}, \quad (4.7)$$

where v_F is the velocity at the wall.

The transport equation for k is solved (or, for the components of the normal stresses if a second moment closure is used).

4.3.2 Boundary conditions for turbulence

For the $k - \varepsilon$ model, Dirichlet condition is imposed at the wall for both k and ε . Their values at the edge of the boundary face are implemented in the code as:

$$k_F^{(n+1)} = \frac{(U_k^2)^{(n)}}{C_\mu^{1/2}} = k_P^{(n)}, \quad (4.8)$$

$$\varepsilon_F^{(n+1)} = \varepsilon_P^{(n)} + \frac{(U_k^3)^{(n)}}{\kappa y_P}, \quad (4.9)$$

where ε_P is defined above in Equation (3.64).

For the second moment closure the conditions are:

$$\frac{\partial \overline{u'_i u'_j}}{\partial y} n_j = 0 \quad \text{if} \quad i = j, \quad (4.10)$$

$$\overline{u'_i u'_j}^{(n+1)} = U_\tau^{(n)} U_k^{(n)}, \quad (4.11)$$

$$\overline{u'_i u'_k} = \overline{u'_j u'_k} = 0, \quad (4.12)$$

$$\varepsilon_F^{(n+1)} = \varepsilon_P^{(n)} + \frac{(U_k^3)^{(n)}}{\kappa y_P}, \quad (4.13)$$

4.4 Final remarks

In this chapter the overall numerical procedure and notes on the implementation of the wall function in *Code_Saturne* 2.0 are summarised.

Chapter 5

URANS Computation of Flow Within 2-D Vertical and Tilted Cavities

5.1 2-D vertical enclosure (Betts cavity [11])

5.1.1 Case description

2-D buoyancy-driven flows in a vertical cavity have been computed numerically. Dimensions of the cavity are: $H \times L = 2.18m \times 0.0762m$, leading to an aspect ratio $A = H/L$ of 28.6. The cold and hot long walls are isothermal (Figure 5.1), whilst the other walls are insulated (adiabatic). The Prandtl number (Pr) of the fluid is taken as 0.71 (air), and the temperature of the fluid and other fluid properties are chosen such that the Rayleigh number, defined as:

$$Ra = \frac{\rho^2 g \beta \Delta T L^3}{\mu^2} Pr, \quad (5.1)$$

where $\Delta T = T_h - T_c = 34^\circ C$, with the subscripts h and c denoting the hot inlet temperature and cold wall temperature respectively, takes a value of 1.86×10^6 .

The reference buoyant velocity, V_0 , used for scaling results below, is defined as:

$$V_0 = \sqrt{\beta g \Delta T L}, \quad (5.2)$$

The local Nusselt number based on distance between the cold and hot sides, L , is defined as:

$$Nu_L = \frac{hL}{K}, \quad (5.3)$$

where K is the thermal conductivity of the fluid and h is the surface heat flux coefficient defined as:

$$h = \frac{q_\omega}{\Delta T}, \quad (5.4)$$

with q_ω the wall heat flux per unit area obtained from Fourier's law:

$$q_\omega = -K \left. \frac{\partial T}{\partial x_n} \right|_{wall}, \quad (5.5)$$

where x_n denotes the direction normal to the wall.

The properties of the fluid considered in the present thesis are illustrated in table 5.1.

Flow properties	Values
Thermal expansion coefficient β ($1/^\circ C$)	0.0033
Thermal diffusivity α (m^2/s)	2.37×10^{-5}
Density ρ (kg/m^3)	1.187
Specific heat capacity C_p ($J/kg.K$)	1005.38
Thermal conductivity Γ ($W/m.K$)	0.026
Kinematic viscosity ν (m^2/s)	1.59×10^{-5}
Dynamic viscosity μ ($kg/m.s$)	1.8×10^{-5}
Gravity g (m/s^2)	9.81
Temperature difference ΔT ($^\circ C$)	18
Temperature of reference $T_0 = \frac{T_h + T_c}{2}$ ($^\circ C$)	25

Table 5.1: Flow properties.

Thermal and dynamic boundary conditions for the present test cases are summarized in Table 5.2:

Type	Thermal boundary conditions	Dynamic boundary conditions
X=0 (Isothermal wall at T_h)	$T_h = 34^0C$	$U = 0, V = 0$ (Adherence of the fluid to the wall)
X=L (Isothermal wall at T_c)	$T_c = 16^0C$	
Y=0 (Adiabatic wall)	$\frac{\partial T}{\partial y} = 0$	
Y=H (Adiabatic wall)	$\frac{\partial T}{\partial y} = 0$	

Table 5.2: Thermal and dynamic boundary conditions for 2-D computations.

5.1.2 Computational mesh and numerical methods

In order to choose the most appropriate computational grids to use for both high- and low-Re models, a number of grids with different node densities and distributions, and different near-wall non-dimensional y^+ distances, have been tested. These tests are detailed in Appendix D. As a result of these grid sensitivity tests, the mesh used for the computation of these 2-D cavities using high-Re models with wall functions is a 80×20 uniform coarse grid, shown in Figure 5.2-a. For the computations using low-Re models 120×80 non-uniform mesh has been employed with grid nodes clustered towards the walls to resolve the steep gradients in these regions. This is shown in Figure 5.2-b. Parameters of both grids are given in Table 5.3.

Spatial discretization was achieved using a second-order central difference scheme (CDS), whilst for time discretization the implicit first-order Euler scheme was employed with a time step of $\delta t = 0.01$, giving a maximum CFL number of 0.5. Simulations were run to obtain steady state conditions, typically requiring around 20000 time steps (approximately 4 hours on an Intel Duo-Core processor computer).

	2-D Coarse Grid	2-D Fine grid
Density	80×20	120×80
Size of near-wall cell Y	0.0038	0.0002
Y^+ [min, max]	[3, 11]	$[10^{-5}, 0.01]$

Table 5.3: Parameters of 2-D coarse and fine computational meshes.

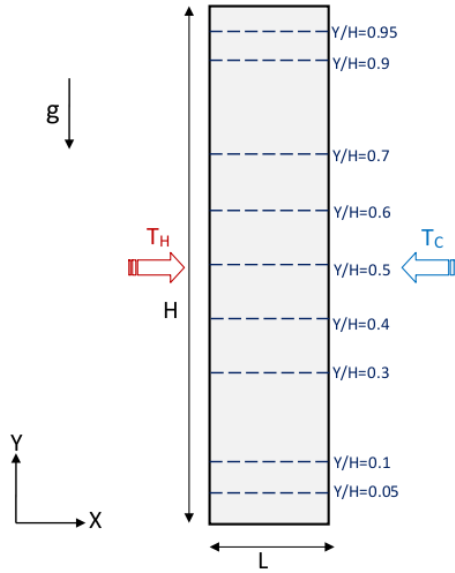


Figure 5.1: Geometry of 2-D vertical cavity. Location of plot lines are indicated.

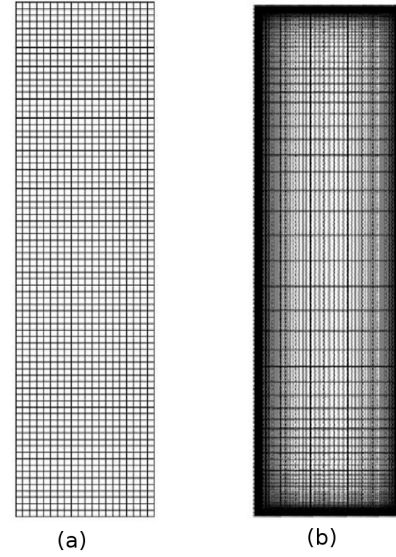


Figure 5.2: 2-D computational meshes for high and low-Re modelling of the vertical cavity.

5.1.3 Qualitative results

To give a qualitative picture of the flow, Figures 5.3 to 5.5 illustrate contours of temperature, velocity magnitude and turbulent kinetic energy respectively inside the vertical enclosure resulting from different high and low-Re models. The general pattern is similar between models, with fluid near wall moving upwards wall to impinge on the top surface, and that near the cold wall downwards to impinge on the bottom wall. There are some qualitative differences visible between predictions of the thermal boundary layer thickness, particularly towards the upper and lower ends of the cavity, as a result of differences in the near-wall and outer modelling details.

Contours of the velocity magnitude shown in Figure 5.4 show a single circulation formed by the fluid moving up the hot wall side and down the cold wall side of the cavity. This confirms the comments above. Again, the predicted pattern is similar between the models, although the most noticeable feature of this comparison is that the *LRR* gives the lowest peaks, and the *SSG* the highest. The *SST* scheme appears to give slightly higher velocity peaks than the elliptic relaxation based model.

The single circulation cell in the centre of the cavity leads to peak turbulence levels in this region. The second moment closures give lower values of turbulent kinetic energy comparing with the $k - \varepsilon$ and $\varphi - f$ models which show significant high turbulence in

the core of the cavity.

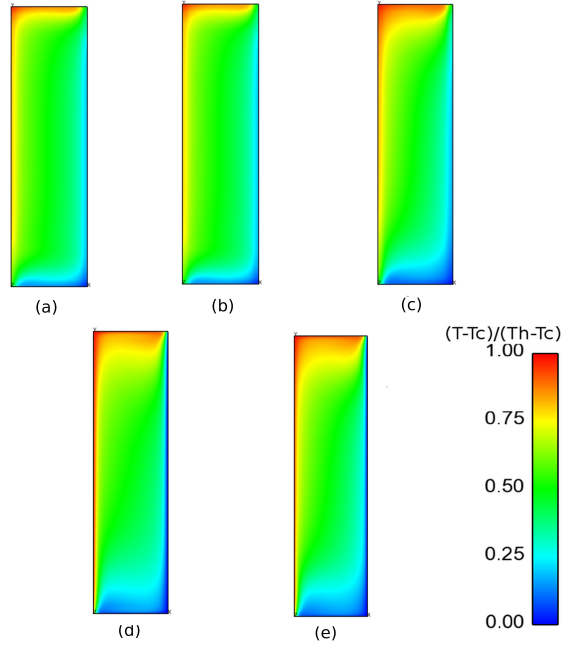


Figure 5.3: Temperature contours inside the vertical cavity 2.18×0.0762 . (a) $k - \varepsilon$, (b) LRR , (c) SSG , (d) $k - \omega SST$, (e) $\varphi - f$.

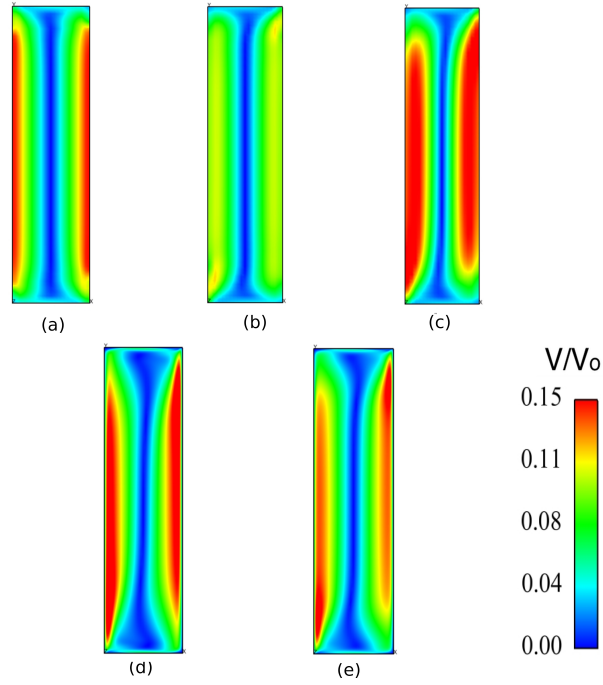


Figure 5.4: Velocity magnitude contours inside the vertical cavity 2.18×0.0762 . (a) $k - \varepsilon$, (b) LRR , (c) SSG , (d) $k - \omega SST$, (e) $\varphi - f$.

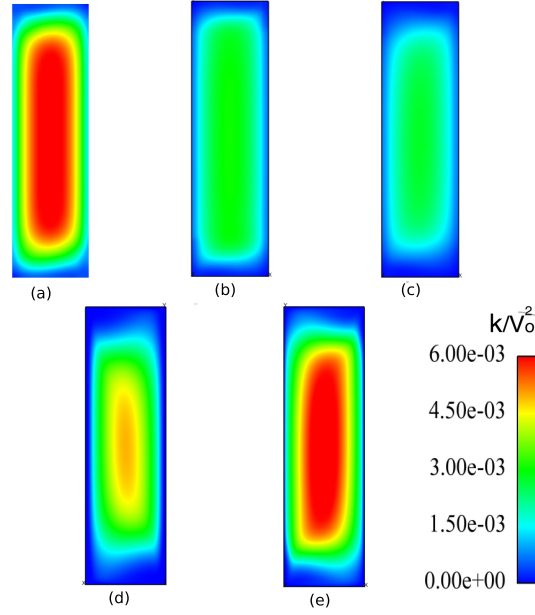


Figure 5.5: Turbulent kinetic energy contours inside the vertical cavity 2.18×0.0762 . (a) $k - \varepsilon$, (b) LRR , (c) SSG , (d) $k - \omega$ SST , (e) $\varphi - f$.

5.1.4 Quantitative results

5.1.4.1 Comparison between different standard wall functions embedded in *Code_Saturne 2.0*

In order to evaluate the performance of wall functions, one and two-velocity-scale and scalable wall functions have been used in conjunction with the high-Re $k - \varepsilon$ model in the present thesis. Figures 5.6 to 5.9 show, respectively, profiles of mean temperature, mean vertical velocity and rms vertical velocity fluctuations at different heights across the cavity, and the local Nusselt number distribution along the heated wall. Comparisons with the benchmark data of Betts and Bokhari [11] show that the standard two velocity scale wall function performs best. The other two formulations misrepresent the temperature distribution, especially towards the end walls. Profiles of mean vertical velocity show that the three wall functions inadequately predict the velocity near the top and bottom walls where the experiments show a slight deviation from the linear velocity profile that is still predicted by standard wall function calculations here. The one-velocity-scale and scalable wall functions show greater discrepancies than the two-velocity wall function, especially in the impingement regions near the top and bottom walls of the cavity. In these regions the wall-shear stress is low, and it might be expected that schemes based on the log-law and local equilibrium assumptions would not perform so well. Some attempts at improving the performance of the “two-velocity-scale wall

function” are presented in section 5.4.

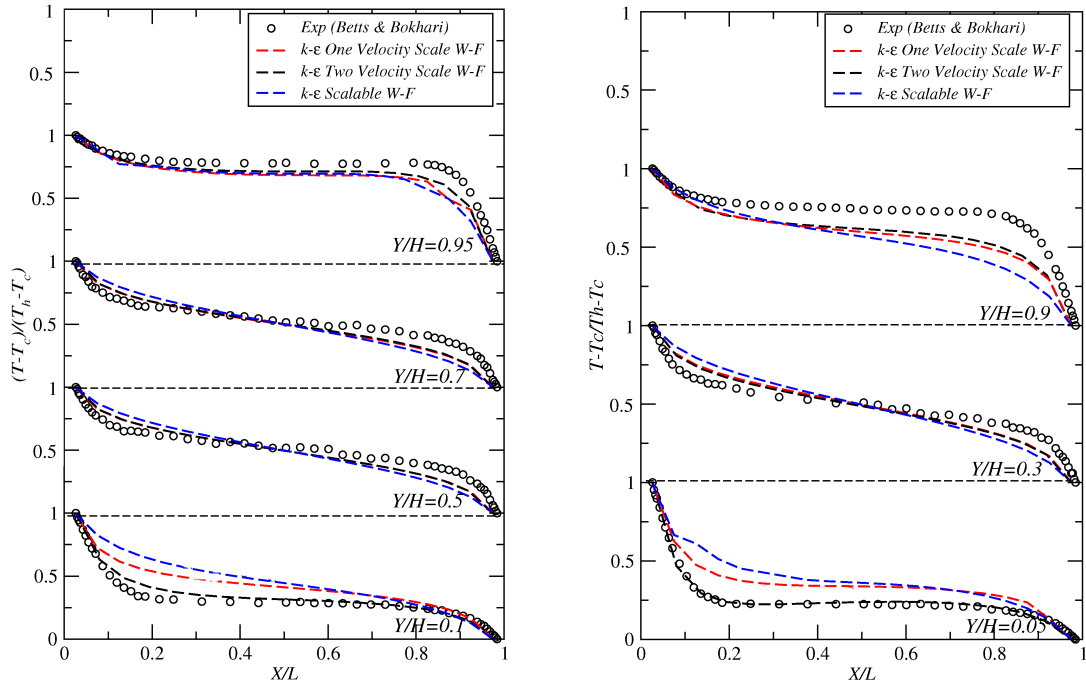


Figure 5.6: Mean temperature profiles at different locations inside the vertical cavity, comparison between different wall functions and experimental data.

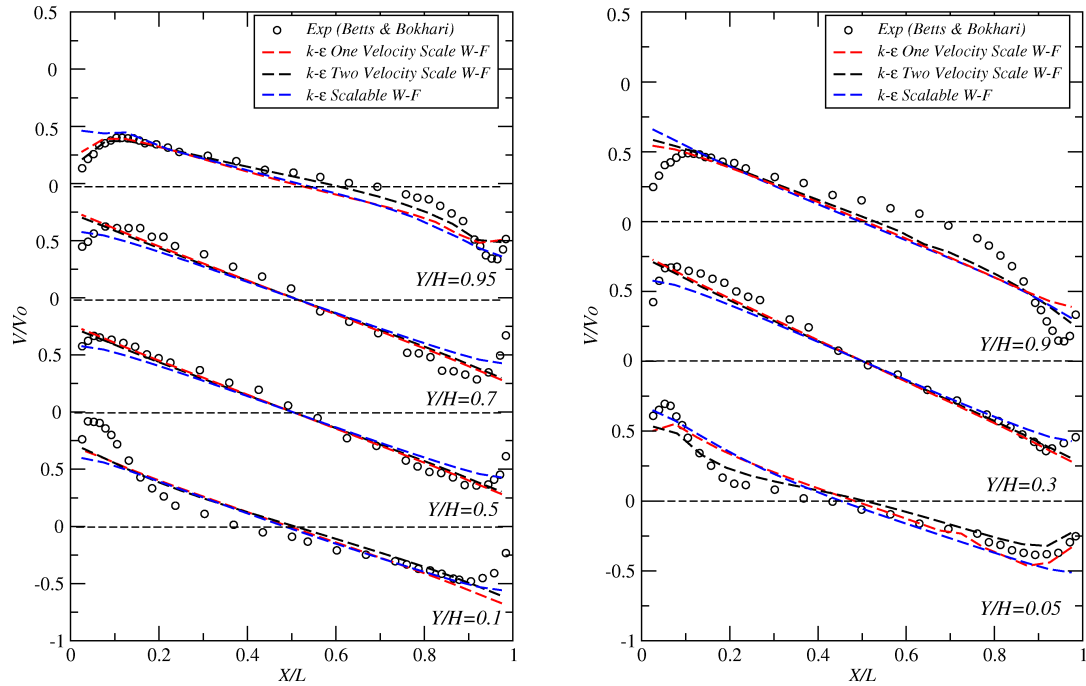


Figure 5.7: Mean vertical velocity profiles at different locations inside the vertical cavity, comparison between different wall functions and experimental data.

As might be expected with a linear EVM, the rms vertical velocity fluctuations are underpredicted at the central vertical location of the cavity, compared with experimental data. Turbulence levels are lower near the two end walls, where slight differences are shown between the three wall function treatments. The two-velocity scale wall function predicts the near-wall values slightly better than the other formulations, although none captures the small peaks shown in the measured data near the bottom left and top right corners.

Overall heat transfer is overpredicted by all the wall function formulations, and particularly by the scalable wall function. This is linked to its poor predictions of mean temperature and velocity, described earlier.

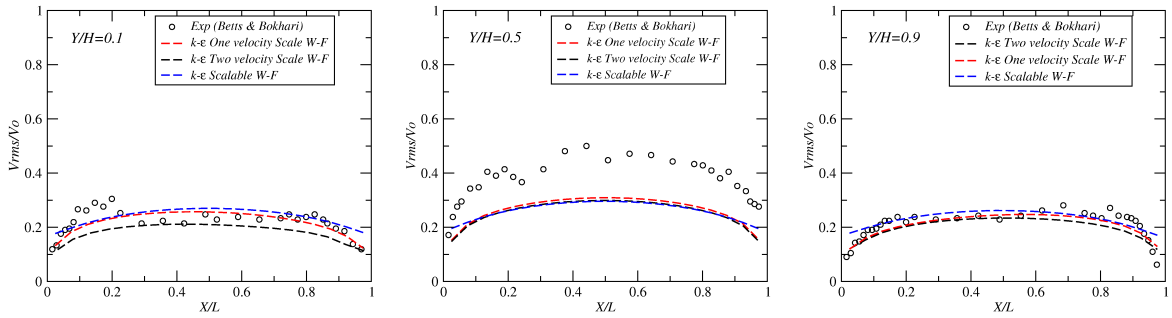


Figure 5.8: Rms fluctuating vertical velocity profiles at different locations inside the vertical cavity, comparison between different wall functions and experimental data.

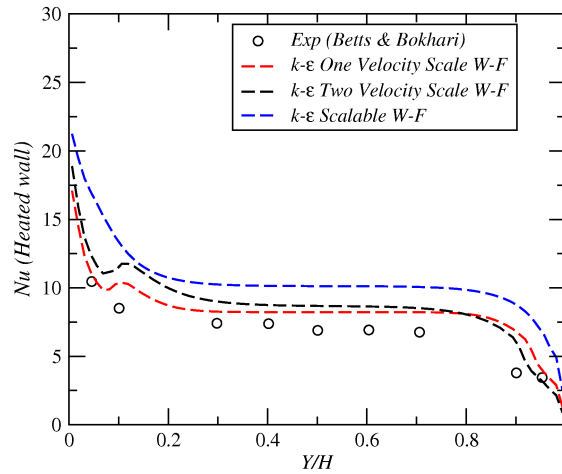


Figure 5.9: Local Nusselt number distribution along hot wall of the vertical cavity, comparison between different wall functions and the experimental data.

5.1.4.2 Model validation for buoyancy-driven flows inside the vertical cavity

In order to test the ability of RANS turbulence models embedded in *Code_Saturne* 2.0 to predict the buoyancy-driven internal flows, computations have been made of the flow in the vertical rectangular enclosure using both high- and low-Re models. These tests include examining the ability of the models to predict the correct flow physics, and comparing their computational resource requirements. High-Re models tested include the $k - \varepsilon$ [53] and second moment closure models of Launder-Reece-Rodi, *LRR* [60] and Speziale-Sarkar-Gatski, *SSG* [81], all combined with the two-velocity-scale wall treatment. Low-Reynolds number models tested include Menter's shear Stress Transport *SST* [68], and elliptic relaxation models, namely the $\varphi - f$ [61] and $\varphi - \alpha$ [13] (for the 60° where the $\varphi - f$ model failed). Details of all these schemes and their coefficients are given in Appendix B.

Figure 5.10 shows profiles of the dimensionless mean temperature $(T - T_c) / (T_h - T_c)$ at four heights inside the tall cavity. Results are presented for both high and low-Re models, together with the measurements of Betts and Bokhari [11]. The experimental data show that in the core region, between around $X/L = 0.3$ and 0.7 , there is an approximately linear variation of temperature across the cavity, indicating that most of the heat transfer is due to turbulent mixing and only a small portion of the total heat flux is due to molecular conduction across the cavity. The measurements also show that between the conductive sub-layers and this core region, buffer zones exist where the variation of temperature is not linear. Of the high-Re models, both $k - \varepsilon$ and *SSG*, using the “two-velocity-scale wall function”, give generally good agreement with experimental data, while the *LRR* model deviates from the data significantly, particularly towards the insulated end walls. Both low-Re schemes give very similar predictions, in good agreement with the measurements, for all locations inside the vertical cavity.

Profiles of the dimensionless vertical velocity at four Y locations in the cavity are shown in Figure 5.11, and compared with experimental data of Betts and Bokhari [11]. The figure shows that, as flow accelerates down the cold side, there exists a linear variation of the vertical velocity in the centre of the cavity between around $Y/H = 0.3$ and 0.7 . Near the walls the experimental measurements do show some differences in behaviour between the hot and cold sides: on the hot side the fluid accelerates from the bottom corner, reaching a peak velocity at around $Y/H = 0.3$, it then decelerates slightly as the boundary layer spreads, before exhibiting a more rapid deceleration as the top wall is approached. On the cold side, however, the flow reaches its peak velocity not far from the starting corner, near $Y/H = 0.9$ then slows as it moves downward, retaining

a roughly constant velocity peak between $Y/H = 0.7$ and 0.3 before decelerating again close to the bottom wall. As far as the model performance goes, most schemes give a fairly good representation of the linear velocity profiles in the central region of the cavity, apart from the *SSG* model which returns a rather too steep velocity gradient across the cavity. The low-Re schemes generally appear to give a better representation of the near-wall regions than the high-Re models with wall functions, particularly close to the end walls. The *SST* does, however, slightly overpredicts the velocity peak values in the cavity mid-height, whilst the $\varphi - f$ scheme gives generally good agreement with experimental data.

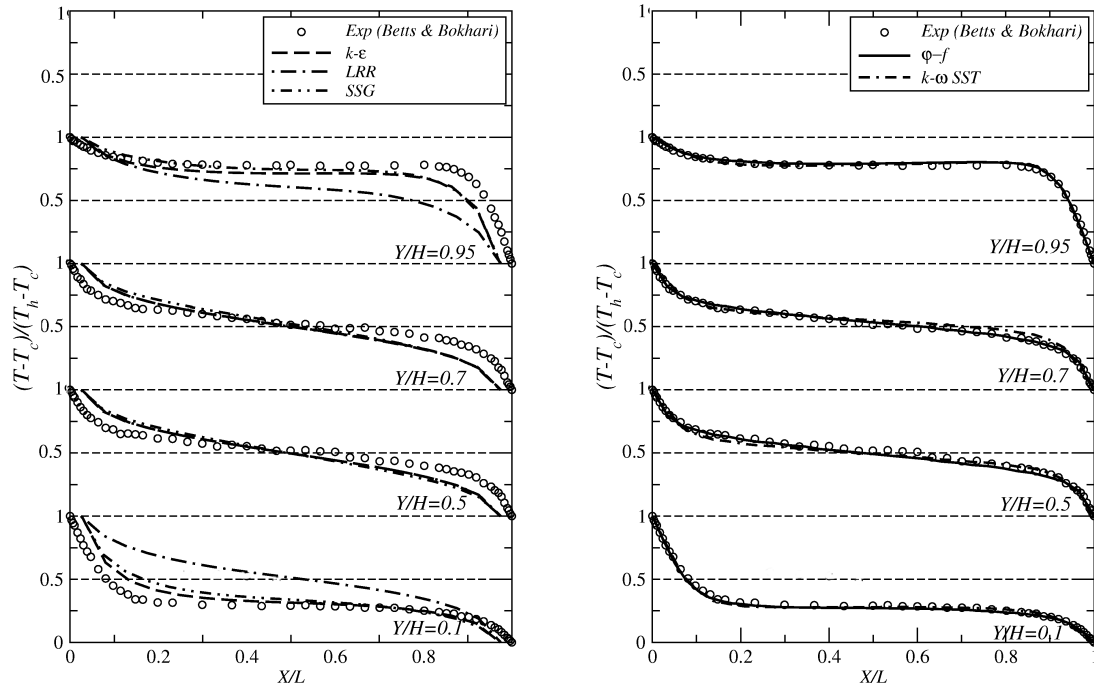


Figure 5.10: Mean temperature profiles at different locations inside the vertical cavity, comparison between RANS models and experimental data.

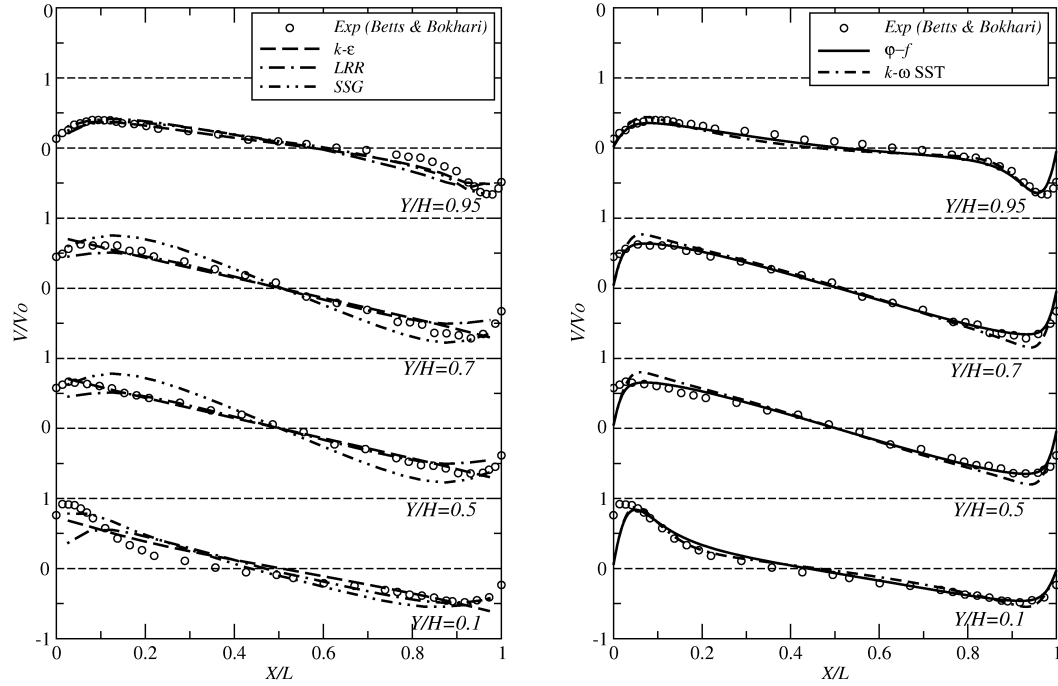


Figure 5.11: Mean vertical velocity profiles at different locations inside the vertical cavity, comparison between RANS models and experimental data.

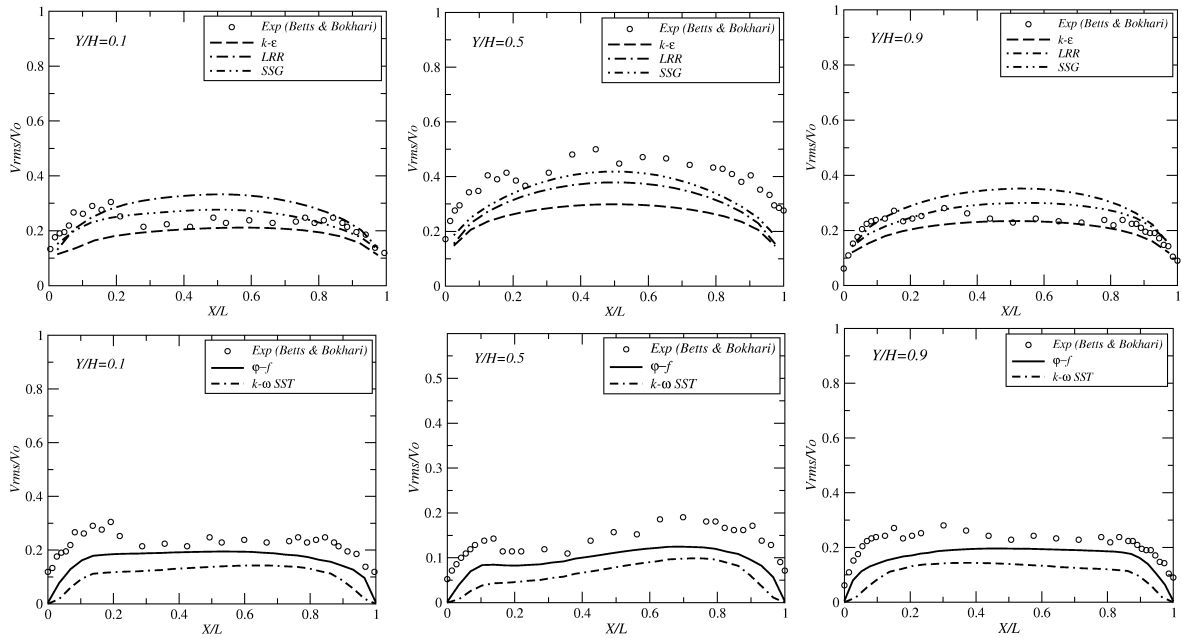


Figure 5.12: Rms fluctuating vertical velocity profiles at different locations inside the vertical cavity, comparison between RANS models and experimental data.

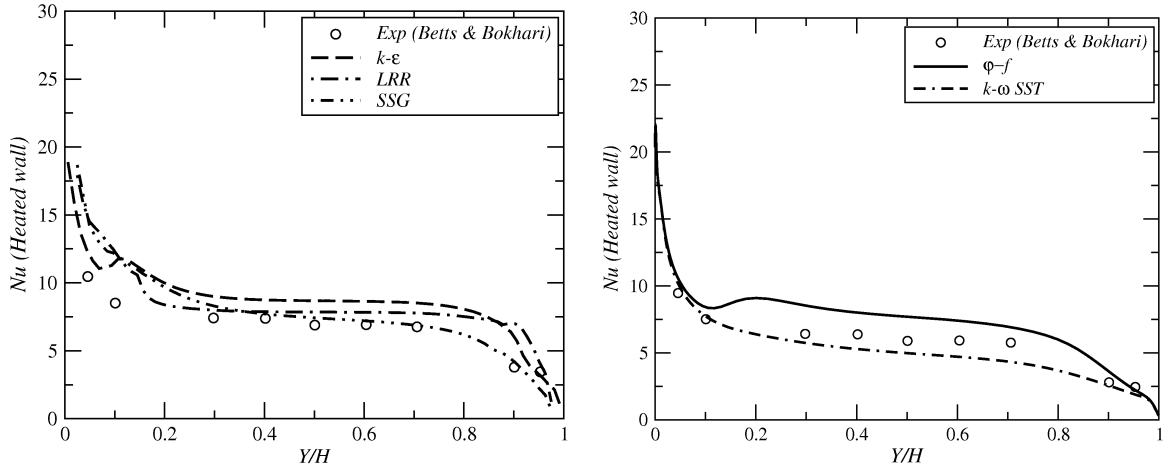


Figure 5.13: Local Nusselt number distribution along hot wall of the vertical cavity, comparison between RANS models and experimental data.

Figure 5.12 shows the variation of the rms fluctuating vertical velocity component parallel to the long walls at three heights inside the cavity (near the top and bottom walls and in the cavity core, the other positions does not show significant changes). Results are shown from the high and low-Re models. As suggested by the earlier contour plots of turbulent kinetic energy, Figure 5.5, the maximum levels are generally found in the central region of the cavity. The eddy-viscosity schemes, as might be expected, generally underpredict the levels of V_{rms} , which in most regions is the streamwise rms velocity component. The stress transport models return better predictions at the cavity mid-height ($Y/H = 0.5$), with the *SSG* performing slightly better than the *LRR* scheme, both at mid-cavity cavity height and towards the end regions.

As a final comparison for the vertical cavity case, Figure 5.13 shows the predicted and measured Nusselt number along the hot wall. Heat transfer is constant over most of the cavity height where turbulent mixing is high. Most models give a reasonable representation of this, with the two low-Re approaches generally being closer to the data than the schemes employing the wall function.

5.2 2-D tilted stable enclosure at 60°

Turning attention now to the cavity under stable stratification, tilted at 60° to the horizontal, contours of temperature, velocity and turbulent kinetic energy inside the cavity from high and low-Re models are illustrated in Figures 5.15 to 5.17. The flow inside this tilted cavity generally shows a similar behaviour to that in the vertical tall

cavity. The flow is characterised by a single circulation motion in the middle of the cavity as also found in the previous test case. Concerning the RANS turbulence model predictions, very similar conclusions can be drawn in this case as in the vertical cavity case, presumably due to the moderate angle of inclination here resulting in a similar behaviour in the two cases.

Dimensionless mean temperature and vertical velocity profiles are shown in Figures 5.18 and 5.19 at four height locations within the tilted cavity at 60° . Comparisons between both high and low-Re models with experimental data of Cooper et al. [25] are presented here. In this case, converged results could not be obtained using the $\varphi - f$ model, and so instead the results shown are from the newer alternative $\varphi - \alpha$ scheme as an example of a blending factor based model. Thermal predictions inside the tilted cavity are similar to those in the vertical one. This confirms the comments above, with a uniform temperature in the middle section of the cavity because of high mixing in this region and a linear variation of velocity caused by the presence of a one large circulation motion inside the enclosure. For the 60° tilted cavity case, the peaks of vertical velocity in Figure 5.19 are slightly lower than those in the vertical case. This can be explained by the fact that in the inclined cavity the gravity contribution in the momentum equation is divided into two non-zero components, and in consequence, the component of buoyancy force parallel to the tall walls is smaller than that in the vertical cavity. In general, the low-Re models, including *SST* and $\varphi - \alpha$, give better thermal field predictions than the high-Re models used in conjunction with wall function. However, the velocity profiles show some discrepancies between measurements and the predictions from both high- and low-Re models.

Figure 5.20 shows profiles of the dimensionless rms fluctuating vertical velocity V_{rms}/V_o at three vertical locations inside the tilted enclosure. Comparing the experimental data between the present test case and the vertical one (Figure 5.12), one can see that the overall levels are generally slightly lower in the inclined case, although there are now more noticeable peaks in V_{rms} levels near both hot and cold walls. The models do generally show a reduction in V_{rms} levels from those predicted in the vertical case, although they also predict a reduction in the near-wall regions, resulting in profile shapes that do not capture the near-wall V_{rms} peaks shown by measured data.

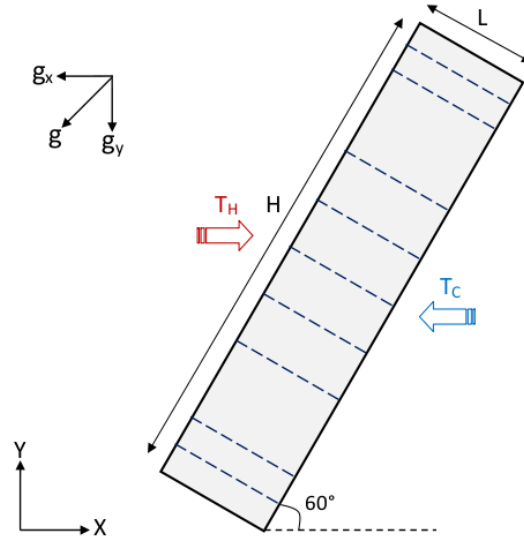


Figure 5.14: Geometry of 2-D vertical cavity. Location of plot lines are indicated.

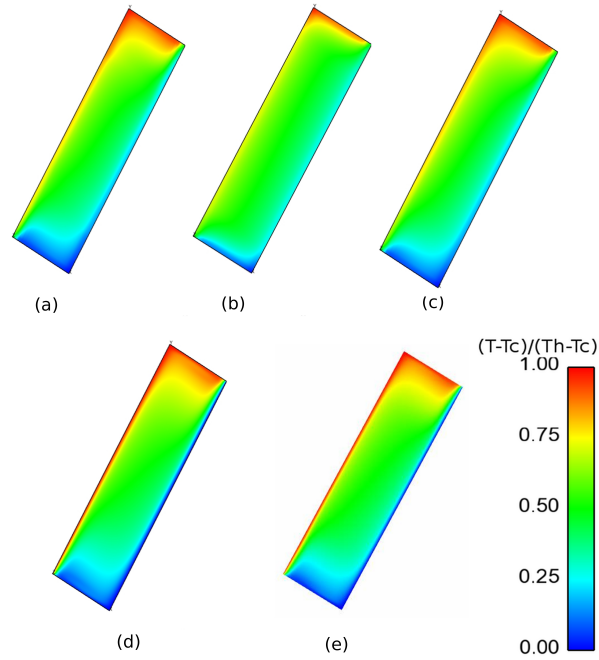


Figure 5.15: Temperature contours inside the 60° tilted cavity. (a) $k - \varepsilon$, (b) LRR , (c) SSG , (d) $k - \omega SST$, (e) $\varphi - \alpha$.

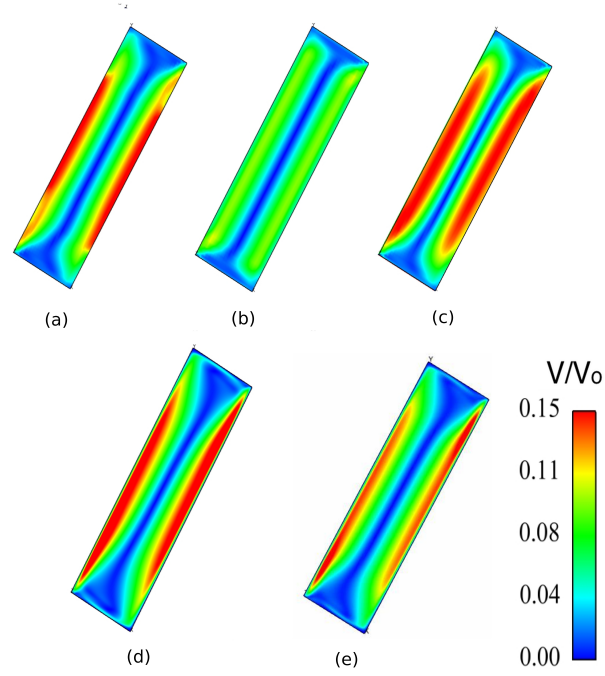


Figure 5.16: Velocity magnitude contours inside the 60° tilted cavity. (a) $k - \varepsilon$, (b) LRR , (c) SSG , (d) $k - \omega SST$, (e) $\varphi - \alpha$.

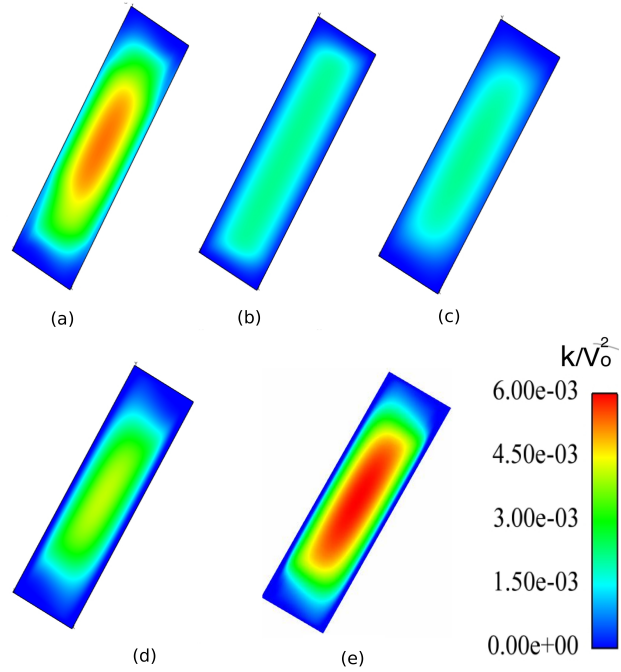


Figure 5.17: Turbulent kinetic energy contours inside the 60° tilted cavity. (a) $k - \varepsilon$, (b) LRR , (c) SSG , (d) $k - \omega SST$, (e) $\varphi - \alpha$.

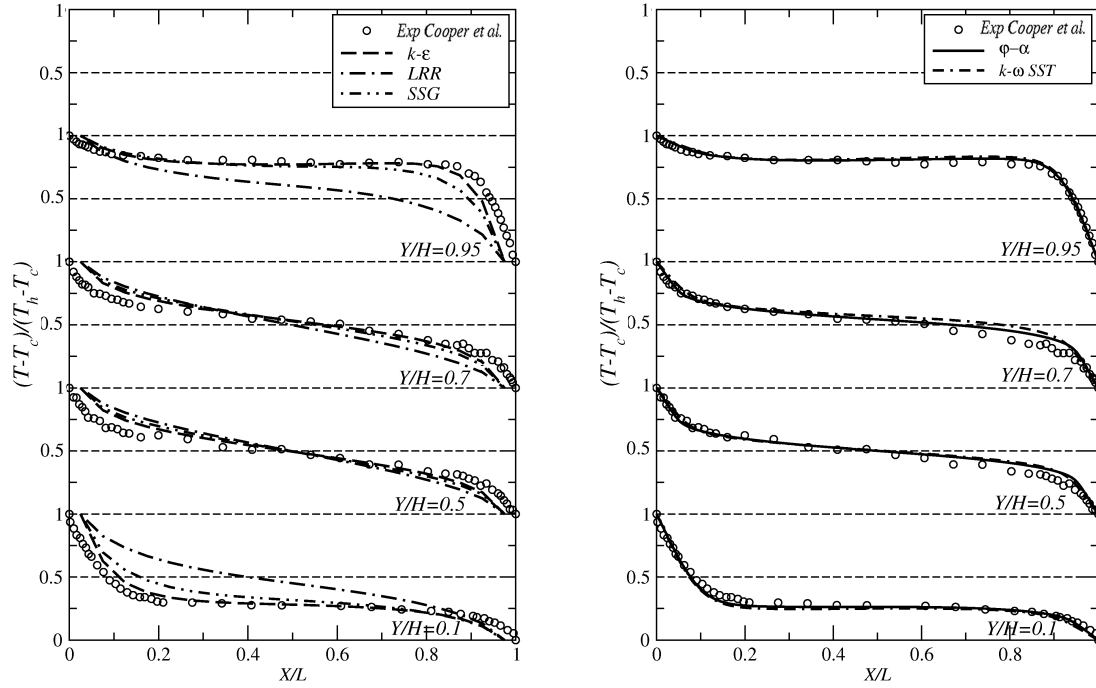


Figure 5.18: Mean temperature profiles at different locations inside the 60° tilted cavity, comparison between RANS models and experimental data.

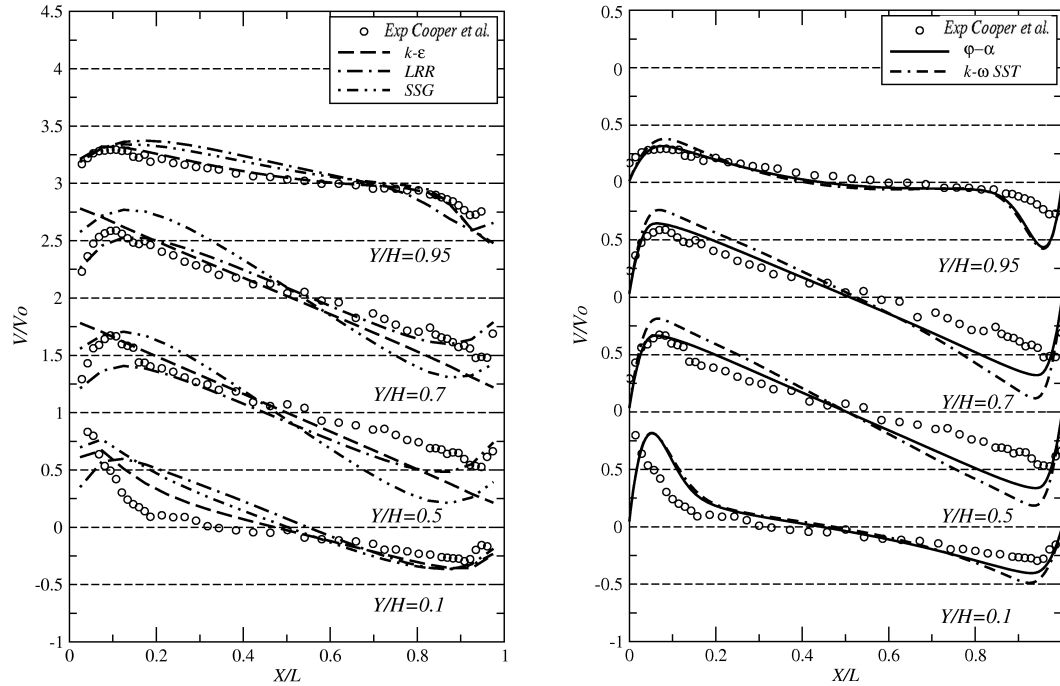


Figure 5.19: Mean vertical velocity profiles at different locations inside the 60° tilted cavity, comparison between RANS models and experimental data.

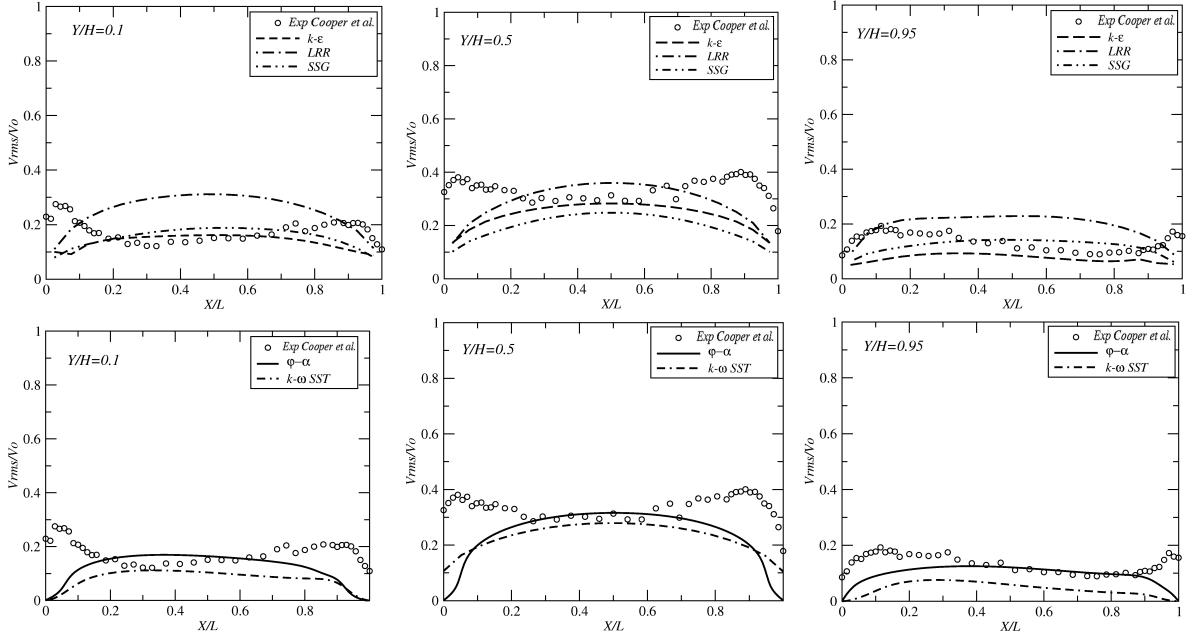


Figure 5.20: Rms fluctuating vertical velocity profiles at different locations inside the 60° tilted cavity, comparison between RANS models and experimental data.

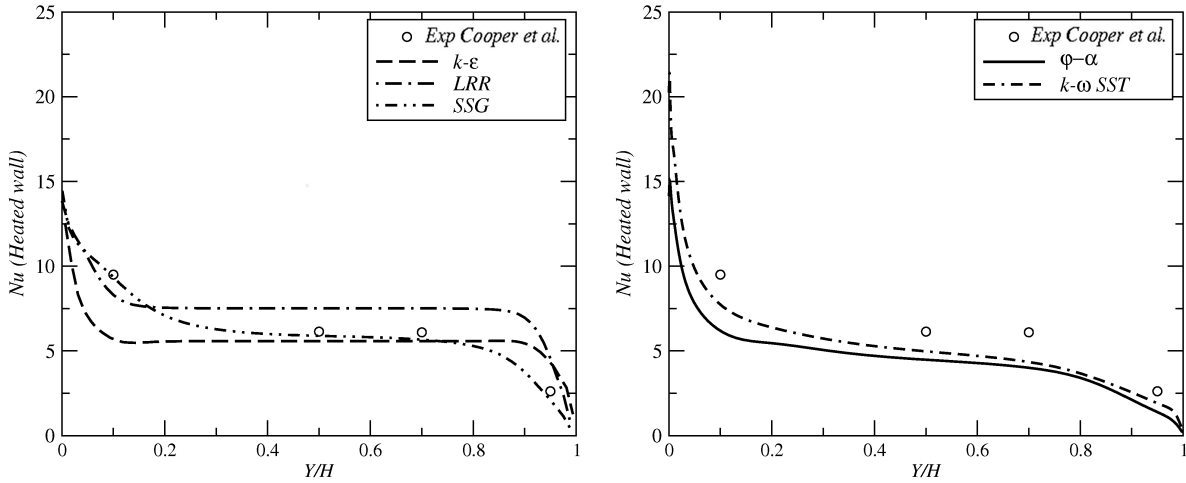


Figure 5.21: Local Nusselt number distribution along hot wall of the 60° tilted cavity, comparison between RANS models and experimental data.

Local Nusselt number profiles predicted by high and low-Re models, Figure 5.21, are very close in shape to those in the vertical tall cavity, however the predictions of the low-Re $\varphi - \alpha$ scheme show lower heat transfer than the $\varphi - f$ ones in the vertical case, which are now closer to the measured data.

5.3 2-D tilted unstable enclosure at 15°

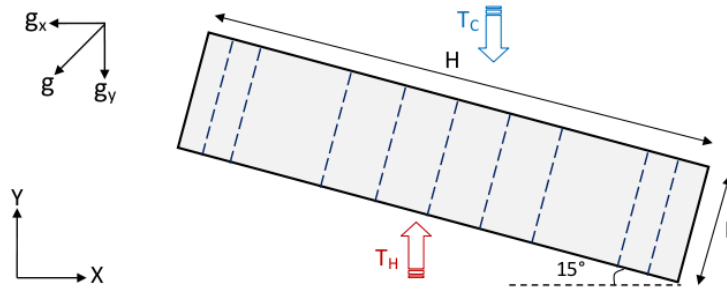


Figure 5.22: Geometry of 2-D vertical cavity. Location of plot lines are indicated.

In order to show the influence of unstable stratification on the buoyancy-driven cavity flow, the cavity is tilted here at 15° to the horizontal and heated from the lower side. The flow inside tilted cavity is characterised by the appearance of multiple cells throughout the cavity. This suggests that the real flow is no longer two-dimensional. The measurements of Cooper et al. [25] confirm this behaviour by showing four longitudinal circulations inside the enclosure. When applied in the present 2-D domain, the RANS turbulence models tested below show two different behaviours. High-Re models in general (and particularly the stress transport schemes) capture a set of rolls (Figures 5.24 and 5.25) and thermal plumes (Figure 5.23) over the entire cavity length. However the low-Re models are not able to capture either of these features and show instead one large circulation in the central region similar to that seen in the previous stable test cases. Although the number of mesh cells in the low-Re model grid is greater than in the wall function one, the non-uniform grid used to ensure good near-wall refinement means that the grid in the cavity core is actually coarser than that used with the high-Re models, and it might not be sufficiently fine to allow the roll-cells to develop. A finer mesh is created and used for the 3-D simulations using low-Re models in chapters 6 and 7.

In order to give further information about the flow within the 2-D 15° unstable cavity, profiles of time-averaged temperature, vertical velocity and rms vertical velocity component are shown in Figures 5.26 to 5.28. All models fail here to predict the correct thermal and dynamic patterns, with profiles of temperature and velocity at different locations deviating significantly from the experimental data of Cooper et al. [25]. The reason of this failure is not so much the model performance, but the nature of the flow inside the unstable cavity, which is 3-dimensional and unsteady. In a later chapter this case will be studied using a full 3-D geometry, employing both highly resolved LES and

unsteady RANS approaches, which are potentially capable of capturing the unsteady 3-D structures.

As a final comparison between the three enclosures studied here, vertical, stable tilted at 60° and unstable tilted at 15° to the horizontal, vector plot comparisons are presented in Figure 5.29, obtained from computations using the SSG second moment closure. The above comments are confirmed in this figure which shows a large circular motion in both vertical and 60° stable cavities, while for the 15° unstable cavity, the flow contains a number of roll cells over the entire cavity.

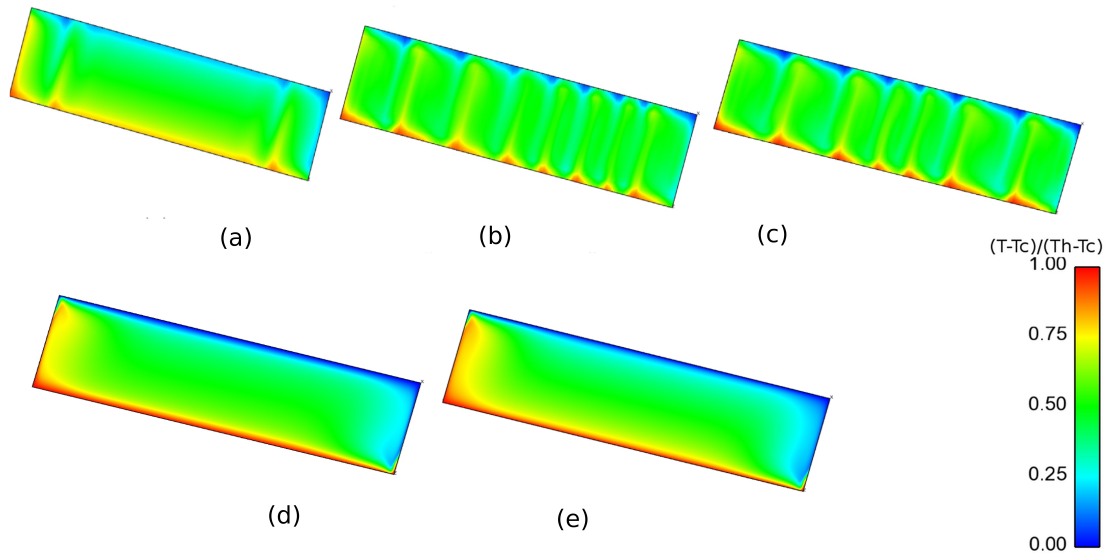


Figure 5.23: Temperature contours inside the tilted unstable cavity at 15° . (a) $k-\epsilon$, (b) LRR , (c) SSG , (d) $k-\omega SST$, (e) $\varphi-f$.

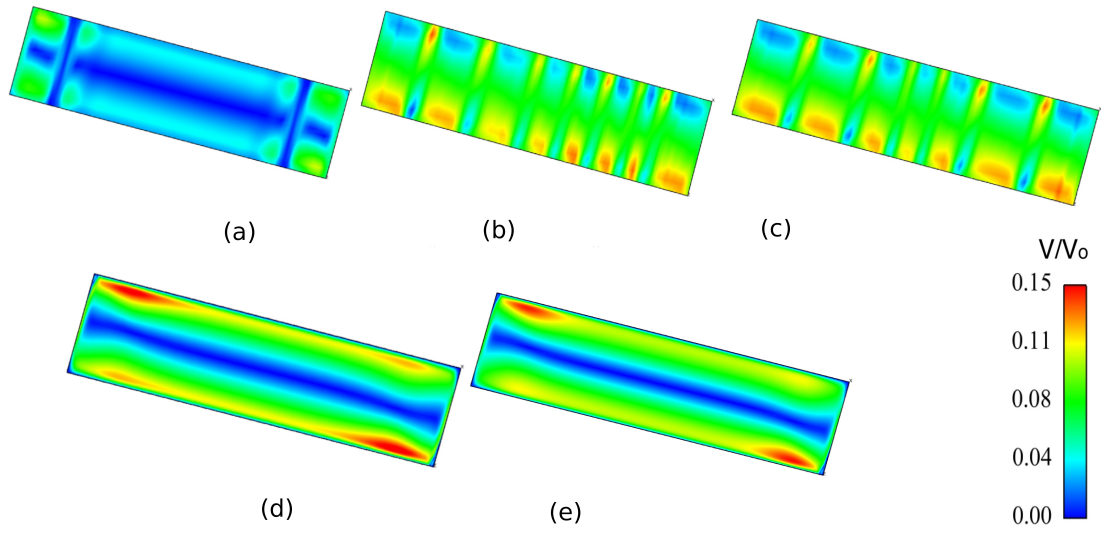


Figure 5.24: Velocity magnitude contours inside the tilted unstable cavity at 15° . (a) $k - \varepsilon$, (b) LRR , (c) SSG , (d) $k - \omega SST$, (e) $\varphi - f$.

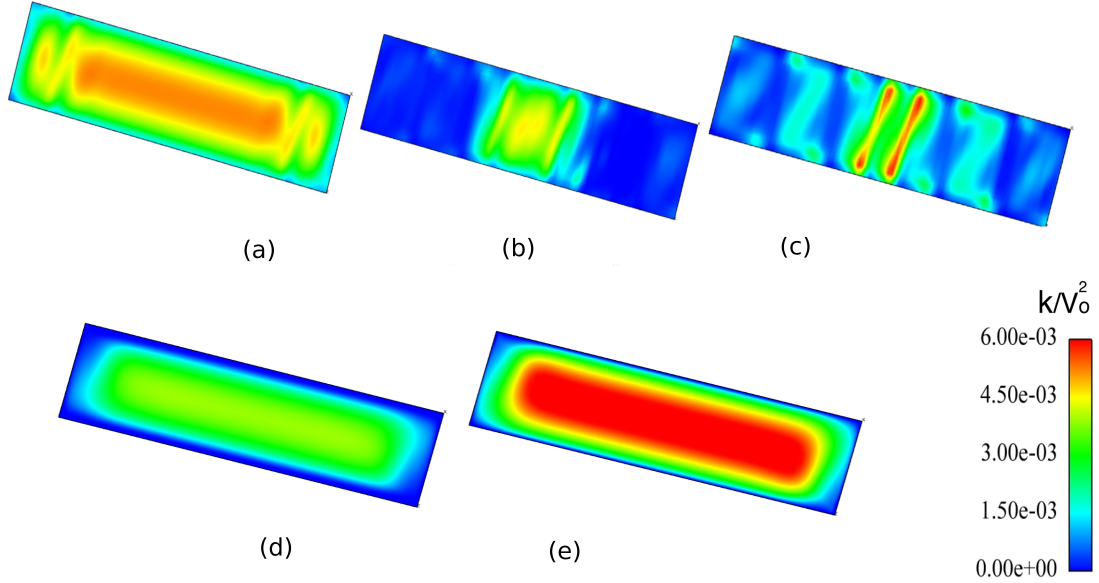


Figure 5.25: Turbulent kinetic energy contours inside the tilted unstable cavity at 15° . (a) $k - \varepsilon$, (b) LRR , (c) SSG , (d) $k - \omega SST$, (e) $\varphi - f$.

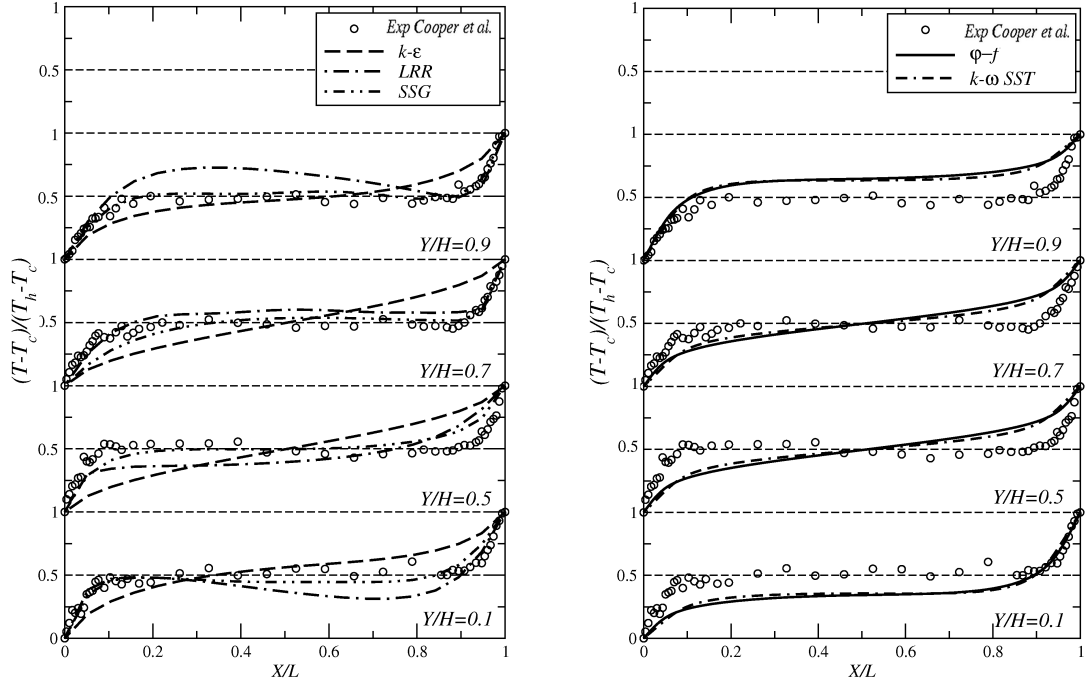


Figure 5.26: Mean temperature profiles at different locations inside the vertical cavity, comparison between RANS models and experimental data.

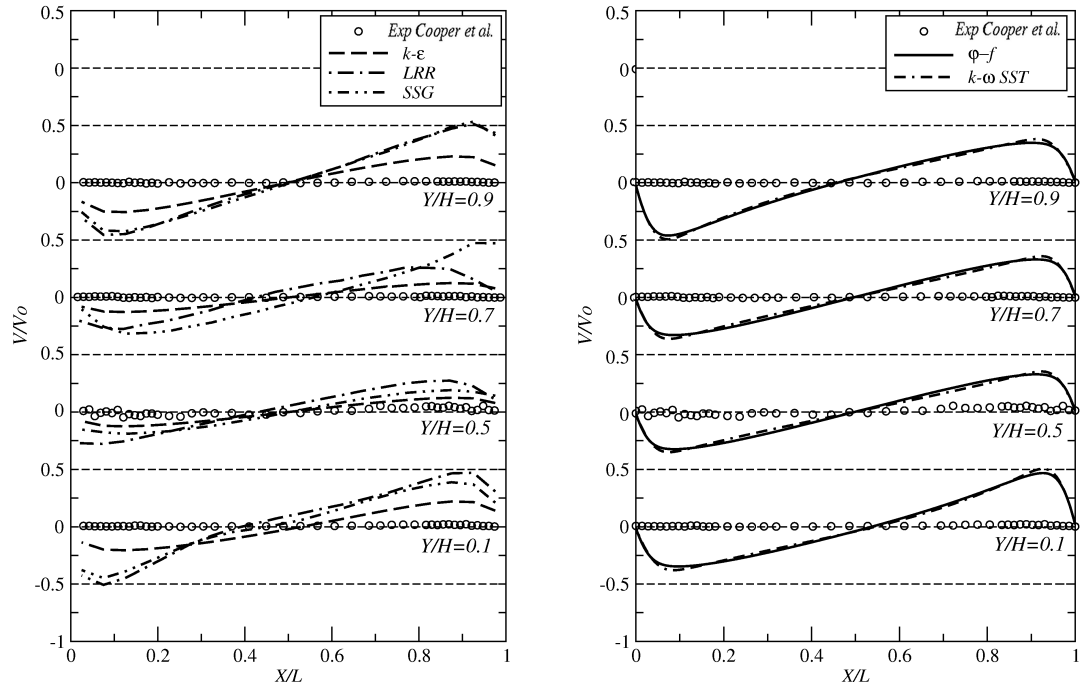


Figure 5.27: Mean vertical velocity profiles at different locations inside the vertical cavity, comparison between RANS models and experimental data.

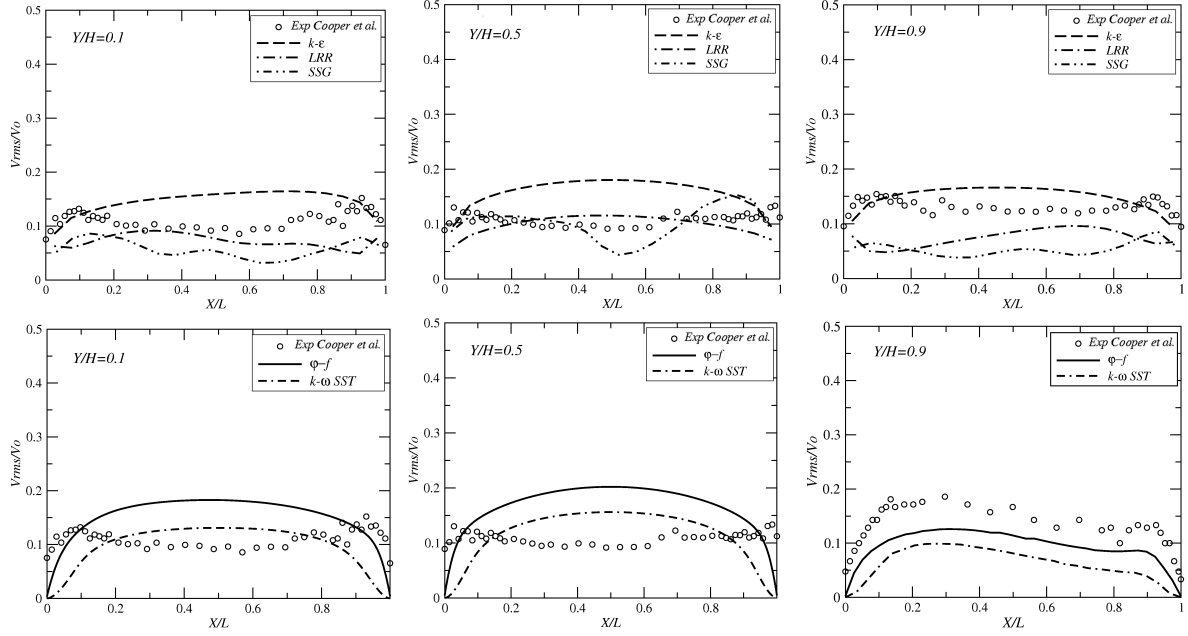


Figure 5.28: Rms fluctuating vertical velocity profiles at different locations inside the vertical cavity, comparison between RANS models and experimental data.

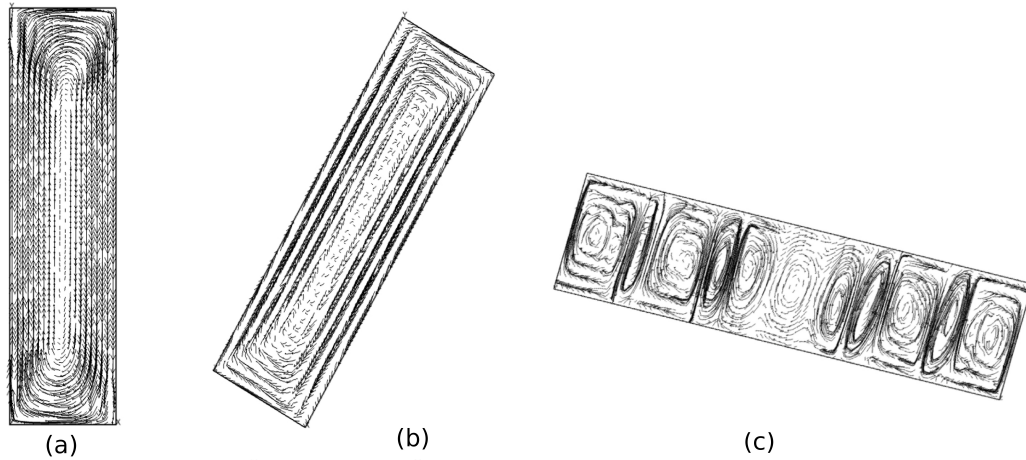


Figure 5.29: Velocity vectors resulting from SSG second moment closure computation. Comparison between 2-D cavities: (a) vertical, (b) stable tilted at 60° , (c) unstable tilted at 15° .

5.4 Refinement of the standard one- and “two-velocity-scale wall function” in *Code_Saturne* 2.0

In Section 5.1.4.1, comparisons between different formulations of wall treatment embedded in *Code_Saturne* 2.0 including one-velocity-scale, two-velocity-scale and scalable wall functions used with High-Re models have been performed. The “two-velocity-scale wall function” was shown to perform best amongst these in predicting the buoyancy-driven flow inside the vertical cavity, although it still showed some discrepancies with experimental data, particularly in the local Nusselt number. In order to try improving the predicted results, a further refinement has thus been tested with the one- and “two-velocity-scale wall functions”. As explained in Chapter 3, this refinement was to modify the boundary condition value imposed for epsilon at the near-wall node, to be consistent with what is conventionally employed instead of that is originally implemented in *Code_Saturne* 2.0 (see section 3.5.6 in Chapter 3).

Profiles of dimensionless mean temperature, vertical velocity, turbulent kinetic energy and Nusselt number distribution along the heated wall of the vertical cavity, using the $k - \varepsilon$ model with original and corrected versions of the wall functions, are shown in Figures 5.30 to 5.34. Temperature predictions using $k - \varepsilon$ with the modified “one-velocity-scale wall function” do not show improvement, except near the top wall of the cavity. However, the modified “two-velocity-scale wall function”, shown on the right hand side of Figure 5.30 shows better agreement than the old formulation compared with the measured data, especially near the top and bottom insulated walls, with only a very slight deviation from the measurements in the middle of the cavity.

Profiles of mean vertical velocity presented in Figure 5.31 also show better predictions using the modified formulation of “two-velocity-scale wall function”, compared with the original predictions.

Profiles of turbulent kinetic energy and dissipation rates are also presented here in Figures 5.32 and 5.33. The modification of the the ε boundary conditions at the near-wall node (Dirichlet boundary condition for ε), produces a noticeable change in ε and consequently k , particularly in the central region of the cavity where the flow is more turbulent.

A significant improvement of the predicted heat transfer rate, using the modified “two-velocity-scale wall function”, is shown on the right hand side of Figure 5.34. In general, however, no improvement has been shown using the modification in the one-velocity-scale wall treatment formulation.

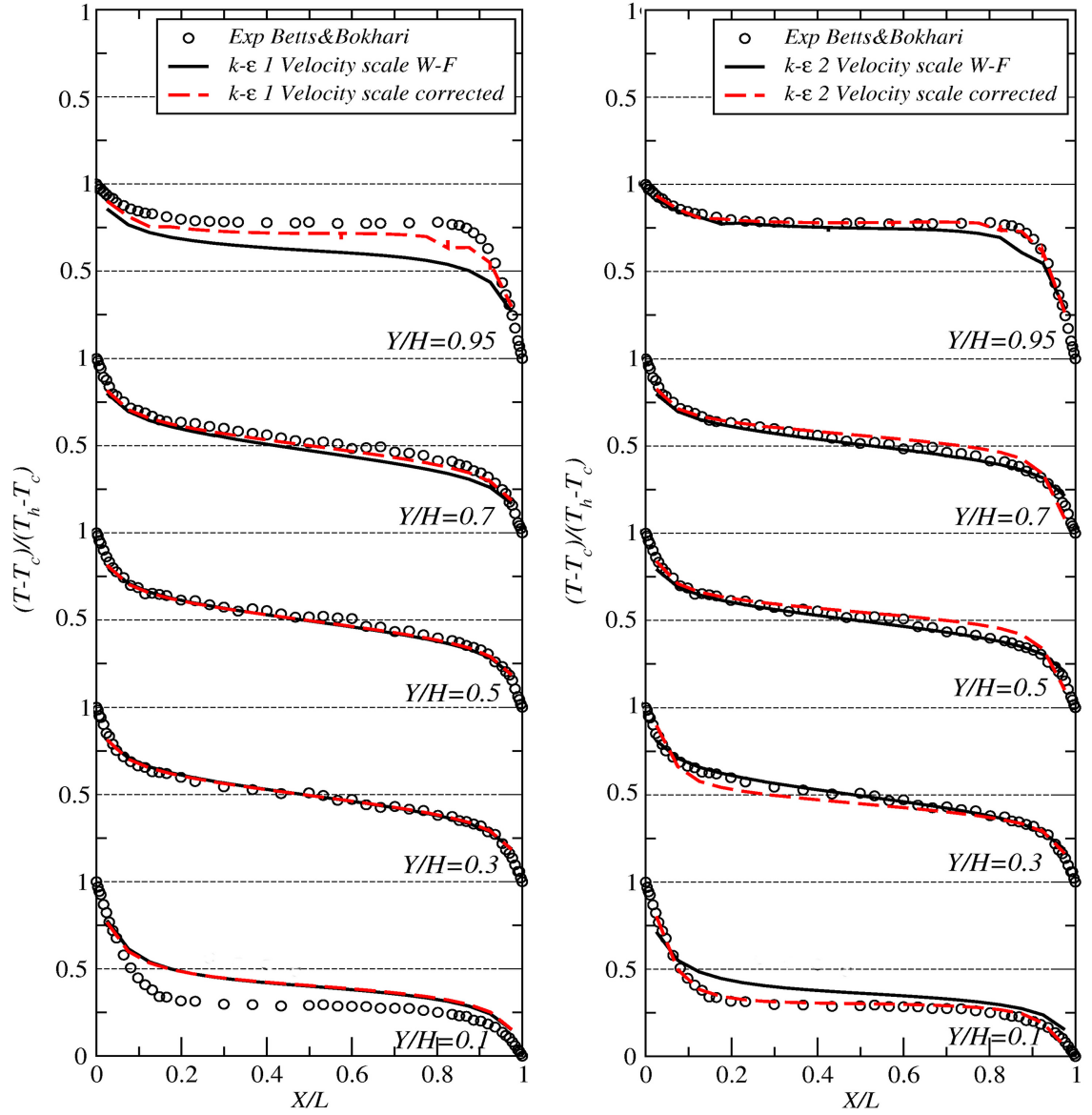


Figure 5.30: Mean temperature profiles at different locations inside the vertical cavity, comparison between corrected and old versions of wall functions with experimental data.

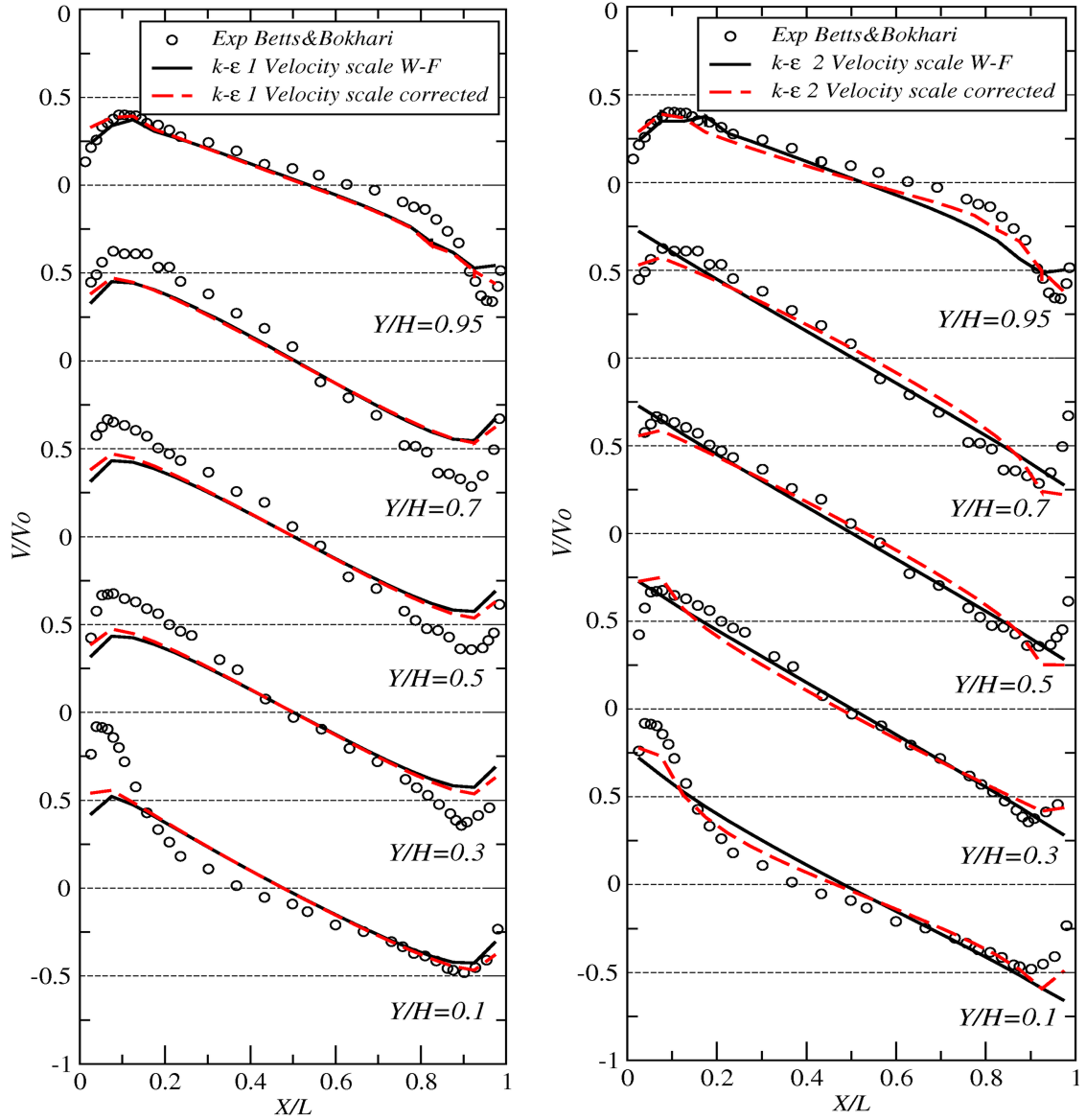


Figure 5.31: Mean vertical velocity profiles at different locations inside the vertical cavity, comparison between corrected and old versions of wall functions with experimental data.

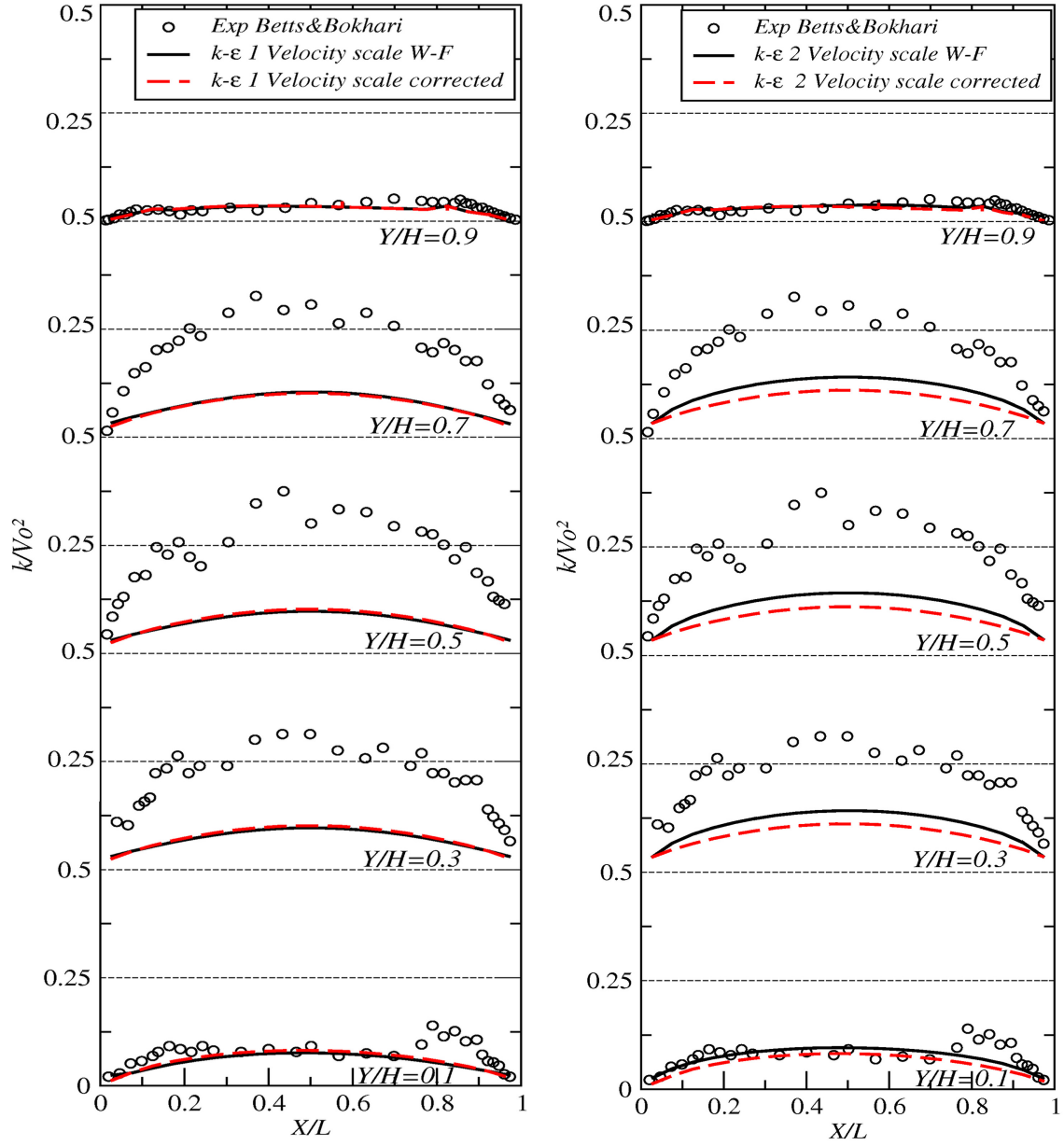


Figure 5.32: Mean turbulent kinetic energy profiles at different locations inside the vertical cavity, comparison between corrected and old versions of wall functions with experimental data.

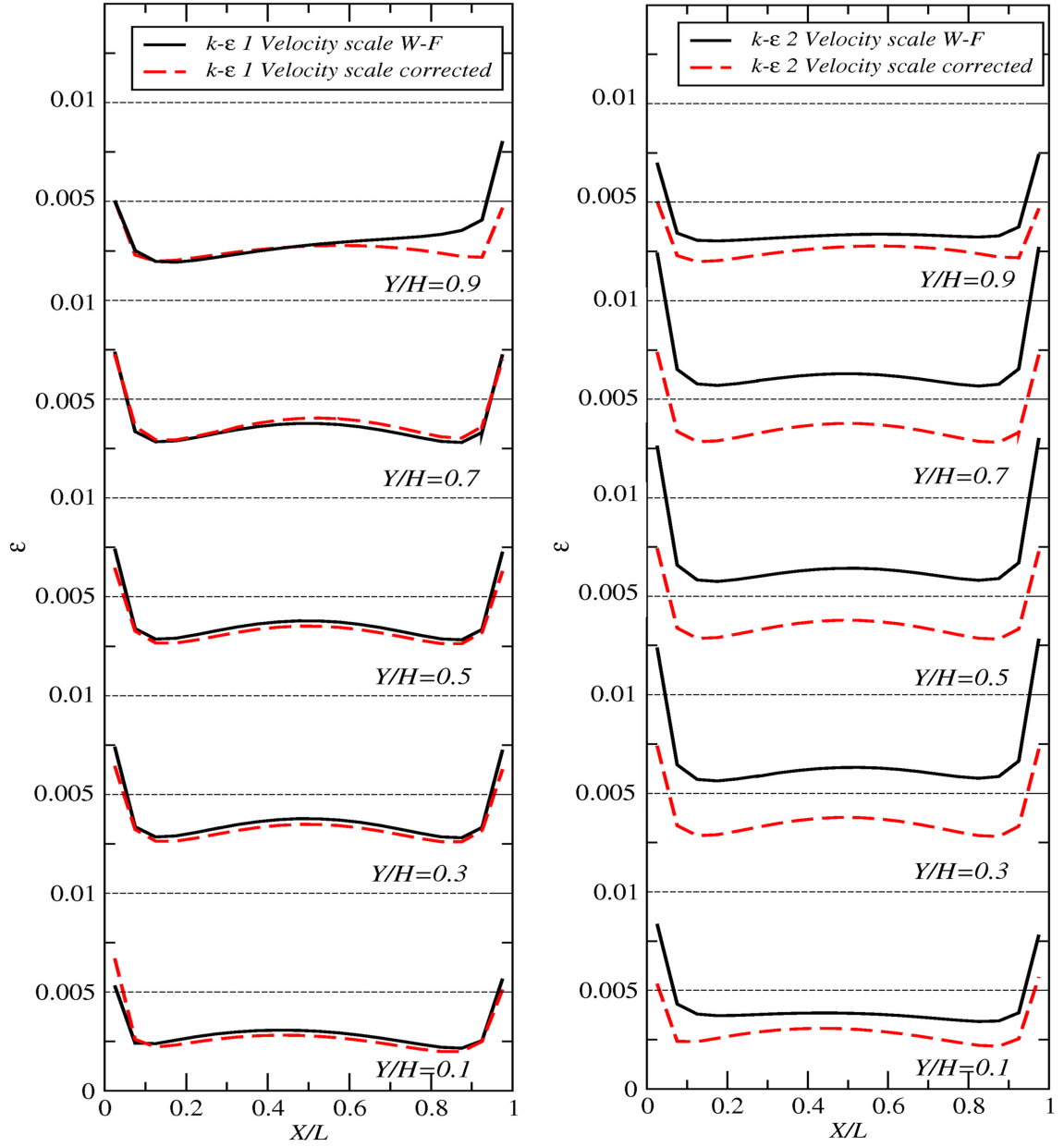


Figure 5.33: Mean dissipation rate profiles at different locations inside the vertical cavity, comparison between the corrected and old versions of wall functions with experimental data.

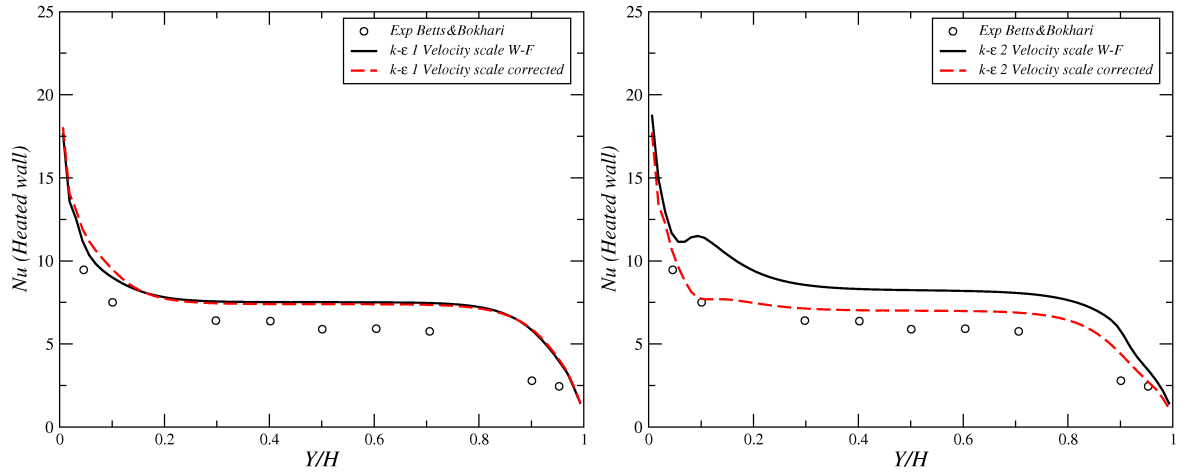


Figure 5.34: Local Nusselt number distribution along hot wall of the vertical cavity, comparison between corrected and old versions of wall functions with experimental data.

5.5 Concluding remarks

This chapter has described the modelling of buoyant flow inside a two-dimensional vertical cavity and inclined ones at 60° under stable stratification and 15° under unstable stratification using different RANS schemes. After the selection of an appropriate grid and the “two-velocity-scale wall function” for high-Reynolds-number models, the cases have been computed with a range of models and predictions compared to available measurements.

In both the vertical and stable 60° tilted cavities, a single large circulation cell is present, with boundary layers near the walls, and maximum turbulence levels in the central region of the cavity. In the vertical case the mean velocity and thermal fields were well reproduced by both low-Re models ($k - \omega SST$ and $\varphi - f$). However, profiles of velocity and temperature obtained from high-Re schemes deviate slightly from measurements near the walls, due to the wall function strategy embedded in *Code_Saturne* 2.0. Heat transfer was also generally slightly better predicted by the low-Re schemes. The vertical Reynolds normal stress profiles were reasonably well reproduced by the stress transport models, although generally underpredicted by the eddy viscosity schemes, as might be expected. Recently an adaptive wall function with the elliptic blending model has been developed by Billard et al. [12], its use can be promising to tackle the flaws of the simple wall function embedded in *Code_Saturne* 2.0 and further versions for the computation of buoyant and separated flows.

The overall flow pattern in the cavity inclined at 60° , with the upper side heated, is

similar to that of the vertical case, and the model performance, as far as the mean field is concerned, was also mostly similar. One noticeable difference in the measurements between the two cases is that there is a reduction in turbulence levels in the cavity core region in the inclined case, although levels in near-wall regions do not decrease significantly. The models do generally predict a decrease in turbulence levels in the inclined case, but in both near-wall and core regions, so the profile shapes of the rms velocity are not particularly well captured.

Concerning the flow pattern inside the 15° inclined cavity, a multi-cellular motion is shown by the high-Re models. Nevertheless, all the model predictions disagree with experimental data due to the presence unsteady structures as found in Rayleigh Benard convection problems. These cannot be reproduced using a 2-D geometry.

Despite the “two-velocity-scale wall function” performing better than the other forms, results using it still showed some discrepancies with measurements in the vertical cavity. As described in Chapter 3 the boundary value for ε has thus been modified, to conform with a widely-used form. This modification led to improvement of thermal, dynamic and heat transfer fields within the vertical heated enclosure. This modified wall functions is used with all high-Re models, including $k - \varepsilon$ and second moment closure, in all the following RANS computations.

Chapter 6

Buoyancy-Driven Flow Within the 3-D Tilted Enclosure Under Unstable Stratification

6.1 Introduction

From the previous results of buoyancy-driven flow within a 2-D cavity inclined at 15° to the horizontal, it has been found, for some not surprisingly, that all RANS models fail to predict the correct behaviour of the flow with a 2-D geometry. Experimental data of Cooper et al. [25] showed the existence of a set of four longitudinal vortices, corresponding to the Benard problem [10]. In this Chapter, computation of flow inside a 3-D unstably stratified enclosure tilted at 15° to the horizontal is conducted using highly-resolved LES, and a range of URANS schemes are tested for validation purposes.

The dimensions of the cavity are: $H \times L \times W = 2.18m \times 0.0762m \times 0.52m$, to match those used by Cooper et al. [25], leading to a lengthwise aspect ratio $A = H/L$ of 28.6 and a spanwise aspect ratio $B = W/L$ of 6.82. The cold and hot long walls are isothermal (Figure 6.1), the temperature difference ΔT takes the value of 18°C , the other walls are insulated (adiabatic). The Prandtl number (Pr) of the fluid is taken as 0.71 (air), and the temperature of the fluid and other fluid properties are chosen such that the Rayleigh number, defined in Equation 5.1, takes the value of 0.86×10^6 .

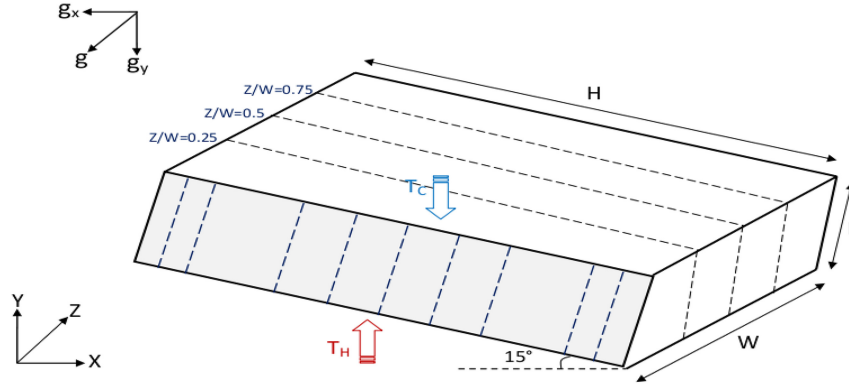


Figure 6.1: Geometry of 3-D cavity inclined at 15° to horizontal (unstable stratification). Location of plot lines are indicated.

Thermal and dynamic boundary conditions for the present test case are summarised in table (6.1).

Type	Thermal boundary conditions	Dynamic boundary conditions
X=0 (Isothermal wall at T_h)	$T_h = 34^\circ C$	$\left\{ \begin{array}{l} U = 0 \\ V = 0 \\ W = 0 \end{array} \right\}$ (Adherence of the fluid to the wall)
X=L (Isothermal wall at T_c)	$T_c = 16^\circ C$	
Y=0 (Adiabatic wall) Y=H (Adiabatic wall)	$\frac{\partial T}{\partial y} = 0$	
Z=0 (Adiabatic wall) Z=0.52 (Adiabatic wall)	$\frac{\partial T}{\partial x} = 0$	

Table 6.1: Thermal and dynamic boundary conditions for 3-D calculation.

6.2 Computational mesh and numerical methods

The present numerical simulations are carried out using the finite-volume code, Code_ *Saturne* [8]. The computational mesh used for the present LES is structured and non-uniform, consisting of three blocks (in order to maintain a fine resolution in the core

of the cavity), as shown in Figure 6.2. It uses around three million cell volumes, with appropriate clustering in the near wall regions to give non-dimensional near-wall node distances at the differentially heated walls of Δy^+ around 1. The grid spacing in wall units also satisfies the constraints $\Delta x^+ < 40$, $\Delta z^+ < 20$.

Spatial discretization is achieved using a second-order central difference scheme (CDS), whilst the second-order Crank-Nicolson scheme is employed for the time discretization and the time step is $\delta t = 10^{-3}s$, resulting in a maximum CFL number of 1. The simulation required 30000 time steps and approximately 250 hours in 24 CPUs, to reach a fully developed turbulent flow state, and at least a further 170000 time steps for statistical averaging of the flow field.

For the URANS computations, a second-order central difference scheme is employed for spatial discretization (with slope test activated for temperature). Time discretization is via the implicit first order scheme with a time step of $\delta t = 10^{-2}s$. For high-Reynolds-number models a coarse and uniform mesh of 80000 cells is used. For the low-Reynolds-number model two non-uniform grids are used: The first one contains around one million cells (being more refined near the wall than the high-Re grid, but coarser in the core region) and the other is the LES mesh described above. Characteristics of the LES and URANS calculations are summarised in Table 6.2.

Case	LES SST (finer mesh)	Low-Re models (SST fine mesh)	High-Re models
$L \times H \times W$	0.0762×2.18×0.52	0.0762×2.18×0.52	0.0762×2.18×0.52
$N_L \times N_H \times N_W$	100×200×150	80×120×100	20×80×50
$\Delta x^+ \times \Delta y^+ \times \Delta z^+$	(< 40) × 1 × (< 20)	$y^+ = 1$	$y^+ = 11$
$\delta t (s)$	10^{-3}	10^{-2}	10^{-2}
Max CFL	1	1	1
Normalised CPU time (on 24 Cores)	1	0.3	0.02

Table 6.2: Characteristics of LES and URANS simulations.

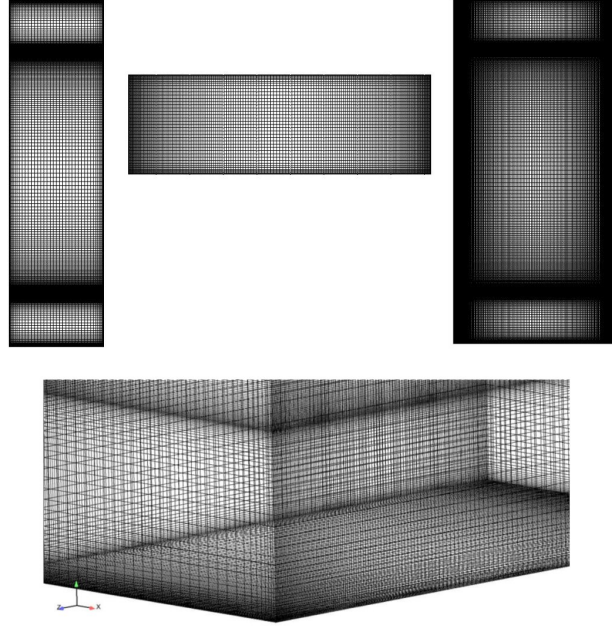


Figure 6.2: 3-D computational mesh for LES.

6.3 Assessment of LES resolution

As a first, a-priori, assessment of the LES resolution on the grid described above, the grid spacing can be compared to an estimate of the Kolmogorov length scale η (the size of small dissipative scales). This latter is here obtained from the viscosity, ν , and the dissipation rate, ε , (taken from a precursor converged and validated RANS simulation), and is defined as

$$\eta = \left(\frac{\nu^3}{\varepsilon} \right)^{\frac{1}{4}} \quad (6.1)$$

Figure 6.3 illustrates profiles of the ratio of the grid spacings (ΔX , ΔY and ΔZ) to the Kolmogorov length scale η along the three mid-section lines of the unstably stratified case. Pope [76] suggested that the maximum dissipation takes place at a wavenumber k of $0.26/\eta$ corresponding to a wavelength scale $\lambda = 2\pi/k$ of 24η and suggesting a grid spacing down to around 12η is needed to resolve a considerable part of the dissipative scales. As seen in Figure 6.3, the ratio of grid spacing to Kolmogorov scale in the present LES is smaller than 10 over nearly all of the cavity (and smaller than 5 over much of it), suggesting that a substantial portion of the dissipative processes is resolved

in the present LES.

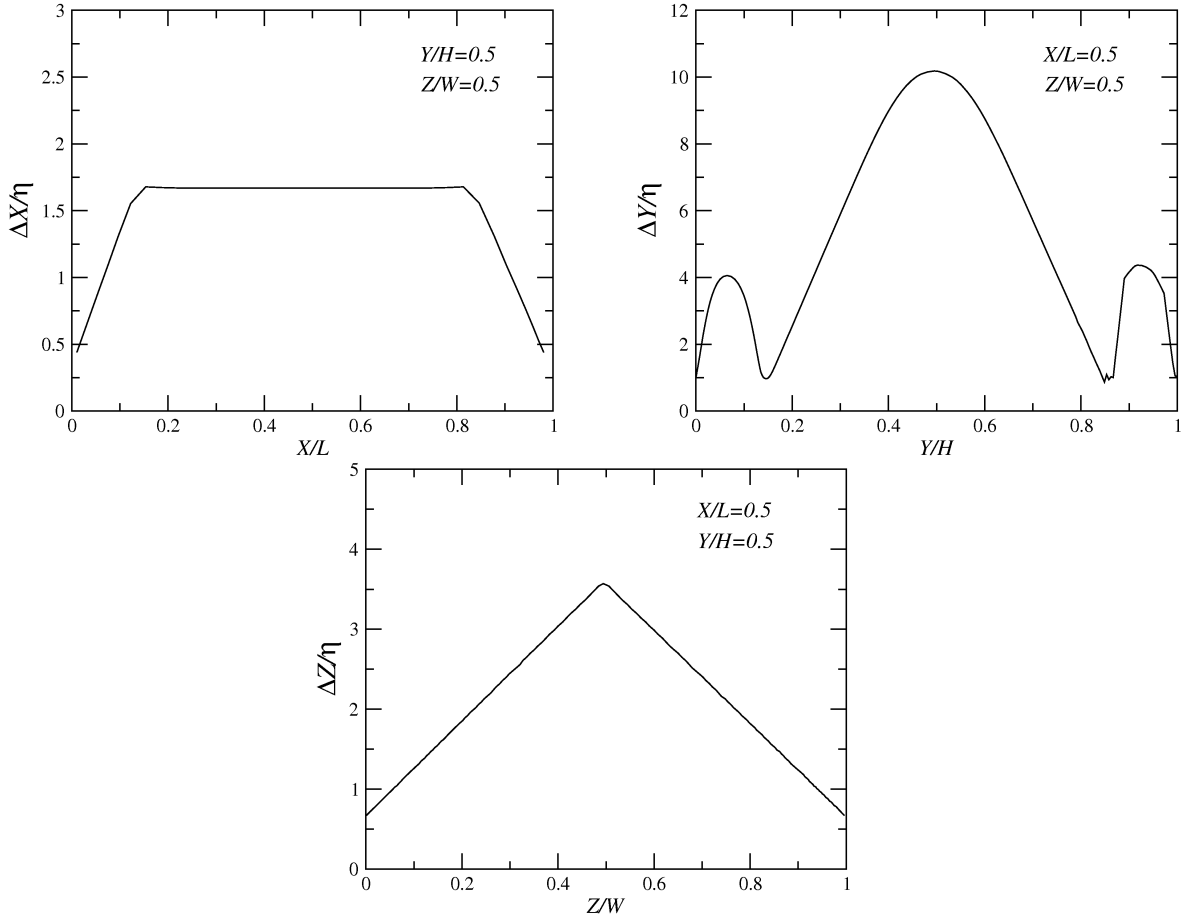


Figure 6.3: Profiles of the ratio of grid spacings to the Kolmogorov length scale at three middle planes (X/L ($Y/H = 0$ and $Z/W = 0$), Y/H ($X/L = 0$ and $Z/W = 0$), Z/W ($X/L = 0$ and $Y/H = 0$)) within the unstably stratified cavity.

A further indication of the LES resolution is provided by examining the ratio of the modelled sub-grid-scale turbulent viscosity (Equation 3.78) to the implied turbulent viscosity of the resolved scales (obtained from the resolved turbulent stresses and mean velocity gradients). Figure 6.4 shows example profiles of this ratio for the unstably stratified enclosure, again along the three mid-section lines, and it is found to be less than 1% (and considerably less than this over much of the cavity).

The above results indicate that at this moderate Rayleigh number the small scale dissipative scales are largely resolved on the present grid. For this unstable case, much of the turbulent mixing occurs in the unsteady roll-cells which are largely resolved in the LES, and consequently the contribution of the sub-grid-scale model is fairly small.

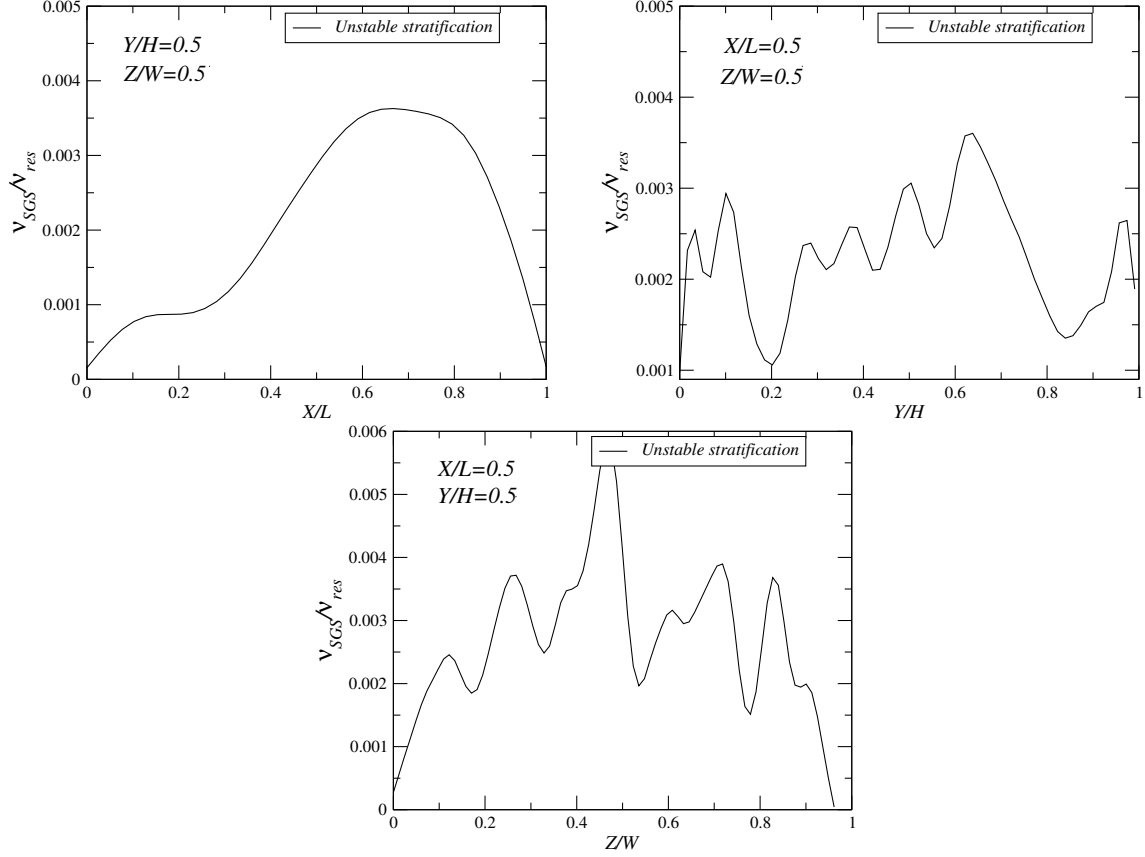


Figure 6.4: Profiles of the ratio of the sub-grid (SGS) viscosity to the resolved turbulent viscosity at three middle planes (X/L ($Y/H = 0$ and $Z/W = 0$), Y/H ($X/L = 0$ and $Z/W = 0$), Z/W ($X/L = 0$ and $Y/H = 0$)) within the unstably stratified cavity.

6.4 Qualitative results

To begin with a qualitative picture of the flow field, Contours of temperature and velocities are first presented within the 15° enclosure under unstable differential heating in order to shed light on the flow physics inside the tilted cavity at this particular angle of inclination. When the tilted enclosure is heated from the lower side, unsteady structures dominate the flow and most turbulence models would be expected to capture such a behaviour.

Figures 6.5 to 6.8 represent predictions of instantaneous temperature contours obtained from a highly resolved LES and some high-Reynolds-number models including the $k - \varepsilon$ and SSG models and the low-Reynolds-number turbulence model $k - \omega$ SST at the three middle sections (X, Y), (X, Z) and (Y, Z) (the SST scheme is used here rather than the $\varphi - f$ model because it is a widely used and validated, the $\varphi - f$ model failed to converge for the tilted test cases in the previous chapter). The results of the

latter model are presented for two fine meshes (Table 6.2). Results of both LES and URANS show the presence of thermal plumes and instabilities along the height and width of the tilted cavity. By simulating the full 3-D flow, longitudinal vortices are captured by LES and almost all the URANS models, similar to the structures noticed in the experiments of Cooper et al [25]. The predictions of the SST model shown in Figure 6.8 show different results when two different meshes are used. The computation using the finer mesh (the one used for LES computation) shows the correct flow pattern, with unstable roll cells, which are not present in the coarser grids predictions, suggesting that the SST $k - \omega$ model needs a very fine grid resolution in the core of the cavity, as well as the near wall region, in order to capture the flow unsteadiness.

In order to give deep understanding of the 3-D flow features within the unstably stratified cavity, Figure (6.9) shows the instantaneous coherent structures obtained from the LES computation, using the Q -criterion which is defined, according to Hunt et al. [50], as:

$$Q = \frac{1}{2} (\Omega_{ij}\Omega_{ij} - S_{ij}S_{ij}) \quad (6.2)$$

where $S_{ij} = \frac{1}{2} \left(\frac{\partial U_i}{\partial x_j} + \frac{\partial U_j}{\partial x_i} \right)$ is the strain-rate tensor, $\Omega_{ij} = \frac{1}{2} \left(\frac{\partial U_i}{\partial x_j} - \frac{\partial U_j}{\partial x_i} \right)$ is the vorticity tensor. $Q > 0$ means the vorticity tensor dominates that of the rate of strain. Inside the unstably stratified enclosure the complexity of the computed flow is clearly visible; a large number of coherent structures are captured inside the cavity.

Contours of the instantaneous dimensionless temperature and V and W velocity components obtained from the LES computation, illustrated in Figures 6.10 and 6.11, suggest the presence of a large number of small vortices, which thoroughly mix the fluid across the cavity, leading to practically isothermal conditions over most of the cavity, with the temperature being the average of the hot and cold side temperatures.

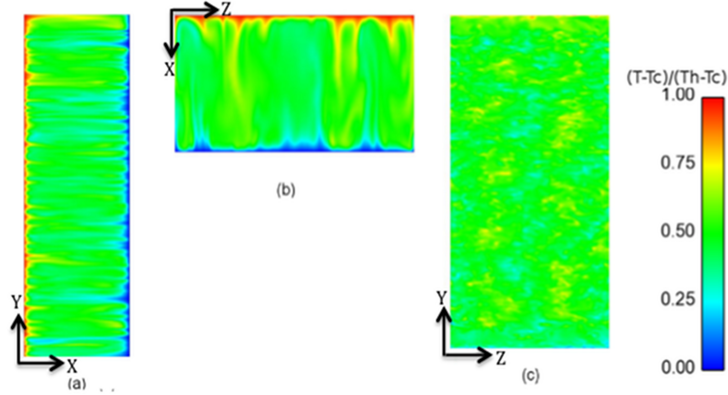


Figure 6.5: Instantaneous temperature contours at mid-width of the unstably stratified cavity obtained from LES: (a) plane (X, Y) , (b) plane (X, Z) , (c) plane (Y, Z) .

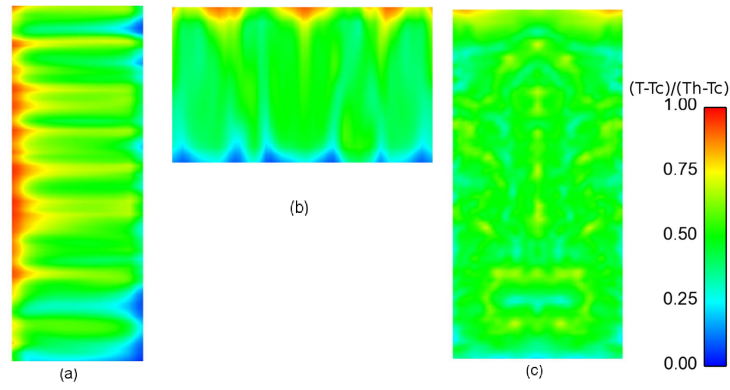


Figure 6.6: Instantaneous temperature contours at mid-width of the unstably stratified cavity obtained from $k - \varepsilon$ model: (a) plane (X, Y) , (b) plane (X, Z) , (c) plane (Y, Z) .

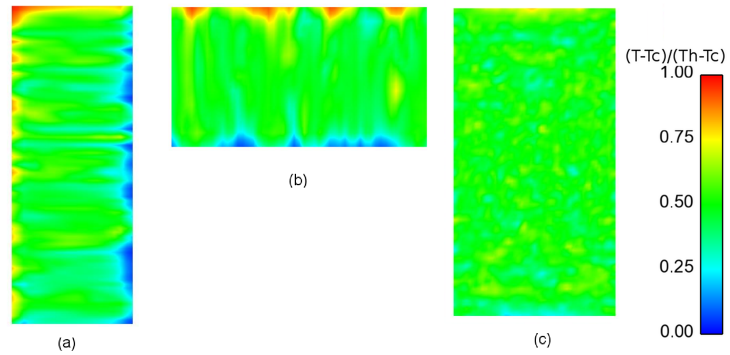


Figure 6.7: Instantaneous temperature contours at mid-width of the unstably stratified cavity obtained from SSG model: (a) (X, Y) , (b) (X, Z) , (c) (Y, Z) .

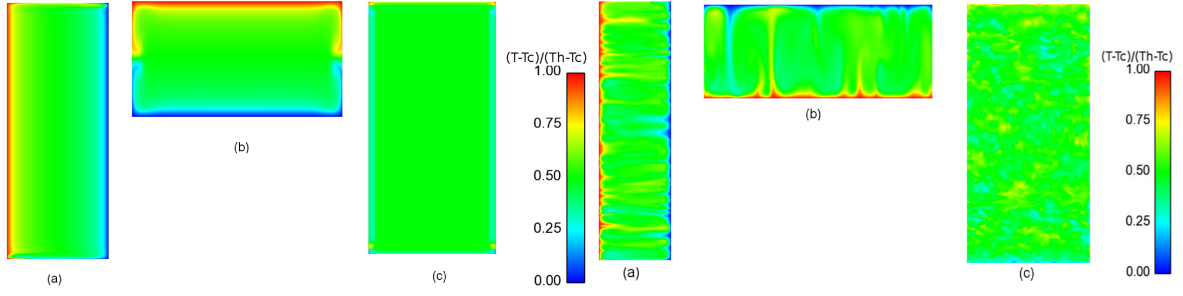


Figure 6.8: Instantaneous temperature contours at mid-width of the unstably stratified cavity obtained from SST $k-\omega$ model. Left: 1 million cell mesh, right: finer LES mesh.

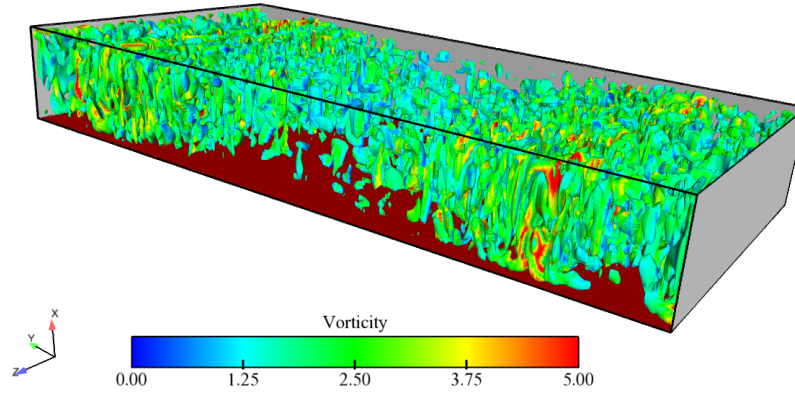


Figure 6.9: LES results: Iso-surfaces of Q -criteria coloured by vorticity in the unstably stratified cavity.

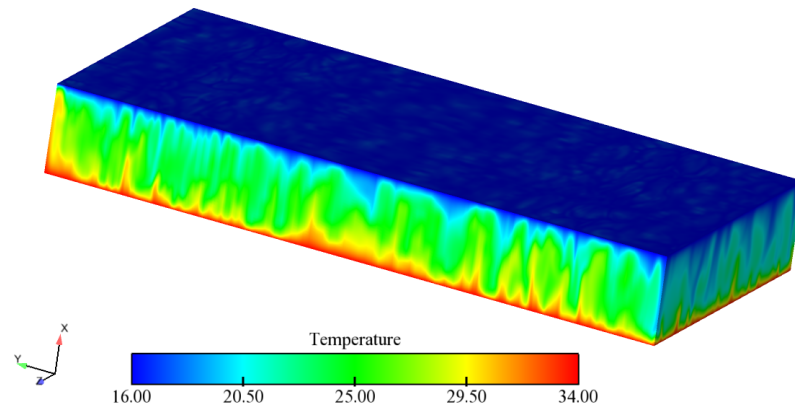


Figure 6.10: LES results: instantaneous temperature contours in the unstably stratified cavity.

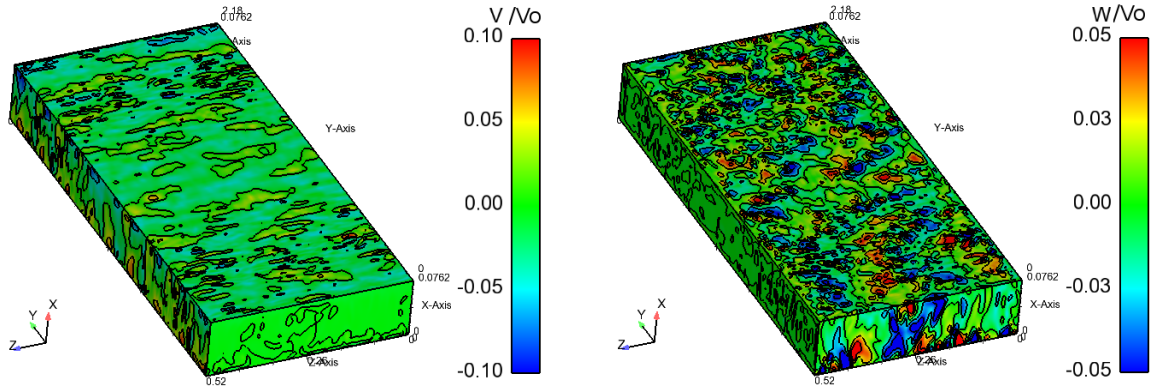


Figure 6.11: LES results: instantaneous velocity contours inside the unstably stratified cavity. Left: V velocity, right: W velocity.

Time-averaged temperature contours at three longitudinal and spanwise cross sections, Figure 6.12, also confirm the above observations: the temperature is constant throughout much of the cavity, due to high mixing, and takes the average between the hot and cold temperatures. These predictions are also in agreement with the experimental findings of Cooper et al. [25].

Figures 6.13, 6.14 and 6.15 show time-averaged contours of the three dimensionless velocity components (U , V , W), predicted by LES, along three longitudinal and spanwise sections. The contours of the wall-normal and spanwise velocity components (U and W) across the spanwise planes (right hand side of Figures 6.13 and 6.15) show that in the unstably stratified enclosure there are four longitudinal vortices which cut across all the spanwise monitoring sections and therefore extend over most of the cavity. These observations are consistent with the findings of the Cooper et al. experimental study [25]. The contours of the wall-parallel velocity (V), on the right of Figure 6.14, show that inside the unstably stratified cavity there are possibly four weak longitudinal cells across the spanwise direction which transport the fluid up and down the inclined direction. Velocity component contours along longitudinal sections (left hand side of Figures 6.13, 6.14 and 6.15) also show circular convection cells between the two differentially heated walls, along the height of the cavity. Temperature differences (leading to density differences), and the associated gravitational forces, cause the fluid to rise then fall forming streamwise rolls.

As a final qualitative comparison, the vector plots at three spanwise sections obtained from LES and high and Low-Re models ($k - \varepsilon$, LRR, SSG and SST) results are illustrated in Figure 6.16. These plots confirm the comments above by showing around

four large longitudinal rolls across the spanwise mid-plane ($Y/H = 0.5$).

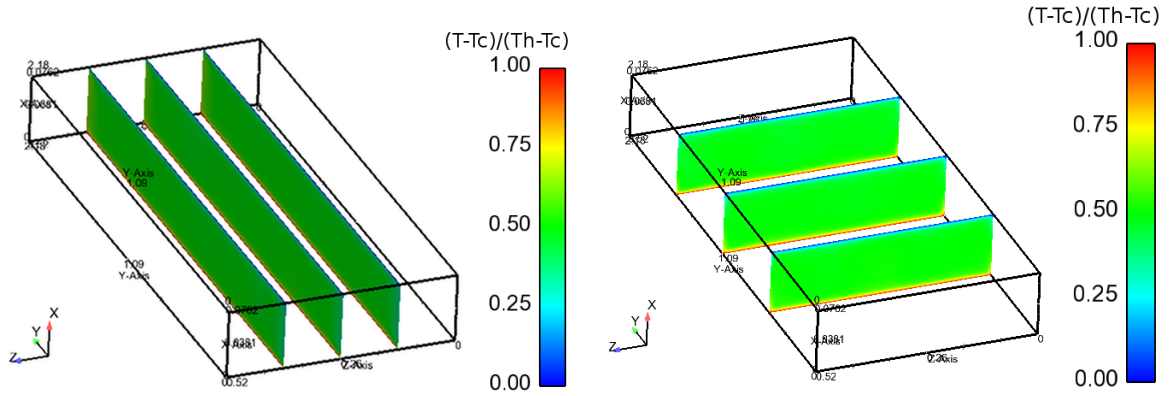


Figure 6.12: LES results: time averaged temperature contours at three longitudinal and spanwise cross-sections of the unstably stratified cavity.

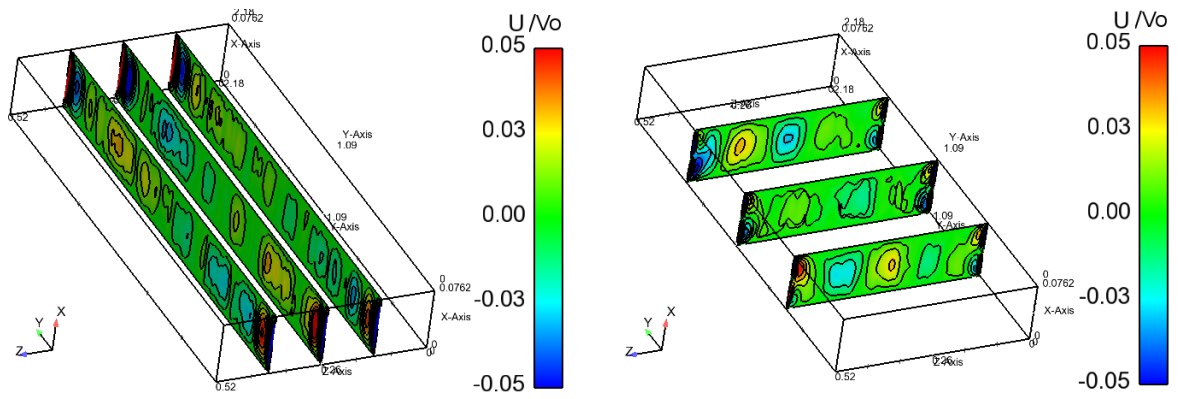


Figure 6.13: LES results: time averaged wall-normal (U) velocity contours at three longitudinal and spanwise sections of the unstably stratified cavity.

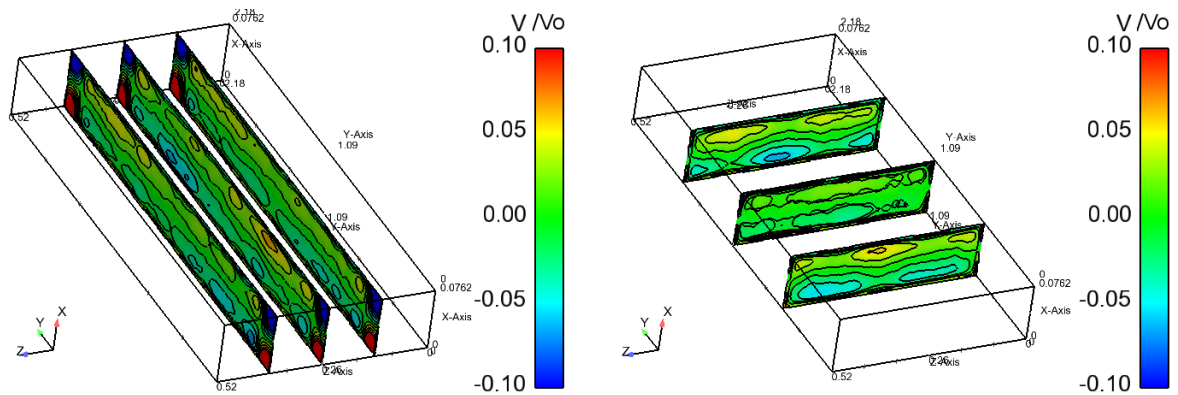


Figure 6.14: LES results: time averaged wall-parallel (V) velocity contours at three longitudinal and spanwise sections of the unstably stratified cavity.

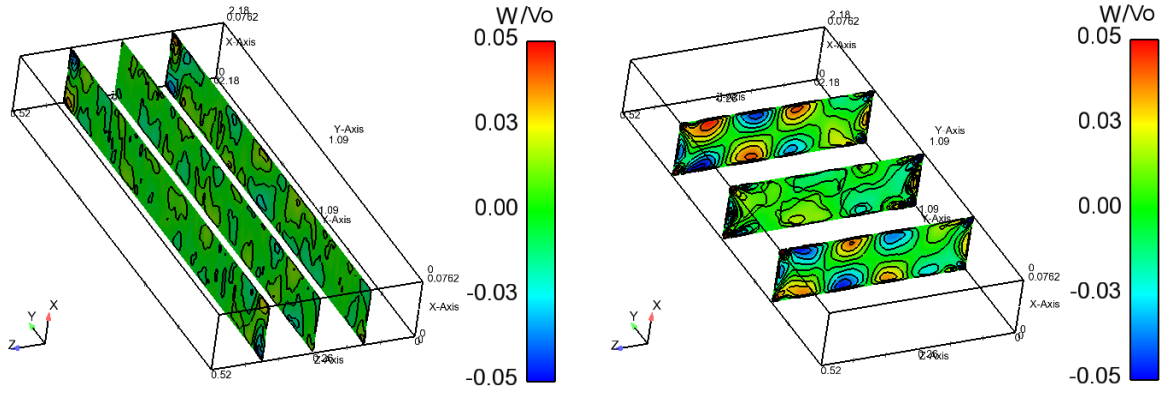


Figure 6.15: LES results: time averaged spanwise (W) velocity contours at three longitudinal and spanwise sections of the unstably stratified cavity.

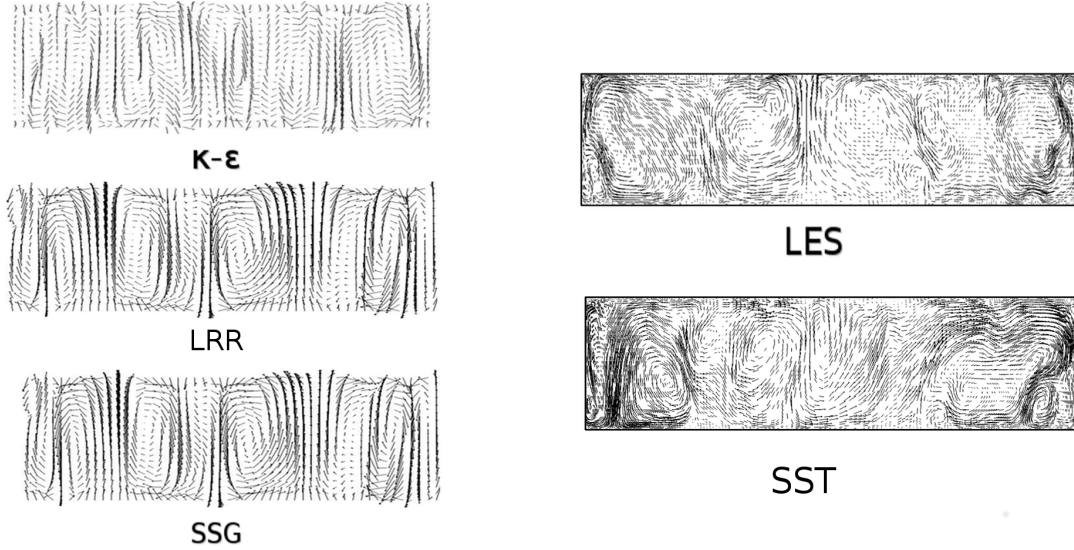


Figure 6.16: LES and URANS results: vector plots of velocity magnitude at the spanwise mid-section ($Y/H = 0.5$) of the unstably stratified enclosure.

6.5 Quantitative results

Turning attention to the quantitative results within the unstably stratified cavity, Figure 6.17 shows comparisons of profiles of the dimensionless time-averaged temperature, normalised by the temperature difference ($T_h - T_c$), along four traverse lines normal to the hot and cold sides ($Y/H = 0.05, 0.3, 0.5$ and 0.95), within two spanwise planes ($Z/W = 0.5$ and $Z/W = 0.75$). The comparisons include the LES predictions and the experimental data of Cooper et al. [25] for the unstable stratification. The LES

profiles are in good agreement with the experimental data, reflecting the fact that in the unstable case the strong mixing leads to an isothermal core, at a temperature which is the average of that of the hot and cold sides.

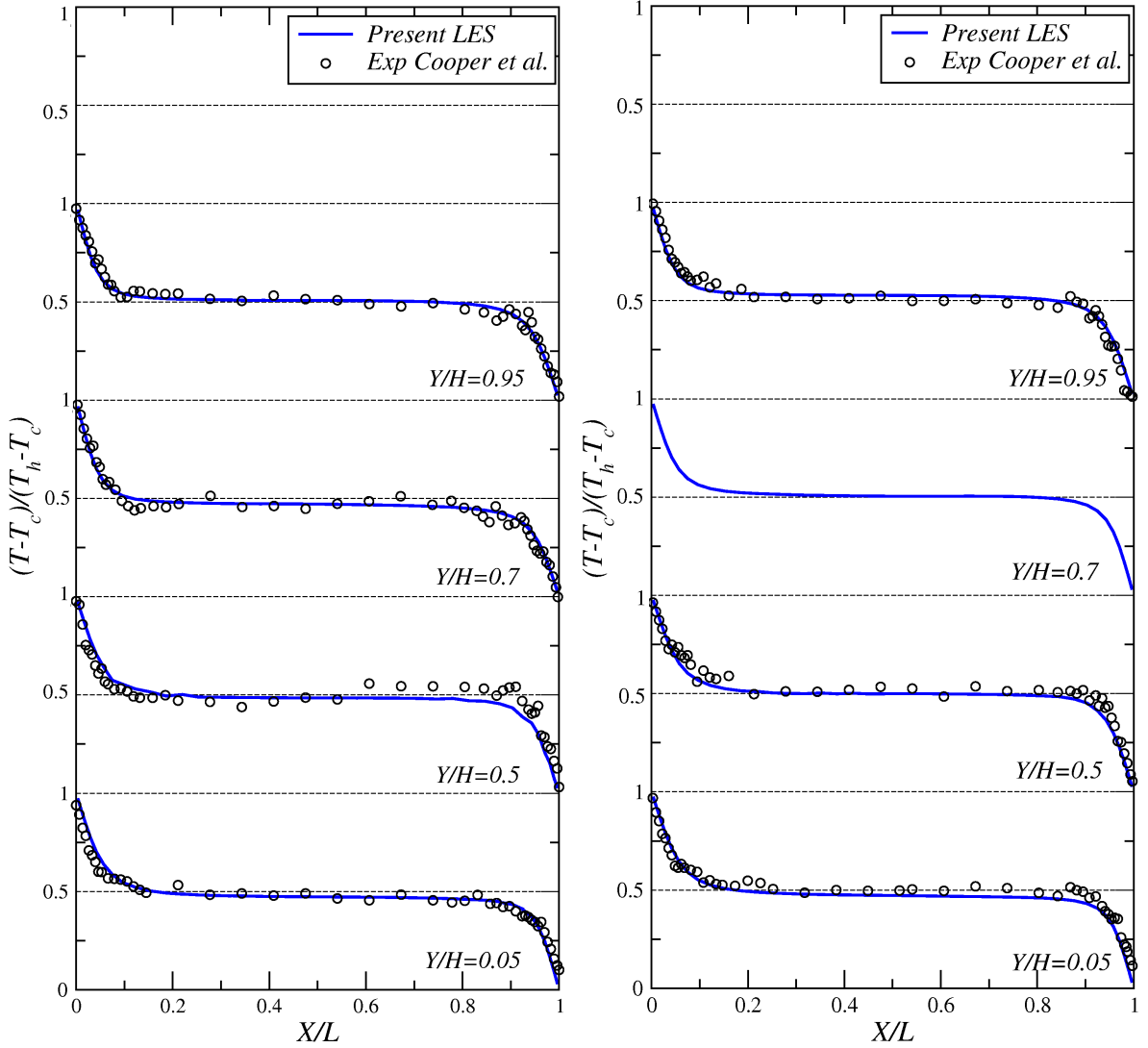


Figure 6.17: LES results: time-averaged temperature profiles at four longitudinal locations and at two spanwise sections inside the unstably stratified enclosure. Left: $Z/W = 0.5$, right: $Z/W = 0.75$.

The unsteady RANS predictions on the central plane $Z/W = 0.5$, using the high-Re $k - \varepsilon$, the LRR and SSG second-moment closures and the $k - \omega$ SST scheme (using the two different fine meshes), are compared with the present LES and the experimental data [25] and are shown in Figure 6.18. As seen above, almost all URANS models, including standard $k - \varepsilon$ and second-moment closures, are able to reproduce the strong

mixing effects present in the 15° unstable enclosure. The low-Re SST $k - \omega$ however needs the finer grid resolution in the core of the cavity, as well as the near wall region, in order to capture the unsteady mixing, and hence its results on the coarser grid show much poorer agreement with the LES and experimental data.

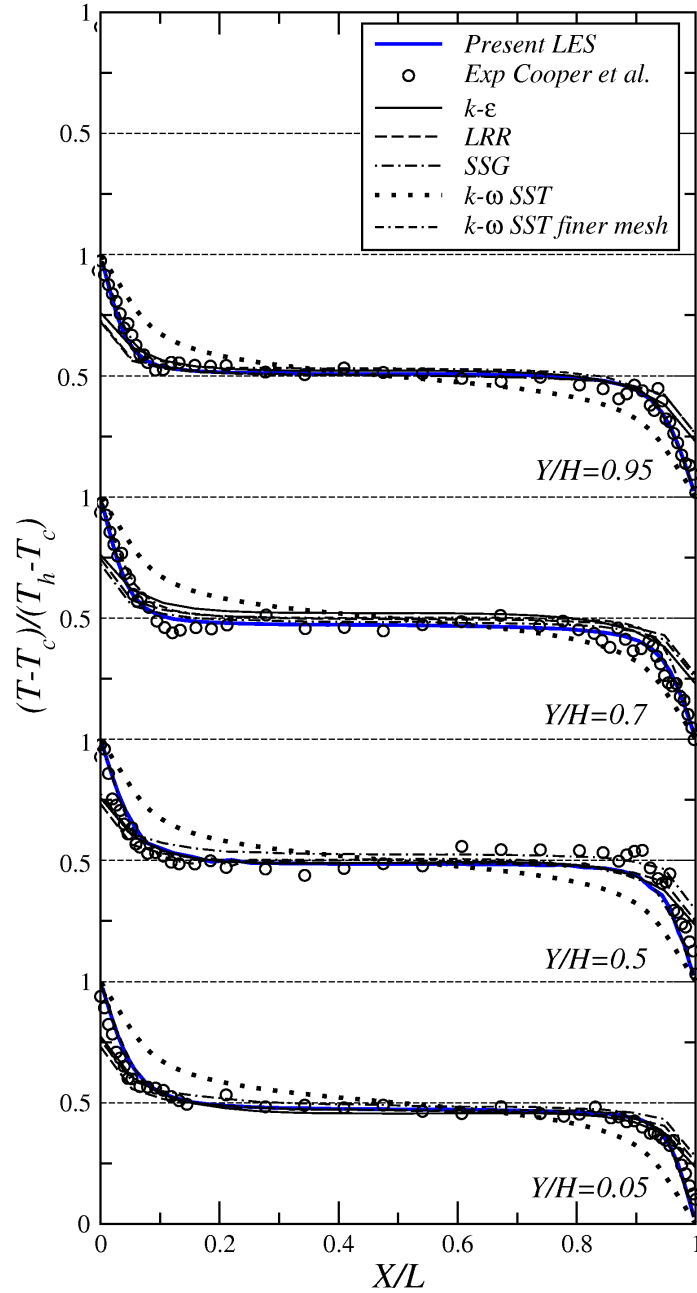


Figure 6.18: URANS results: time-averaged temperature profiles at four longitudinal locations on the middle spanwise section ($Z/W = 0.5$) inside the unstably stratified enclosure.

Figures 6.19 and 6.20 present respectively comparisons of time-averaged dimensionless velocity profiles for the wall-normal U and the wall-parallel V velocity components normalised by the buoyant velocity V_0 along traverse lines normal to the hot and cold sides, within two central longitudinal planes ($Z/W = 0.5$ and $Z/W = 0.75$). The main feature of these profiles is that the velocity shows an almost linear variation across the cavity, with the fluid moving upwards along the hot wall and downwards along the cold one. The velocity levels are very low in comparison to those for a vertical cavity. This is a consequence of the practically isothermal conditions across much of the cavity, caused by the strong mixing, due to the presence of the streamwise vortices. The LES profiles are in close agreement with the measurements, apart from some profiles of the wall-normal component where the experimental data exhibit some scatter. The profiles predicted by the unsteady RANS models, in Figure 6.21, are generally in close agreement with those of the LES and experimental data, as expected since the URANS models should be able to capture the relatively slow, unsteady, structures present in the flow. The only exception is the SST $k - \omega$ scheme when used on a fairly coarse grid in the core of cavity, which overestimates the wall-parallel V velocity. As noted in the thermal predictions above, the model performance does, however, improve when a finer grid is used. The LRR model also tends to over-estimate the wall-normal U velocity close to the top and bottom insulated walls, possibly due to its pressure-strain model (and particularly the wall-reflection terms in that) not responding correctly to the change in direction of the wall-normal velocity component in these regions.

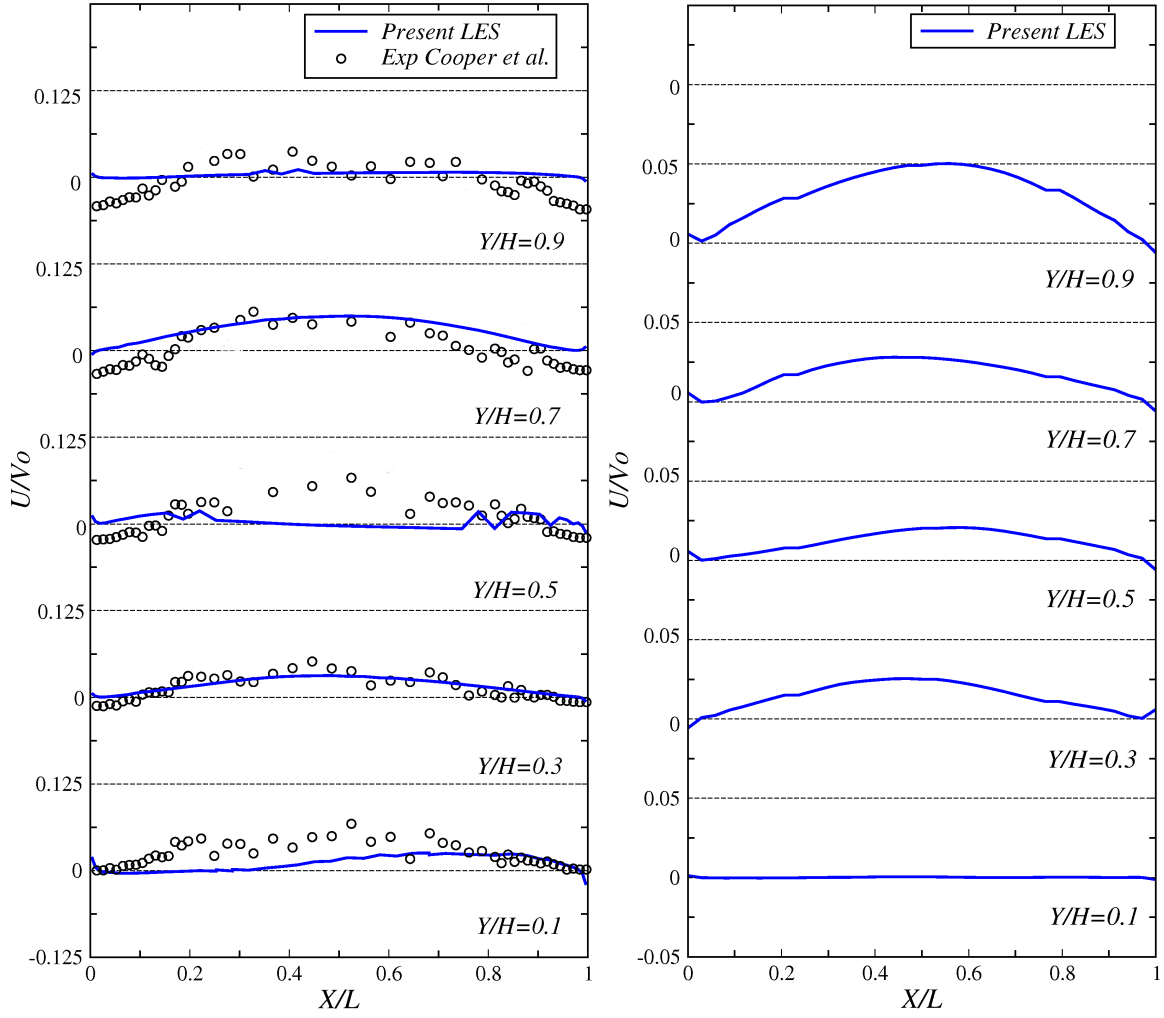


Figure 6.19: LES results: time-averaged U velocity profiles at five longitudinal locations inside the unstably stratified enclosure. Left: $Z/W = 0.5$, right: $Z/W = 0.75$.

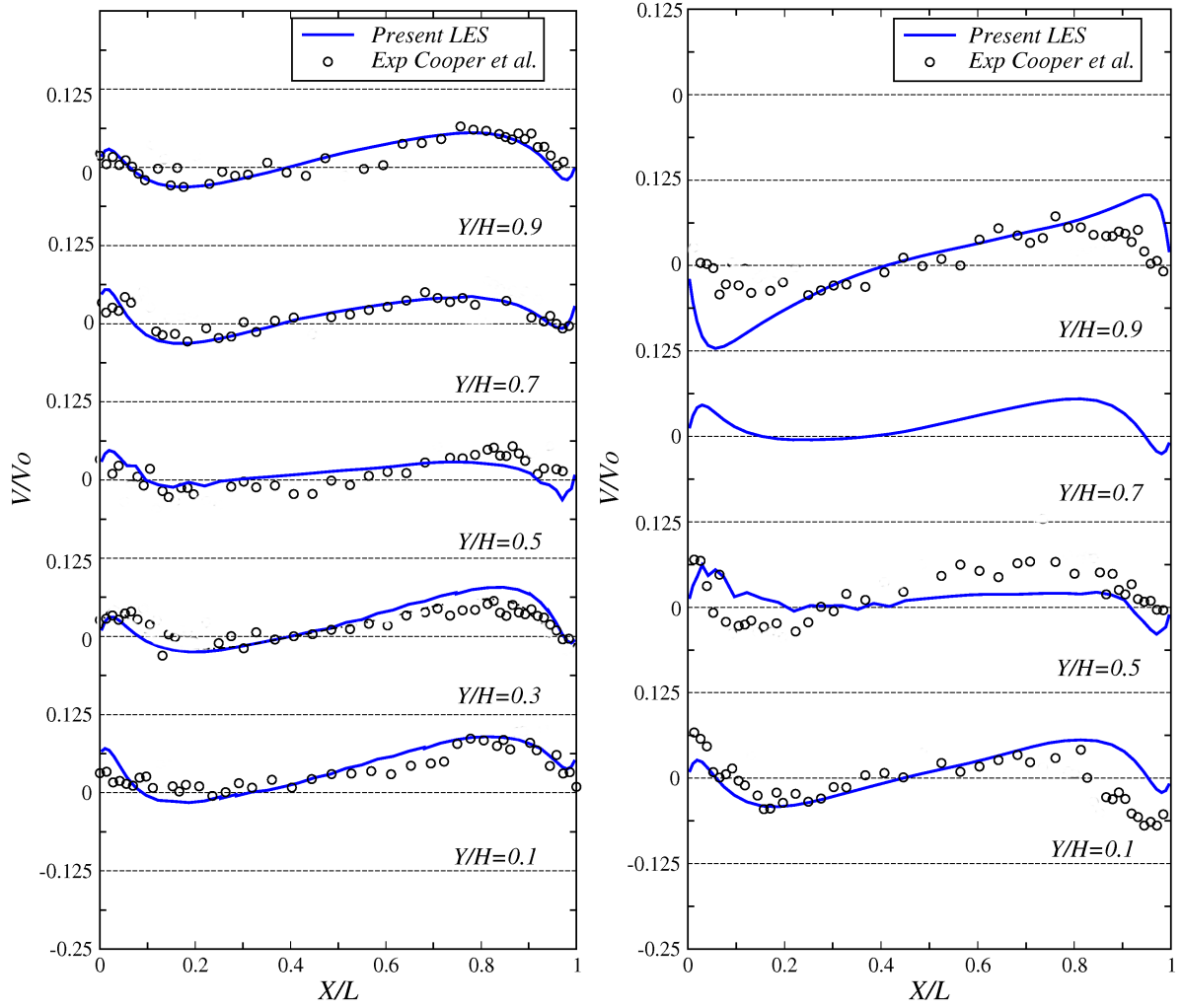


Figure 6.20: LES results: time-averaged V velocity profiles at five longitudinal sections inside the unstably stratified enclosure. Left: $Z/W = 0.5$, right: $Z/W = 0.75$.

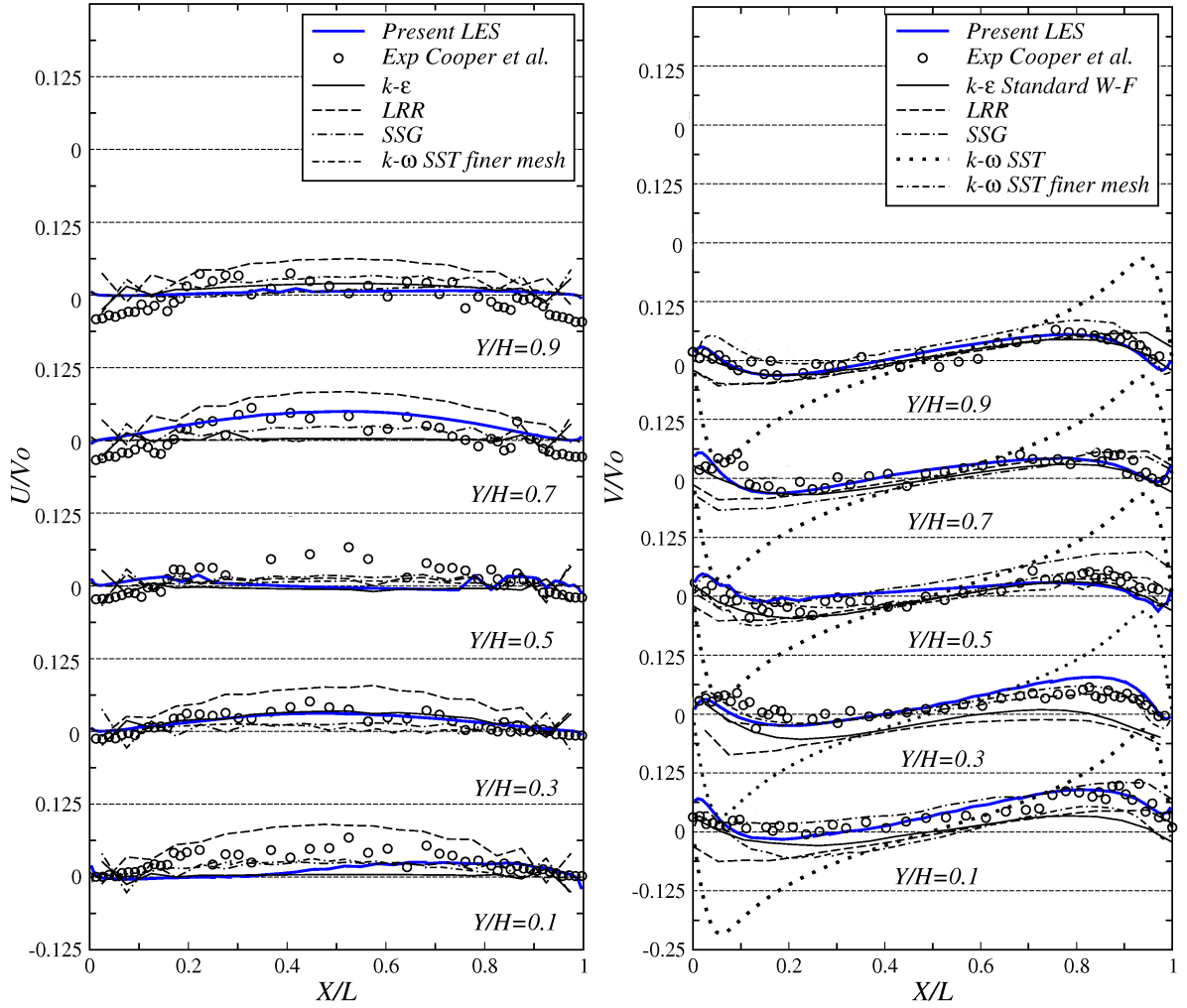


Figure 6.21: URANS results: time-averaged velocity profiles at five longitudinal locations and at the middle spanwise section ($Z/W = 0.5$) inside the unstably stratified enclosure. Left: U velocity, right: V velocity.

Figures 6.23 to 6.27 present profile comparisons of turbulence parameters, which include the temperature variance, the turbulence intensities and the turbulent heat fluxes. As mentioned in Chapter 3 above, URANS fluctuation profiles include both the resolved and the modelled components. In order to quantify the intensity of the resolved large-scale unsteadiness and its relative contribution to the total budget of the turbulence kinetic energy k , comparisons between the modelled and resolved k in the core of the unstably stratified cavity obtained from URANS models are presented in Figure 6.22. One denotes, k_m , the time-average of the kinetic energy obtained from the time-accurate solution of the k -equation as follows:

$$k_m(x, y, z) = \lim_{t \rightarrow \infty} \frac{1}{t} \int_0^t k(t', x, y, z) dt', \quad (6.3)$$

where $k(t', x, y, z)$ is the solution of the transport equation for k at point (x, y, z) at time t' with turbulent fluctuations relative to the phase-averaged velocity components. k_m quantifies the amount of the turbulence kinetic energy modelled by the turbulence closure model. The resolved kinetic energy, k_r , on the other hand is the amount of energy due to the large-scale, coherent motions in the flow, which are resolved directly by solving the URANS equations. It is defined as follows:

$$k_r = \lim_{t \rightarrow \infty} \frac{1}{t} \int_0^t \frac{1}{2} (u''^2 + v''^2 + w''^2) dt', \quad (6.4)$$

where $u'' = u - \bar{u}$, u is the instantaneous, phase-averaged velocity component obtained from the solution of the URANS equations, and \bar{u} is its time-averaged value. The wall-normal fluctuation $\overline{u'u'}$, for example, is calculated from the $k - \varepsilon$ model as:

$$\overline{u'u'} = \frac{1}{2} (k_r + k_m) = \frac{1}{2} (\overline{uu} - \bar{u} \bar{u}) + \frac{2}{3} k_m, \quad (6.5)$$

The other turbulence quantities are calculated in the same way.

It is evident from Figure 6.22 that the resolved kinetic energy (k_r) produced by the coherent periodic vortex shedding accounts for a significant percentage of the total energy in the core of the unstably stratified enclosure where it appears to overwhelm k_m for all URANS models ($k - \varepsilon$, LRR, SSG and $k - \omega$ SST). It is important to emphasise that the flow in the core of the cavity is highly three-dimensional and unsteady. It is featured by the presence of dominant large scales which can be resolved by URANS and this is what explains the high values of the resolved k .

For the unstably stratified case, starting with the wall-parallel $\overline{v'v'}$ and spanwise

$\overline{w'w'}$ components of the Reynolds stress tensor, Figures 6.24 and 6.25, the LES and experimental profiles are in close agreement, with uniformly high levels across the cavity. This is consistent with the presence of strong mixing. The LES and experimental profiles of the wall-normal component $\overline{u'u'}$, Figure 6.23, show a more gradual increase from the walls, but the same levels as the other two components in the cavity core. Profiles of the shear stress $\overline{u'v'}$ are also presented here, in Figure 6.26, with LES predictions showing similar levels of $\overline{u'v'}$ near the top and bottom walls, and slightly lower levels in the centre of the cavity. URANS model predictions are generally close to LES data except the $k - \varepsilon$ model which overpredicts the shear stress $\overline{u'v'}$.

The measured temperature variance $\overline{t't'}$ profiles, in Figure 6.27, display a uniform distribution similar to that of the wall-parallel and spanwise velocity fluctuations. The LES profiles, however, return higher near-wall peaks than the experimental ones, as do most of the URANS models. These discrepancies might indicate possible errors in the near-wall measurements of the fluctuating temperature, maybe due to radiation or other wall-proximity effects. The LES profiles of the turbulent heat fluxes (corresponding experimental profiles are not available) show that those of the wall-normal component $\overline{u't'}$, Figure 6.28, mirror the variation of the profiles of the wall-normal Reynolds stress component, with a gradual rise across the near-wall regions and uniform core distribution. For the wall parallel component $\overline{v't'}$, Figures 6.29, the LES profiles show high near wall peaks and core values lower than those of the wall-normal turbulent heat flux. The main feature of the profiles of the spanwise component of the turbulent heat flux $\overline{w't'}$, Figure 6.30, is that this component is an order of magnitude lower than the other two. All the unsteady RANS models return predictions of the rms temperature very close to those of the LES and the measurements. For the turbulent heat fluxes, the unsteady RANS predictions are in qualitative agreement with the LES, though there are noticeable quantitative deviations. This might be related to the use of the effective diffusivity approximation for modelling the turbulent heat fluxes, which in some complex flows is not able to give a correct prediction of all the turbulent heat flux components. The use of more advanced models like the EB-RSM of Hanjalić and Manceau [65] with GGDH can improve the performance of the second moment closure.

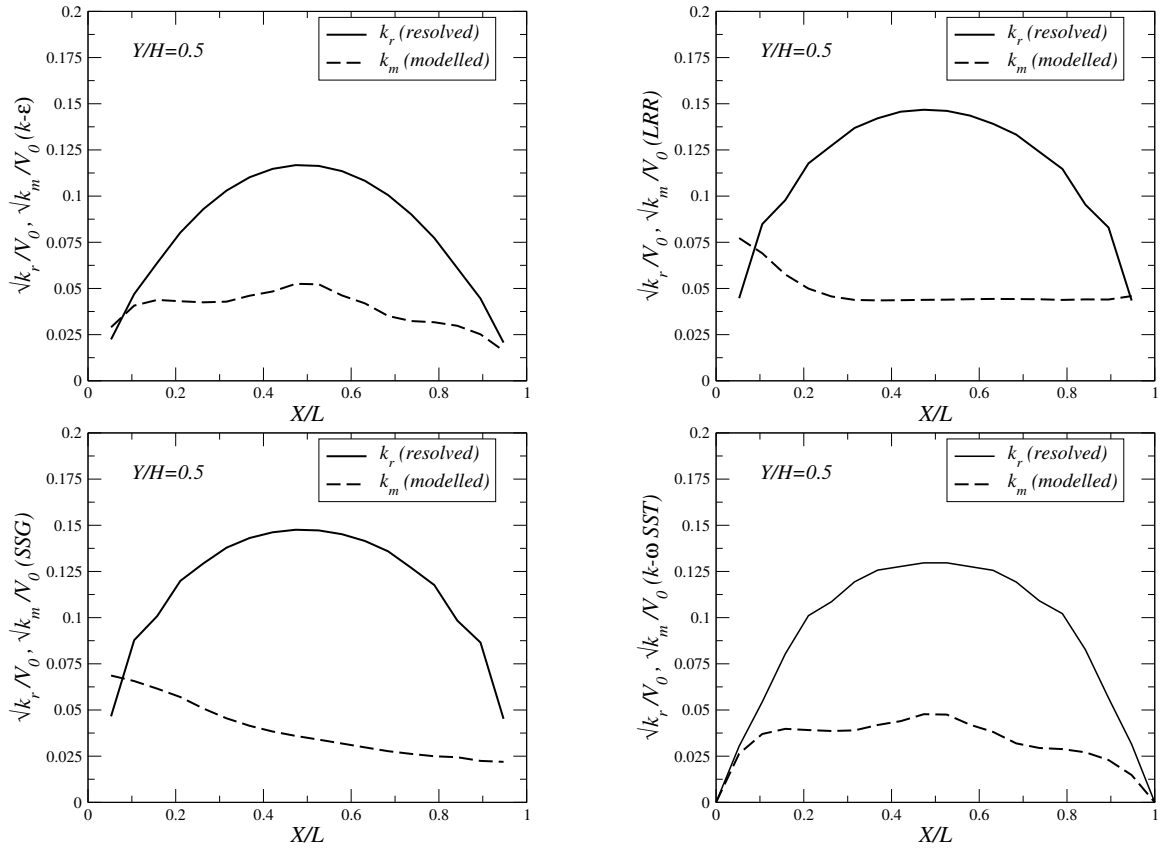


Figure 6.22: Comparisons between resolved and modelled k of the wall-normal rms velocity fluctuation $\sqrt{u'^2}$ at the the middle location ($Y/H = 0.5$, $Z/L = 0.5$) inside the unstably stratified cavity.

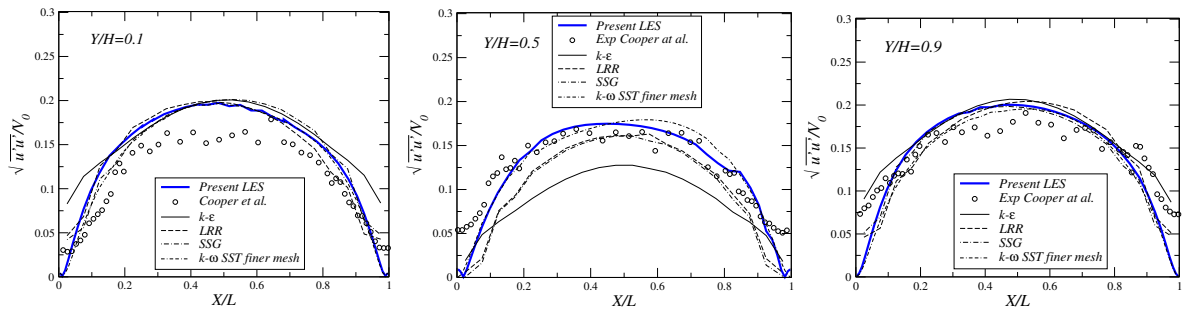


Figure 6.23: Time-averaged rms wall-normal velocity $\sqrt{u'u'}$ at three longitudinal locations ($Y/H = 0.1, 0.5, 0.9$) inside the 15° unstably stratified cavity.

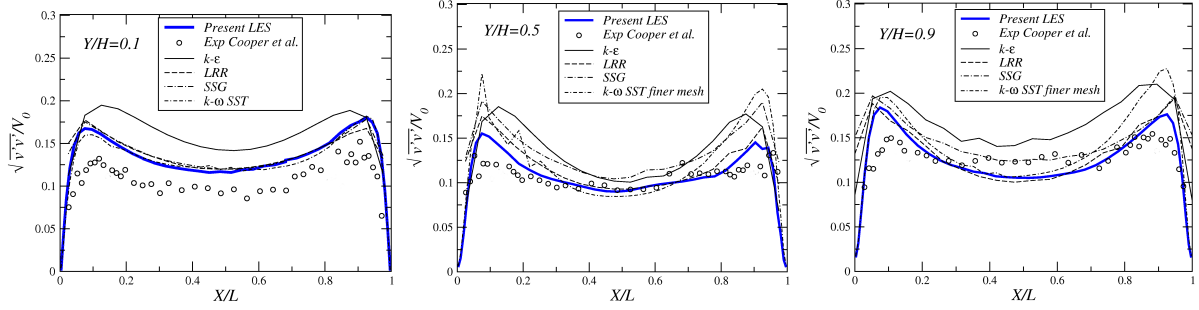


Figure 6.24: Time-averaged rms wall-parallel velocity $\sqrt{v'v'}$ at three longitudinal locations ($Y/H = 0.1, 0.5, 0.9$) inside the 15° unstably stratified cavity.

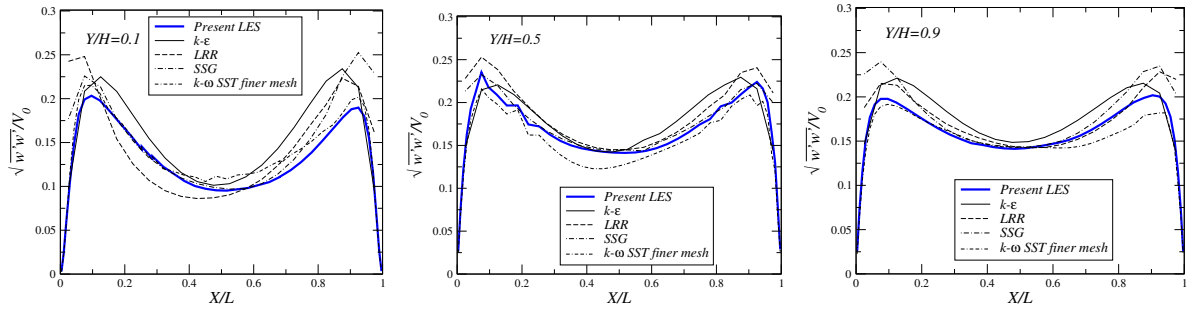


Figure 6.25: Time-averaged rms spanwise velocity $\sqrt{w'w'}$ at three longitudinal locations ($Y/H = 0.1, 0.5, 0.9$) inside the 15° unstably stratified cavity.

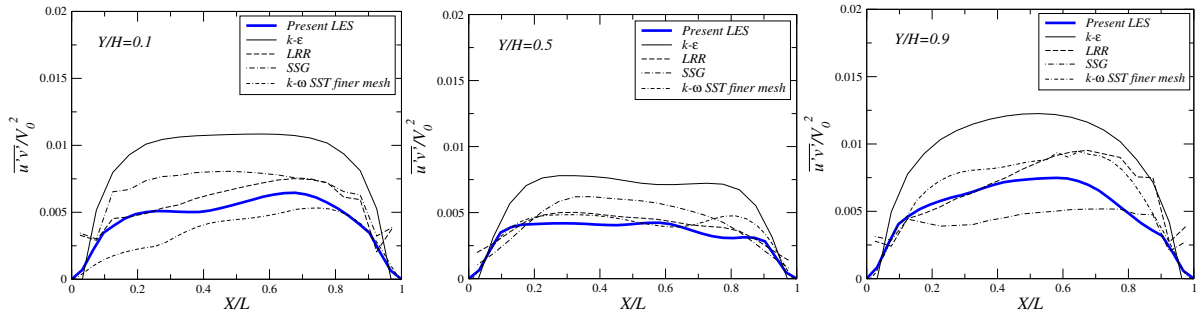


Figure 6.26: Time-averaged turbulent shear stress $\overline{u'v'}$ at three longitudinal locations ($Y/H = 0.1, 0.5, 0.9$) inside the 15° unstably stratified cavity.

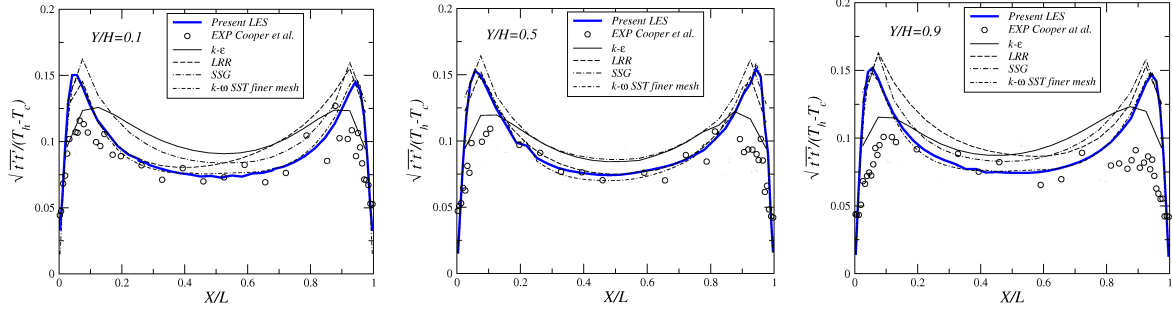


Figure 6.27: Time-averaged rms temperature $\sqrt{t't'}$ at three three longitudinal locations ($Y/H = 0.1, 0.5, 0.9$) inside the 15° unstably stratified cavity.

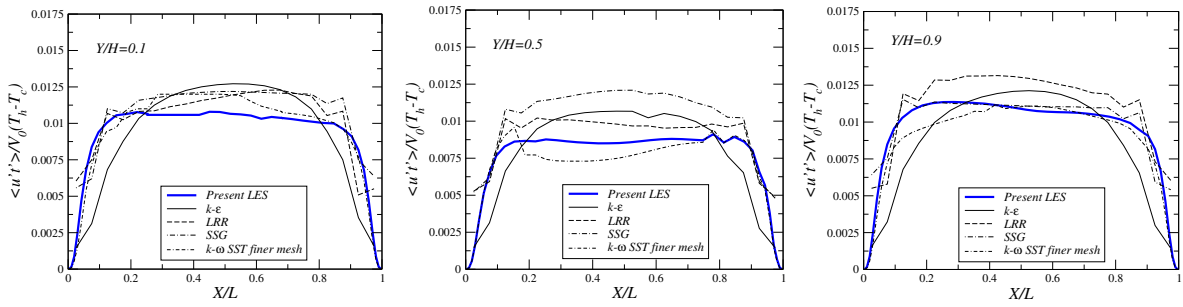


Figure 6.28: Time-averaged rms wall-normal heat flux $\overline{u't'}$ at three longitudinal locations ($Y/H = 0.1, 0.5, 0.9$) inside the 15° unstably stratified cavity.

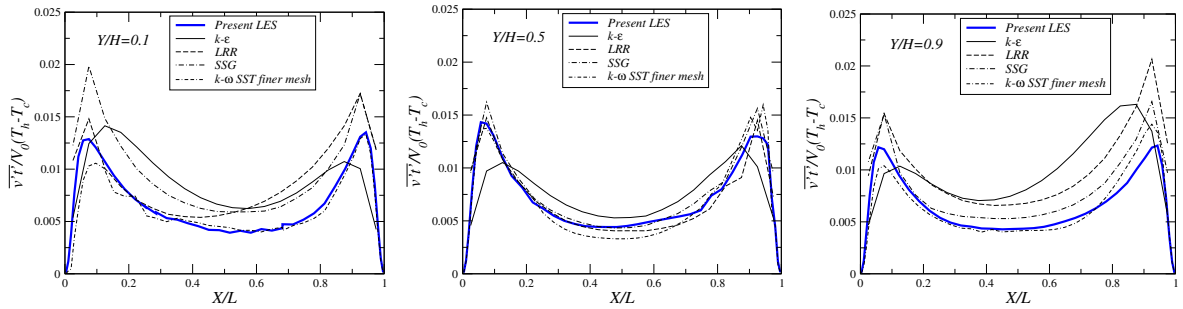


Figure 6.29: Time-averaged rms wall-parallel heat flux $\overline{v't'}$ at three longitudinal locations ($Y/H = 0.1, 0.5, 0.9$) inside the 15° unstably stratified cavity.

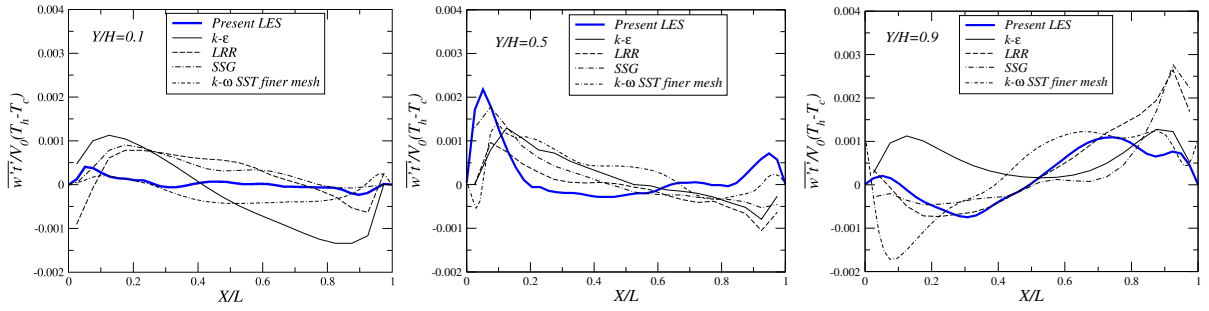


Figure 6.30: Time-averaged rms spanwise heat flux $\overline{w't'}$ at three longitudinal locations ($Y/H = 0.1, 0.5, 0.9$) inside the 15° unstably stratified cavity.

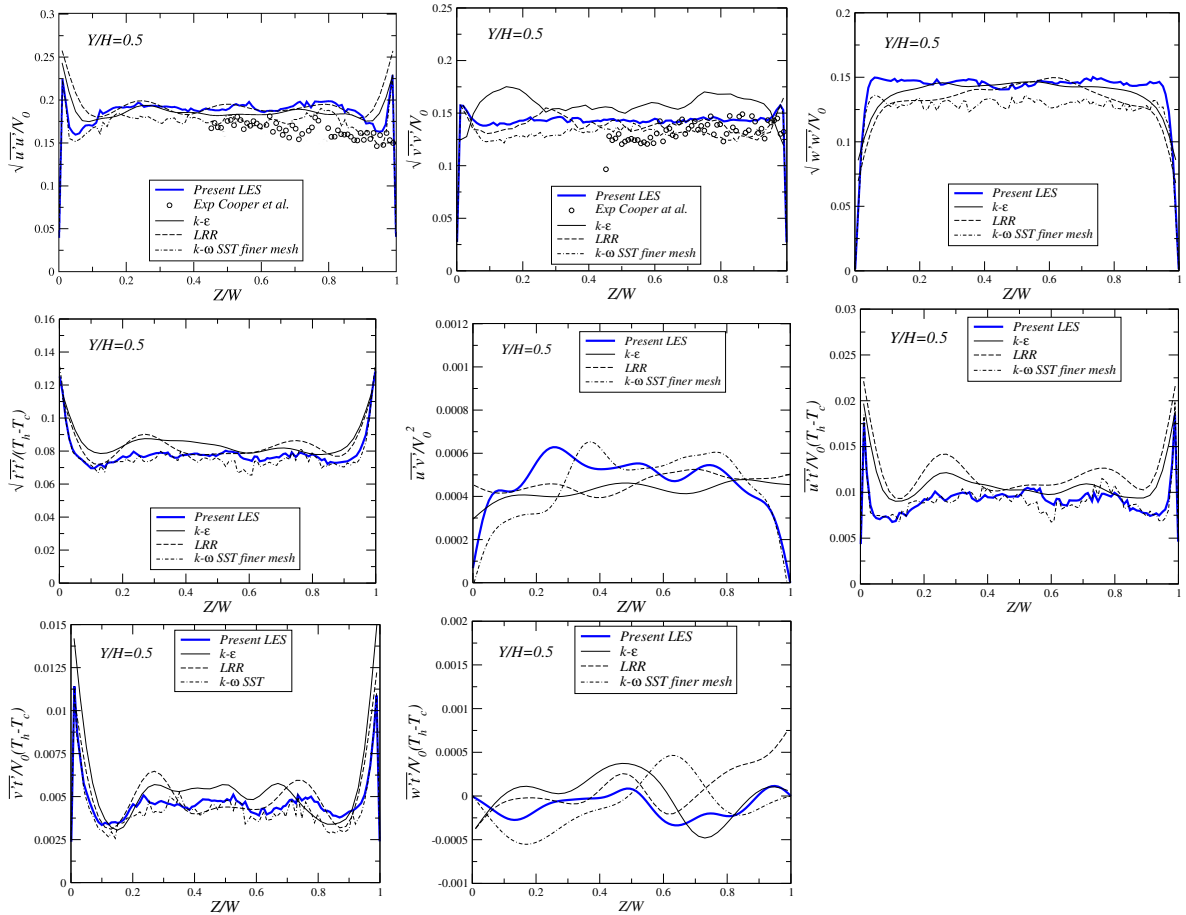


Figure 6.31: Time-averaged Reynolds stresses and heat fluxes along the spanwise cross-section, at the longitudinal central location ($Y/H = 0.5$) of the 15° unstably stratified cavity.

The corresponding rms velocity fluctuations and heat fluxes along spanwise cross-sections, at the $Y/H = 0.5$ longitudinal traverse, are also plotted and presented in

Figure 6.31. It was mentioned earlier that LES successfully captured the four longitudinal vortices present in the spanwise cross sections, in agreement with the experiment of Cooper et al. [25]. Once again, profiles of rms velocity fluctuations suggest the presence of these unsteady structures. The LES profiles of rms velocity fluctuations are in close agreement with the available measured data, showing a uniform level across the spanwise extent, because of the high mixing over most of the cavity. The URANS schemes used here again show a good performance in predicting the turbulence quantities except for some deviations of profiles of the $\overline{u'v'}$ component and heat fluxes comparing with the LES data.

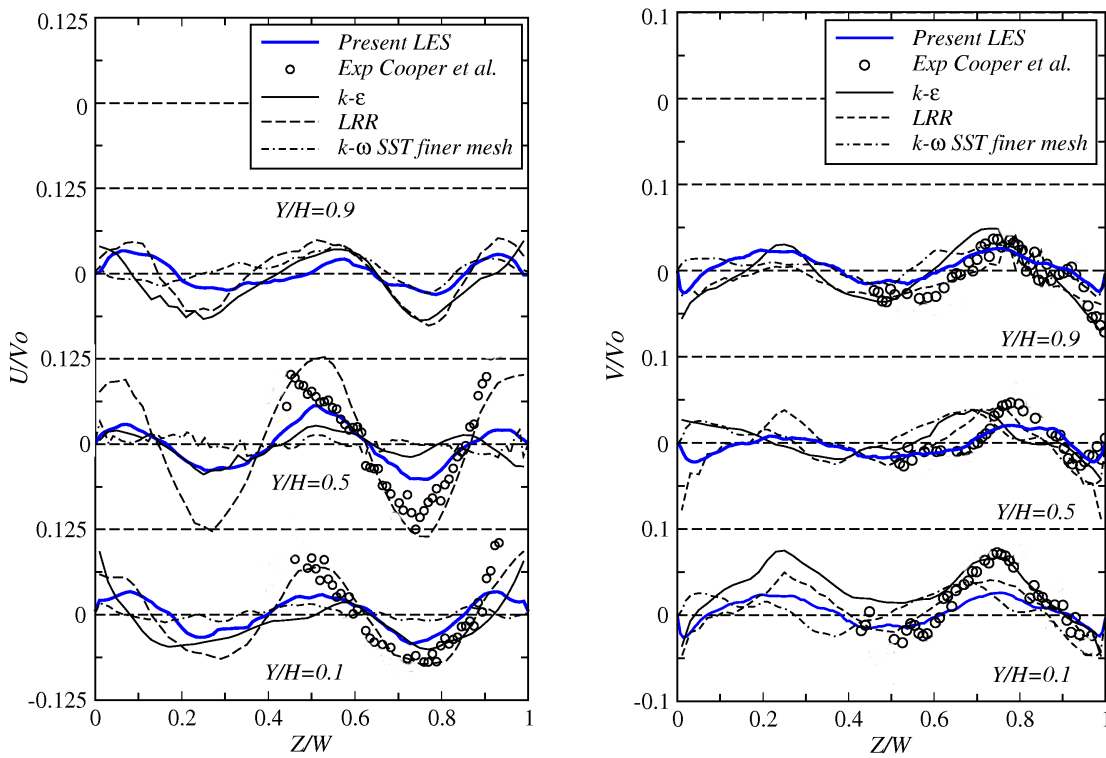


Figure 6.32: Time-averaged velocity profiles along the spanwise cross-section, at three longitudinal traverses inside the unstably stratified enclosure. Left: U velocity, right: V velocity.

Further comparisons of LES and URANS results with the available measurements have also been carried out, this time along three spanwise traverses. Profiles of the dimensionless wall-normal U and wall-parallel V velocities, in the spanwise Z direction, half-way between the hot and cold surfaces, are illustrated in Figure 6.32. A sinusoidal shape of the profiles of wall-normal and wall-parallel velocities is predicted by both LES and URANS with two peaks at around $Z/W = 0.25$ and 0.75 . This is consistent

with the experimental data of Cooper et al. [25] which suggest the presence of the longitudinal vortices, for which more evidence from the LES computation has been presented in Figure 6.16. As far as the RANS models are concerned, it is found that the second moment closure is best in reproducing the three-dimensionality implied by the LES and measurements.

Figures 6.33 to 6.36 show the LES temporal density power-spectra plotted against the Strouhal number, which is the dimensionless frequency defined as fL/V_o , of the fluctuations of temperature and the three velocity components (U , V , W) at two probe locations A (near the bottom insulated wall) and B (the centre of the cavity). The spectral distributions are obtained by recording time histories of flow parameters at the selected locations and subsequently carrying out a Fast Fourier Transform. For the present unstably stratified cavity, there is little variation in the spectral distribution of the velocity components. Energy levels start to fall more rapidly for Strouhal numbers (dimensionless frequencies) greater than 0.1. The spectral distribution of the temperature shows higher power densities of the dominant frequencies compared with the velocity components. These findings confirm the conclusions reached from earlier comparisons that in the unstably stratified cavity, due to the strong mixing, conditions in the cavity core are highly homogeneous and isotropic. The FFT analysis obtained from LES shows that the range of dominant frequencies is between Strouhal number values of around 0.01 and 0.1, or frequency values of $0.03Hz$ and $0.3Hz$, with corresponding power densities of around 0.01 for the velocities and 0.5 for the temperature. These features are consistent with the measurements, which suggest the presence of slow-moving large scale flow structures of low frequencies (less than $0.5Hz$). Comparing the FFT at the two monitoring points, one finds that towards the centre of the cavity (Probe B) the power-spectra density of the dominant frequencies is slightly higher than near the bottom wall (Probe A).

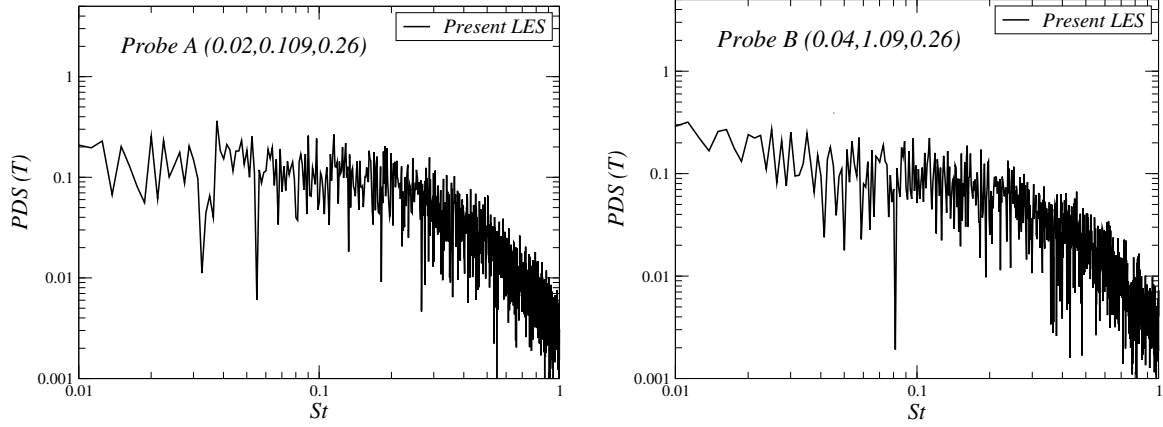


Figure 6.33: LES results: Temporal power spectrum of temperature at the monitoring points A and B inside the 15° unstable stratified cavity.

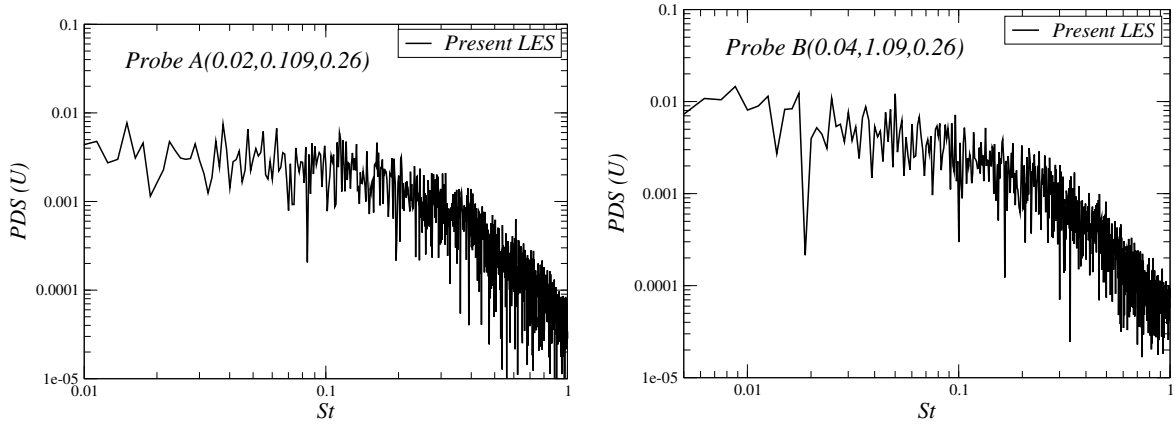


Figure 6.34: LES results: Temporal power spectrum of U velocity at the monitoring points A and B inside the 15° unstable stratified cavity.

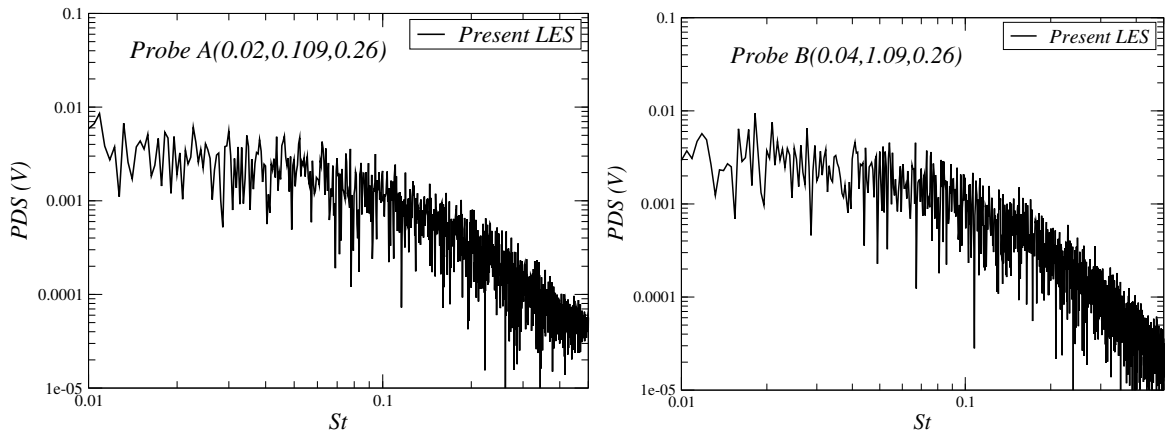


Figure 6.35: LES results: Temporal power spectrum of V velocity at the monitoring points A and B inside the 15° unstable stratified cavity.

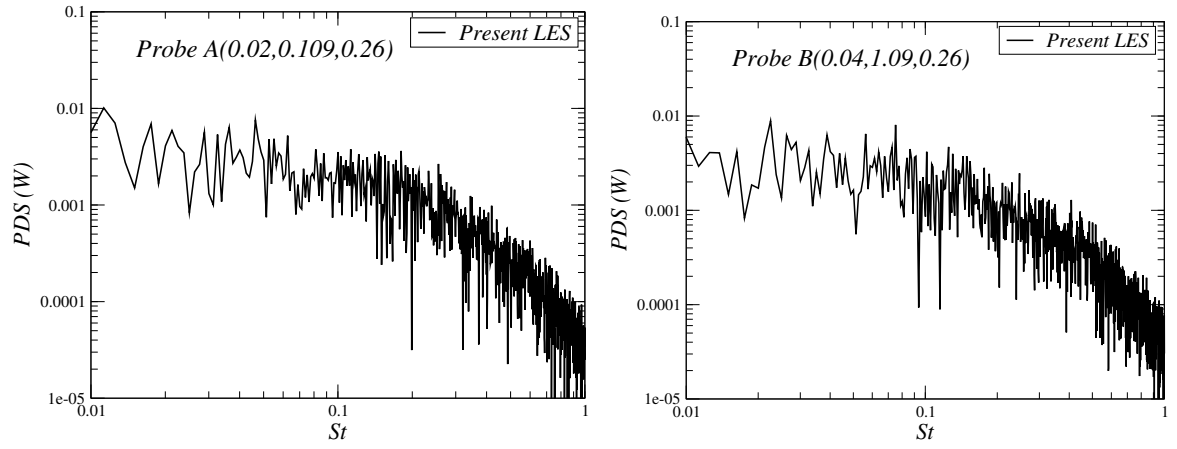


Figure 6.36: LES results: Temporal power spectrum of W velocity at the monitoring points A and B inside the 15° unstable stratified cavity.

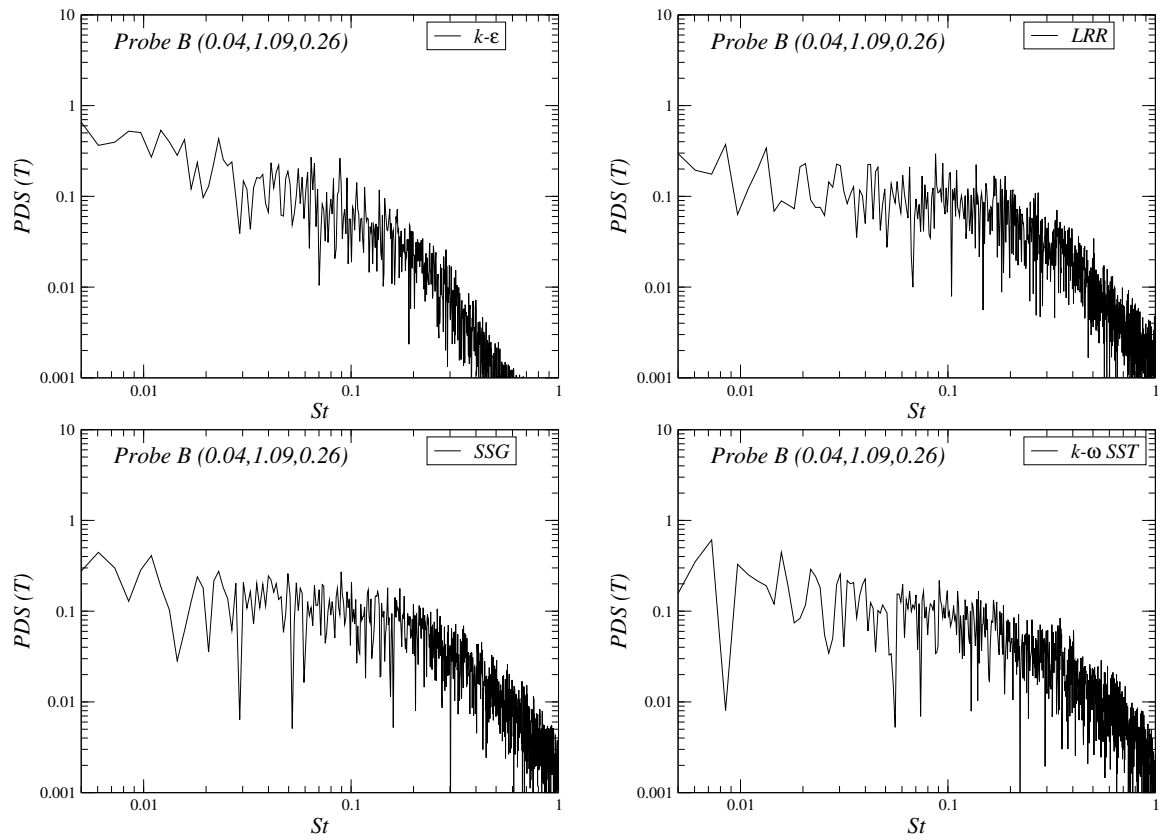


Figure 6.37: URANS results: Temporal power spectrum of temperature at the monitoring point B inside the 15° unstable stratified cavity.

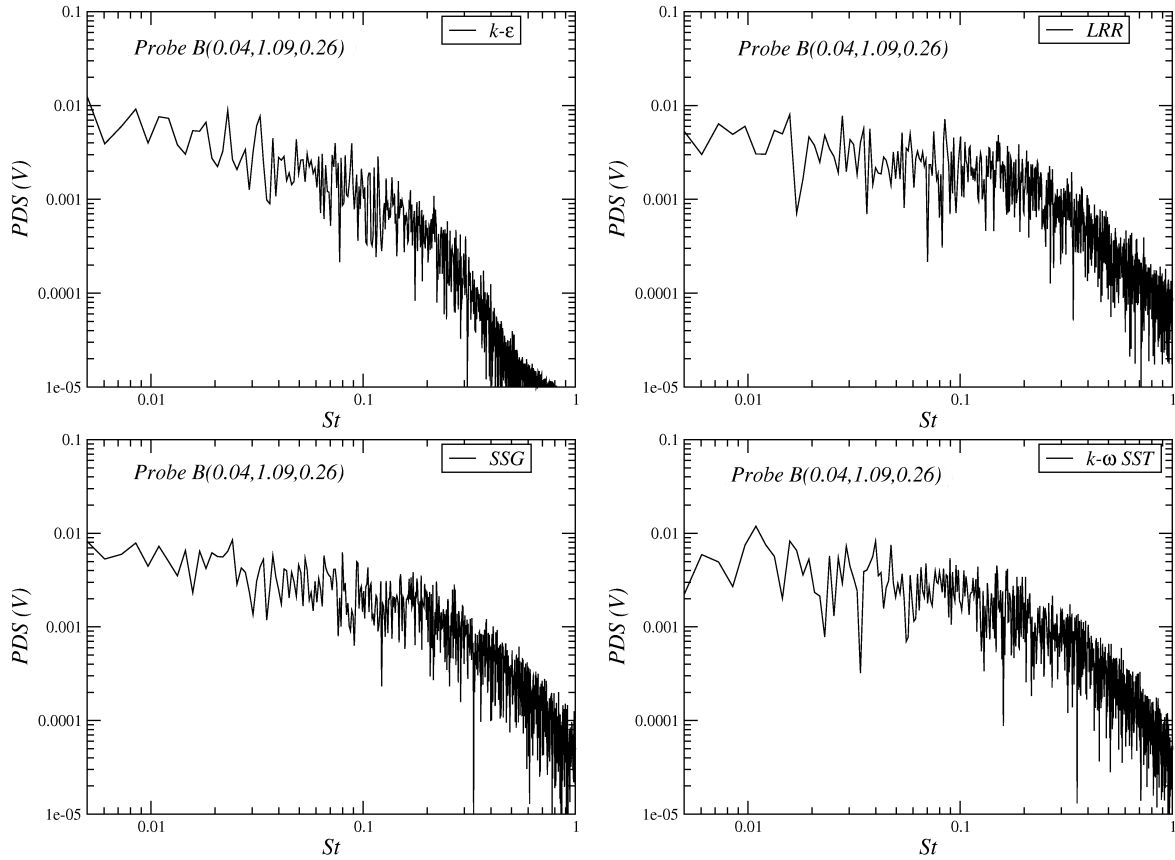


Figure 6.38: URANS results: Temporal power spectrum of V velocity at the monitoring point B inside the 15° unstable stratified cavity.

The corresponding power spectra predicted by the URANS models at Probe B location for temperature and wall-parallel velocity are shown in Figures 6.37 and 6.38, where it can be seen that they do broadly reproduce the range of dominant frequencies and their densities. These buoyancy-driven flows do not perhaps contain as wide a range of high frequency fluctuations as would be found in some forced convection flows, and thus the general characteristics of the spectra appear similar to the LES ones, although as would be expected the RANS schemes show a more rapid decay of spectral energy at higher frequencies, particularly in the case of the $k - \varepsilon$ model. Nevertheless, in reproducing the larger scale structures the RANS schemes are able to return very similar time-averaged flow features to the LES, as already seen in the results above.

Attention is now turned to local Nusselt number comparisons. Figures 6.39 and 6.40 present the variation of the time-averaged local Nusselt number along two longitudinal lines, over the hot and cold surfaces of the unstably stratified enclosure respectively. Once more, there is close agreement between the LES predictions and the available

experimental data, showing uniform levels over the length and width of both sides. This is consistent with the isothermal conditions observed in the temperature contour plots. The LES profiles also exhibit an oscillatory behaviour, consistent with the presence of vortex structures normal to the longitudinal direction. The experimental data are not sufficiently detailed to either confirm or contradict this. Among the unsteady RANS predictions, those of the high-Re $k - \varepsilon$ are consistently closer to the LES and experimental data, while LRR's second moment closure overestimates the overall heat transfer slightly near the top and bottom walls, maybe as a result of the turbulent heat fluxes being modelled through the eddy diffusivity approximation in *Code_Saturne* 2.0. The local Nusselt number distribution on the cold surface, Figure 6.40, shows a similar pattern.

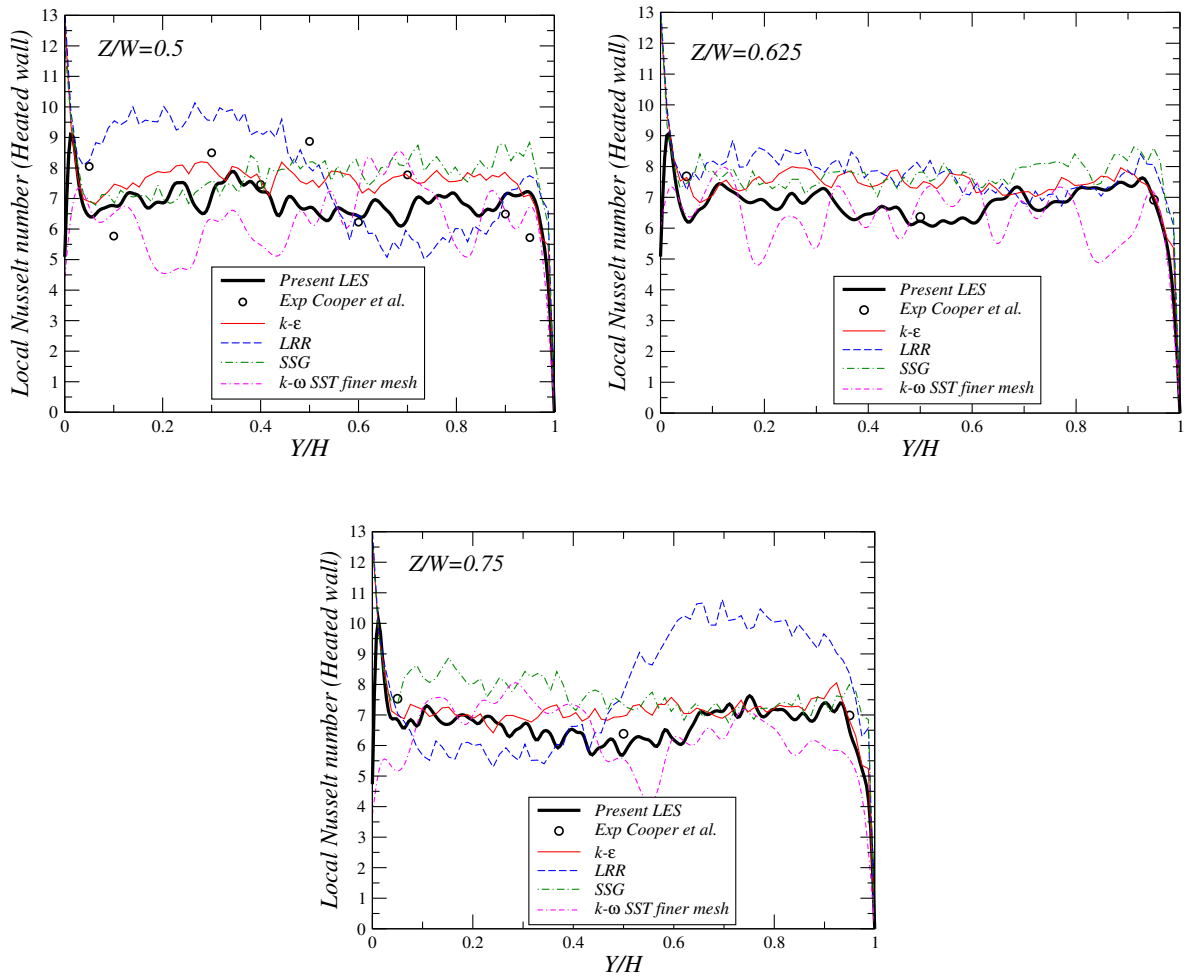


Figure 6.39: Profiles of time-averaged local Nusselt number at the spanwise locations $Z/W = 0.5, 0.625, 0.75$ along the heated wall of the 15° unstable cavity.

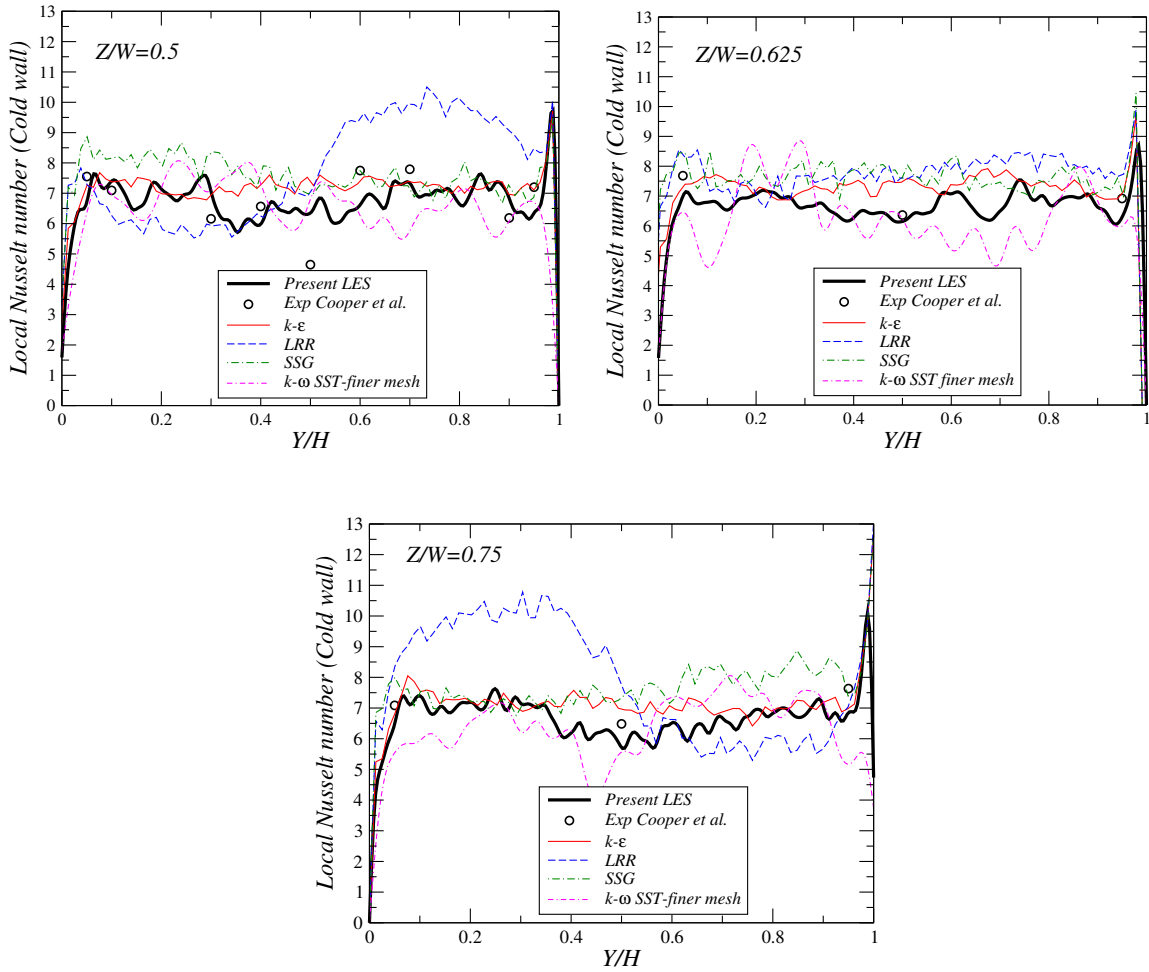


Figure 6.40: Profiles of time-averaged local Nusselt number at the spanwise locations $Z/W = 0.5, 0.625, 0.75$ along the cold wall of the 15° unstable cavity.

6.6 Concluding remarks

The flow within the unstably stratified cavity, inclined at 15° angle of inclination, has been deeply investigated using a well resolved LES and URANS techniques. The unstable stratification causes the formation of four longitudinal vortices which extend over the entire length of the cavity and four longitudinal cells in the spanwise direction. These vortices lead to strong mixing, which results in practically isothermal conditions over most of the cavity and in an “isotropic and homogeneous turbulence” field. Because of the near isothermal conditions, the time-averaged buoyancy-induced wall-parallel motion is substantially lower than what is found in the vertical case. Another consequence of the isothermal conditions and the homogeneous turbulence field is the uniform Nusselt number over the hot and cold sides, both in the longitudinal and

spanwise directions.

Comparisons with URANS predictions show that all models tested, the high-Re $k - \varepsilon$, the LRR and SSG second-moment closures and the low-Re $k - \omega$ SST are able to reproduce the unsteady three-dimensional structures, and thus capture the broad features of the flow. The low-Re $k - \omega$ SST model, however, needs substantially finer meshes than the three high-Re models.

As far as the local Nusselt number predictions are concerned, somewhat surprisingly, the profiles returned by the high-Re $k - \varepsilon$ model are consistently close to those of the LES predictions, while the local Nu profiles of the LRR and the SST scheme show some deviations. One possible explanation for the poorer second-moment predictions is the use of the effective diffusivity approximation for the turbulent heat fluxes within *Code_Saturne* 2.0, even when the Reynolds stresses are modelled through second-moment closures. It is feasible that improvements could be achieved by using more advanced representations for the heat fluxes, possibly even by simply moving to the generalised gradient diffusion hypothesis (GGDH) formulation or even better by solving the transport equation of $\overline{\theta^2}$ by using of algebraic schemes like the three and four extended algebraic models, $k - \varepsilon - \overline{\theta^2}$ and $k - \varepsilon - \overline{\theta^2} - \varepsilon_\theta$, which were proposed by Hanjalić [36]. The use of EB-RSM model of Manceau and Hanjalić [65] and EB-AFM of Manceau [64] can be advantageous for computing turbulent heat fluxes when buoyant flow are involved.

Chapter 7

Buoyancy-Driven Flow Within the 3-D Tilted Enclosure Under Stable Stratification

7.1 Introduction

After a detailed investigation of the flow inside the 15° unstably stratified cavity, presented in the previous chapter, computations of flow within a 15° stably stratified enclosure (heated from the upper side), Figure 7.1, are presented in this chapter. The dimensions of the cavity and aspect ratio, together with boundary conditions, are similar to the unstably stratified enclosure. The only difference is that the temperature difference between the differentially heated walls, ΔT , takes the value of 34°C , leading to a slightly higher Rayleigh number of 1.5×10^6 .

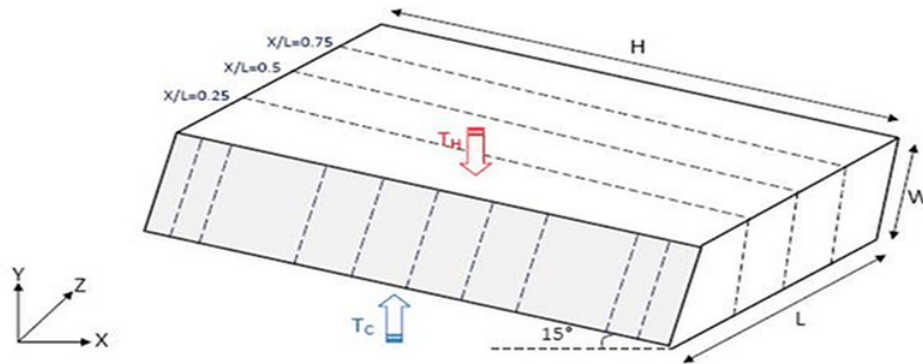


Figure 7.1: Geometry of 3-D cavity inclined at 15° to horizontal (stable stratification). Location of plot lines are indicated.

7.2 Computational mesh and numerical methods

The computations of flow within the stably stratified tilted enclosure have also been carried out using Code_*Saturne* [8]. The same numerical steps as for the unstable stratified enclosure are followed. In order to draw a comparison between unstable and stable stratifications in the present thesis, the same computational mesh, spatial and time numerical schemes are used, and the boundary conditions are also similar except that the stably stratified cavity is heated from the upper side.

The flow physics within the stably stratified cavity are different from those inside the unstably stratified one, and therefore the CPU time consumed for the stably stratified case is slightly different. The LES simulation required 30000 time steps, and approximately 60 hours in 24 Cores, to reach a fully developed turbulent flow state, and at least a further 30000 time steps for statistical averaging of the flow field. The URANS computations required around 25000 time steps and approximately 2 hours in 24 Cores.

7.3 Assessment of LES resolution

Through an analysis similar to that described for the unstably stratified case in section 6.3 the ratio of the grid spacing Δ to the Kolmogorov length scale for the stably stratified case is estimated to be around 0.5 to 10 (approximately similar to the unstable case), suggesting a good LES resolution of the dissipative scales.

The ratio of the sub-grid-scale (SGS) turbulent viscosity to the turbulent viscosity of the resolved scales, along the three mid-section lines within the stably stratified cavity, are plotted and shown in Figure 7.2. This ratio is slightly higher than for the unstable case (Chapter 6) but still lower than 10%, implying that a considerable part of the dissipative scales here is also well resolved.

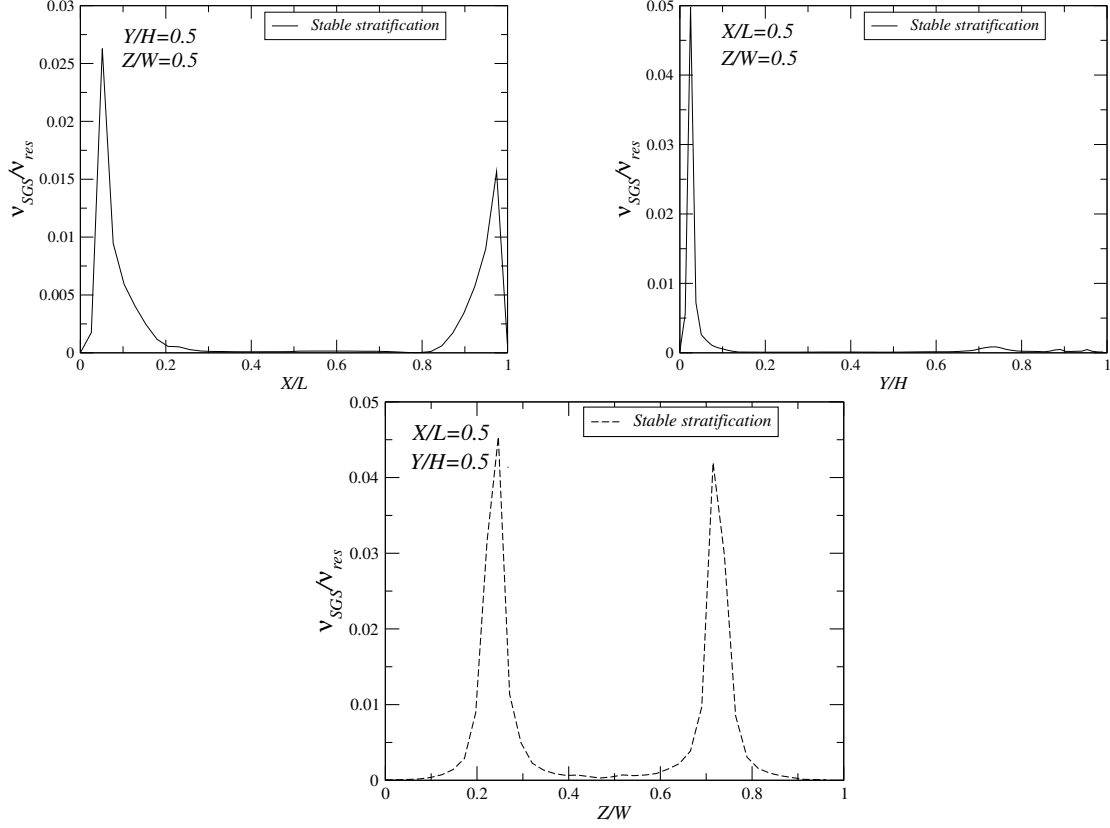


Figure 7.2: Profiles of the ratio of the SGS viscosity to the resolved turbulent viscosity at three middle planes (X/L ($Y/H = 0$ and $Z/W = 0$), Y/H ($X/L = 0$ and $Z/W = 0$), Z/W ($X/L = 0$ and $Y/H = 0$)) within the stably stratified cavity.

7.4 Qualitative results

Figure 7.3 shows instantaneous dimensionless temperature contours in the stably stratified tilted enclosure. The temperature shows a gradual change across the cavity from the cold to the hot side. Near the lower end wall there is an accumulation of cold fluid, and near the top end wall an accumulation of hot fluid. The instantaneous temperature contours suggest that there is a large longitudinal recirculation cell, which transfers fluid along the top wall from the lower end wall to the upper end wall, while along the cold wall the fluid travels in the opposite direction. The time-averaged contours of temperature, plotted at three longitudinal and spanwise locations, illustrated in Figure 7.5, confirm this and agree with the experimental findings of Cooper et al. [25].

The Q -criterion (Equation (6.2)), in Figure 7.4, shows larger and fewer vortices inside the stably stratified enclosure comparing with unstably stratified test case. These 3-D structures are concentrated near the top wall where the hot fluid is accumulated

and near the opposite bottom wall where the cold fluid is accumulated. The interaction of the fluid flow with the insulated side walls causes the rotation of these large vortex shedding and the formation of two large circular cells in the spanwise direction.

The time averaged contours of the three components of velocity (U , V , W) at three longitudinal and spanwise cross sections are illustrated in Figures 7.6 to 7.8. The U and W velocity contours along the spanwise sections (right hand side of Figures 7.6 and 7.8) show the presence of two large longitudinal vortices at each spanwise section. These observations are confirmed by the vector plots of Figure 7.9, and are also consistent with the findings of the Cooper et al. experimental study [25]. The contours of the wall-parallel velocity (V) (right hand side of Figure 7.7) show that in the stable stratification situation, two strong longitudinal cells appear, which transport fluid down the inclined wall along the middle of the cavity and back up the slope, along the side walls. These observations are also in accord with the findings of the Cooper et al. experimental investigation [25].

On the other hand, the contour plots of the three components of the time-averaged dimensionless velocity (U , V , W) along longitudinal planes (left hand side of Figures 7.6, 7.7 and 7.8) show that the wall-normal velocity component (U) implies that along the centre longitudinal plane the motion is predominantly from the hot to the cold side, while within the two longitudinal sections between the centre section and the side walls the wall-normal motion is weak. By contrast, the spanwise velocity component (W) contours show that across the two side-sections, over the upper half the spanwise motion is towards the middle and over the lower half towards the sides. Both the wall-normal and spanwise component contours confirm the presence of two spanwise vortices over the entire length of the cavity. The contours of the wall-parallel velocity component (V), with motion towards the lower end wall along the centre and towards the upper end wall along the sides, also confirm the presence of two longitudinal cells.

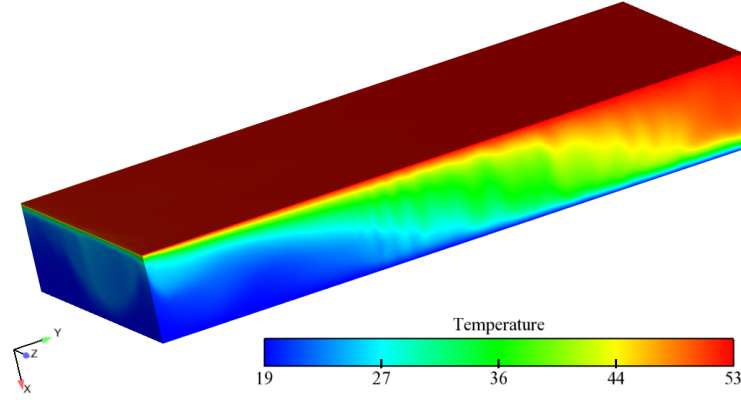


Figure 7.3: LES results: instantaneous temperature contours inside the stably stratified cavity.

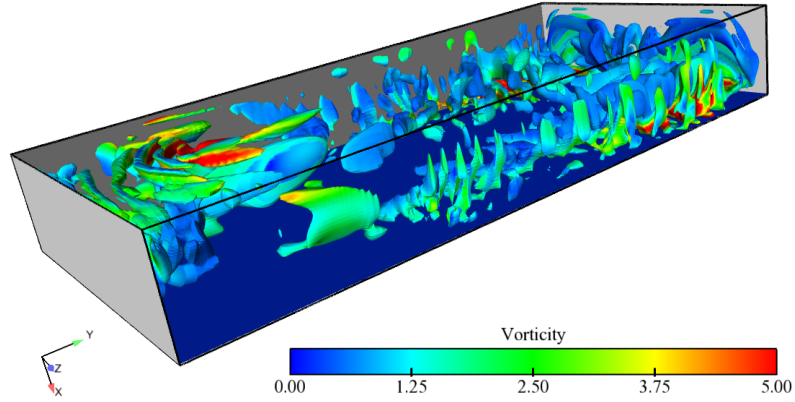


Figure 7.4: LES results: Iso-surfaces of Q-criteria coloured by vorticity inside the stably stratified cavity.

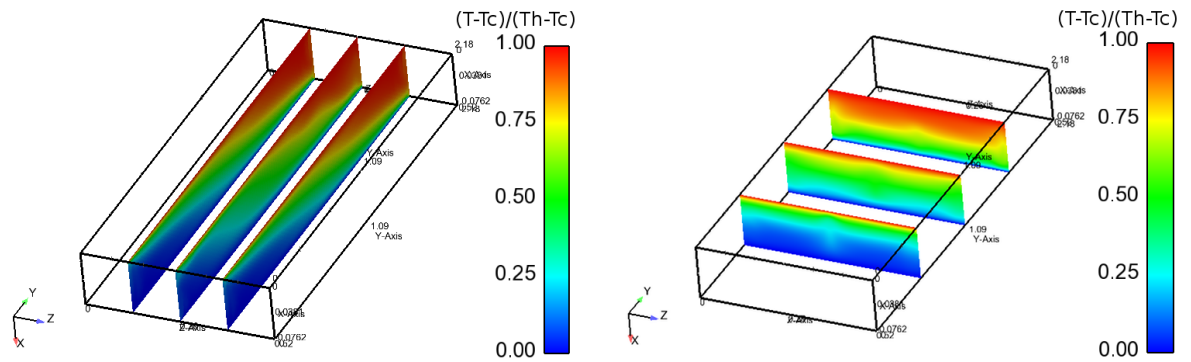


Figure 7.5: LES results: time averaged temperature contours at three longitudinal and spanwise sections of the stably stratified cavity.

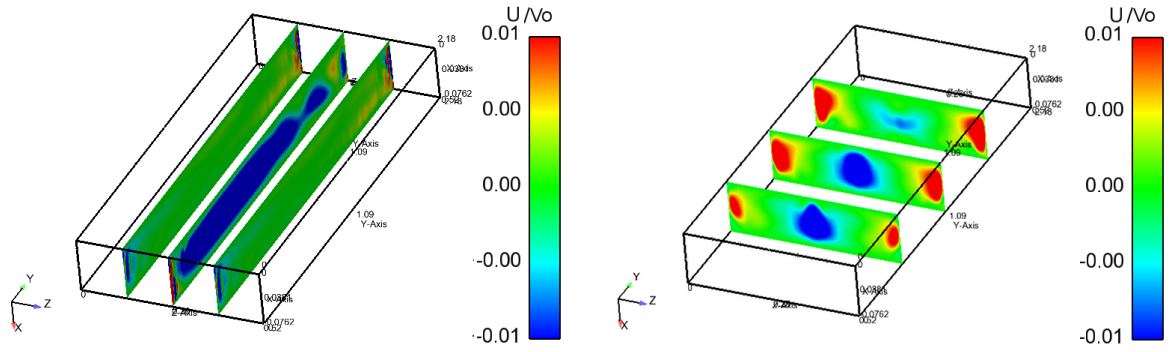


Figure 7.6: LES results: time averaged wall-normal U velocity contours at three longitudinal and spanwise sections of the stably stratified cavity.

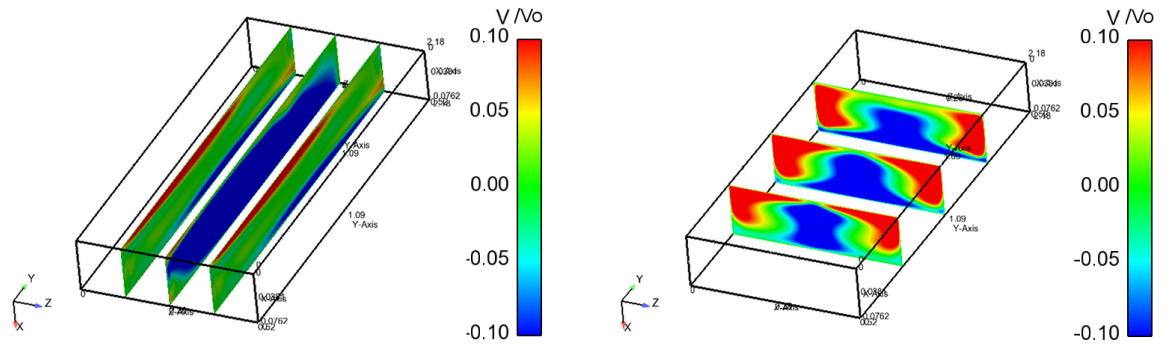


Figure 7.7: LES results: time averaged wall-parallel V velocity contours at three longitudinal and spanwise sections of the stably stratified cavity.

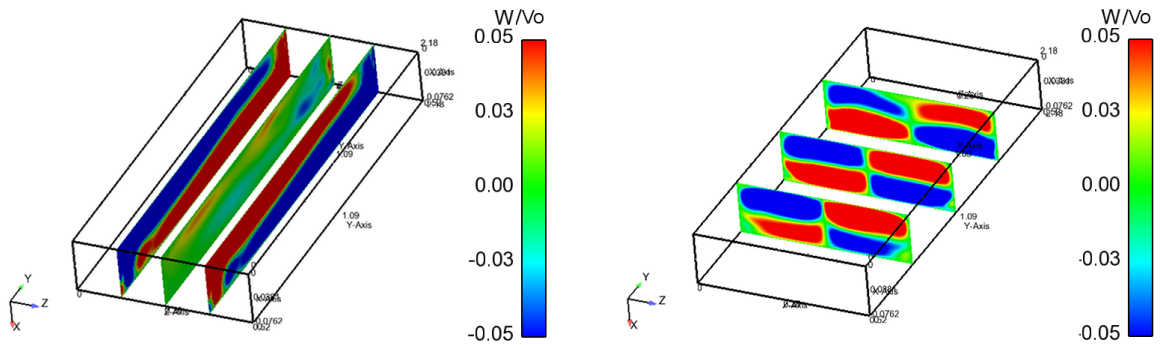


Figure 7.8: LES results: time averaged spanwise (W) velocity contours at three longitudinal and spanwise sections of the stably stratified cavity.

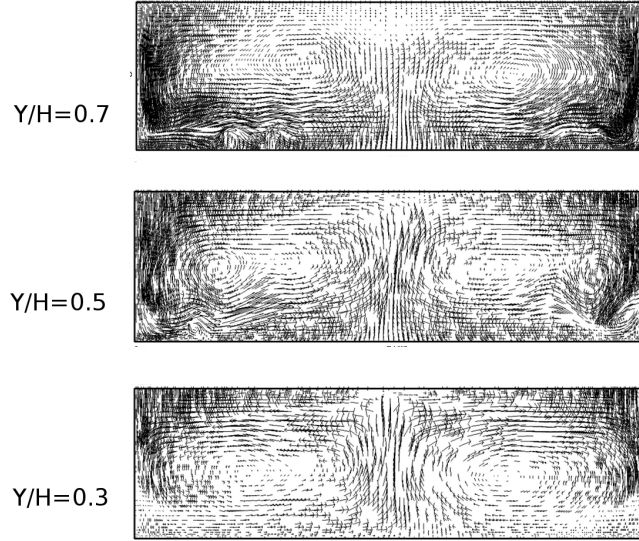


Figure 7.9: LES results: vector plots of velocity magnitude at three spanwise sections of the stably stratified enclosure.

7.5 Quantitative results

After the above qualitative study of the flow within the stably stratified cavity, the quantitative results are presented here. LES results of the dimensionless time-averaged temperature, normalised by the temperature difference $(T_h - T_c)$, are compared with the experimental data of Cooper et al. [25] within two spanwise planes ($Z/W = 0.5$ and $Z/W = 0.75$), at four different longitudinal traverse lines ($Y/H = 0.05, 0.3, 0.5$ and 0.95), and shown in Figure 7.10. For the stable case, in which the mixing is not as strong as in the unstable case, there is a more gradual change in temperature across the cavity and the longitudinal cell transports the hot fluid to the upper and the cooler fluid to the lower end of the cavity. LES thermal predictions are close to the experimental data with some deviations noticeable at the near wall regions. This is probably caused by minor heat losses in the experimental model.

Figure 7.11 illustrates time-averaged profiles of the dimensionless temperature, also normalised by $(T_h - T_c)$, obtained from the unsteady RANS models, compared with the present LES and experimental data. The low-Reynolds number SST model has not been used because, as mentioned earlier in Chapter 6, it requires a much finer grid, making it substantially more expensive. The URANS models used here, including the LRR and $k - \varepsilon$, show close agreement with the present LES data, however, discrepancies

between URANS and the experimental profiles are noticed near the differentially heated walls due to same reasons mentioned above for the LES predictions.

Time-averaged dimensionless profiles of the U and V components of velocity, normalised by the buoyant velocity V_0 , obtained from LES for the stably stratified test case are presented in Figures 7.12 and 7.13, respectively. The wall-normal U velocity shows a low negative peak in the central region, which is consistent with the presence of the two large streamwise vortices identified by the contour plots discussed earlier. In common with previous comparisons there is close agreement between the LES and measured profiles. Wall-parallel V velocity profiles for the stable case, Figure 7.13, on the other hand, show that, as also indicated by the contour plots in Figure 7.7, the wall-parallel velocity is now considerably stronger with a downward component. The LES and experimental profiles are in close agreement.

The corresponding results of U and V velocity components obtained from URANS predictions, shown in Figure 7.14, reproduce qualitatively the same behaviour as LES and the measured data, but none of the models results in profiles which are in close quantitative agreement with the LES/experimental ones. All the URANS profiles show considerably weaker wall-parallel motion and a nearly anti-symmetric variation across the cavity. This leads to the conclusion that the RANS models tested here have failed to reproduce the three-dimensional features shown in the LES predictions and the experimental data. This is in contrast to the findings of Omranian [72], who demonstrated that the LRR second-moment closure, used with a more advanced wall function to model the viscous layer, did reproduce the three-dimensional flow structures, and maybe points to the benefits that could be obtained by using a more accurate modelling of the near-wall layer in such a stably-stratified case. The work of Dehoux et al. [31] using EB-RSM with GGDH showed good predictions of heat fluxes for the stably stratified test cases. The use EB-RSM model of Manceau and Hanjalić [65] or EB-AFM model of Manceau [64] can be very promising to predict the 3-D flow features in the 15° stably stratified enclosure.

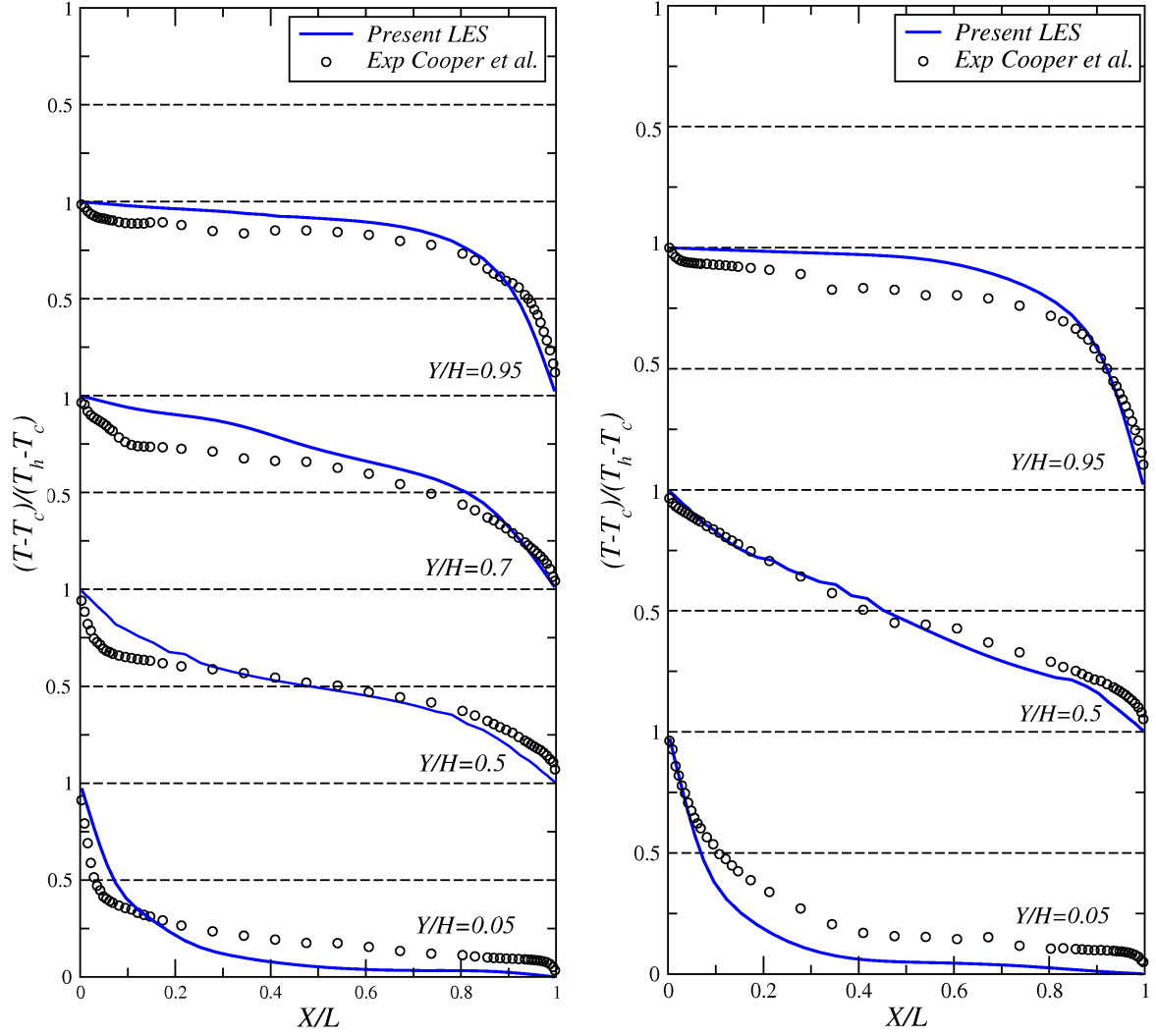


Figure 7.10: LES results: time-averaged temperature profiles at four longitudinal locations and at two spanwise sections inside the stably stratified enclosure. Left: $Z/W = 0.5$, right: $Z/W = 0.75$.

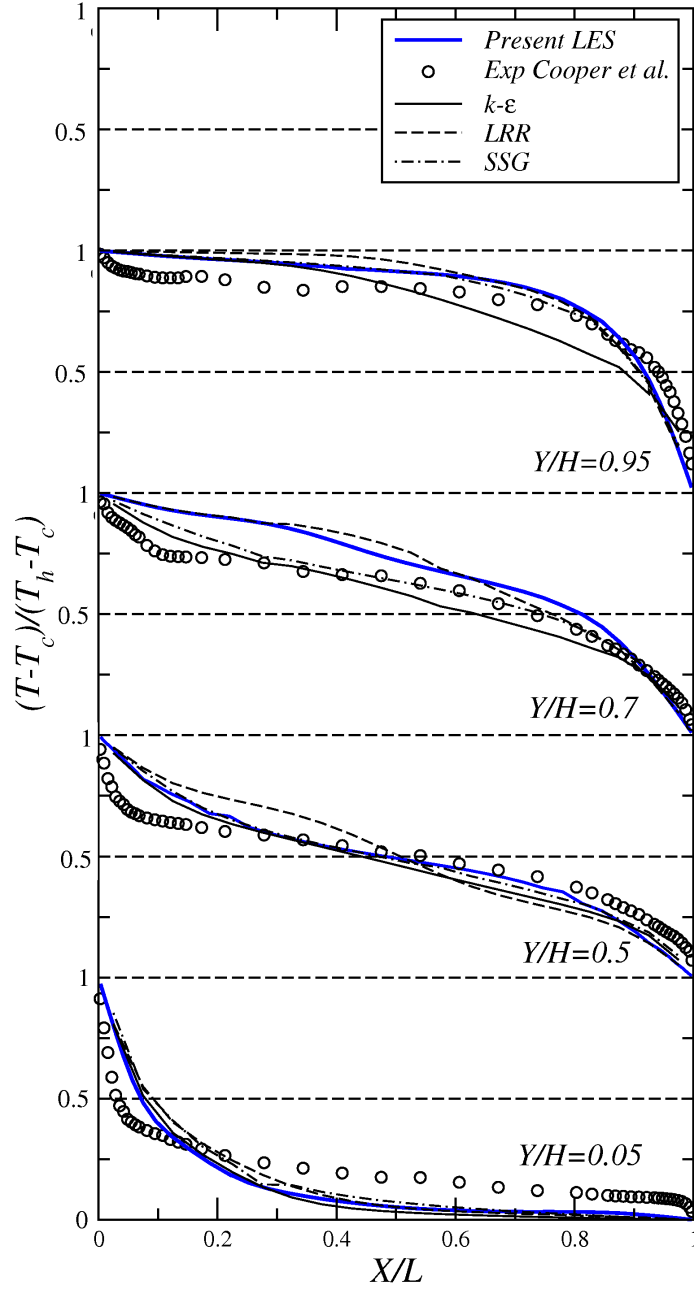


Figure 7.11: URANS results: time-averaged temperature profiles at four longitudinal locations on the central spanwise section ($Z/W = 0.5$) inside the stably stratified enclosure.

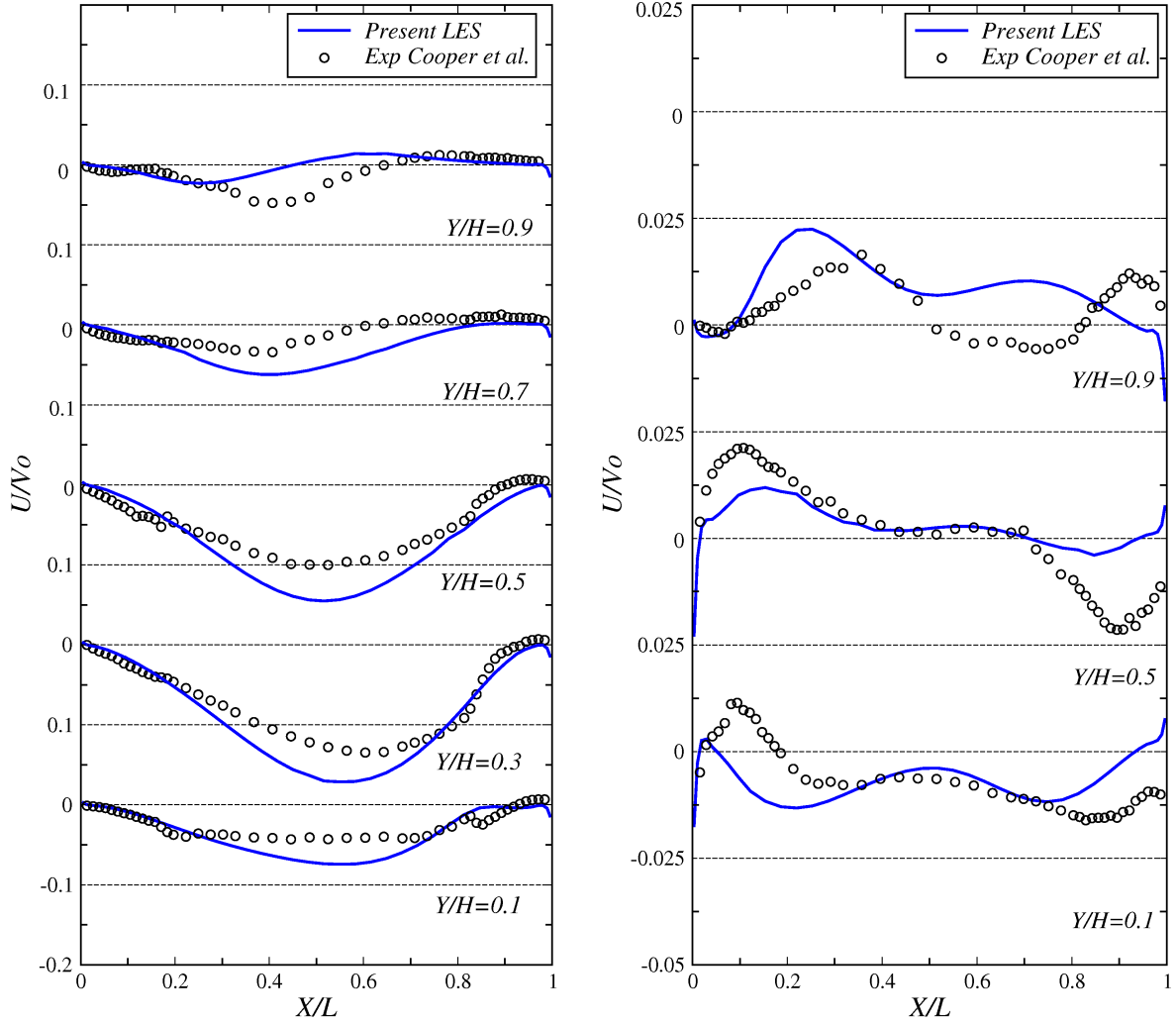


Figure 7.12: LES results: time-averaged U velocity profiles at four longitudinal locations and at two spanwise sections inside the stably stratified enclosure. Left: $Z/W = 0.5$, right: $Z/W = 0.75$.

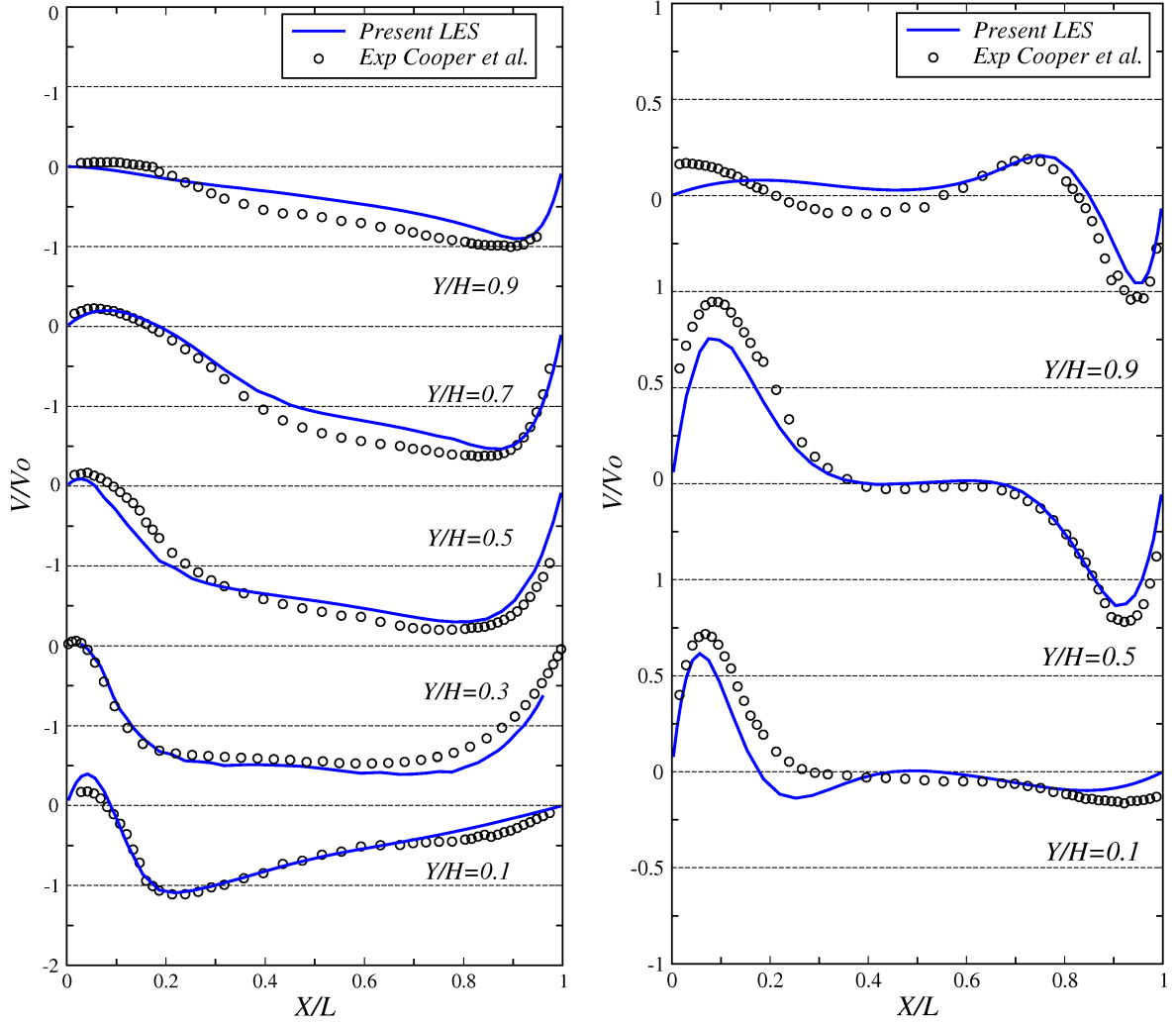


Figure 7.13: LES results: time-averaged V velocity profiles at four longitudinal locations and at two spanwise sections inside the stably stratified enclosure. Left: $Z/W = 0.5$, right: $Z/W = 0.75$.

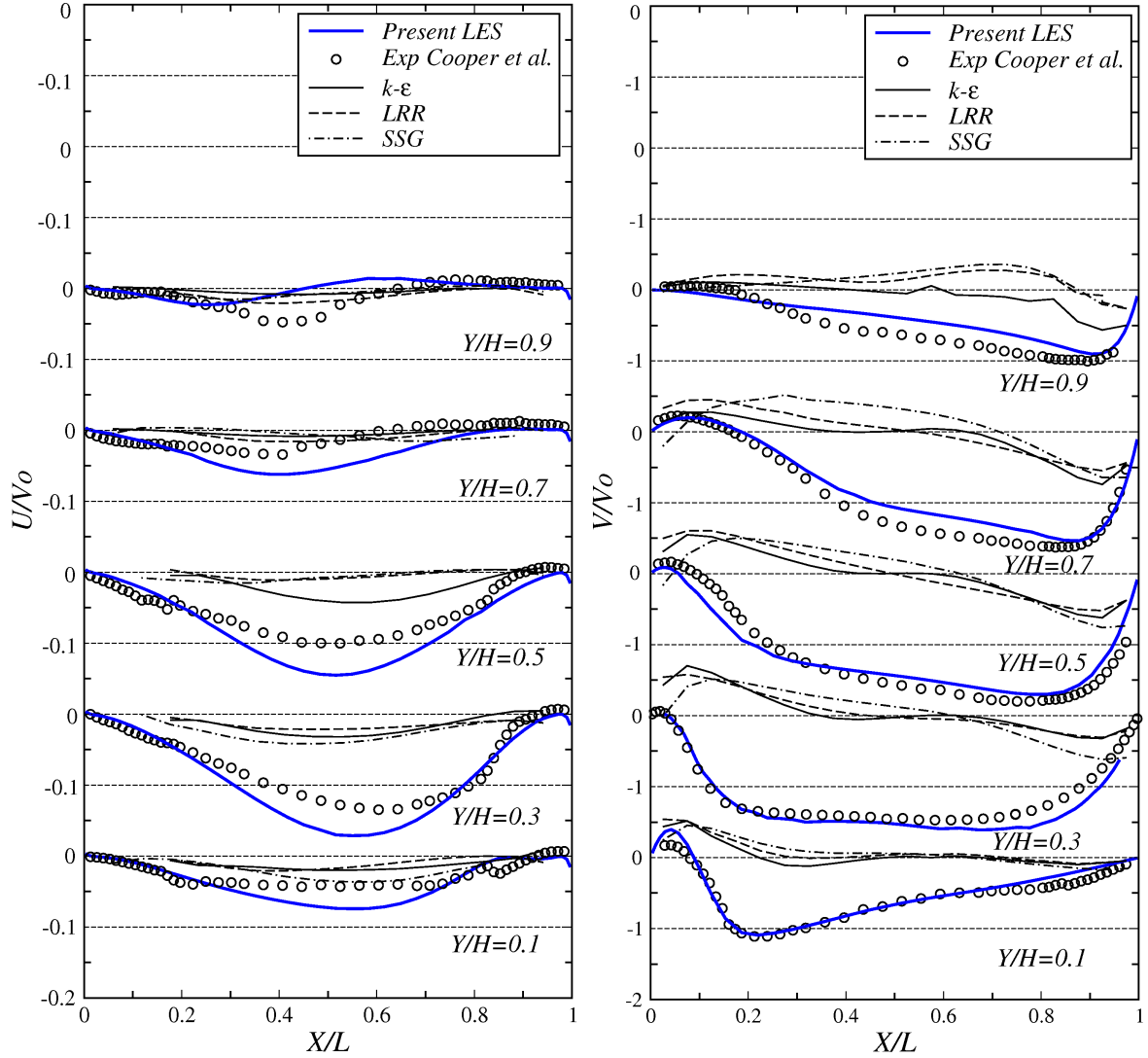


Figure 7.14: URANS results: time-averaged velocity profiles at five longitudinal locations and at the central spanwise section ($Z/W = 0.5$) inside the stably stratified enclosure. Left: U velocity, right V velocity.

The rms turbulence fluctuations and shear stresses inside the stably stratified enclosure are illustrated in Figures 7.15 to 7.19. The dynamic field statistics, Figures 7.15 to 7.18 and the temperature variance, Figure 7.19, are lower than those in the unstable case, discussed in the previous chapter, and also have a more non-uniform distribution. The former is due to the absence of mixing through small-scale vortices and the latter is due to the stabilising effect of the temperature gradient. Some deviations now do appear between the LES and the available experimental profiles, though this might be simply that they are more noticeable because of the lower magnitudes involved. For the turbulent heat fluxes only the wall-parallel component $\overline{v't'}$ is presented, Figure 7.20,

because the wall normal and spanwise components are two orders of magnitude lower and hence practically zero. The $\overline{v't'}$ component of the turbulent heat flux shows large variations across the cavity, from the hot to the cold walls, and also appears to be high near the lower end and to reduce to practically zero near the upper end. The former is a consequence of the non-uniform temperature and flow fields which develop in the stable case, as illustrated in the contour plots discussed earlier, while the latter may be caused by the fact that along the longitudinal mid-plane, there is flow impingement at the lower end. Again in most cases, especially at the $Y/H = 0.1$ and $Y/H = 0.5$ locations, there is reasonable qualitative agreement between the unsteady RANS profiles and the LES/experimental ones, but with significant quantitative deviations which are larger than for the unstably stratified case.

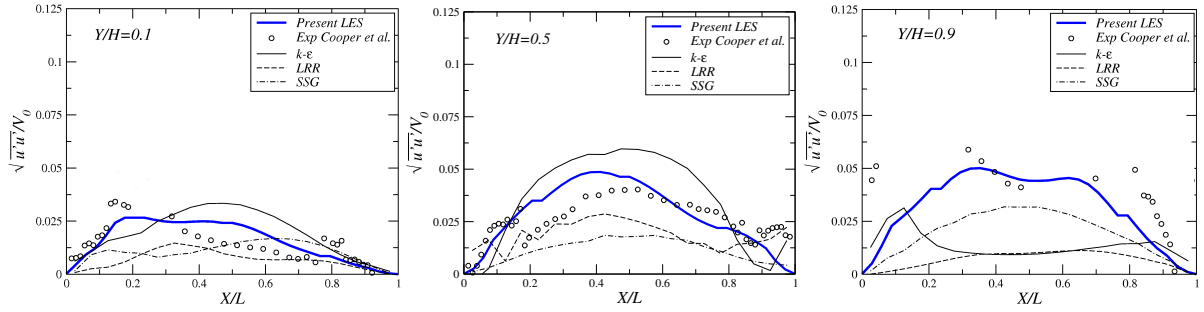


Figure 7.15: Time-averaged rms wall-normal velocity $\sqrt{u'u'}$ at three longitudinal locations inside the 15° stably stratified cavity.

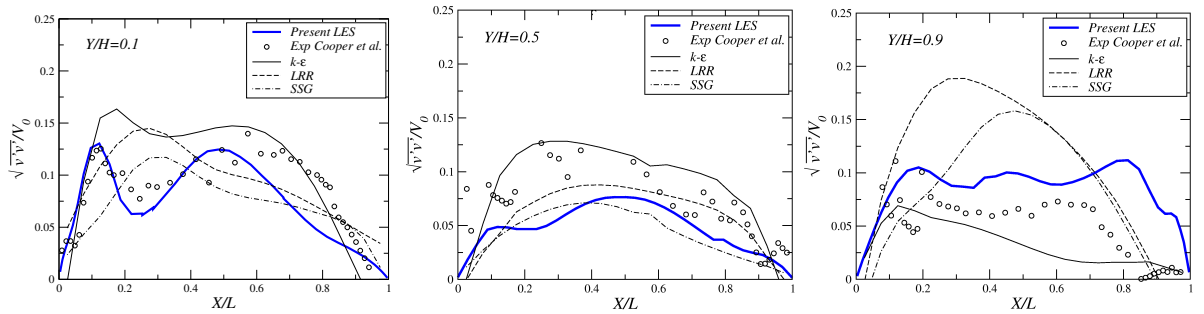


Figure 7.16: Time-averaged rms wall-parallel velocity $\sqrt{v'v'}$ at three longitudinal locations inside the 15° stably stratified cavity.

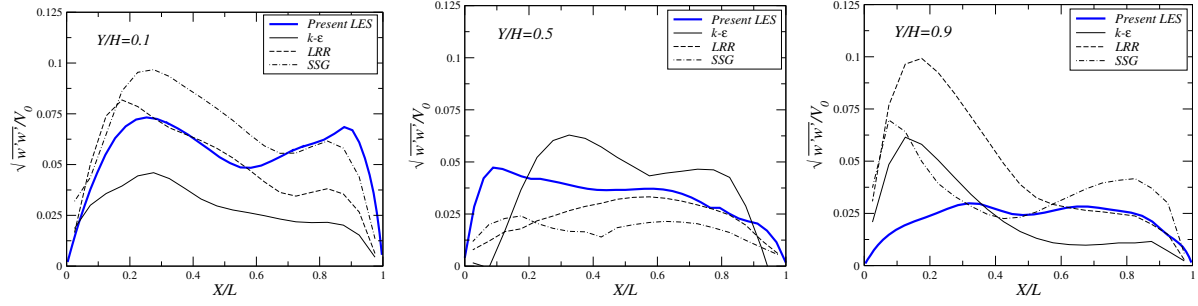


Figure 7.17: Time-averaged rms spanwise velocity $\sqrt{w'w'}$ at three longitudinal locations inside the 15° stably stratified cavity.

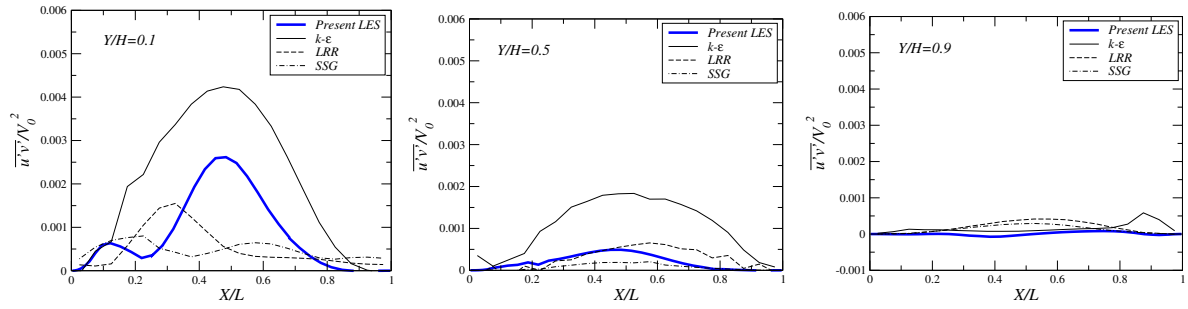


Figure 7.18: Time-averaged shear stress $\overline{u'v'}$ at three longitudinal locations inside the 15° stably stratified cavity.

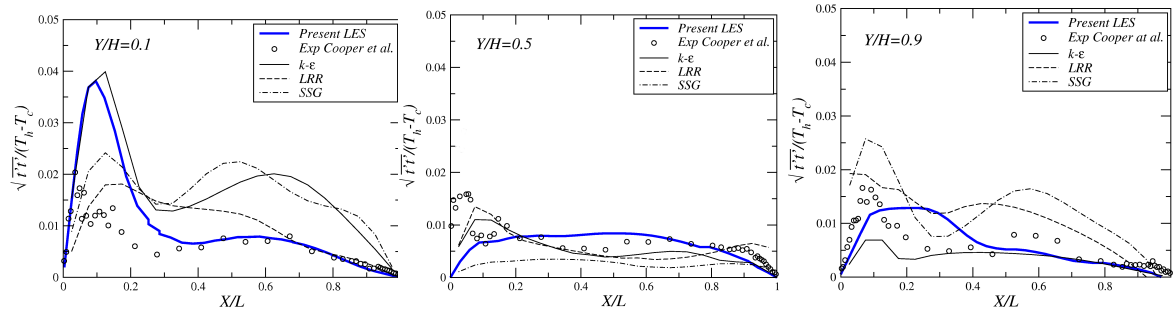


Figure 7.19: Time-averaged rms temperature $\sqrt{t't'}$ at three longitudinal locations inside the 15° stably stratified cavity.

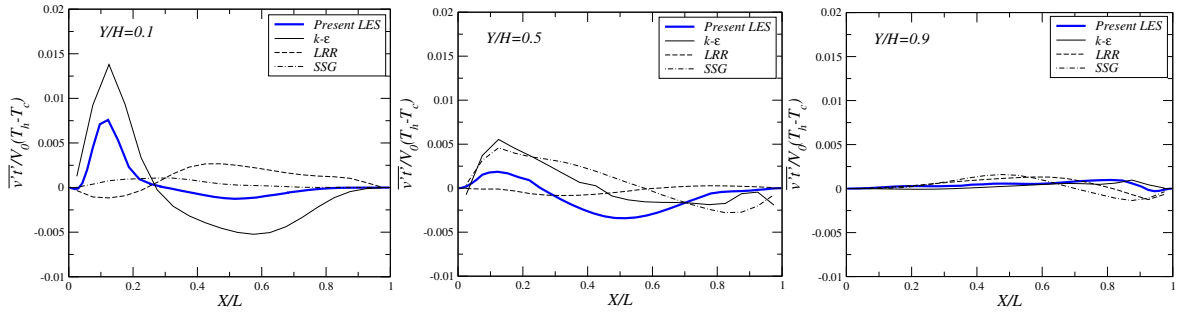


Figure 7.20: Time-averaged rms wall-parallel heat flux $\overline{v't'}$ at three longitudinal locations inside the 15° stably stratified cavity.

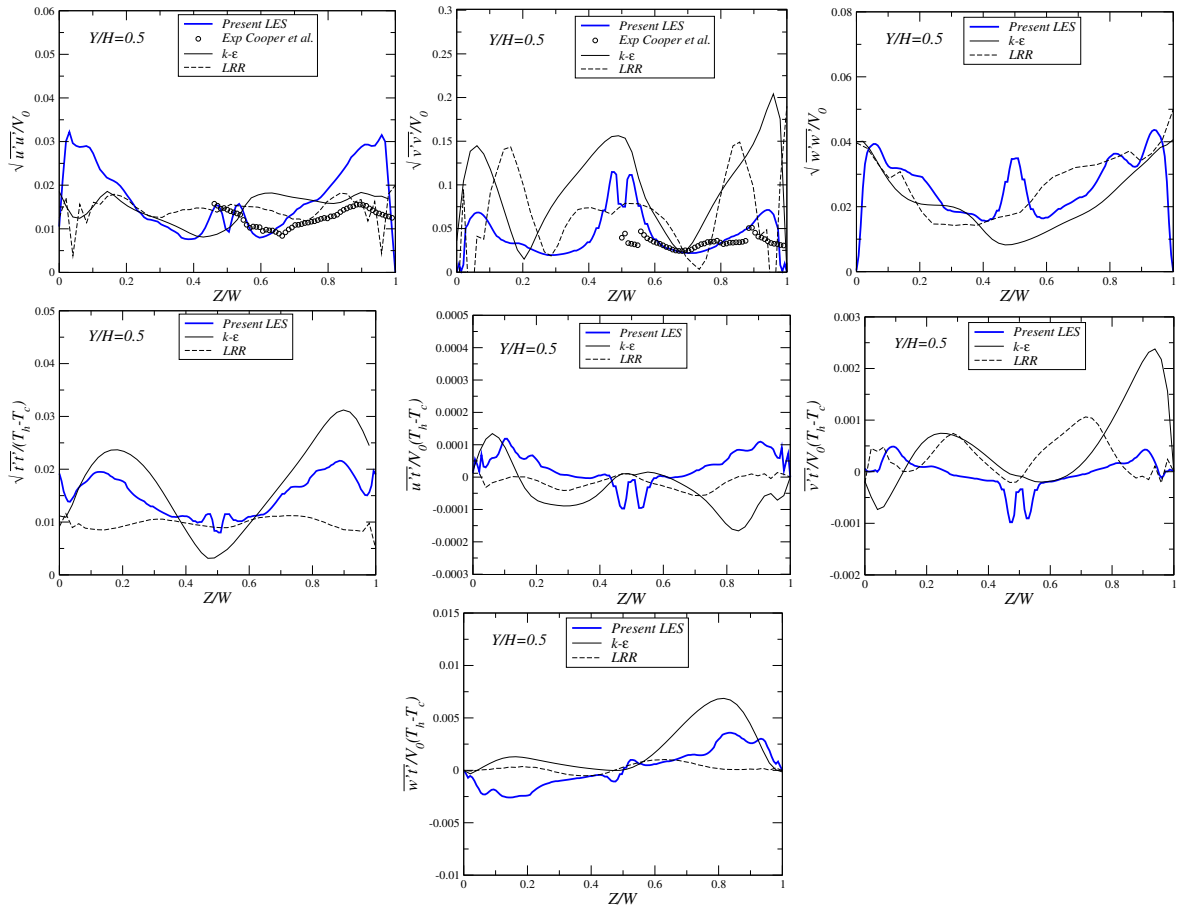


Figure 7.21: Time-averaged Reynolds stresses and heat fluxes along the spanwise cross-section, at the longitudinal central location ($Y/H = 0.5$) of the 15° stably stratified cavity.

The corresponding rms profiles and heat fluxes along the spanwise middle section ($Y/H = 0.5$) are presented in Figure 7.21. The LES data, which is in close agreement

with the available measured data, show a symmetry in the spanwise direction because of the presence of two longitudinal large circular rolls along the width of the cavity. None of the RANS models appears to display a distinctive predictive advantage. The common factor among the URANS models tested here is the simple eddy diffusivity model to represent the turbulent heat flux vector, which is unlikely to fully capture all its components in such a flow, and hence may lead to some of the deviations noted from the LES and measured data.

Profiles of the U and V velocity components at three longitudinal locations and at the middle spanwise cross-section within the stably stratified cavity obtained from both LES and URANS are also presented here in Figure 7.22. Comparison with the Cooper et al. [25] data show that the LES data agree with the measurements on the fact that there are two large circular rolls over the spanwise section, which is also qualitatively illustrated in Figure 7.9. RANS models generally show close agreement with LES/experiment data.

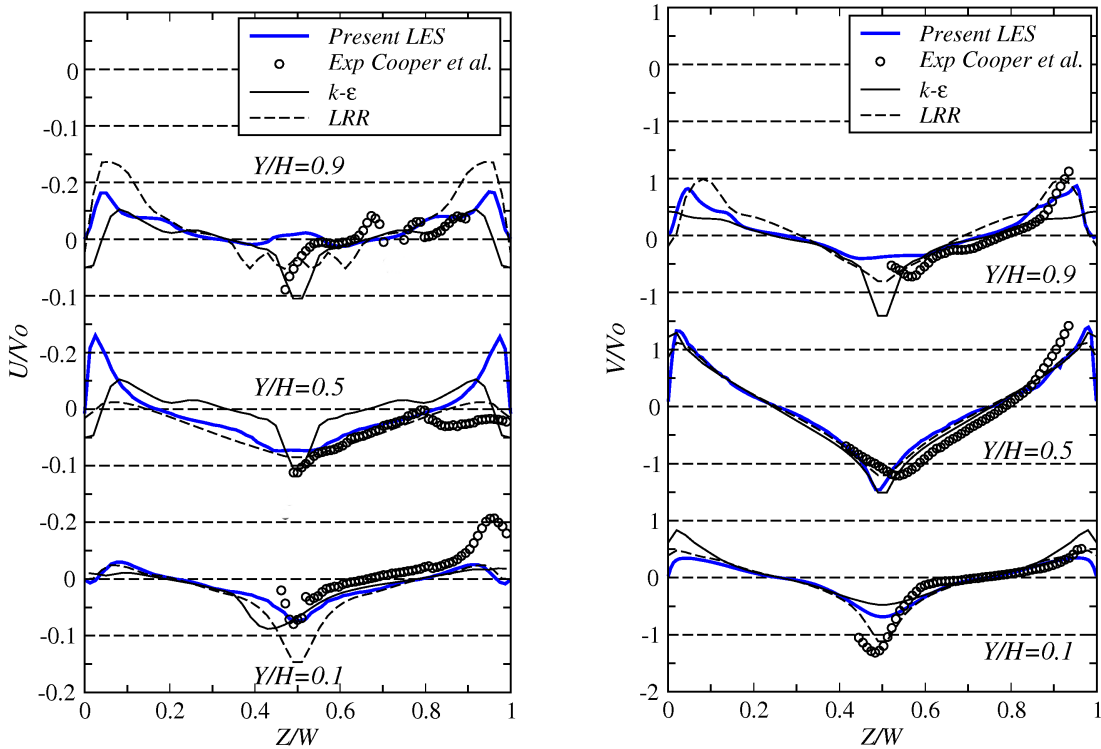


Figure 7.22: Time-averaged velocity profiles along the spanwise cross-section, at three longitudinal traverses inside the stably stratified enclosure. Left: U velocity, right: V velocity.

The temporal power spectrum of temperature and the three components of velocity within the stably stratified cavity, at the same two points A and B used when examining the unstable case, are presented in Figures 7.23 to 7.26. There are noticeable differences in the spectral variation for the different velocity components and also at different locations, with both the maximum energy levels and the frequency range over which the spectral energy remains constant changing between points A and B . The spanwise velocity component also shows a more rapid decay of spectral energy at higher frequencies than the other components. In comparison with the unstable test case, discussed earlier in Chapter 6, LES data, in accord with the measurements, show that there is an attenuation in energy levels (around 0.005) and also a reduction in the size of the frequency range over which the spectral energy remains constant. These differences are consistent with the presence of smaller scale vortices in the unstable case, which increase turbulence levels and also make the turbulence more isotropic and homogeneous.

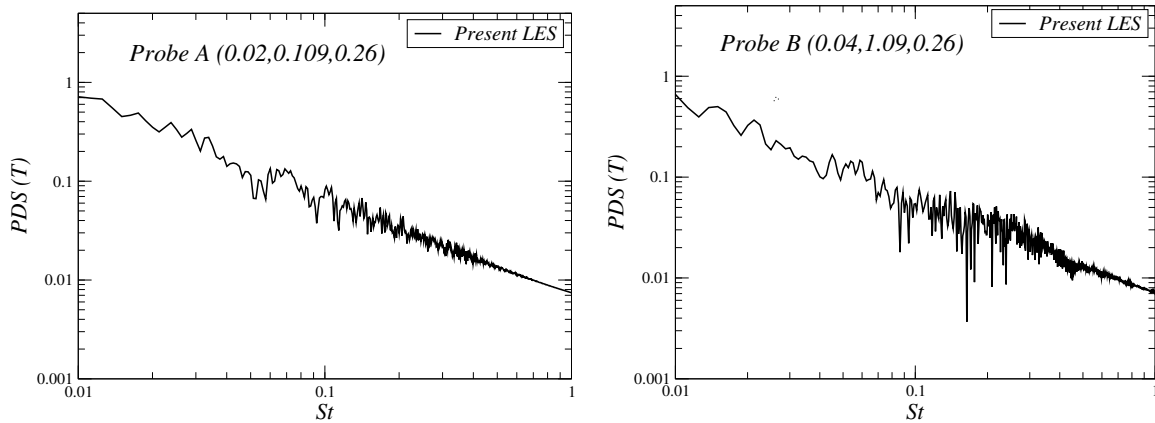


Figure 7.23: LES results: Temporal power spectrum of Temperature at the monitoring points A and B inside the 15° stable stratified cavity.

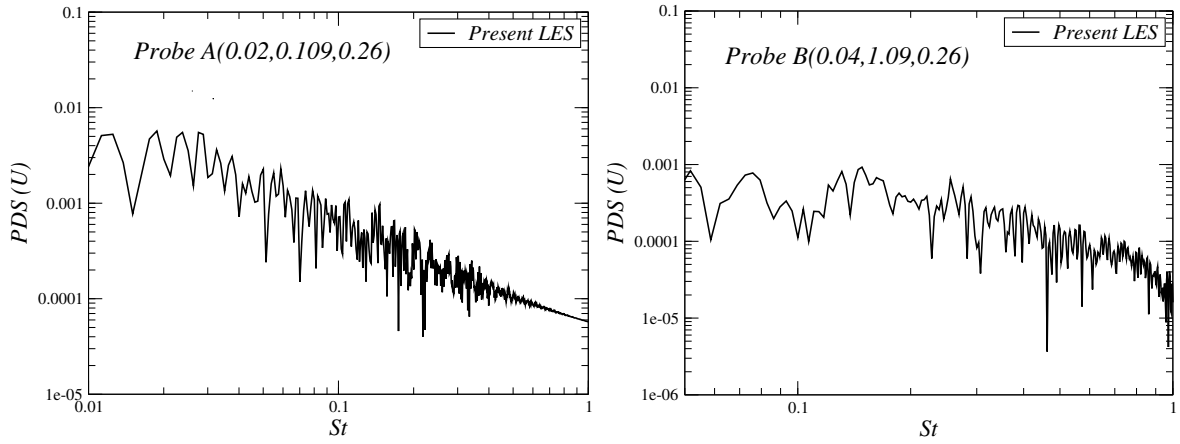


Figure 7.24: LES results: Temporal power spectrum of U velocity at the monitoring points A and B inside the 15° stable stratified cavity.

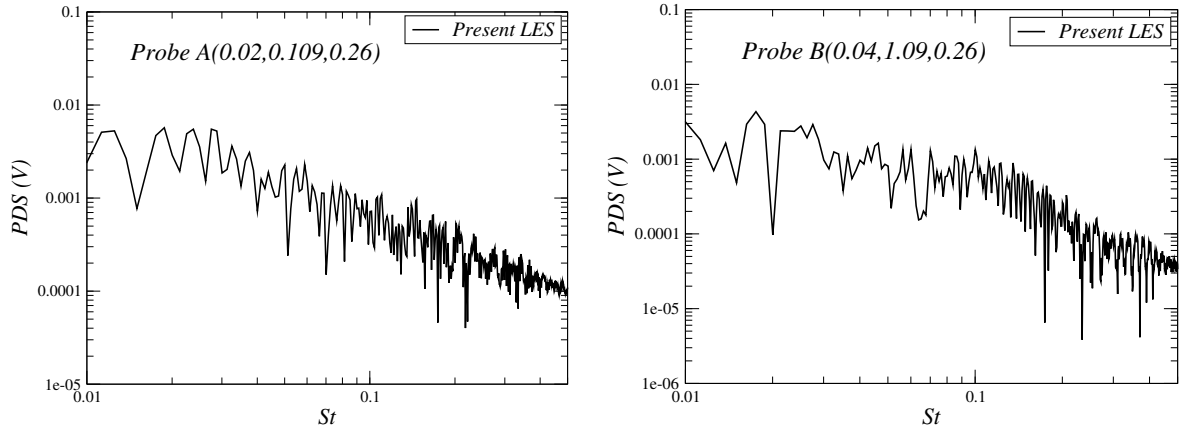


Figure 7.25: LES results: Temporal power spectrum of V velocity at the monitoring points A and B inside the 15° stable stratified cavity.

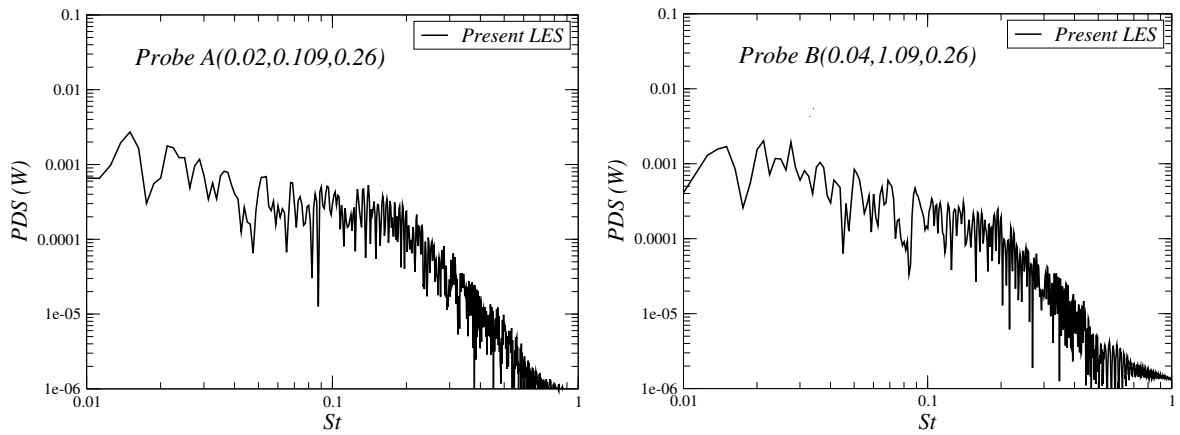


Figure 7.26: LES results: Temporal power spectrum of W velocity at the monitoring points A and B inside the 15° stable stratified cavity.

The comparisons of the local Nusselt number profiles with the experimental data of Cooper et al. [25] for the stable case are presented in Figures 7.27 and 7.28. The LES and measured profiles show an anti-symmetric variation in local Nusselt number in the longitudinal direction, over both sides, and uniformity in the spanwise direction. Over the hot side, Nusselt number levels are higher at the lower end and then fall monotonically towards the upper end, while over the cold side this variation is reversed. While agreement between the LES and measured profiles is generally close, the measured values are higher near the upper end of the hot side and the lower end of the cold side. Again, the possibility of minor heat losses in the experiment might account for this deviation. As far as the unsteady RANS computations are concerned, as also noted in the unstable case comparisons, Chapter 6, the high-Re $k - \varepsilon$ model is consistently close to the LES predictions.

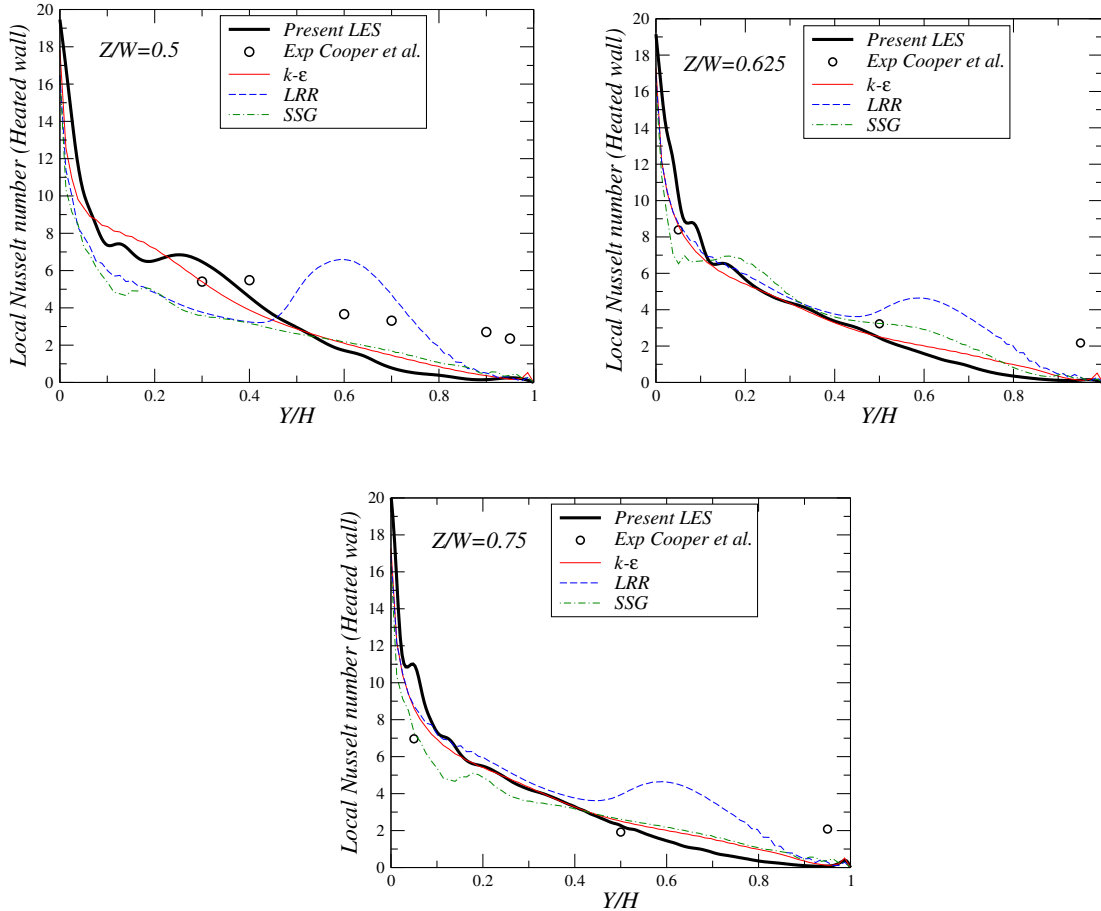


Figure 7.27: Profiles of time-averaged local Nusselt number at the spanwise locations $Z/W = 0.5, 0.625, 0.75$ along the heated wall of the 15° stably stratified cavity.

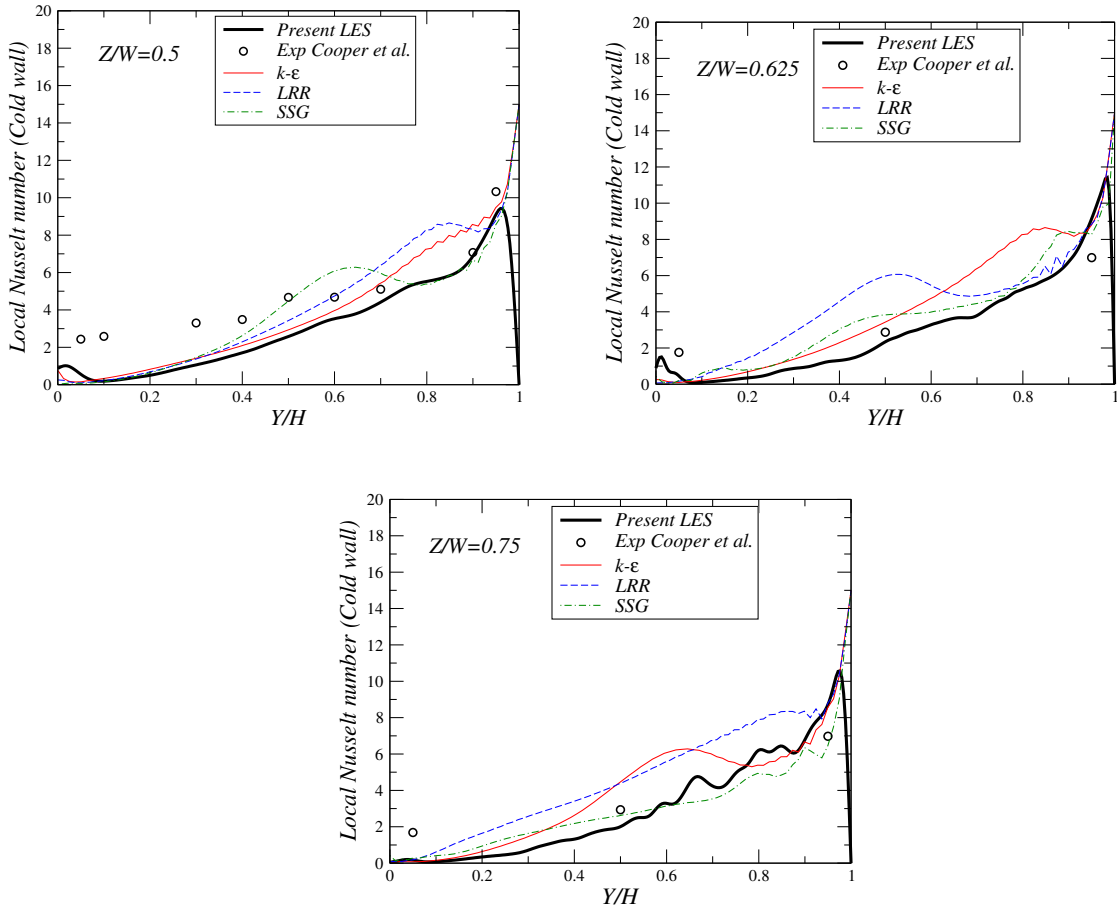


Figure 7.28: Profiles of time-averaged local Nusselt number at the spanwise locations $Z/W = 0.5, 0.625, 0.75$ along the cold wall of the 15° stably stratified cavity.

7.6 Concluding remarks

A highly resolved LES and URANS computations of buoyancy-driven flow within the 15° stably stratified cavity have been conducted, the results of which have been presented and discussed in this chapter. In such a case, the three-dimensionality is caused by the thermally insulated side walls. Their presence causes the formation of two counter-rotating longitudinal vortices and two strong longitudinal cells, which transport fluid from the upper end to the lower end of the cavity along the middle and from the lower end to the upper end along the side walls. As a result, the fluid temperature changes more gradually from the hot to the cold side and there is a rise in the core fluid temperature from the lower to the upper end of the cavity. This temperature variation in turn causes strong longitudinal variations in the local Nusselt number. Over the hot side the Nusselt number is high at the lower end and low at the upper end of the cavity, while over the cold side the local Nusselt number variation is reversed. Velocity and

temperature fluctuations are considerably weaker than for the unstably stratified case and also confined to lower frequencies.

For the stably stratified case, the challenge is in reproducing the three-dimensional flow structures which arise as a result of the lateral wall effects and weak buoyancy influences. None of the RANS models tested was able to fully reproduce these features, although further research within the author's group, Omranian [72], suggests that the use of more advanced wall functions, Craft et al [27], with second-moment closures can result in significant predictive improvements in this case. The work of Dehoux et al. [31] using the EB-RSM model of Manceau [65] with GGDH also showed advantageous predictions of flow inside the stably stratified test cases.

Chapter 8

Buoyancy-Driven Flow Within the Horizontal Annular Penetration Cavity

8.1 Introduction

After a detailed investigation of buoyancy-driven flow inside unstably and stably stratified tilted rectangular cavities, one turns attention into more complex buoyant flow, the penetration annular enclosure.

In several Advanced Gas Cooled Reactors (AGCRs), boiler penetrations protrude horizontally from the vertical wall of a pressurised vessel, Figure 8.1. The length of these penetrations is long compared with their diameter. At the bottom and top of the boilers, the penetrations contain tubes that carry water and steam respectively into and out of the boilers. In both cases the tubes are colder than the ambient pressurised carbon dioxide gas. The number of tubes within the penetrations ranges from 3 to 44, and tube size varies significantly. The tubes are supported along their length by a number of support plates, also intended to act as gas baffles. However, an angular gap exists between the plates and the outer penetration sheath tube to accommodate expansion and bowing of the tubes. Because of the high gas pressure and thermal stresses, these gaps do not offer a significant resistance to the flow reaching the end of the penetrations.

The flow in and out of the penetration is driven by the difference in temperature between the hot reactor gas and the cold tube at the centre. Because of the absence of any measured validation data for this test case, a major aim for the present thesis is to perform a highly resolved LES, in order to provide full and accurate data of the

thermal and dynamic fields of the flow in the penetration, and the rate of heat transfer to/from the central tube, and to determine how far the flow can be driven inside the penetration. Some initial URANS simulations are conducted in order to determine appropriate boundary conditions and to provide an initial qualitative and quantitative view of the flow patterns found in the problem.

The dimensions and boundary conditions of the enclosure modelled here are illustrated in Figure 8.2. The dimensions of the external vessel I , D , W are $1m$, $5m$ and $3m$, respectively, while the dimensions of the horizontal penetration are the length $L = 5.68m$, the inner tube diameter $h = 0.026m$, and the penetration diameter $H = 0.343m$. At the top inlet of the domain the pressure is set as constant, with the axial and spanwise velocity components (W and U) set to zero. A zero gradient condition is applied to the vertical velocity, V , whilst the initial temperature is set at $300^\circ C$, and relatively low levels of turbulence are prescribed ($k = 0.01V_0^2$ and $\varepsilon = 0.09(k^2/3\nu)$). At the exit of the domain zero gradient conditions are applied to all variables. Symmetry conditions are applied at the left side of the container. The inner cylinder wall is maintained at a temperature of $65^\circ C$, whilst all the other walls are adiabatic.

The Prandtl number (Pr) of the fluid is taken here as 0.7 (CO_2), and the temperature of the fluid and other fluid properties are chosen such that the Rayleigh number, defined as:

$$Ra = \frac{\rho^2 g \beta \Delta T \left(\frac{H-h}{2}\right)^3}{\mu^2} Pr \quad (8.1)$$

where $\Delta T = T_h - T_c$, with the subscripts h and c denoting the hot inlet temperature and cold wall temperature, respectively, takes a value of 1.5×10^6 .

The reference buoyant velocity V_0 , used for scaling results below, is defined as:

$$V_0 = \sqrt{\beta g \Delta T \left(\frac{H-h}{2}\right)} \quad (8.2)$$

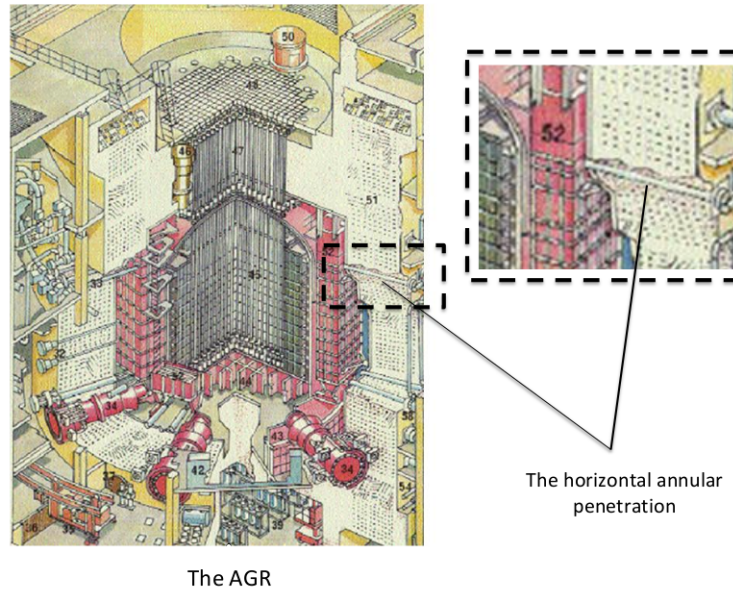


Figure 8.1: Sketch of the annular horizontal penetration cavity and its position in the AGR.

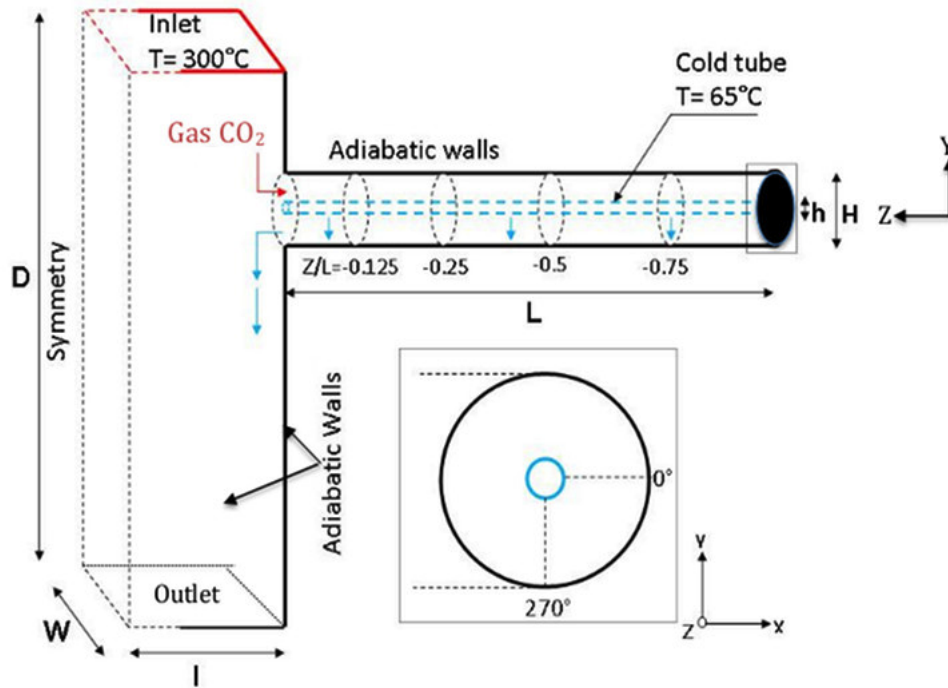


Figure 8.2: Geometry and boundary conditions of 3-D annular penetration cavity. Location of plot lines are indicated.

8.2 Computational mesh and numerical methods

The computational mesh used for the present LES and the SST $k-\omega$ model is structured and non-uniform, consisting of four blocks, as shown in Figure 8.3. It uses around six million cell volumes, with appropriate clustering in the near wall regions to give non-dimensional near-wall node distances around the circular walls of $\Delta y^+ \simeq 1$. Spatial discretization is achieved using a second-order central difference scheme (CDS), whilst the second-order Crank-Nicolson (C-N) scheme is employed for the time discretization and the time step is $\delta t = 10^{-5}s$, resulting in a maximum CFL number of 0.5. The simulation required 60000 time steps, which corresponds to approximately 120 hours in 60 CPU processors, to reach a fully developed turbulent flow state, and at least a further 200000 time steps for statistical averaging of the flow field. For the URANS simulations, the spatial discretization scheme employed is the second order central difference scheme and the implicit first order Euler scheme for time discretization. The mesh used for the high-Re model simulation is of about 200000 cells and correspondingly larger time step, still giving a maximum CFL number of 1. Characteristics of the LES and URANS calculations are summarised in Table 1.

Case (cylinder)	LES	$k - \omega$ SST	$k - \varepsilon$
$(H - h) \times L$	0.1715×5.68	0.1715×5.68	0.1715×5.68
$N_{(H-h)} \times N_L$	100×200	100×200	40×30
$\Delta (H - h)^+ \times \Delta L^+$	$(\leq 1) \times (\leq 20)$	$y^+(max) = 1$	$y^+(max) = 30$
$\delta t (s)$	10^{-5}	10^{-2}	10^{-2}
Max CFL	0.5	1	1
Normalised CPU time (on 60 Cores)	1	0.2	0.06

Table 8.1: Characteristics of LES and URANS simulations.

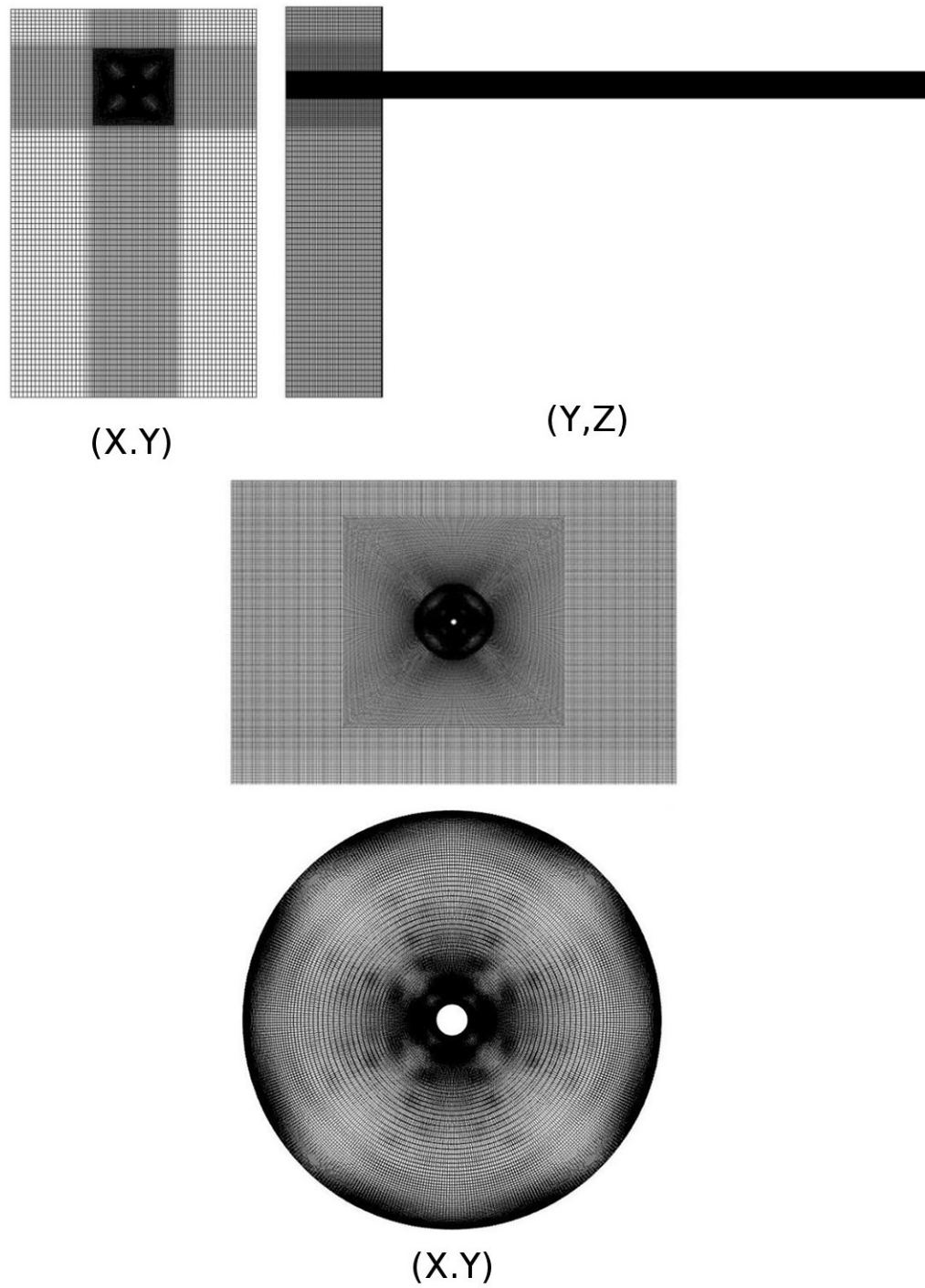


Figure 8.3: 3-D computational mesh for LES.

8.3 Assessment of LES resolution

Since the aim of the present work is to perform a highly resolved LES of pure buoyancy-driven flow inside a cylindrical penetration enclosure, the temporal and spatial resolutions should be fine enough to capture all but the very smallest turbulent scales. This was first checked by calculating the mesh size to the Kolmogorov length scale ratio, in Figure 8.4, which gave a maximum value of around 5 along the gap between the inner and the outer cylinders.

Further assessment of the resolution of the LES is achieved by checking the ratio of the SGS turbulent viscosity to the resolved one, this ratio gives a maximum value of around 0.15 which indicates a well resolved dissipative motion. The dominant scales in the present case are the large eddies which are all well resolved in addition to a substantial part of the dissipative scales.

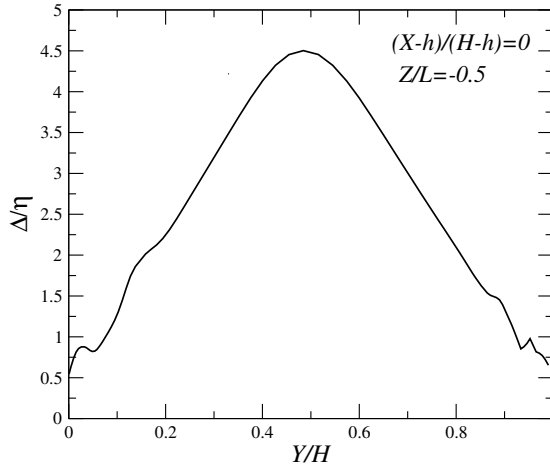


Figure 8.4: Ratio of the grid spacing to the Kolmogorov length scale along the gap between the inner and outer cylinders $(X - h) / (H - h) = 0$, $Z/L = -0.5$.

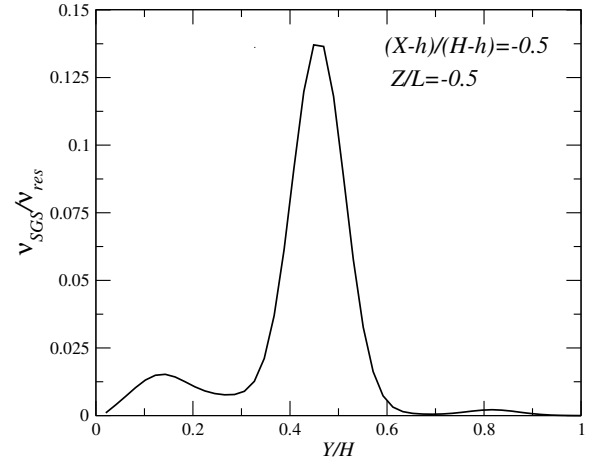


Figure 8.5: Ratio of the SGS turbulent viscosity to the resolved viscosity along the gap between the inner and outer cylinders $(X - h) / (H - h) = 0$, $Z/L = -0.5$.

8.4 Qualitative results

8.4.1 Time-dependent results

The instantaneous temperature and the three components of velocity W , V , U contours at a fully developed turbulent flow state, on both middle (Y , Z) section and three spanwise cross-sections $Z/L = -0.25$, -0.5 and -0.75 inside the horizontal penetration obtained from LES, $k - \omega$ SST and $k - \varepsilon$ models are shown in Figures 8.6 to 8.9 respectively. The difference in temperature between the inlet and the cold inner tube of the cylindrical penetration creates a buoyancy force. This causes the fluid cooled by the inner tube to move downwards from the central tube towards the lower wall of the horizontal annular penetration. This cooling of the inner tube then results in warm fluid drawn into the penetration and moving along its top half towards the closed end. While the cooled fluid in the lower half of the penetration moves in the opposite direction and eventually spills out of the open end and moves downwards. The velocity contours represented in Figures 8.7, 8.8 and 8.9 suggest the existence of a number of unsteady eddies of different sizes dispersed inside the cylindrical penetration. These unsteady features are concentrated in the lower part of the penetration between the concentric cylinders. A somewhat different flow behaviour is noticed when comparing velocity distributions at the three (X , Y) cross sections, with more of unsteadiness being noticeable towards the left open end of the penetration. Instantaneous contours of temperature and velocity components resulting from RANS models (Figures 8.6-b-c to 8.9-b-c) also suggest that the flow is unsteady, and hence these models are able to resolve some large-scale unsteady structures in this flow.

Vector plots at different axial positions (Z/L) within the penetration enclosure, illustrated in Figure 8.10, confirms the presence of different scales more noticeable at bottom half of the penetration as mentioned above in the different time-dependent contour plots.

In order to show further features of flow within the penetration annular enclosure, the iso-surfaces of Q -criterion (Equation 6.2) are presented in Figure 8.11. Coherent structures of different size are dispersed in the bottom half of the penetration where the fluid flow descends by buoyancy force towards the bottom outer surface of the annulus and then flows out through the open end towards the outlet.

3-D Streamline plots, in Figure 8.12, show the direction of the buoyant flow inside the penetration. These streamlines show that the large scale vortices, which exist in the bottom half of the penetration, rotate in spiraling movement until it reaches the open end of the penetration then falls towards the exit.

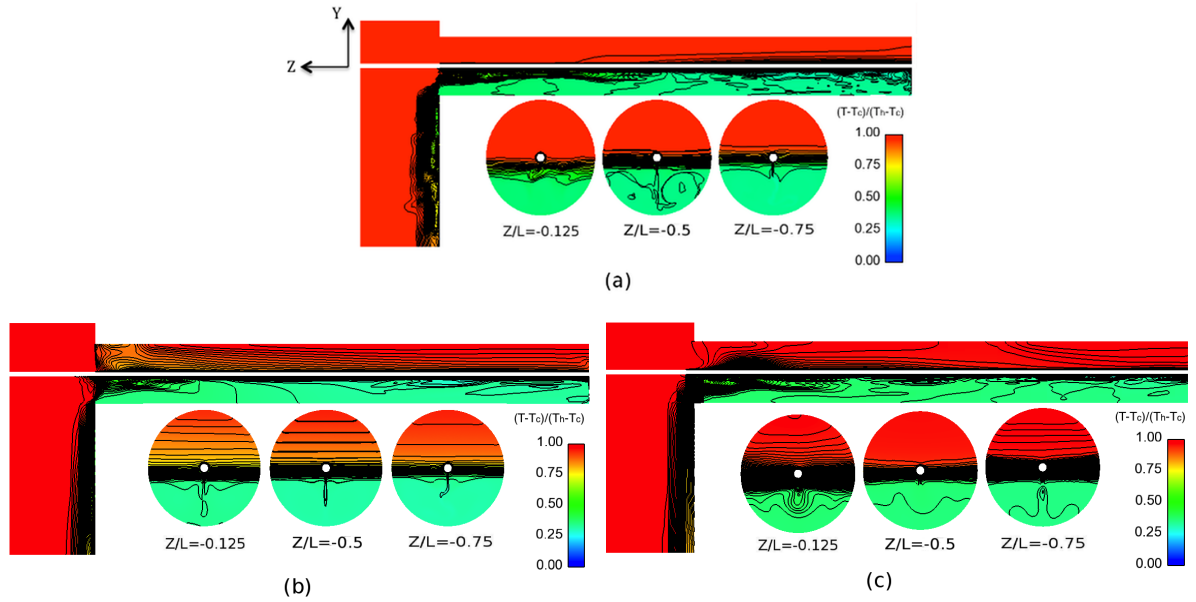


Figure 8.6: Instantaneous temperature contours at fully turbulent conditions and at middle cross section $X/W = 0$ (magnified view of the penetration) and three cross sections $Z/L = -0.25, -0.5, -0.75$. (a) LES, (b) SST $k - \omega$, (c) $k - \epsilon$.

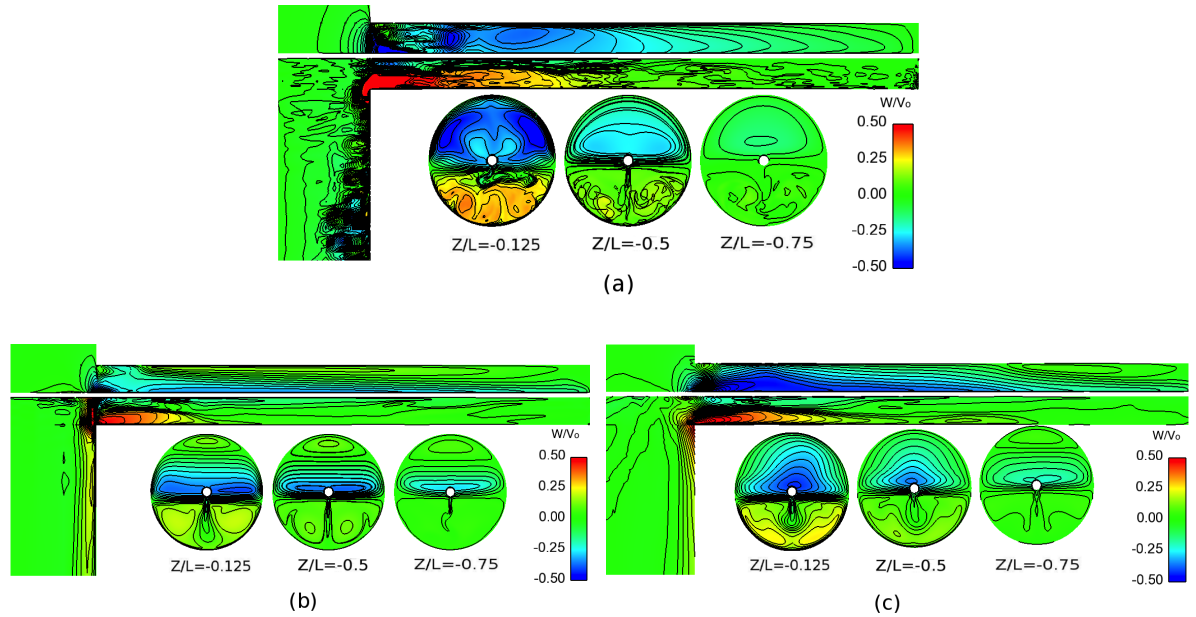


Figure 8.7: Instantaneous axial velocity (W) contours at fully turbulent conditions and at the middle cross section $X/W = 0$ (magnified view of the penetration) and three cross sections $Z/L = -0.25, -0.5, -0.75$. (a) LES, (b) SST $k - \omega$, (c) $k - \epsilon$.

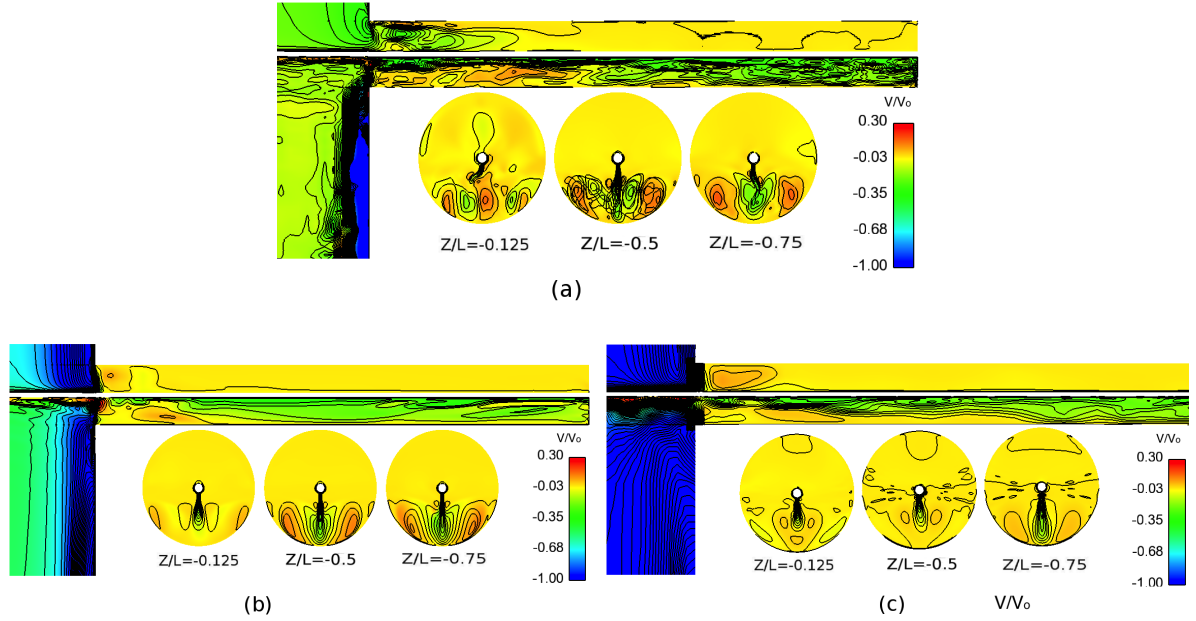


Figure 8.8: Instantaneous vertical velocity (V) contours at fully turbulent conditions and at the middle cross section $X/W = 0$ (magnified view of the penetration) and three cross sections $Z/L = -0.25, -0.5, -0.75$. (a) LES, (b) SST $k - \omega$, (c) $k - \epsilon$.

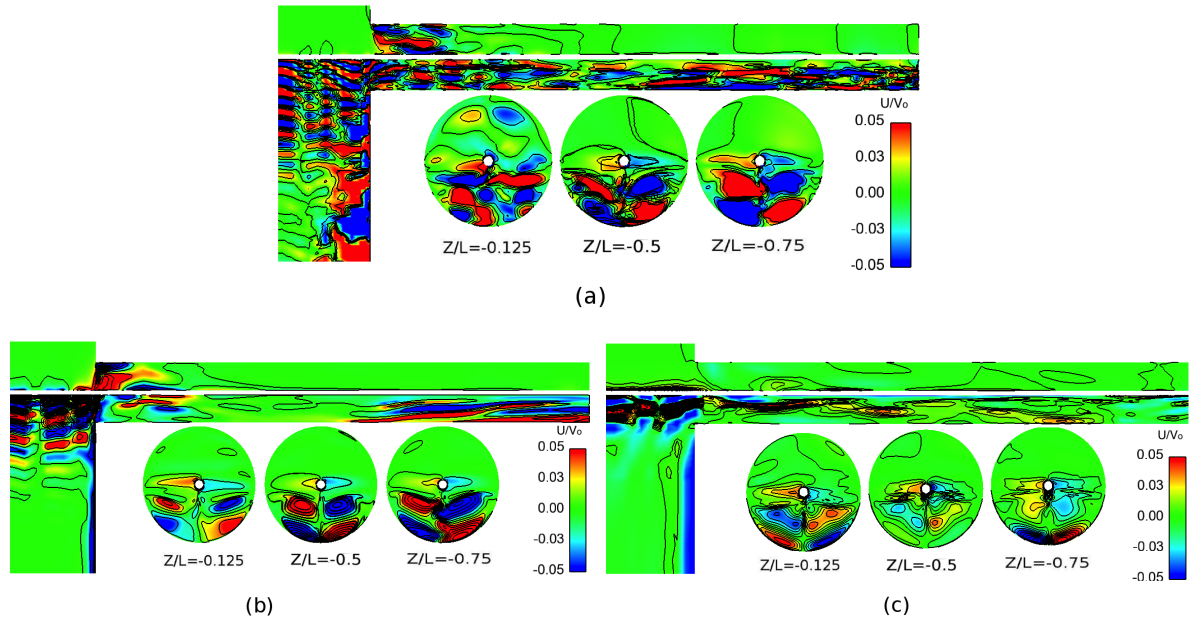


Figure 8.9: Instantaneous spanwise velocity (U) contours at fully turbulent conditions and at the middle cross section $X/W = 0$ (magnified view of the penetration) and three cross sections $Z/L = -0.25, -0.5, -0.75$. (a) LES, (b) SST $k - \omega$, (c) $k - \epsilon$.

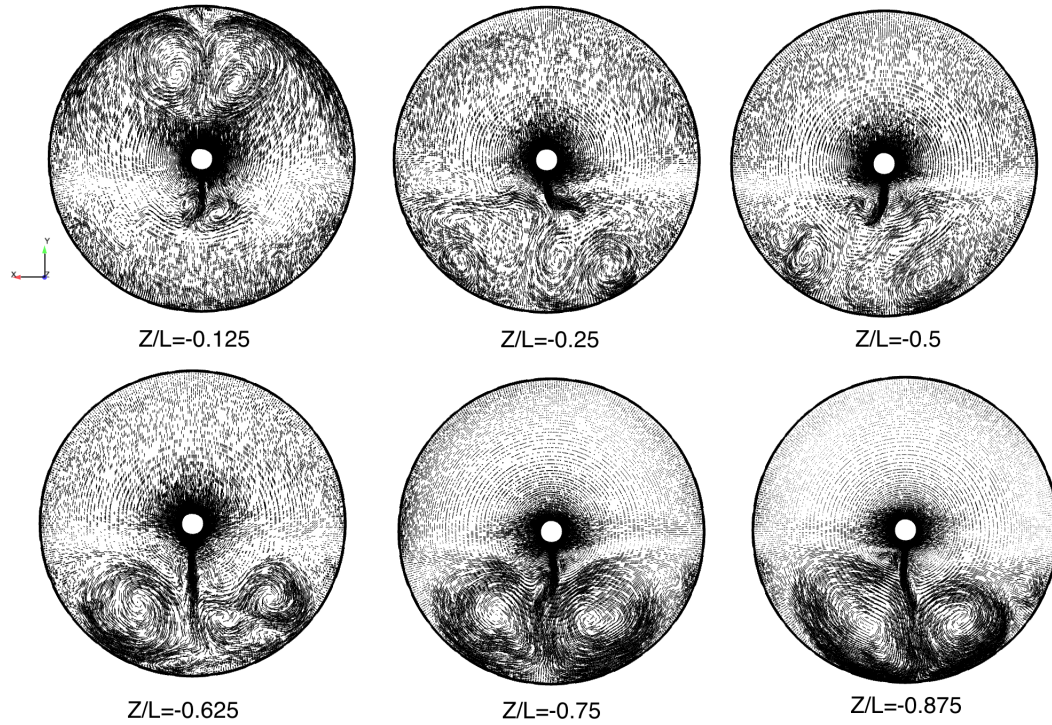


Figure 8.10: LES results: vector plots of velocity magnitude at different axial sections of the penetration enclosure.

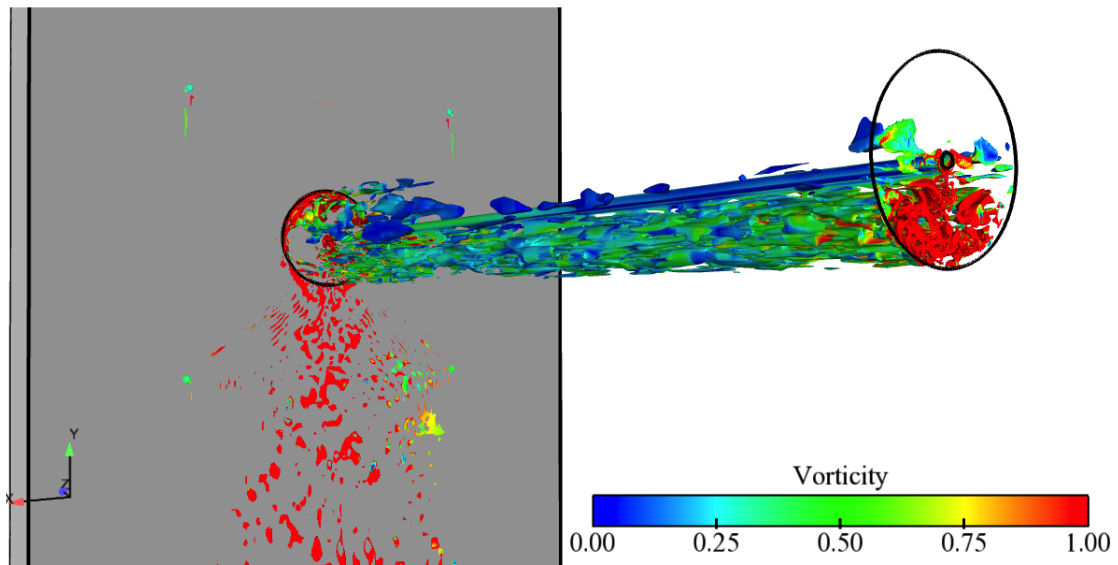


Figure 8.11: LES results: Iso-surfaces of Q-criteria coloured by vorticity inside the penetration enclosure.

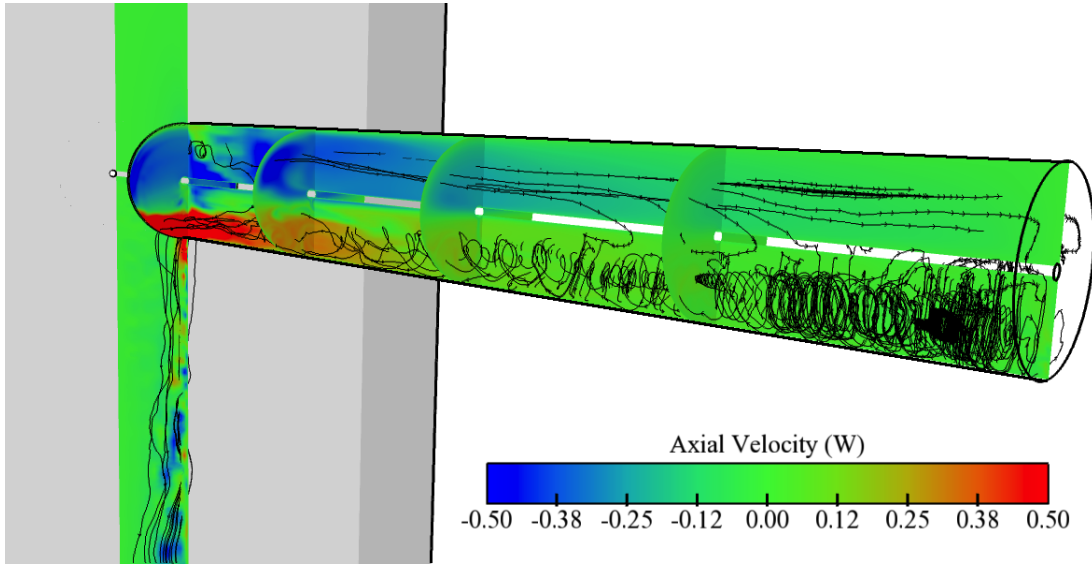


Figure 8.12: LES results: streamline plots inside the penetration enclosure.

Time dependent pictures are presented here in order to shed light on the flow physics within this particular case and to give further information of the dynamic and evolution of the buoyancy-driven flow inside the penetration with the elapsed simulation time. Instantaneous contours of temperature and the three components of velocity W , V , U , plotted along three middle sections, (X, Y) , (Y, Z) , (X, Z) , and at different time intervals t (number of time step divided by 1000) are presented in Figures from 8.13 to 8.15. Across the (X, Y) middle plane, in Figure 8.13, the axial velocity, W , distribution shows the development of the flow across the horizontal axis of the penetration. It confirms that over the upper half of the cross-section the fluid moves towards the closed end of the penetration and over the lower half it has the opposite direction. Moreover, contours of the vertical velocity component V show that the fluid falls from the central cold tube towards the bottom wall due to the buoyancy force effect. The spanwise U velocity contours also confirm that the flow inside the penetration oscillates forming downward eddies of different sizes. Across the (Y, Z) middle section, in Figure 8.14, the component of velocity parallel to the horizontal axis of the penetration, W , also shows the evolution of the flow along the penetration. The flow gradually penetrates further and further into the annular cylinder from the upper half of the opening, and by the end of the simulation, it extends over the entire length of the penetration. V and U velocity distributions confirm the presence of dominant large structures noticed inside the penetration and smaller ones are noticed near the closed end wall of the penetration. The corresponding contours of the three components of velocity across the (X, Z) middle section, in Figure 8.15, confirm the presence of different structures

in the flow which are more noticeable near the closed end of the penetration.

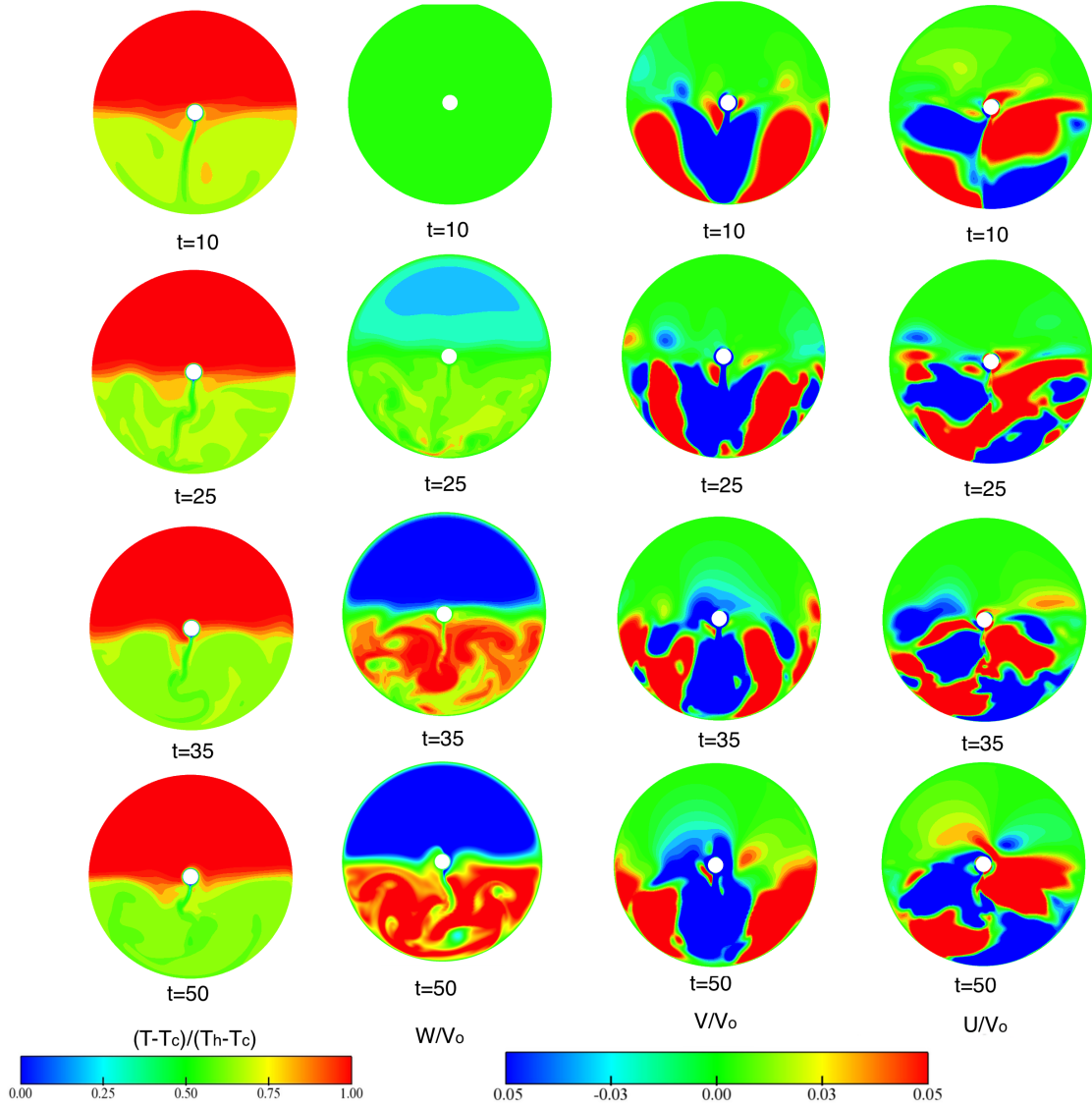


Figure 8.13: LES results: dimensionless T , W , V and U contours across the central (X, Y) plane ($Z/L = -0.5$) of the annular penetration at different time steps.

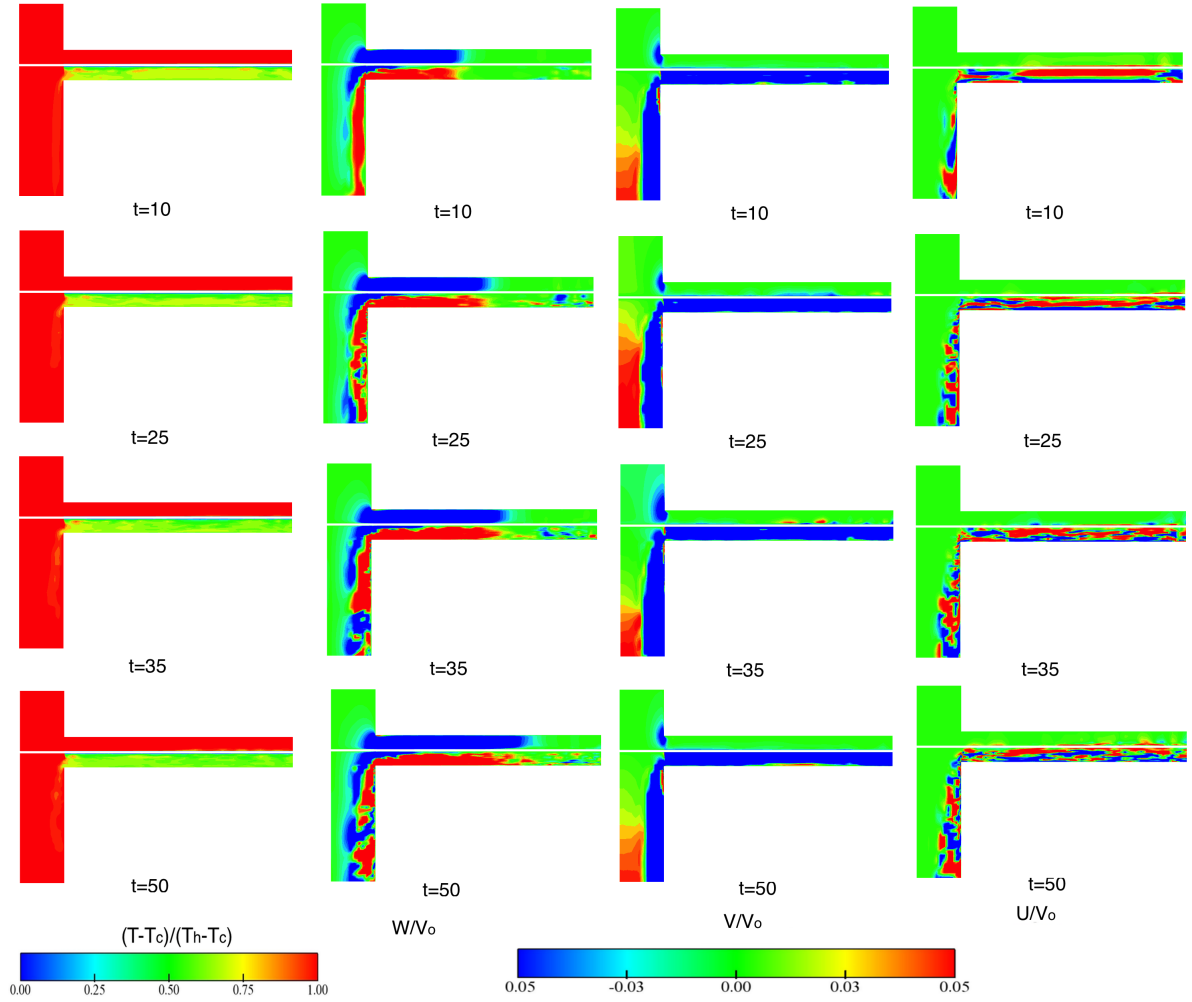


Figure 8.14: LES results: dimensionless T , W , V and U contours across the central (Y, Z) plane ($X/W = 0$) of the annular penetration at different time steps.

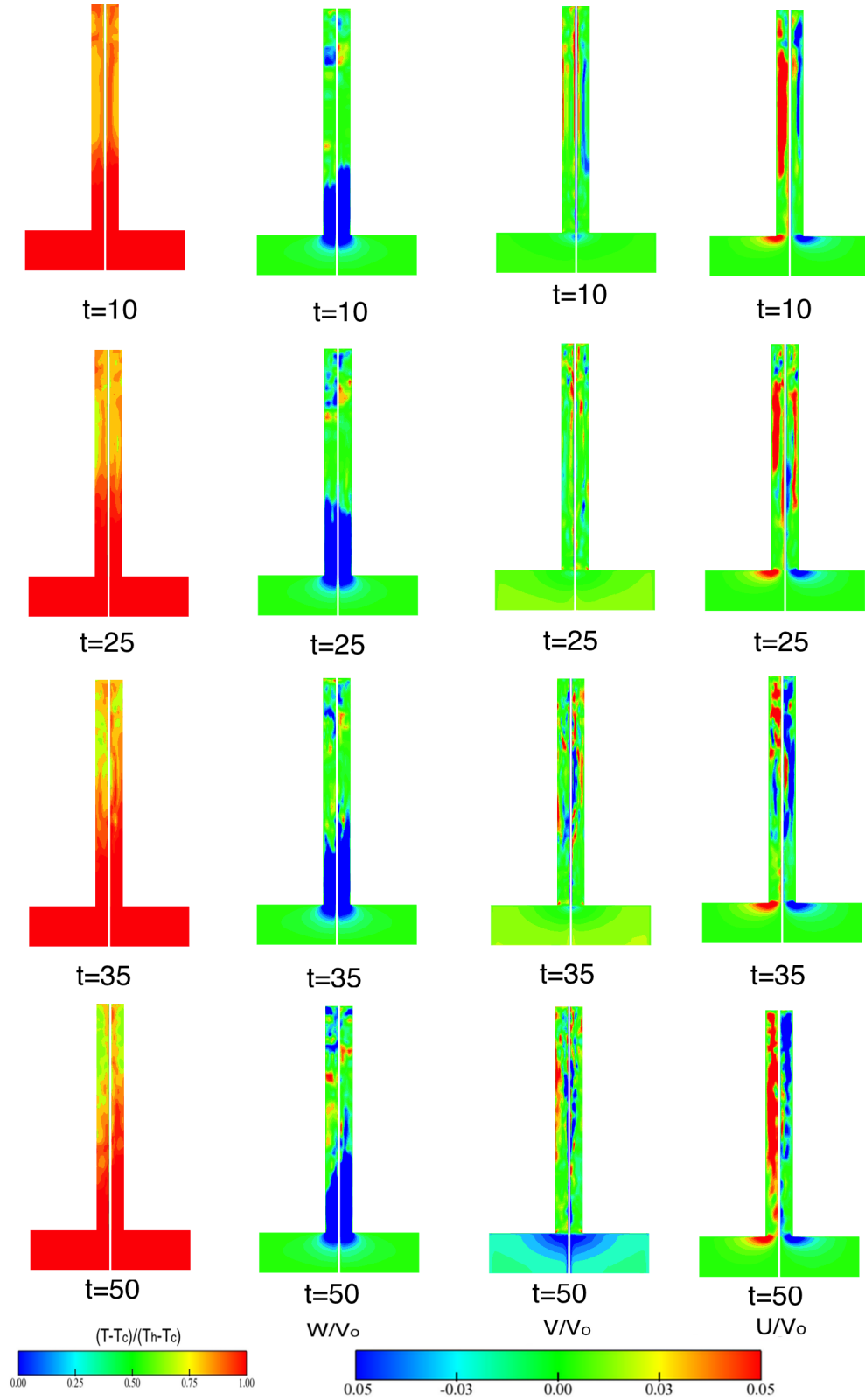


Figure 8.15: LES results: dimensionless T , W , V and U contours across the central (X, Z) plane ($Y/D = 0$) of the annular penetration at different time steps.

8.4.2 Time-averaged results

Contours of the time-averaged temperature, for the three components of velocity and the total turbulent kinetic energy at the central (X, Y) and (Y, Z) cross-sections of the penetration obtained from LES, SST $k - \omega$ and $k - \varepsilon$ models are shown in Figures 8.16 and 8.17 respectively. A similar behaviour of the thermal field is shown in the LES and URANS predictions. The flow is cooled while moving downward towards the surface of the outer tube, resulting in largely cold fluid in the lower half of the annulus, with the temperature value equal to around the average of the hot and cold temperatures, and warmer fluid in the upper half, the $k - \varepsilon$ model show a slightly colder flow at the lower part of the horizontal penetration compared to the other models.

Contours of axial velocity W show a negative motion over the upper half of the cross-section, indicating that the fluid penetrates inside the annular penetration and reaches the closed end, and a positive motion over the lower half of the cross-section, which suggest that this fluid changed direction towards the open end of the penetration. Contours of the vertical V and the spanwise U velocities show downward circular cells from both LES and URANS but the axial cross-section figure shows more large dominant eddies from LES compared to the URANS qualitative results. Moreover, The $k - \varepsilon$ scheme returns less unsteadiness in the flow and therefore it predicts smaller structures in comparison to the LES. The differences in the $k - \varepsilon$ predictions can be attributed to the diffusive nature of the effective diffusivity approximation and also to the use of the log-law-based wall function. While the SST is also an effective-viscosity model, it includes a viscosity limiter, which reduces the turbulent viscosity in regions of high strain rates. This feature makes it more likely to predict flow unsteadiness.

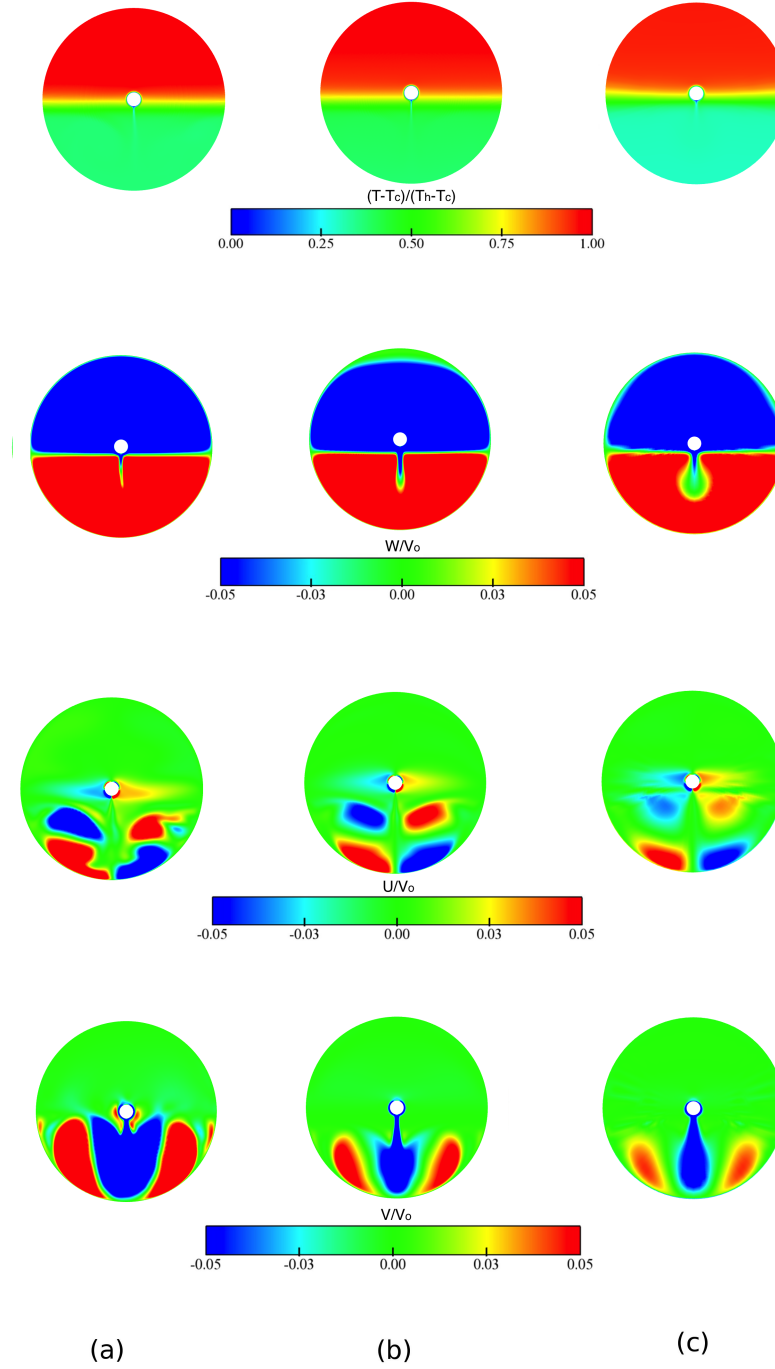


Figure 8.16: LES and URANS: Time averaged contours of dimensionless temperature T and velocity components W , V , U at the central spanwise plane of the annular penetration, obtained from: (a) LES, (b) SST $k-\omega$, (c) $k-\epsilon$.

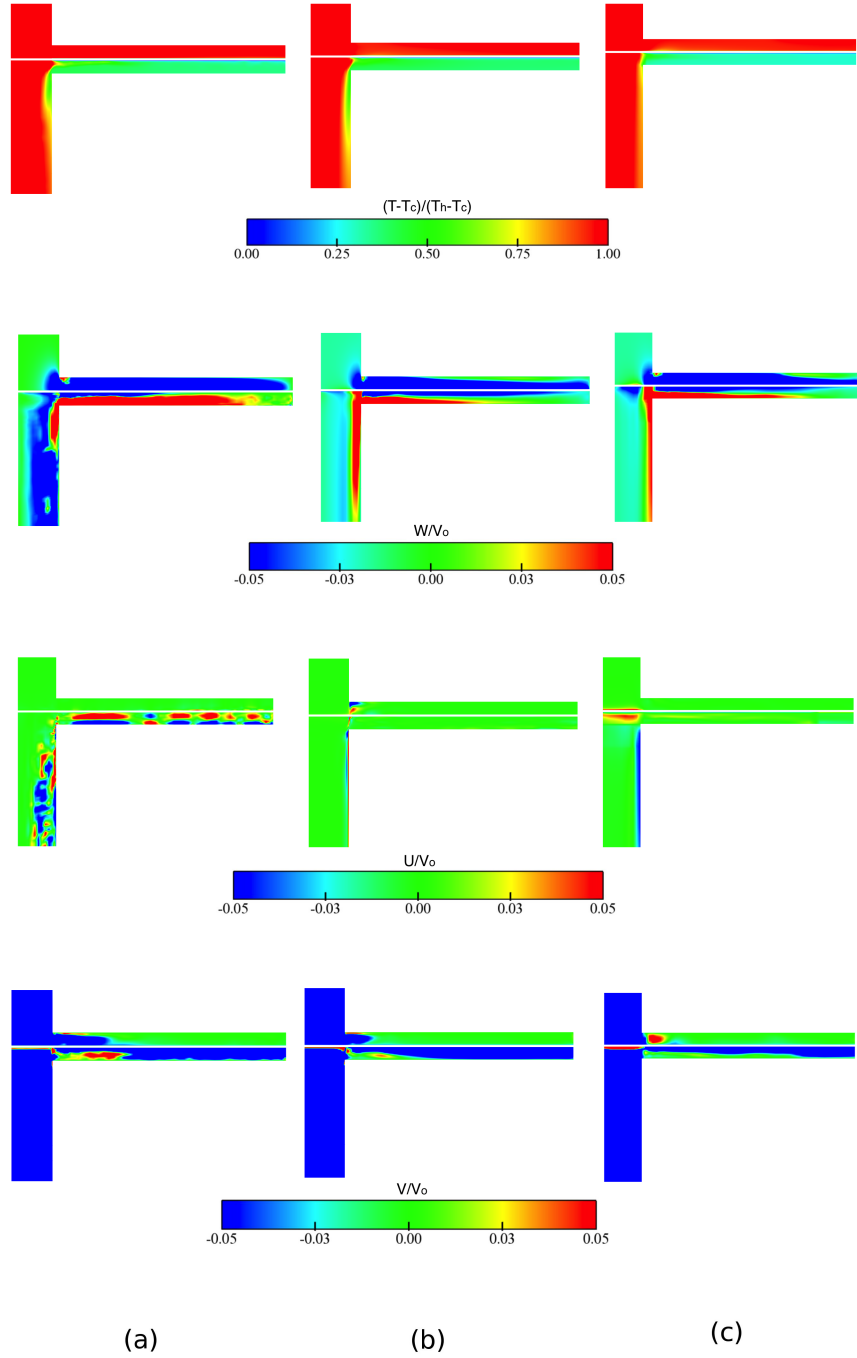


Figure 8.17: LES and URANS: Time averaged contours of dimensionless temperature T and velocity components W , V , U at the central axial plane of the annular penetration, obtained from: (a) LES, (b) SST $k - \omega$, (c) $k - \varepsilon$.

8.5 Quantitative results

In this section, the following quantitative results are presented at two angular positions: 0° , which corresponds to the horizontal radius of the annular penetration (See Figure 8.2 for geometry definition), and 270° , which corresponds to the lower vertical radius. The results are not presented for the angular position 90° because there is not much happening in the upper region of the penetration. The results are not plotted at the angular position 180° due to symmetry.

Figures 8.18 to 8.21 show, respectively, time-averaged profiles of temperature normalised by temperature difference ΔT and the three components of velocity W , V and U normalised by the buoyant velocity scale V_0 , at three traverse lines, $Z/L = -0.25$, -0.5 and -0.75 , and at the angular position of 0° . LES and RANS predictions show that the temperature is low at the vicinity of the inner tube, and then increases away from it, maintaining a fairly uniform value over a substantial part of the gap radius between the inner and the outer tube. The general pattern of thermal profiles is similar for all axial cross-sections, with the time-averaged temperature obtained from the SST $k-\omega$ and the LES being in generally good agreement. However, the LES does show a slight decrease in the temperature level in the outer part of the gap as one moves from the open towards the closed end of the penetration, whilst the SST and $k-\varepsilon$ models appear to give a more uniform value along the penetration length. Profiles of temperature obtained from $k-\varepsilon$ deviate from LES and SST near the closed end of the horizontal annular penetration, this may be attributed to the simple wall function employed with this model which assumes a logarithmic variation of the near-wall velocity. The SST and $k-\varepsilon$ schemes show predictions at the middle of the horizontal penetration ($Z/L = -0.5$), which are in good agreement with the LES data. The normalised time-averaged vertical velocity component V is virtually zero over much of the annular gap, but takes negative values close to the inner tube as the fluid there gets cooled and descends. The axial and spanwise velocities W and U also show negative values at the vicinity of the cold tube. The two components of velocity, W and U , remain negative in the annular gap and increase in magnitude while approaching the outer wall of the annulus. RANS schemes agree with these predictions except for some deviations of the $k-\varepsilon$ model near the inner tube for the same reasons mentioned above.

Turning attention now to the angular position of 270° , equivalent profiles to those discussed above are shown at the three different cross-sections of $Z/L = -0.25$, -0.5 and -0.75 in Figures 8.22 to 8.25 respectively. A different behaviour of the flow is noticed at this angular position. The profiles of the time-averaged temperature obtained

from RANS schemes are again in close agreement with the present LES except for some deviations in the $k - \varepsilon$ predictions at the position ($Z/L = -0.25$). The temperature is low close to the cold inner tube and then increases to reach a fairly uniform value across the lower part of the annular gap. LES and SST results show slightly higher temperatures close to the open end of the horizontal annular penetration compared to other locations as one moves from the open end towards the closed end at the right hand side of the penetration. As also seen at the angular position 0° , this may be due to the warm fluid being entrained into the penetration from the surrounding domain. In Figure 8.23, at the location near the open end ($Z/L = -0.25$), The axial velocity W is negative close to the inner tube and then increases significantly to reach a maximum normalised value of 0.3 at around $(Y - h)/(H - h) = 0.7$, this suggests that when the cold fluid falls downward, it then moves back towards the open left end of the penetration. The W velocity is lower as one moves towards the closed end, simply because amount of flow penetration reduces with distance from the open end. In Figure 8.24, the magnitude of the vertical velocity V starts from zero at the underside of the cold inner tube and then increases as the cooled fluid falls towards the lower wall. It reaches a maximum at around $(Y - H)/(H - h) = 0.1$ before decreasing back to zero at the surface of the outer tube. At position $Z/L = -0.25$, the maximum downward velocity is slightly higher than at the other locations. At this location a region of positive (upward) velocity is also noted in the LES beyond $(Y - h)/(H - h)$ approx. 0.4 and somewhat closer to the outer tube in RANS results. This is a result of flow interaction which occurs at the penetration inlet, and at locations further inside the penetration, the vertical velocity across this lower section is always directed downwards. The magnitude of the spanwise U velocity presented in Figure 8.25 is very low compared to that of the other components because the flow is mostly directed vertically. RANS predictions of the dynamic field are close to the present LES data except for some deviations in those of the $k - \varepsilon$ model. As noted earlier, the SST $k - \omega$ scheme has a viscosity limiter, while the $k - \varepsilon$ version embedded in *Code_Saturne* 2.0 does not. This feature results in lower turbulent viscosities in regions of high shear and probably explains why the SST predicts stronger oscillations and therefore better agreement with the present LES.

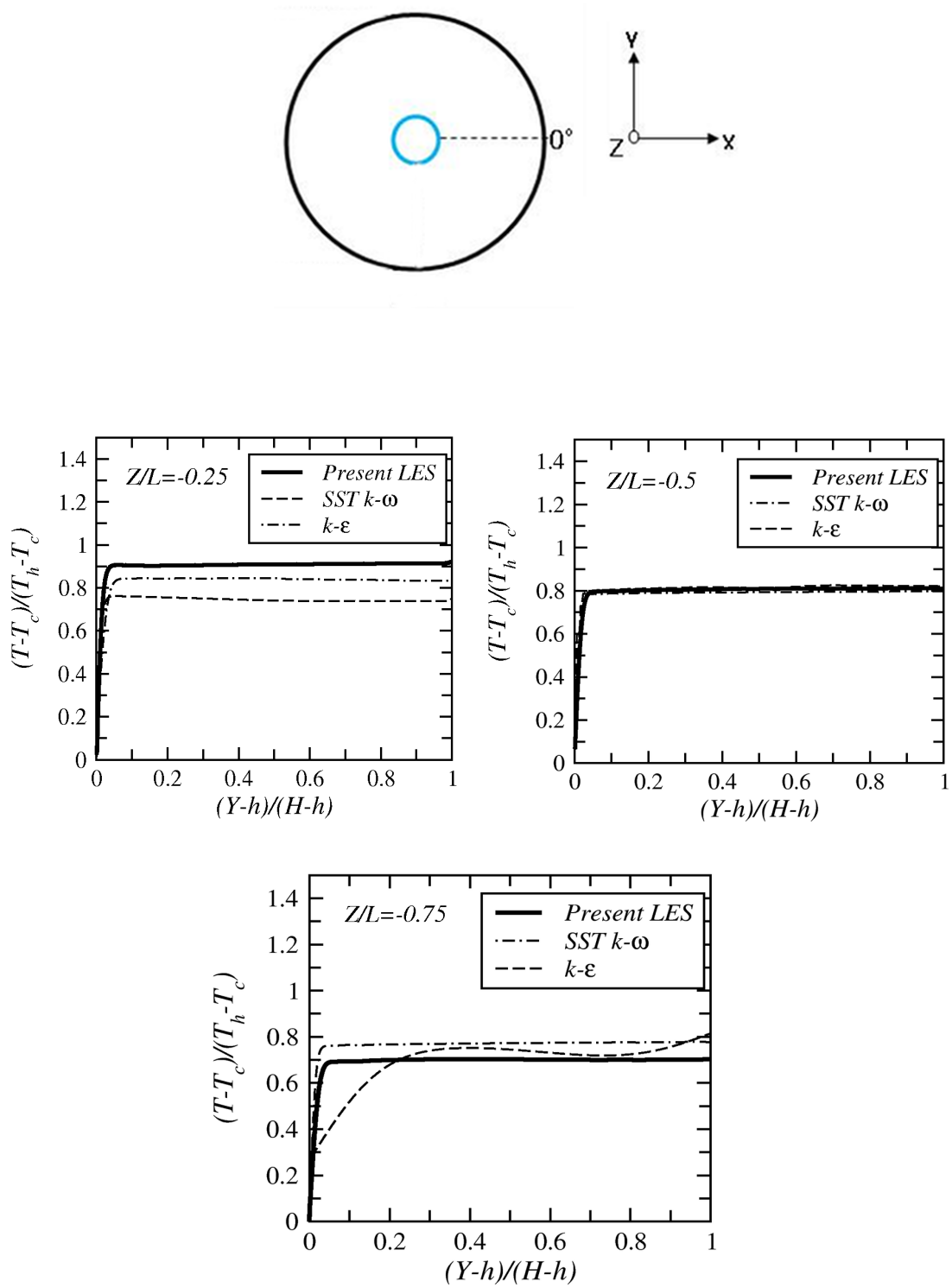


Figure 8.18: Time-averaged dimensionless temperature at angular position 0° on three locations inside the penetration ($Z/L = -0.25, -0.5, -0.75$).

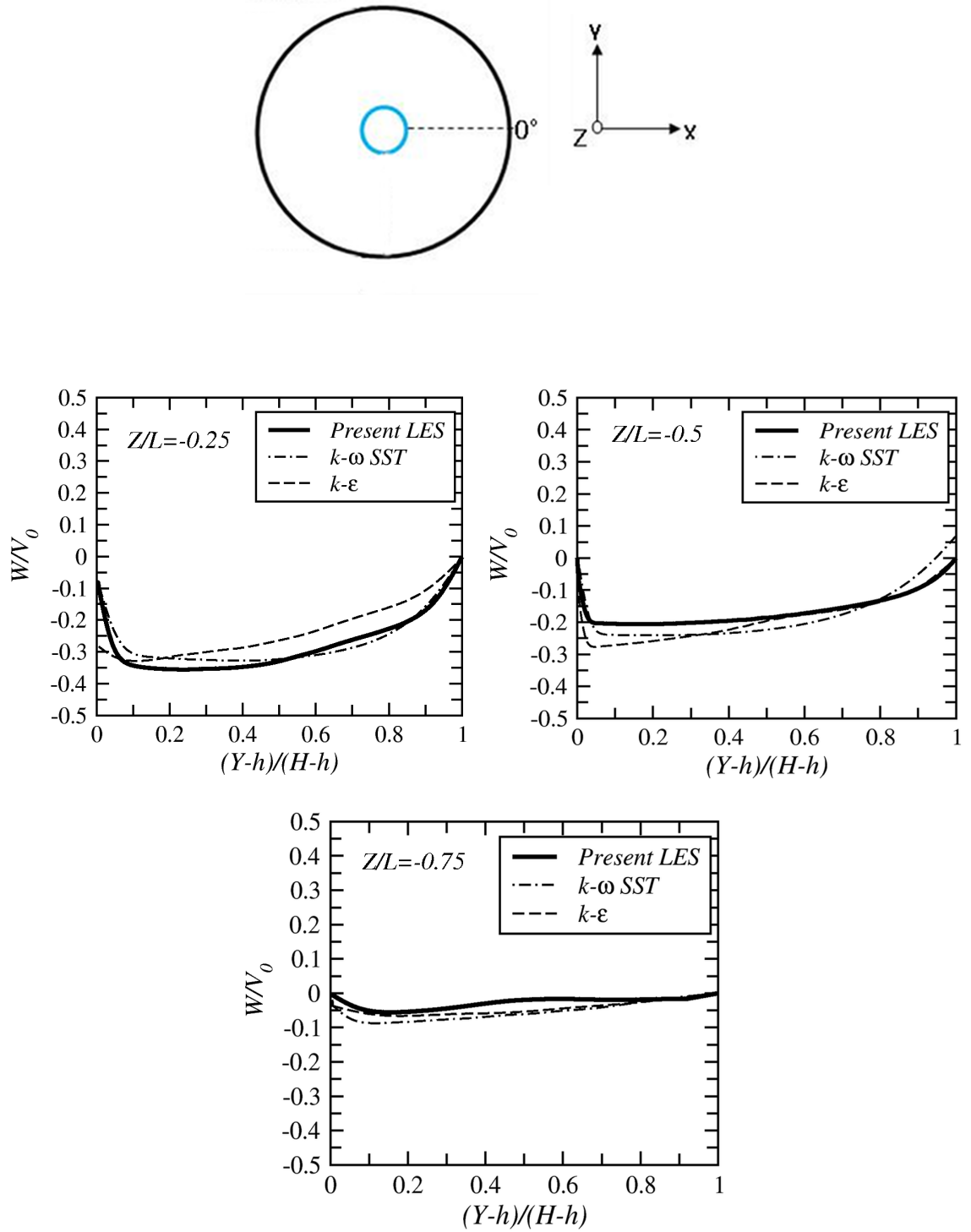


Figure 8.19: Time-averaged dimensionless axial velocity W at angular position 0° on three locations inside the penetration ($Z/L = -0.25, -0.5, -0.75$).

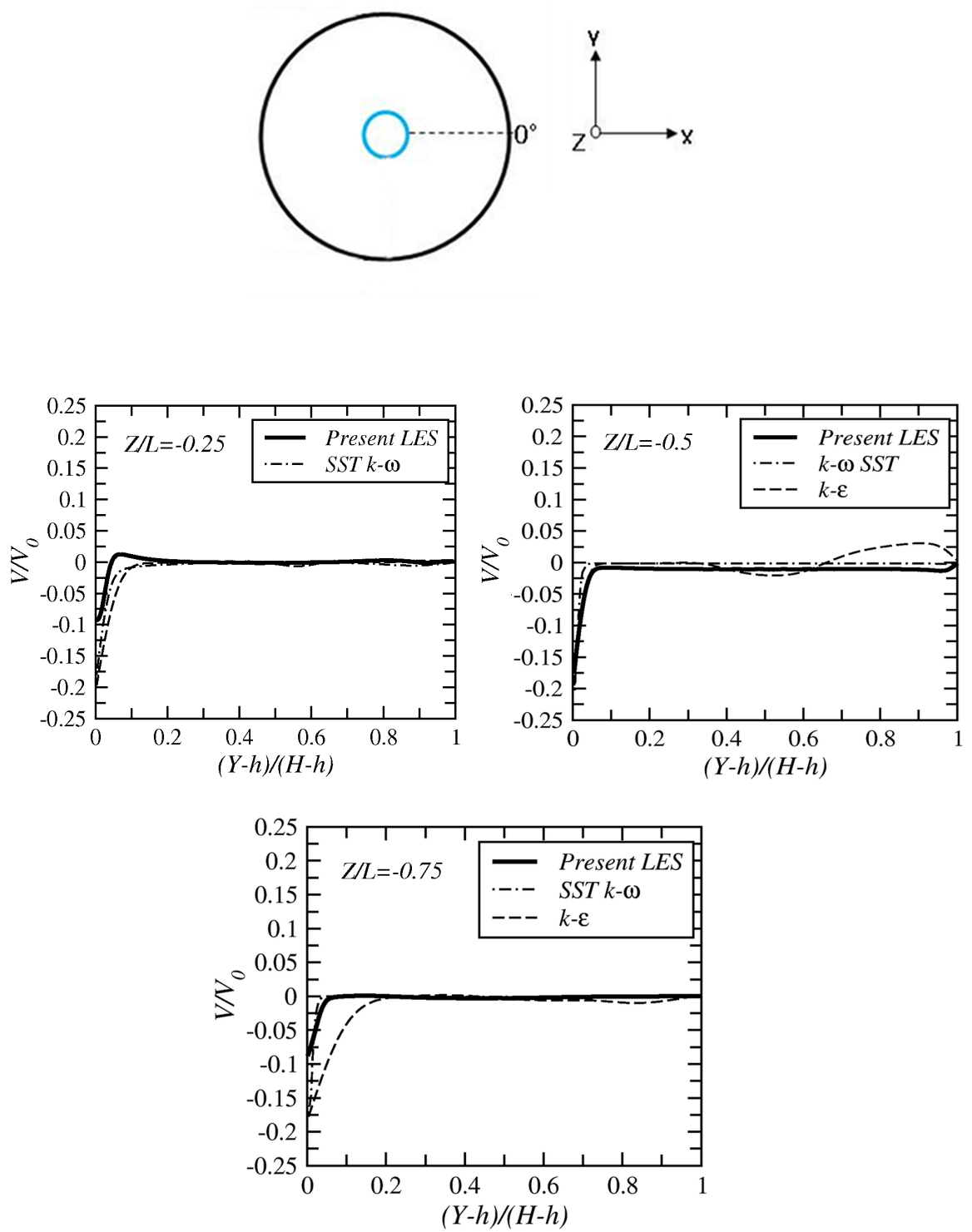


Figure 8.20: Time-averaged dimensionless vertical velocity V at angular position 0° on three locations inside the penetration ($Z/L = -0.25, -0.5, -0.75$).

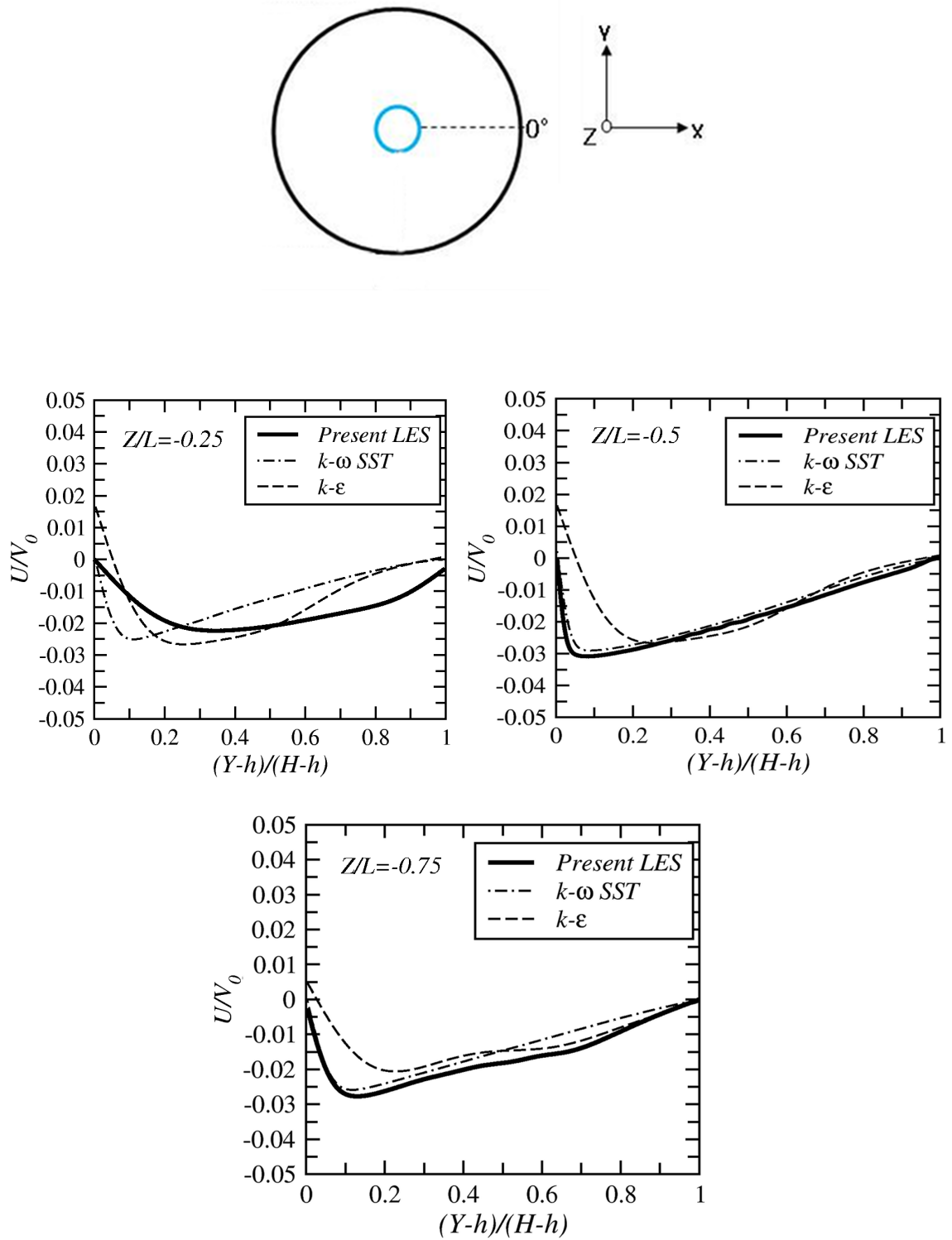


Figure 8.21: Time-averaged dimensionless spanwise velocity U at angular position 0° on three locations inside the penetration ($Z/L = -0.25, -0.5, -0.75$).

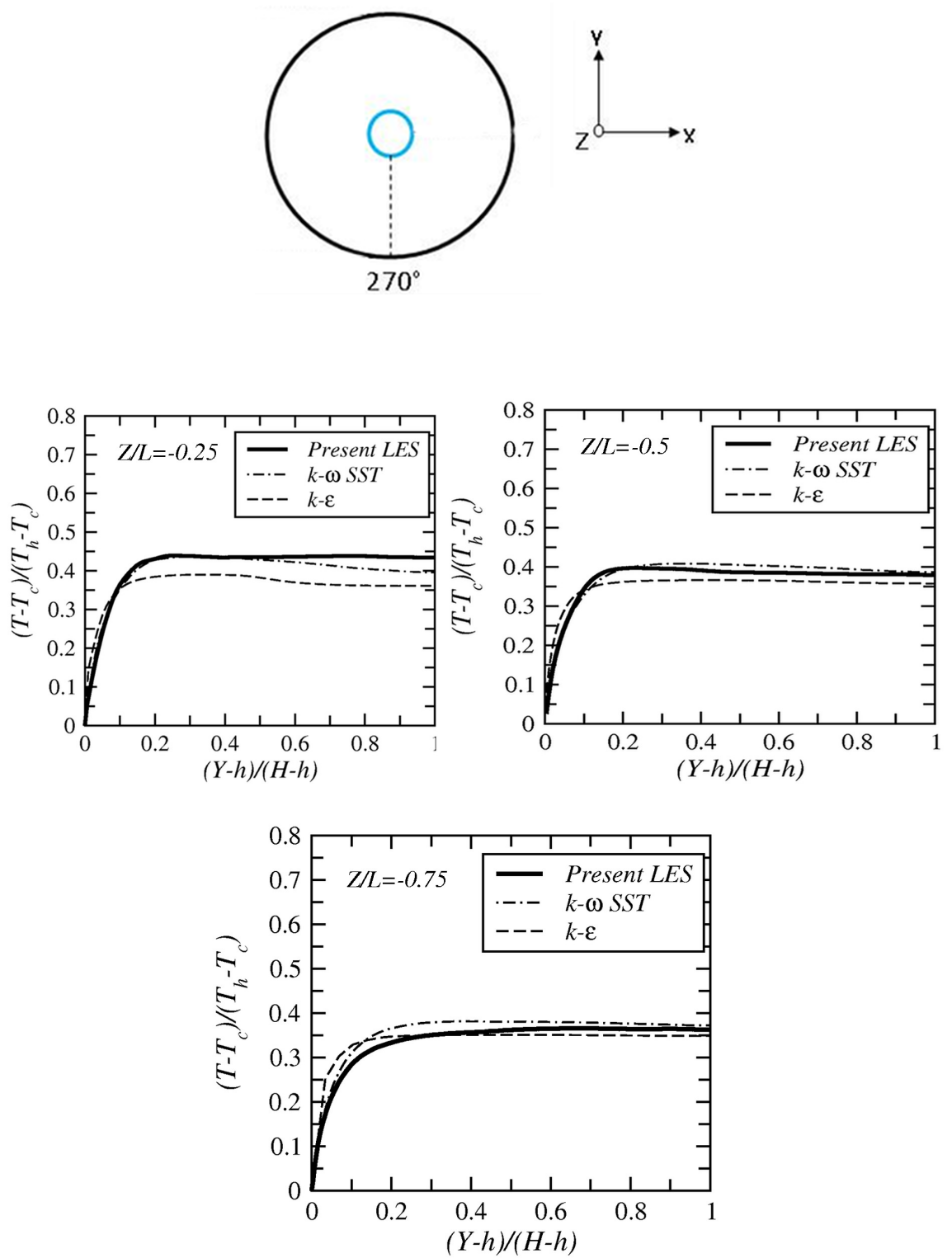


Figure 8.22: Time-averaged dimensionless temperature at angular position 270° on three locations inside the penetration ($Z/L = -0.25, -0.5, -0.75$).

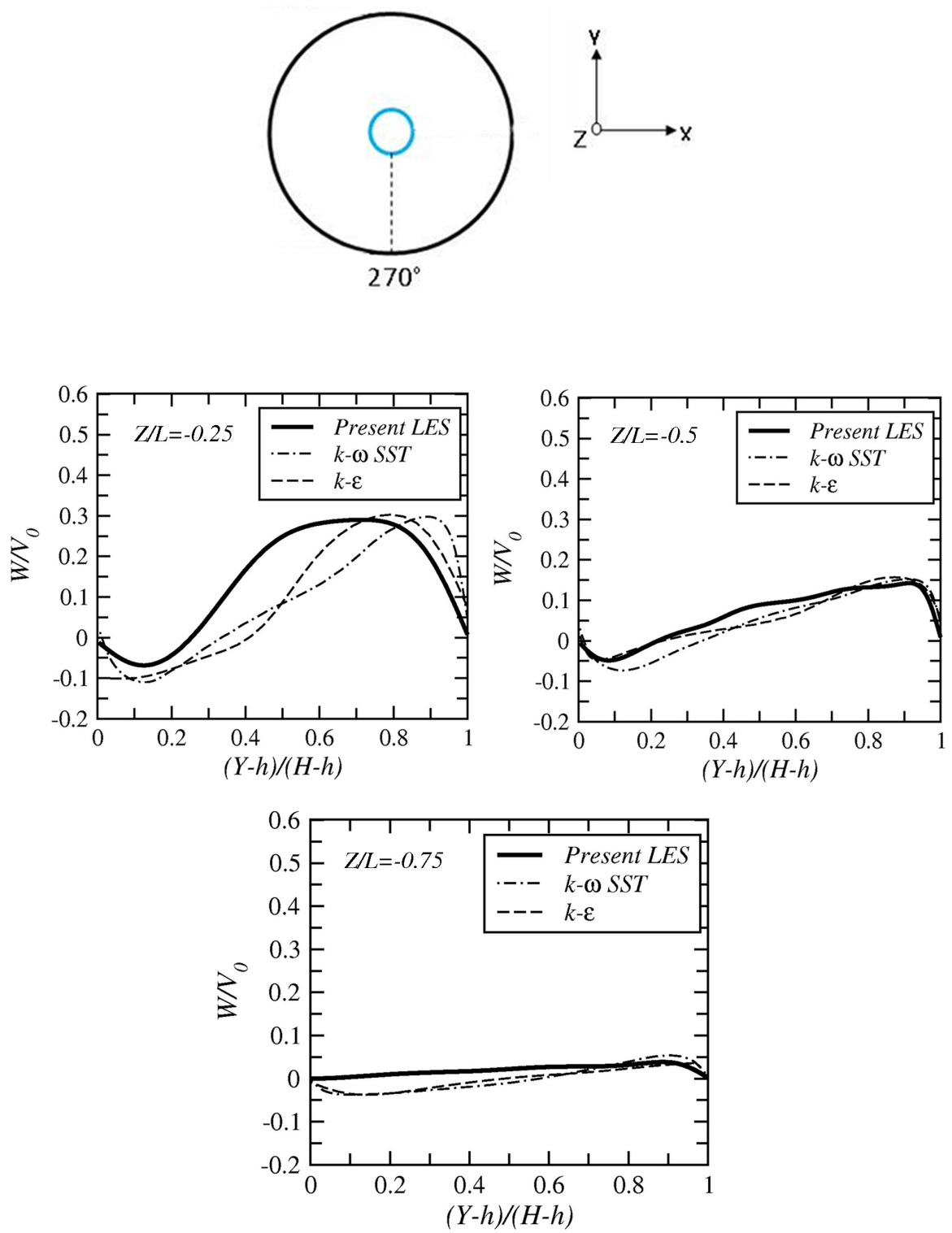


Figure 8.23: Time-averaged dimensionless axial velocity W at angular position 270° on three locations inside the penetration ($Z/L = -0.25, -0.5, -0.75$).

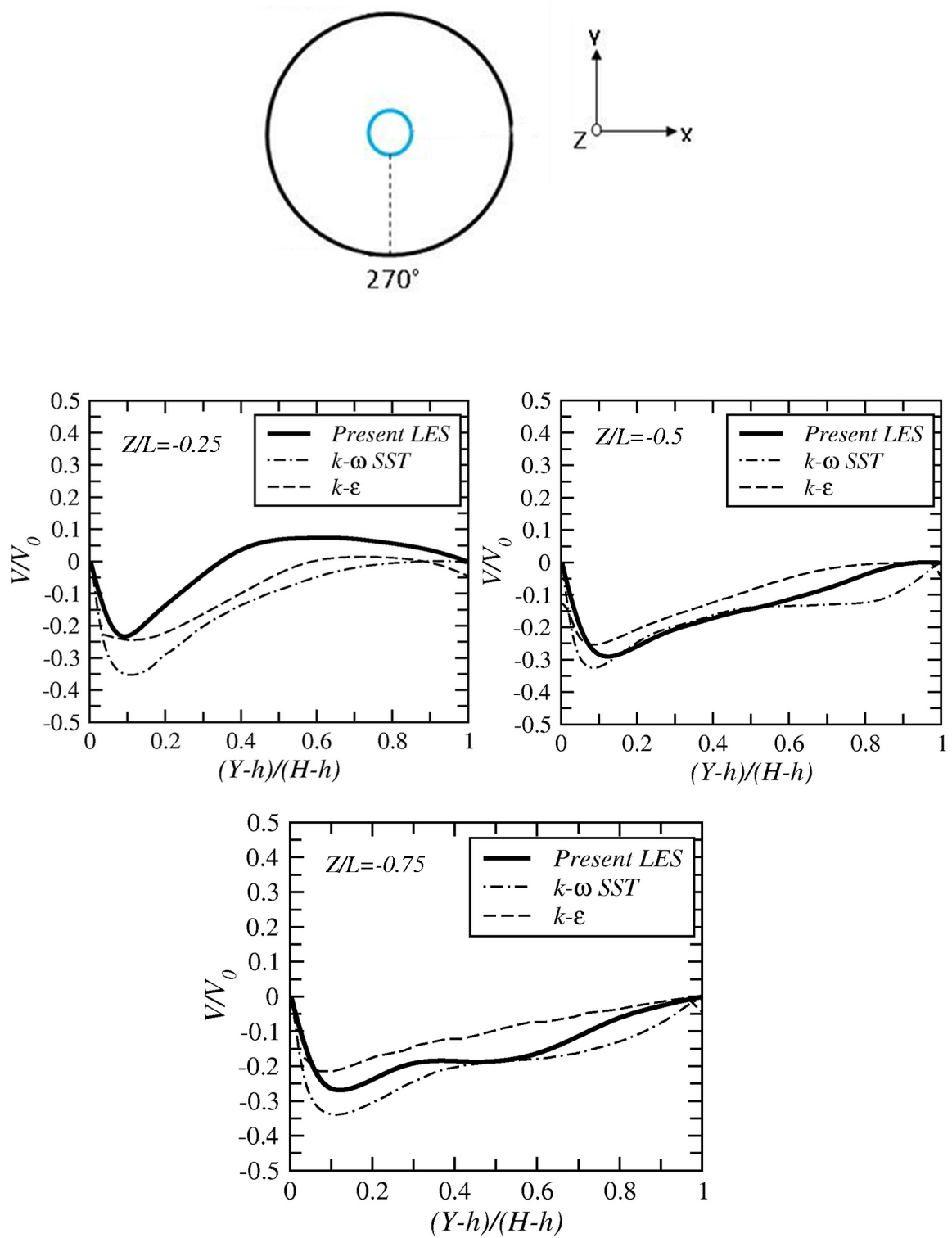


Figure 8.24: Time-averaged dimensionless vertical velocity V at angular position 270° on three locations inside the penetration ($Z/L = -0.25, -0.5, -0.75$).

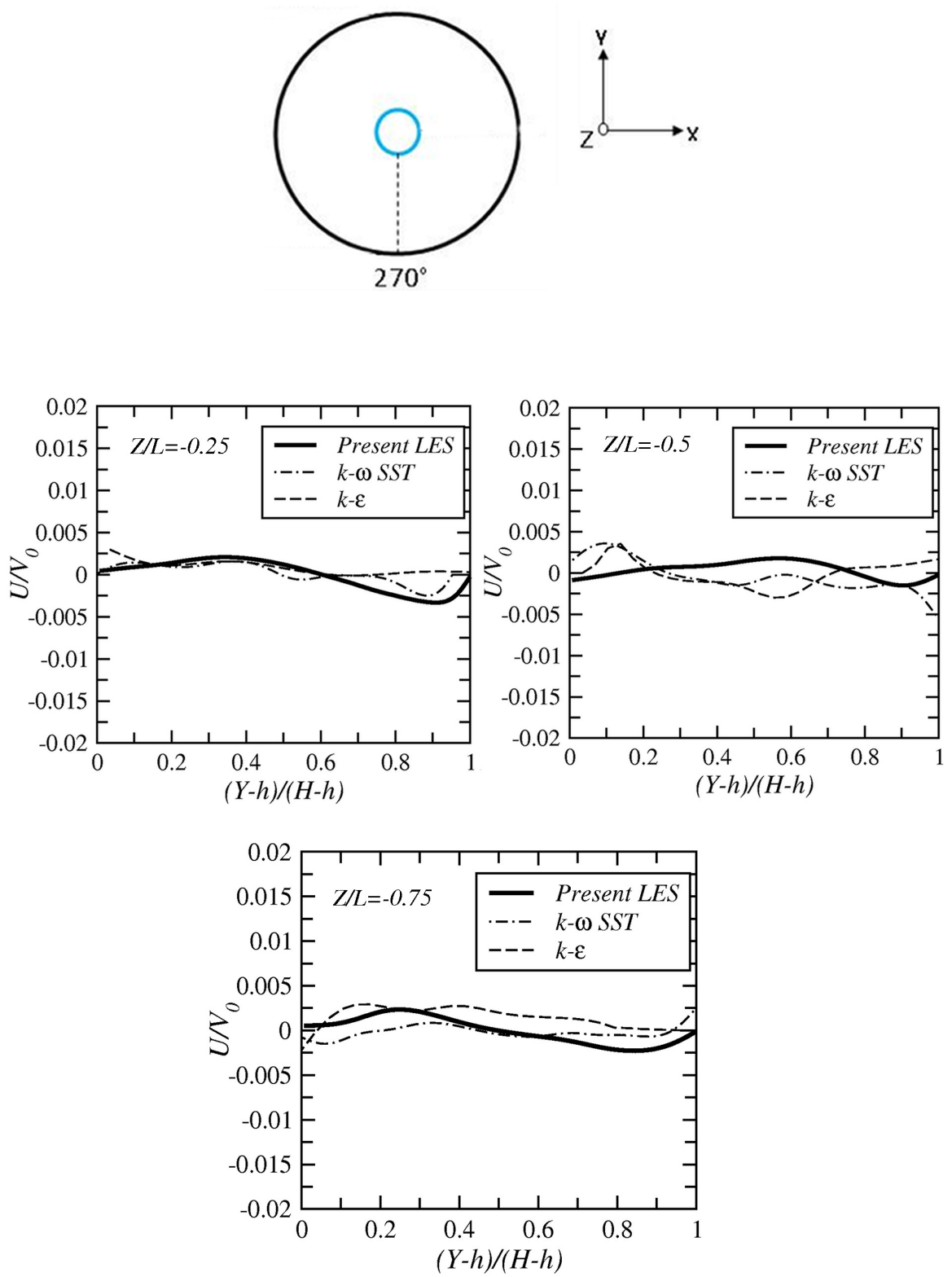


Figure 8.25: Time-averaged dimensionless spanwise velocity U at angular position 270° on three locations inside the penetration ($Z/L = -0.25, -0.5, -0.75$).

Temperature variance $\overline{t't'}$ and Reynolds stress components $\overline{w'w'}$, $\overline{v'v'}$ and $\overline{u'u'}$, at angular position of 270° and at three cross-sections along the penetration $Z/L = -0.25$, -0.5 and -0.75 , are presented in Figures 8.26 to 8.29. The temperature variance reaches it's maximum close to the inner tube at approx. $(Y - H) / (H - h) = 0.1$, where the mixing is very high and then decreases to reach a zero value after $(Y - H) / (H - h) = 0.4$. The LES also shows that the temperature variance generally decreases as one moves from the open end towards the closed end of the penetration, its lower value is in the middle of the horizontal penetration. At $Z/L = 0.25$ and 0.5 , the SST $k - \omega$ scheme produces predictions close to LES in comparison to the $k - \varepsilon$ model near the inner tube, but overpredicts $\overline{t't'}$ slightly over the rest of the annular gap. At $Z/L = -0.75$, there is closer accord between the LES and SST predictions, but the $k - \varepsilon$ continues to predict a very steep drop in the levels of temperature variance away from the inner cylinder. The deviations from RANS models might be attributed to the fact that both the RANS models in this study do not include a transport equation for the temperature variance. Consequently only the contributions arising from the resolved temperature fluctuations are taken into account. LES results of Reynolds stresses $\overline{w'w'}$, $\overline{v'v'}$ and $\overline{u'u'}$, in Figures 8.27 to 8.29, show that the anisotropy is dominant in this case, $\overline{w'w'}$ and $\overline{v'v'}$ are very low in the middle of the horizontal penetration and reach their higher value near the open end ($Z/L = -0.25$) where there are more unsteady structures. Turbulence levels are higher at the two ends of the penetration (especially the open end) and lower in the middle. The $k - \varepsilon$ scheme, because as noted earlier generally returns a less unsteady flow field, it also underpredicts the three Reynolds stress components and shows more isotropy in comparison to the SST $k - \omega$ model. The latter shows good qualitative agreement with the LES data but also shows some deviations more specifically for the spanwise component $\overline{u'u'}$ at the location ($Z/L = -0.5$).

The total turbulent kinetic energy k along the annular gap at angular position of 270° and at three locations across the length of the penetration $Z/L = -0.25$, -0.5 and -0.75 , is presented in Figure (8.30). LES data show that the total k reaches its maximum value at the top quarter of the annular gap, as expected, where there is more mixing and the buoyancy force is high which produces more energy, then an attenuation of energy occurs as one moves towards the closed end of the annular penetration. The SST scheme shows close agreement with the LES at the location ($Z/L = -0.25$) but overpredicts the total k profiles as one moves towards the closed end of the penetration. The $k - \varepsilon$ scheme underpredicts the modelled turbulent kinetic energy, due to its dissipative nature which dumps most of the structures present in the flow.

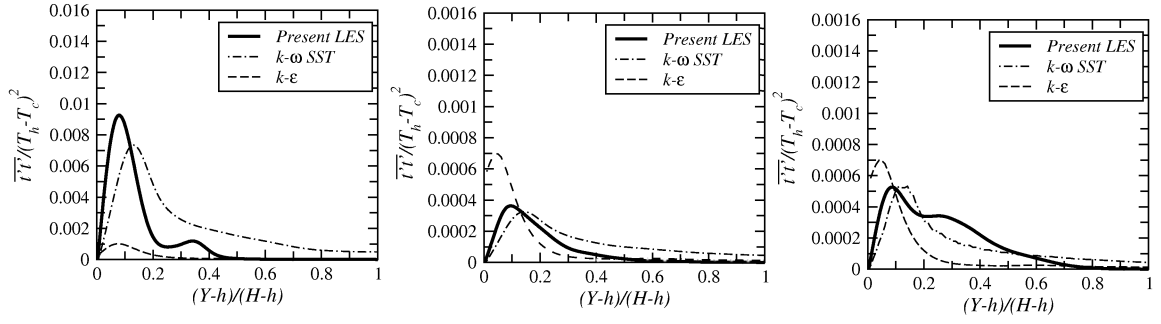


Figure 8.26: Time-averaged dimensionless temperature variance $\overline{t't'}$ at angular position 270° on three locations ($Z/L = -0.25, -0.5, -0.75$).

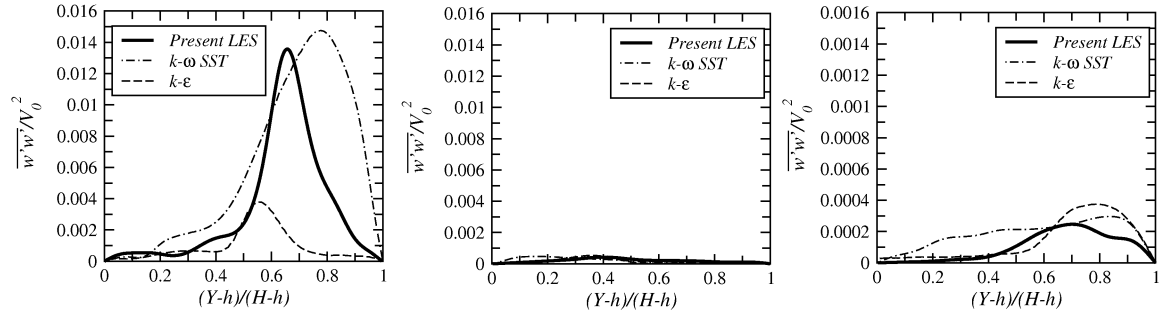


Figure 8.27: Time-averaged dimensionless Reynolds stress component $\overline{w'w'}$ at angular position 270° on three locations inside the penetration ($Z/L = -0.25, -0.5, -0.75$).

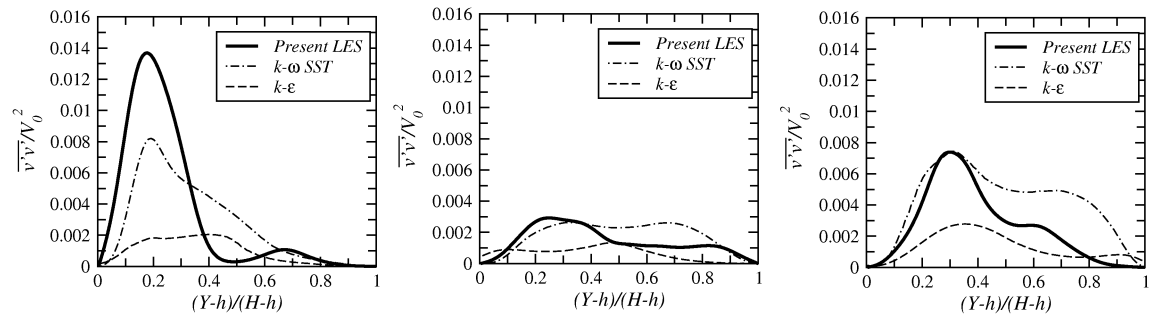


Figure 8.28: Time-averaged dimensionless Reynolds stress component $\overline{v'v'}$ at angular position 270° on three locations inside the penetration ($Z/L = -0.25, -0.5, -0.75$).

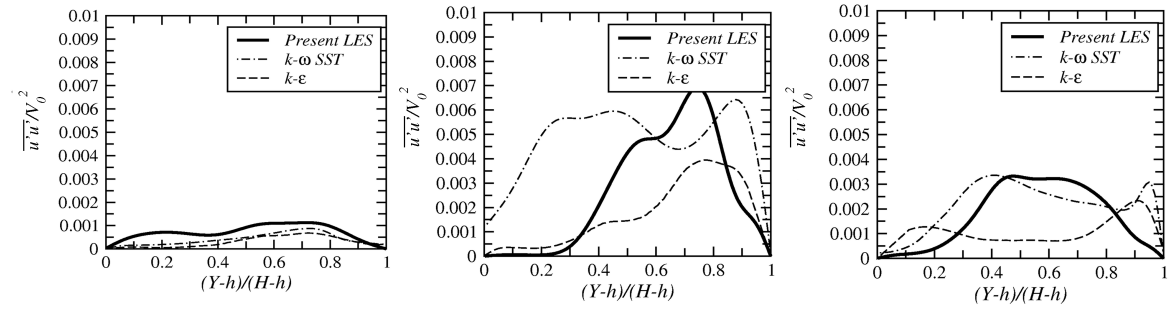


Figure 8.29: Time-averaged dimensionless Reynolds stress component $\overline{u'u'}$ at angular position 270° on three locations inside the penetration ($Z/L = -0.25, -0.5, -0.75$).

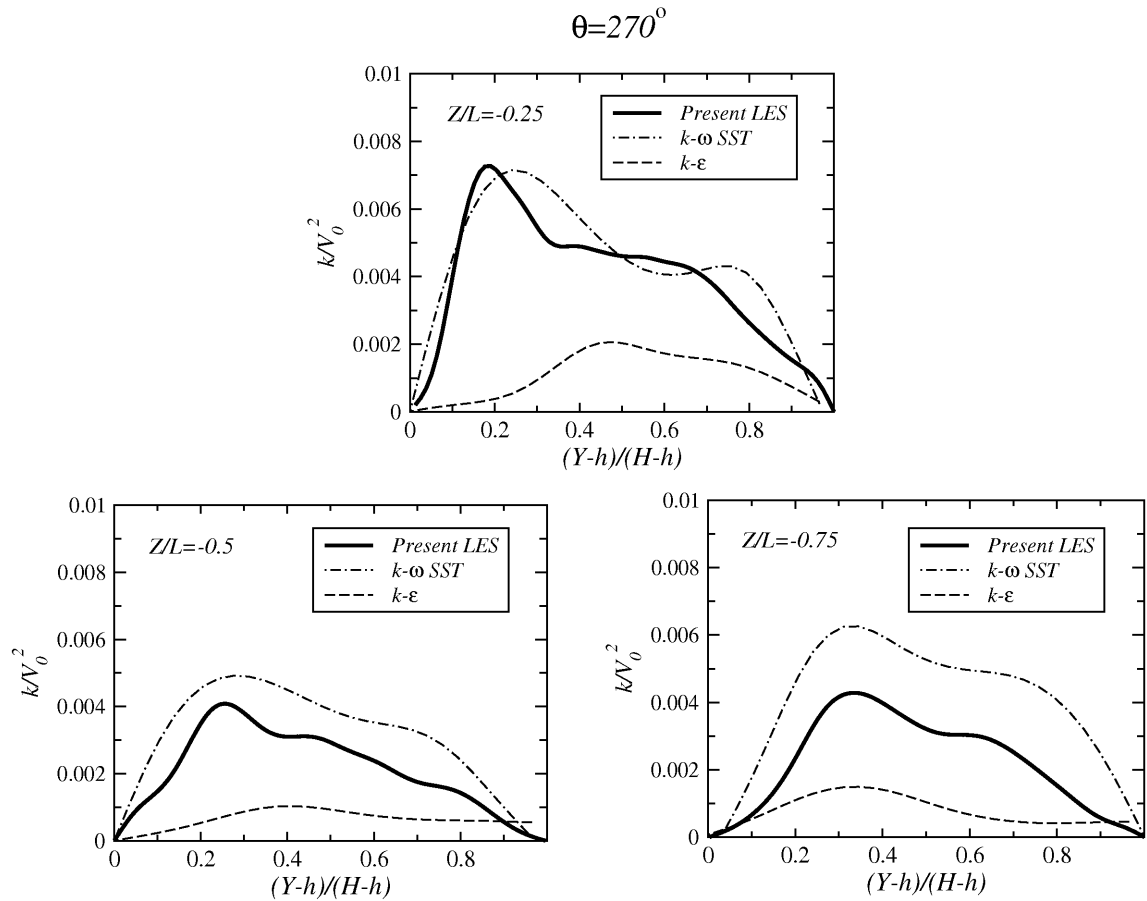


Figure 8.30: Time-averaged dimensionless total turbulent kinetic energy at angular position 270° on three locations inside the penetration ($Z/L = -0.25, -0.5, -0.75$).

Figure 8.31 shows the variation of time-averaged local Nusselt number around the cold inner tube at three positions along the penetration $Z/L = -0.25, -0.5$ and -0.75 . Results obtained from both RANS schemes are in close agreement with the present LES data. The same distribution is shown along the cylindrical penetration at the three axial locations, with a slightly lower heat transfer rate close to the open end of the penetration, this is consistent with the thermal quantitative results mentioned above. The LES together with RANS schemes show a high level of heat transfer between the angular position 0° and 270° , this can be explained by the higher temperature at the upper part of the cylindrical penetration. It decreases to reach a minimum which corresponds to the angular position 270° . It then increases again beyond that point because the boundary layer starts to become thinner again. The $k - \varepsilon$ model agrees with the other models but shows some discrepancies around the 270° region. The use of the log-law-based wall function is the most likely the cause.

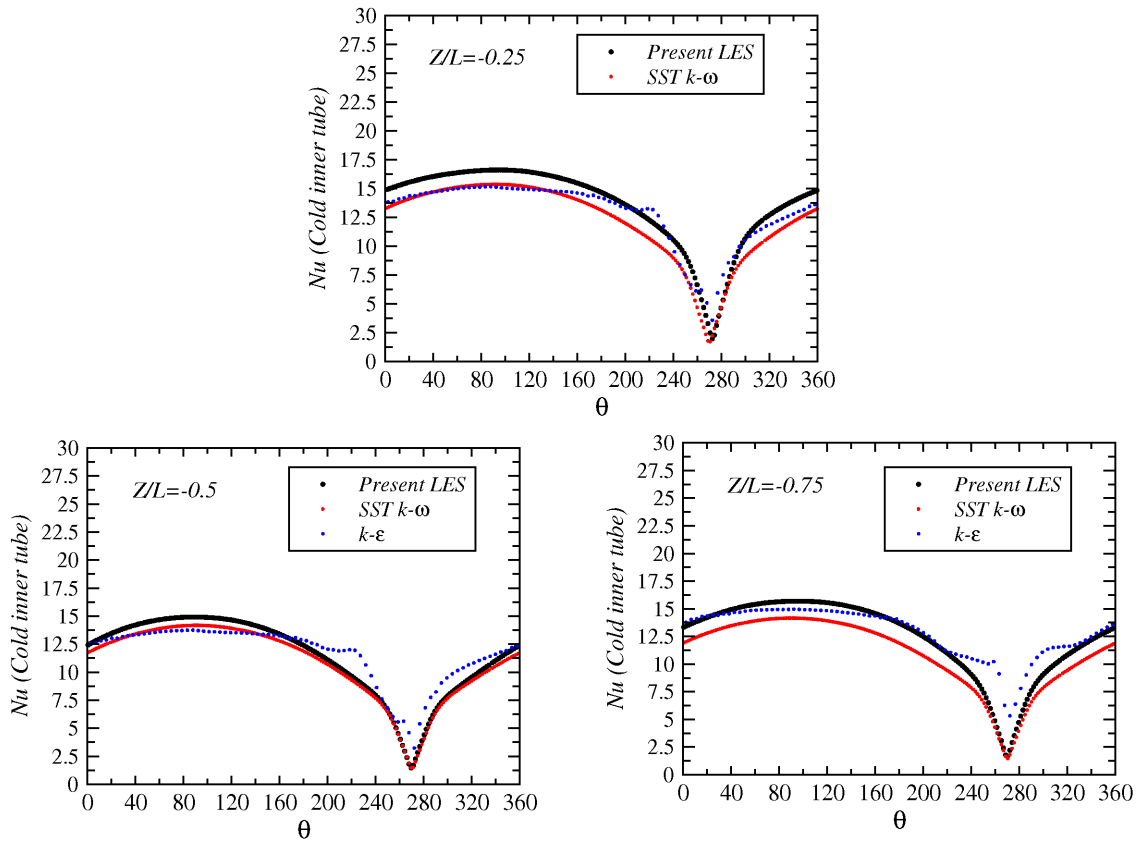


Figure 8.31: Time-averaged local Nusselt number around the inner cold tube on three locations inside the penetration ($Z/L = -0.25, -0.5, -0.75$).

As a final LES result, the temporal power density spectrum profiles of temperature T , W and V velocities at a location A which has the coordinates: $(X - h) / (H - h) = 0$, $(Y - h) / (H - h) = -0.5$ and $Z/L = -0.5$, are presented in Figure 8.32. The FFT analysis shows clear dominant peaks of energy and their values vary from one physical quantity to another at a Strouhal number ranging between 0.0001 and 0.02. The FFT of the axial, W , velocity shows a clear peak at $St = 0.002$, its maximum value is 0.01, this corresponds to the presence of a set of slow large structures at the bottom half of the penetration which may cause fatigue to the bottom outer wall of the cylindrical penetration. The Power spectra of T and V also show a range of dominant energy peaks which have the values of 1 and 0.01 respectively. This also suggests the presence of a set of structures at the bottom of the horizontal annular penetration.

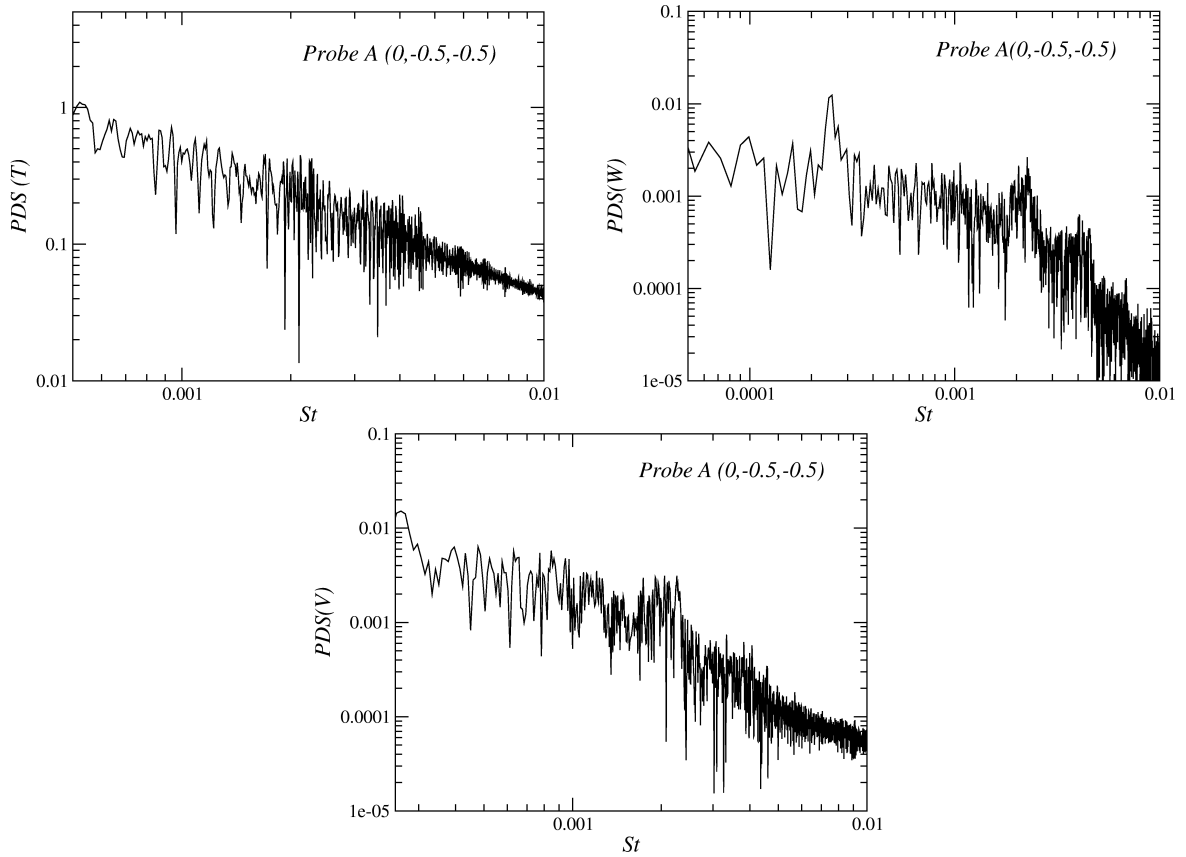


Figure 8.32: Density power spectrum of temperature T and W , V velocity components at probe location $A ((X - h) / (H - h) = 0, (Y - h) / (H - h) = -0.5, Z/L = -0.5)$ inside the horizontal annular penetration.

8.6 Concluding remarks

Turbulent natural convection flow within an industrial application, referred to here as an annular horizontal penetration, has been investigated using a highly resolved LES. One of the aims has been to provide validation data for URANS modelling, and two eddy-viscosity RANS models have also been employed to simulate the flow. As the fluid is cooled by the inner tube, it generally descends towards the bottom of the annulus and flows out of the open end of the penetration. It is replaced by warm fluid which enters mostly through the upper section of the open annulus end. In agreement with earlier URANS work of Omerian [72], LES predictions return large-scale unsteady flow structures inside the penetration which can be captured by RANS models when applied in a time-dependent flow solver. Qualitative and quantitative comparisons show a reasonable agreement between the LES and RANS results, particularly in the mean thermal and velocity fields. The low-Re SST $k - \omega$ model requires a substantially finer mesh than needed for the high-Reynolds-number $k - \varepsilon$ model. There are some discrepancies from the RANS models. This is thought to be due to the use of the effective viscosity approximation for modelling the heat fluxes and the use of the simple wall function with the high-Re model. The temperature variance and some Reynolds stress components are provided here. The $k - \varepsilon$ model shows some discrepancies probably due to the use of the log-law based wall function and the fact that the *Code_Saturne* 2.0 version of the $k - \varepsilon$ does not include any viscosity limiter to reduce the value of the turbulent viscosity in regions of high shear.

The overall heat transfer rate on the inner cylinder surface appears to be fairly constant along the penetration length, but with slightly higher values towards the open end. In the circumferential direction the maximum heat transfer occurs, as would be expected, on the upper surface of the inner tube. The URANS schemes show good agreement of the local Nusselt number comparing with the present LES data except some deviations from the $k - \varepsilon$ model at angular position of 270° . The temporal power density spectrum of thermal and dynamic quantities show a range of dominant peaks of energy which implies the presence of different unsteadiness in the flow and mostly concentrated in the bottom half of the penetration.

Chapter 9

Conclusions and Recommendations for Future Work

9.1 Conclusions

Convection phenomena induced by body forces have been the subject of extensive research efforts. The reliable computation of buoyant flow is important in a number of engineering sectors. Buoyancy-driven flows are physically complex. It is therefore important to have accurate and efficient numerical simulation models. Highly-resolved LES is the principal technique adopted in the present thesis. The effectiveness of the URANS approach is tested for the computation of different challenging test cases:

- URANS model validation of buoyancy-driven flow inside the 2-D vertical cavity
- URANS computation of buoyancy-driven flow inside the 60° tilted cavity under stable stratification
- URANS computation of buoyancy-driven flow inside the 15° tilted cavity under unstable stratification
- URANS and highly-resolved LES of buoyancy-driven flow within 3-D 15° unstably and stably stratified tilted enclosures
- URANS and highly-resolved LES of buoyancy-driven flow of industrial application: the horizontal annular penetration enclosure

2-D vertical cavity

In the present thesis, a turbulent buoyant flow calculation inside a vertical and inclined cavity has been carried out using different RANS models. After a selection of a convenient grid and what is referred to in *Code_Saturne* 2.0 as the “two-velocity-scale wall function” for high-Re models, the two-dimensional buoyancy-driven flow within the vertical cavity of Betts and Bokhari [11] has been computed using several RANS models. Two flow regions have been identified, a large recirculation motion, and a boundary layer at the wall. In general, velocity and thermal fields were well reproduced by almost all low-Re models. However, profiles of velocity and temperature obtained from high-Re models deviate slightly from measurements near the long walls due to the simple wall function strategy embedded within *Code_Saturne* 2.0.

The “two-velocity-scale wall function” used with the high-Re models was shown to perform best amongst the wall functions embedded in *Code_Saturne* 2.0 in predicting the buoyancy-driven flow inside the vertical cavity, although it still showed some discrepancies with experimental data, particularly in the local Nusselt number. A refinement has been tested with the “one- and “two-velocity-scale wall functions”. By modifying the boundary condition value imposed for ε at the near-wall node, to be consistent with what is conventionally employed instead of that originally implemented in *Code_Saturne* 2.0. Dynamic, thermal predictions and the heat transfer rate using the corrected “two-velocity-scale wall function” showed significant improvements. However the changes to the “one-velocity-scale wall function” did not show any advantageous results.

Recently Billard et al. [12] developed an adaptive wall function to use with elliptic-blending model. This approach can be promising to predict wall bounded and buoyant flows.

2-D tilted cavities at 60° under stable stratification

The second test case was the 2-D buoyancy driven flow within the inclined cavity at 60° to the horizontal, heated from the top side (stable stratification), using different RANS models. It was found that this case is similar, in terms of flow physics and model predictions, to the vertical case. Some differences in the models’ predictions of rms velocity fluctuations have been identified between the two cases. Most of the RANS models result in a reasonable representation of the measured Nusselt number along the hot wall. Low-Re approaches are generally closer to the data than the schemes employing the *Code_Saturne* 2.0 wall function.

2-D 15° tilted cavity under unstable stratification

Highly inclined cavities at angles of 15° are also investigated here. The 15° unstably stratified cavities, even with high spanwise aspect ratios, showed three-dimensional and unsteady behaviour. Attempts to reproduce the flow and thermal conditions within the longitudinal (X, Y) mid-plane through two-dimensional steady RANS computations, proved unsuccessful.

3-D 15° unstably and stably stratified tilted enclosures

Fully three-dimensional LES and URANS simulations of buoyancy driven flow within the 15° tilted cavity are conducted here, under both stable and unstable stratifications. The highly-resolved LES data, in accord with the recent experimental data of Cooper et al. [25], show that free convection flows in differentially heated cavities at high angles of inclination become three dimensional, even at high aspect ratios and for both stable and unstable stratification. In the unstably heated cavity, the unstable stratification causes the formation of four longitudinal vortices which extend over the entire length of the cavity and four longitudinal cells. These vortices lead to strong mixing, which results in practically isothermal conditions over most of the cavity and in an isotropic and homogeneous turbulence field. Because of the near isothermal conditions, the time- averaged buoyancy-induced wall-parallel motion is substantially lower than what is found in either the vertical case, or for the stably stratified inclined case. Another consequence of the isothermal conditions and the homogeneous turbulence field is the uniform Nusselt number over the hot and cold sides, both in the longitudinal and spanwise directions. In the stably heated cavity, the three-dimensionality is caused by the thermally insulated side walls. Their presence causes the formation of two counter-rotating longitudinal vortices and two strong longitudinal cells, which transport fluid from the upper end to the lower end of the cavity along the middle and from the lower end to the upper end along the side walls. As a result, the fluid temperature changes more gradually from the hot to the cold side and there is a rise in the core fluid temperature from the lower to the upper end of the cavity. This temperature variation in turn causes strong longitudinal variations in the local Nusselt number. Over the hot side, the Nusselt number is high at the lower end and low at the upper end of the cavity, while over the cold side the local Nusselt number variation is reversed. Velocity and temperature fluctuations are considerably weaker than for the unstably stratified case and also confined to lower frequencies. Comparisons with URANS predictions show that for the unstably stratified cavity all models tested, the high-Re $k - \varepsilon$, the

LRR and SSG second-moment closures and the $k - \omega$ SST are able to reproduce the unsteady three-dimensional structures present, and thus capture the broad features of the flow. The low-Re SST scheme, however, needs substantially finer meshes than the three high-Re models.

For the stably stratified case, the challenge is in reproducing the three-dimensional flow structures which arise as a result of the lateral wall effects and weak buoyancy influences. None of the models tested was able to fully reproduce these features, although further research within the authors group, Omranian [24], suggests that the use of more advanced wall functions, Craft et al. [27], with second-moment closures can result in significant predictive improvements in this case. Also the work of Dehoux et al. [31] showed good prediction of natural convection flows inside stably stratified test cases using the EB-RSM model [65] with GGDH. As far as the local Nusselt number predictions are concerned, somewhat surprisingly, the profiles returned by the high-Re $k - \varepsilon$ model are consistently close to those of the LES predictions, while the local Nu profiles of the second-moment closures and the SST scheme show some deviations. One possible explanation for the poorer second-moment predictions is the use of the effective diffusivity approximation for the turbulent heat fluxes within *Code_Saturne* 2.0, even when the Reynolds stresses are modelled through second-moment closures.

In conclusion, the LES data generated has further advanced our understanding of the flow physics and the thermal characteristics of natural convection in highly inclined cavities, and provides validation data for two highly challenging natural convection test cases. The unsteady RANS computations showed that the use of RANS in the case of unstably stratified flows is very promising and also point to two areas in which current turbulence modelling practices within *Code_Saturne* 2.0 can be improved: the wall function with high-Re models and modelling heat fluxes.

The horizontal annular penetration enclosure

Turbulent natural convection flow within an industrial application, referred to here as an annular horizontal penetration, has been investigated using a highly resolved LES. This penetration can be found in the AGR's. They play a major role in the operation of cooling of the nuclear reactor. The complex buoyancy-driven flow inside the annular penetration enclosure makes this latter a challenging natural convection case. One of the aims has been to provide validation data for URANS modelling, and two eddy-viscosity RANS models have also been employed to simulate the flow. As the fluid is cooled by the inner tube it generally descends towards the bottom of the annulus and flows out of the open end of the penetration. It is replaced by warm fluid which enters

mostly through the upper section of the open annulus end. In agreement with RANS earlier work of Omranian [72], LES results show there to be large-scale unsteady flow structures inside the penetration that can be captured by RANS models when applied in a time-dependent flow solver. Qualitative and quantitative comparisons show a reasonable agreement between the LES and RANS results, particularly in the mean thermal and velocity fields. The low-Re SST $k - \omega$ model requires a substantially finer mesh than that needed for the high-Reynolds-number $k - \varepsilon$ model. There are some discrepancies in the predictions of the RANS models. This is thought to be due to the use of the effective viscosity approximation, use of the simple wall function with the high-Re model. The temperature variance and some Reynolds stress components are provided here. The $k - \varepsilon$ model shows some discrepancies due to the reasons identified earlier. The overall heat transfer rate on the inner cylinder surface appears to be fairly constant along the penetration length, but with slightly higher values towards the open end. In the circumferential direction, the maximum heat transfer occurs, as would be expected, on the upper surface of the inner tube. The URANS schemes show good agreement of the local Nusselt number comparing with the present LES data except some deviations from the $k - \varepsilon$ model at angular position of 270° . The temporal power density spectrum of thermal and dynamic quantities show a range of dominant peaks of energy which implies the presence of different unsteadiness in the flow and mostly concentrated in the bottom half of the penetration.

9.2 Recommendations for future work

In the present thesis a highly resolved LES has been adopted as the main accurate technique to predict and to provide validation data for different challenging natural convection cases. The LES results provide accurate data for future validation of RANS simulations and improvements of natural convection calculations.

The turbulent flows driven by thermal buoyancy are featured by inherent unsteadiness, energy non-equilibrium, strong pressure fluctuations and others, which pose special challenge to RANS models. The effectiveness of the URANS approach was tested and different high and low-Re RANS schemes have been used in the present thesis. The main flaws here, in some complex situations, were mainly caused by the use of the effective viscosity approximation with RANS models for modelling the heat fluxes. The alignment of the heat flux with the mean temperature-gradient vector can lead to model failure in some cases especially with second moment closure. It is therefore worth using

more advanced models for modelling the heat fluxes. The GGDH can be employed to give better approximation of the streamwise component of the turbulent heat flux. The GGDH takes into account more influential parameters in the calculation of $\overline{u_i' t'}$ such as the Reynolds stresses, but it does not take into account all of the important parameters on which $\overline{u_i' t'}$ depends, such as gravity and mean velocity gradients. More complex algebraic schemes, when the Reynolds stresses are modelled through second-moment closures, can be used in order to include the influence of buoyancy effects on the turbulent heat fluxes. The three and four extended algebraic models, $k - \varepsilon - \overline{\theta^2}$ and $k - \varepsilon - \overline{\theta^2} - \varepsilon_\theta$, which were proposed by Hanjalić [36], have been proven by many researchers to well reproduce the mean flow properties, turbulence second moments, and wall heat transfer in a variety of wall-bounded buoyant flows. The EB-RSM model of Manceau and Hanjalić [65] and EB-AFM of Manceau [64] also showed good predictions of heat fluxes.

Another issue was concluded from the present investigation is the simple wall functions embedded in *Code_Saturne* 2.0 which have been used in the present thesis. The use of more advanced wall function can be very promising for prediction of complex buoyant flows. The UMIST-A [27] and UMIST-N [28] schemes are more advanced and improved analytical wall functions. The UMIST-A approach is based on the analytical solution of simplified near-wall momentum and temperature equations, accounting for pressure gradients and other force fields such as buoyancy. The UMIST-N is based on a local one-dimensional numerical solution of the governing equations. Implementing these two approaches into *Code_Saturne* 2.0 will be very fruitful because they are very well improved to tackle the issues associated with the log-law based wall function.

The flows created by cross-flow separation or impingement require modification to eddy viscosity in order to simulate the wide range of length scales present in such flow. When the strain rate is greater than a certain value, the normal component of the Reynolds stress can become negative. Negative normal stress can lead to an over-prediction of turbulent kinetic energy resulting from very small value of dissipation rate, and finally over-prediction of eddy viscosity. The Reynolds stresses must meet certain constraints to be physically plausible. It will be very useful to improve the *Code_Saturne* 2.0' version of the high-Re $k - \varepsilon$ by introducing a realizability constraint for the turbulent viscosity to ensure Schwartz' inequality. Schumann [78] introduced the realizability constraint. This constraint specifies that all the component energies of the turbulent kinetic energy (the diagonal terms of the Reynolds stress tensor) remain non-negative and all off-diagonal components of the Reynolds stress tensor satisfy Schwartz's

inequality. A paper examining realizability in two-equation turbulence models by Moore and Moore [70] provides a good review of stress-limiting methods for eddy-viscosity models.

Finally, many natural convection applications are involved in the nuclear sector and can be very challenging for future numerical investigations. It will be interesting to examine using LES the same tilted cavities as in the present thesis but with twice the spanwise length and see whether one will get twice as many vortices in the spanwise direction or completely different flow pattern. Testing cavities at other inclination or other stratifications will be very beneficial. Further improvements of RANS models and wall functions can be assessed by using the DNS data of flow within a turbulent differentially heated cavity of aspect ratio 5 and Rayleigh number $Ra = 4.5 \times 10^{10}$, which was conducted by Trias et al. [84]. In the present thesis, the flow inside the 3-D horizontal annular penetration has been investigated with one inner central tube. In several advanced Gas Cooled Reactors (AGR's) these penetrations can contain a set of inner tubes ranging from 3 to 44. These tubes carry water and steam respectively into and out of the boilers. It will be interesting to investigate numerically using URANS and LES the buoyant flow between a set of tubes inside the 3-D penetration.

Bibliography

- [1] H. Abumulaweh. Effects of backward- and forward-facing steps on turbulent natural convection flow along a vertical flat plate. *International Journal of Thermal Sciences*, 41(4):376–385, April 2002.
- [2] Y. Addad, D. Laurence, and M. Rabbitt. Turbulent natural nonconvection in horizontal coaxial cylindrical enclosures: LES and RANS models. *Turbulence Heat and Mass Transfer 5. 26-29 September, Croatia*, 2006.
- [3] Y. Addad, M. Mahmoodilari, and D. Laurence. LES And RANS computations of natural convection in a nearly-horizontal shallow cavity. *International Conference of Heat and Mass Transfer (ICHMT8). 11-16 May, Marrakech, Morocco*, 2008.
- [4] M. Aksouh and A. Mataoui. Numerical study of the turbulent natural convection in an enclosed tall cavity for the high and low Rayleigh number. In *Fourth International Conference on Advanced Computational Methods in Engineering (ACOMEN)*, number 1, Belgium, 26-28 May, 2008.
- [5] F. Ampofo. Experimental benchmark data for turbulent natural convection in an air filled square cavity. *International Journal of Heat and Mass Transfer*, 46(19):3551–3572, September 2003.
- [6] F. Ampofo. Turbulent natural convection of air in a non-partitioned or partitioned cavity with differentially heated vertical and conducting horizontal walls. *Experimental Thermal and Fluid Science.*, 29(2):137–157, January 2005.
- [7] M. Aounallah, Y. Addad, S. Benhamadouche, O. Imine, L. Adjlout, and D. Laurence. Numerical investigation of turbulent natural convection in an inclined square cavity with a hot wavy wall. *International Journal of Heat and Mass Transfer*, 50(9-10):1683–1693, May 2007.

- [8] F. Archambeau, N. Méchitoua, and M. Sakiz. Code_Saturne: a Finite Volume Code for the Computation of Turbulent Incompressible Flows-Industrial Applications. *International Journal of Finite Volumes.*, 1, 2004.
- [9] A. Bairi, N. Laraqi, and J. Garciademaria. Numerical and experimental study of natural convection in tilted parallelepipedic cavities for large Rayleigh numbers. *Experimental Thermal and Fluid Science*, 31(4):309–324, February 2007.
- [10] H. Bénard. Les tourbillons cellulaires dans une nappe liquide transportant de la chaleur par convection en régime permanent. *Annual Chimie Physics.*, 23:62, 1901.
- [11] P. L. Betts and I. H. Bokhari. Experiments on turbulent natural convection in an enclosed tall cavity. *International Journal of Heat and Fluid Flow*, 21(6):675–683, 2000.
- [12] F. Billard, K. Osman, and D. Laurence. Development of adaptive wall functions for an elliptic-blending model. In *THMT-12*. Begel House Inc., 2012.
- [13] F. Billard, J. C. Uribe, and D. Laurence. A new formulation of the v2-f model using elliptic blending and Its application to heat transfer prediction. *Engineering Turbulence Modelling and Measurements 7. 4-6 June, Limassol, Cyprus*, 2008.
- [14] A. Bowles and R. Cheesewright. Direct measurements of the turbulence heat flux in a large rectangular air cavity. *Experimental Heat Transfer: A Journal of Thermal Energy Generation, Transport, Storage, and Conversion.*, 2(1):59–69, 1989.
- [15] A. Castrejon and D. B. Spalding. An experimental and theoretical study of transient free-convection flow between horizontal concentric cylinders. *International Journal of Heat and Mass Transfer*, 31(2):273–284, 1988.
- [16] A. Chakir, M. Souli, and N. Aquelet. Study of a turbulent natural convection in cylindrical annuli of gas-insulated transmission lines 400 kV. *Applied Thermal Engineering.*, 23(10):1197–1208, July 2003.
- [17] R. Cheesewright and K. J. King. Stress distribution in natural convection in a rectangular air cavity. In *9th International Conference on Heat Transfer.*, Turkey, 1990.
- [18] R. Cheesewright, K. J. King, and S. Ziai. Experimental data for the validation of computer codes for the prediction of two-dimensional buoyant cavity flows. *Proceedings of the ASME Meeting, HTD*, 60:75–81, 1986.

- [19] K. Y. Chien. Predictions of channel and boundary-layer flows with a low-Reynolds-number turbulence model. *AIAA journal.*, 20(1):33–38, 1982.
- [20] C. C. Chieng and B. E. Launder. On the calculation of turbulent heat transport downstream from an abrupt pipe expansion. *Journal of Numerical Heat Transfer*, 3:189–207, June 1980.
- [21] S. Choi, E. Kim, M. Wi, and S. Kim. Computation of a turbulent natural convection in a rectangular cavity with the low-Reynolds-number differential stress and flux model. *KSME International Journal.*, 18(10):1782–1798, 2004.
- [22] M. Ciofalo. Large Eddy Simulation: a critical survey of models and applications. In *In Advances in Heat Transfer*, pages 321–408. Academic Press, 1994.
- [23] D. E. Coles and E. A. Hirst. Computation of turbulent boundary layers. In *Proceedings of AFOSR-IFP Stanford Conference*, volume 2, 1969.
- [24] D. Cooper, T. J. Craft, K. Esteifi, H. Iacovides, and A. Omranian. The investigation of buoyant flows in differentially heated cavities. *Turbulence Heat and Mass Transfer 6*, 2009.
- [25] D. Cooper, T.J. Craft, K. Esteifi, and H. Iacovides. Experimental investigation of buoyant flows in inclined differentially heated cavities. *International Journal of Heat and Mass Transfer*, 55(23-24):6321–6339, November 2012.
- [26] M. Corcione. Effects of the thermal boundary conditions at the sidewalls upon natural convection in rectangular enclosures heated from below and cooled from above. *International Journal of Thermal Sciences*, 42(2):199–208, February 2003.
- [27] T. Craft, A. Gerasimov, H. Iacovides, and B. Launder. Progress in the generalization of wall-function treatments. *International Journal of Heat and Fluid Flow.*, 23(2):148–160, April 2002.
- [28] T. J. Craft, S. E. Gant, H. Iacovides, and B. E. Launder. a New Wall Function Strategy for Complex Turbulent Flows. *Numerical Heat Transfer, Part B*, 45(4):301–318, April 2004.
- [29] A. A. Dafa’Alla and P. L. Betts. Experimental study of turbulent natural convection in a tall air cavity. *Experimental Heat Transfer.*, 9(2):165–194, 1996.
- [30] J. Daly Bart. Transport Equations in Turbulence. *Physics of Fluids*, 13(11):2634–2649, November 1970.

- [31] F. Dehoux, Y. Lecocq, S. Benhamadouche, R. Manceau, and L. Brizzi. Algebraic modeling of the turbulent heat fluxes using the elliptic blending approach—Application to forced and mixed convection regimes. *Flow, Turbulence and Combustion*, 88(1-2):77–100, October 2011.
- [32] C. P. Desai and K. Vafai. An investigation and comparative analysis of two- and three-dimensional turbulent natural convection in a horizontal annulus. *International Journal of Heat and Mass Transfer*, 37(16):2475–2504, 1994.
- [33] C. P. Desai and K. Vafai. Experimental and numerical study of buoyancy-induced flow and heat transfer in an open annular cavity. *Int. J. Heat Mass Transfer*, 39(10):2053–2066, 1996.
- [34] H. Dol. A comparative assessment of the second-moment differential and algebraic models in turbulent natural convection. *International Journal of Heat and Fluid Flow*, 18(1):4–14, February 1997.
- [35] H. S. Dol and K. Hanjali. Computational study of turbulent natural convection in a side-heated near-cubic enclosure at a high Rayleigh number. *International Journal of Heat and Mass Transfer.*, 44(12):2323–2344, 2001.
- [36] H.S. Dol, K. Hanjalić, and S. Kenjereš. A comparative assessment of the second-moment differential and algebraic models in turbulent natural convection. *Int. J. of Heat and Fluid Flow*, 18(1):4–14, February 1997.
- [37] V. E. R. Driest. On turbulent flow near a wall. *AIAA Journal*, 23(11):1007–1011, 1956.
- [38] P. A. Durbin. Near-wall turbulence closure modeling without "damping functions". *Theoretical and Computational Fluid Dynamics*, 3(1):1–13, 1991.
- [39] E. Evren-Selamet, V. S. Arpaci, and C. Borgnakke. Simulation of Laminar Buoyancy-Driven Flows in an Enclosure. *Journal of Numerical Heat Transfer*, 22(4):401–420, December 1992.
- [40] J. H. Ferziger and M. Peric. *Computational Methods for Fluid Dynamics*. Springer., 3rd editio edition, 2002.
- [41] W. K. George and S. P. Capp. A theory for natural convection turbulent boundary layers next to heated vertical surfaces. *International Journal of Heat Mass Transfer*, 22:813–826, 1979.

- [42] H. Grotjans and F. R. Menter. Wall functions for general application CFD codes. *ECCOMAS*, pages 1112–1117, 1998.
- [43] H. Hanjalić and B. Launder. *Modelling Turbulence in Engineering*. Cambridge University Press, CAMBRIDGE, 2011.
- [44] K. Hanjalić. Natural convection in partitioned two-dimensional enclosures at higher Rayleigh numbers. *International Journal of Heat and Mass Transfer*, 39(7):1407–1427, May 1996.
- [45] K. Hanjalić. One-point closure models for buoyancy-driven turbulent flows. *Annual Review of Fluid Mechanics*, 32:34–47, 2002.
- [46] K. Hanjalić, M. Popovac, and M. Hadziabdic. A robust near-wall elliptic-relaxation eddy-viscosity turbulence model for CFD. *International Journal of Heat and Fluid Flow*, 25(6):1047–1051, December 2004.
- [47] R. Henkes, F. Vandervlugt, and C. Hoogendoorn. Natural-convection flow in a square cavity calculated with low-Reynolds-number turbulence models. *International Journal of Heat and Mass Transfer*, 34(2):377–388, February 1991.
- [48] C. Ho, Y. Cheng, and C. Wang. Natural convection between two horizontal cylinders inside a circular enclosure subjected to external convection. *International Journal of Heat and Fluid Flow*, 15(4):299–306, August 1994.
- [49] K. Hsieh. Numerical modeling of buoyancy-driven turbulent flows in enclosures. *International Journal of Heat and Fluid Flow*, 25(4):659–670, August 2004.
- [50] J. C. R. Hunt, A. A. Wray, and P. Moin. Eddies, streams, and convergence zones in turbulent flows. *International Journal of Heat and Fluid Flow*, pages 193–208, 1988.
- [51] H. Inaba. Experimental study of natural convection in an inclined air layer. *International Journal of Heat and Mass Transfer*, 27(8):1127–1139, August 1984.
- [52] N. Z. Ince and B. E. Launder. On the computation of buoyancy-driven turbulent flows in rectangular enclosures. *International Journal of Heat and Fluid Flow*, 9:110–117, 1989.
- [53] W. P. Jones and B. E. Launder. The prediction of laminarization With a two-equation model of turbulence. *International Journal of Heat and Mass Transfer*, 15:301–314, 1972.

- [54] W. P. Jones and B. E. Launder. The prediction of laminarization with a two-equation model of turbulence. *International Journal of Heat and Mass Transfer*, 15:301–314, 1972.
- [55] H. J. Kaltenbach, T. Gerz, and U. Schumann. Large-eddy simulation of homogeneous turbulence and diffusion in stably stratified shear flow. *Journal of Fluid Mechanics*, 280:1–40, April 2006.
- [56] S. Kenjere and K. Hanjalić. Prediction of turbulent thermal convection in concentric and eccentric horizontal annuli. *International Journal of Heat and Fluid flow.*, 16(5):429–439, 1995.
- [57] A. T. Kirkpatrick and M. Bohn. An experimental investigation of mixed cavity natural convection in the high Rayleigh number regime. *International Journal of Heat and Mass Transfer*, 29(1):69–82, January 1986.
- [58] R. Kumar. Study of natural convection in horizontal annuli. *International Journal of Heat and Mass Transfer*, 31(6):1137–1148, 1988.
- [59] B. E. Launder and M. M. Gibson. Ground effects on pressure fluctuations in the atmospheric boundary layer. *Journal of Fluid Mechanics.*, 86(3):491–511, 1978.
- [60] B. E. Launder, G. J. Reece, and W. Rodi. Progress in the development of a Reynolds-stress turbulence closure. *Journal of Fluid Mechanics*, 68(03):537, March 1975.
- [61] D. Laurence, J. C. Uribe, and S. V. Utyuzhnikov. A robust formulation of the v2-f model and its applications. *Flow, Turbulence and Combustion*, 73:169–185, 2004.
- [62] F. Liu and J. X. Wen. Developement and validation of an advanced turbulence model for buoyancy driven flows in enclosures. *International Journal of Heat and Mass Transfer*, 42:3967–3981, 1999.
- [63] R. K. Mac Gregor and A. F. Emery. Free convection through vertical plane layers at moderate and high Prandtl number fluids. *Journal of Heat Transfer.*, 91:391–403, 1969.
- [64] R. Manceau. An improved version of the elliptic blending model application to non-rotating and rotating channel flows. In *Proc. 4th Intenational Symposium of Turbulence and Shear Flow Phenomena*, number 18, Williamsburg, VA, USA, 2005.

- [65] R. Manceau and K. Hanjalić. Elliptic blending model: a new near-wall Reynolds-stress turbulence closure. *Physics of Fluids*, 14(2):744–755, 2002.
- [66] N. C. Markatos and K. A. Pericleous. Laminar and turbulent natural convection in an enclosed cavity. *International Journal of Heat Mass Transfer*, 27(5):755–772, 1984.
- [67] Andrew E Mcleod and Eugene H Bishop. Turbulent natural convection of gases in horizontal cylindrical annuli at cryogenic temperatures. *International Journal of Heat and Mass Transfer*, 32(10):1967–1978, 1989.
- [68] F. R. Menter. Two-equation eddy-viscosity turbulence models for engineering applications. *AIAA journal*, 32(8):1598–1605, 1994.
- [69] Y. Miki, K. Fukuda, and N. Taniguchi. Large eddy simulation of turbulent natural convection in concentric horizontal annuli. *International Journal of Heat and Fluid flow.*, 14(3):210–216, 1993.
- [70] J. G. Moore and J. Moore. Realizability in two-equation turbulence models. In *AAIA 30th Fluid Dynamics Conference*, Fluid Dynamics and Co-located Conferences, pages 9999–33729, June 1999.
- [71] S. Muzaferija and D. Gosman. Finite-volume CFD procedure and adaptive error control strategy for grids of arbitrary topology. *Journal of computational physics*, 138(2):766–787, 1997.
- [72] A. Omranian. The Computation of Turbulent Natural Convection Flows. Technical report, The University of Manchester, 2011.
- [73] E. Padilla and A. Silveiraneto. Large-eddy simulation of transition to turbulence in a heated annular channel. *Comptes Rendus Mécanique*, 333(8):599–604, August 2005.
- [74] T. W. J. Peeters and R. A. W. M. Henkes. The Reynolds-stress model of turbulence applied to the natural-convection heated vertical plate. *International of Hear and Mass Transfer*, 35(2):403–420, 1992.
- [75] S. Peng. Large eddy simulation for turbulent buoyant flow in a confined cavity. *International Journal of Heat and Fluid Flow*, 22(3):323–331, June 2001.
- [76] S. B. Pope. *Turbulent Flows*. Cambridge University Press., 2000.

- [77] C. M. RHIE and W. L. CHOW. Numerical study of the turbulent flow past an airfoil with trailing edge separation. *AIAA Journal*, 21(11):1525–1532, November 1983.
- [78] U. Schumann. Realizability of Reynolds-stress turbulence models. *Physics of Fluids*, 20(5):721, May 1977.
- [79] M. A. R. Sharif and W. Liu. Numerical Study of Turbulent Natural Convection in a Side-Heated Square Cavity at Various Angles of Inclination. *Journal of Numerical Heat Transfer*, 43(7):693–716, May 2003.
- [80] L. Snoussi, R. Chouikh, and A. Guizani. Numerical study of the natural convection flow resulting from the combined buoyancy effects of thermal and mass diffusion in a cavity with differentially heated side walls. *Desalination and the Environment.*, 182(1-3):143–150, November 2005.
- [81] C. G. Speziale, S. Sarkar, and T. B. Gatski. Modelling the pressure-strain correlation of turbulence: an invariant dynamical systems approach. *Journal of Fluid Mechanics*, 227:245–272, April 1991.
- [82] Y. S. Tian and T. G. Karayiannis. Low turbulence natural convection in an air filled square cavity. Part I: the thermal and fluid flow fields. *International Journal of Heat and Mass Transfer*, 43(6):849–866, 2000.
- [83] S. Tieszen, A. Ooi, P. Durbin, and M. Behnia. Modeling the natural convection heat transfer and dryout heat flux in a porous debris bed. *Journal of Heat Transfer*, 79(10):110, 2008.
- [84] F. X. Trias, A. Gorobets, A. Oliva, and C. D. Pérez-Segarra. DNS and regularization modeling of a turbulent differentially heated cavity of aspect ratio 5. *International Journal of Heat and Mass Transfer*, 57(1):171–182, January 2013.
- [85] F. X. TRIAS, M. SORIA, A. OLIVA, and C. D. PÉREZ-SEGARRA. Direct numerical simulations of two- and three-dimensional turbulent natural convection flows in a differentially heated cavity of aspect ratio 4. *Journal of Fluid Mechanics*, 586:259, August 2007.
- [86] L. Valencia, J. Pallares, I. Cuesta, and F. X. Grau. Turbulent Rayleigh-Bénard convection of water in cubical cavities: A numerical and experimental study. *International Journal of Heat and Mass Transfer*, 50(15-16):3203–3215, 2007.

- [87] J. P. Van Doormal and G. D. Raithby. Enhancements of the SIMPLE algorithm for predicting incompressible fluid flows. *Numerical Heat Transfer*, 7:147–163, 1984.
- [88] T. Versteegh. Turbulent budgets of natural convection in an infinite, differentially heated, vertical channel. *International Journal of Heat and Fluid Flow*, 19(2):135–149, April 1998.
- [89] C. Y. Warner and A. S. Vrdat. An experimental investigation of turbulent natural convection in air at low pressure along a vertical heated flat plate. *International Journal of Heat and Mass Transfer*, 11:397–406, 1968.
- [90] D. C. Wilcox. Reassessment of the scale-determining equation for advanced turbulence models. *AIAA Journal*, 26(11):1299–1310, 1988.
- [91] D. C. Wilcox. A half century historical review of the k-omega model. In *29th Aerospace Sciences Meeting. Jan. 7-10*, Reno, NV, 1991.
- [92] D. C. Wilcox. *Turbulence modeling for CFD*. 2nd edition, 1998.
- [93] F. Yguel. Etude de la convection naturelle tridimensionnelle dans les cavites fermees de grandes dimensions. Technical report, Poitiers, 1988.
- [94] S. H. Yin, T. Y. Wung, and K. Chen. Natural convection in an air layer enclosed within rectangular cavities. *International Journal of Heat and Mass Transfer*, 21(3):307–315, 1978.

Appendix A

Published papers

A.1 International journal paper

D. Ammour, T. J. Craft, H. Iacovides, Highly Resolved LES and URANS of Turbulent Buoyancy-Driven Flow Within Inclined Differentially-Heated Enclosures. *Flow, Turbulence and Combustion*: Volume 91, Issue 3 (2013), Page 669-696. DOI **10.1007/s10494-013-9497-1**.

D. Ammour, T. J. Craft, H. Iacovides, Numerical Investigation of Turbulent Natural Convection Flow Inside Horizontal Penetration Enclosures in the AGR using highly resolved LES. Submitted paper to *International Journal of Heat and Fluid Flow* (2013).

A.2 List of international conference papers

D. Ammour, T. J. Craft, H. Iacovides. Computation of Turbulent Natural Convection Flow Inside Horizontal Cylindrical Penetration Enclosure Using URANS and LES Approaches. *THMT7 (7th International Symposium on Turbulence, Heat and Mass Transfer)*, September 24-27, 2012, Palermo, Italy.

D. Ammour, T. J. Craft, H. Iacovides. LES and URANS Numerical Analysis of Turbulent Natural Convection Flow Inside 3-D Rectangular Tilted Differentially Heated Enclosures. *ETMM9 (9th International ERCOFTAC Symposium on Engineering Turbulence Modelling and Measurements)*, June 6-8, 2012, Thessaloniki, Makedonia, Greece.

D. Ammour, T. J. Craft, H. Iacovides. Model Validation for Buoyancy-Driven Flows Inside 2-D Differentially-Heated Cavities. *UKHTC (UK Heat Transfer Conference)*, August 30-31, 2011, Leeds, UK.

D. Ammour, T. J. Craft, H. Iacovides. LES and URANS Numerical Analysis of Turbulent Natural Convection Flow Inside 3-D Rectangular Tilted Differentially-Heated Cavities. *PGR*

conference, December 14, 2011, Manchester, UK.

D. Ammour, T. J. Craft, H. Iacovides. The Validation of *Code_Saturne* 2.0 for Buoyancy-Driven Flows In Differentially-Heated enclosures. *PGR conference*, July 1, 2010, Manchester, UK.

Appendix B

RANS models

B.1 Two-Equation EVMs

In general, two equation models solve an equation for the turbulent kinetic energy, k , and one other scale determining transport equation.

The Standard $k - \varepsilon$ model

The most commonly used two-equations turbulence model over the last three decades is the standard ε model [53]. The second transport equation that is solved in the standard $k - \varepsilon$ model is the dissipation of turbulent kinetic energy per unit mass, ε . The standard $k - \varepsilon$ model by Jones and Launder, as described in [53] is as follows,

Eddy Viscosity

$$\nu_t = C_\mu k^2 / \varepsilon, \quad (\text{A.1})$$

Turbulent Kinetic Energy

$$\frac{\partial k}{\partial t} + U_j \frac{\partial k}{\partial x_j} = P_k - \varepsilon + \frac{\partial}{\partial x_j} \left[(\nu + \nu_t / \sigma_k) \frac{\partial k}{\partial x_j} \right], \quad (\text{A.2})$$

Dissipation rate

$$\frac{\partial \varepsilon}{\partial t} + U_j \frac{\partial \varepsilon}{\partial x_j} = C_{\varepsilon 1} \frac{\varepsilon}{k} P_k - C_{\varepsilon 2} \frac{\varepsilon^2}{k} + \frac{\partial}{\partial x_j} \left[(\nu + \nu_t / \sigma_\varepsilon) \frac{\partial \varepsilon}{\partial x_j} \right], \quad (\text{A.3})$$

Closure coefficient and auxiliary relations

$$\begin{aligned} C_{\varepsilon 1} &= 1.44, & C_{\varepsilon 2} &= 1.92, & C_{\mu} &= 0.09, & \sigma_k &= 1.0, & \sigma_{\varepsilon} &= 1.3, \\ \ell &= C_{\mu} k^{3/2} / \varepsilon, \end{aligned} \tag{A.4}$$

This model is implemented in *Code_Saturne* 2.0 and has produced acceptable results for a wide range of buoyancy-driven flows.

The $k - \omega$ model

In $k - \omega$ models the modelled $k - equation$ is solved with an equation for the specific rate of dissipation of turbulent kinetic energy, $\omega = \varepsilon / k$. The most popular $k - \omega$ model is that of Wilcox [90] which is commonly referred to as standard $k - \omega$ model:

Turbulent kinetic energy

$$\frac{\partial k}{\partial t} + U_j \frac{\partial k}{\partial x_j} = P_k - \beta^* k \omega + \frac{\partial}{\partial x_j} \left[(\nu + \sigma^* \nu_t) \frac{\partial k}{\partial x_j} \right], \tag{A.5}$$

Specific Dissipation rate

$$\frac{\partial \omega}{\partial t} + U_j \frac{\partial \omega}{\partial x_j} = \alpha \frac{\omega}{k} P_k - \beta \omega^2 + \frac{\partial}{\partial x_j} \left[(\nu + \sigma \nu_t) \frac{\partial \omega}{\partial x_j} \right], \tag{A.6}$$

Eddy viscosity

$$\nu_t = \frac{k}{\omega}, \tag{A.7}$$

Closure coefficients and auxiliary relations

$$\begin{aligned} \alpha &= 13/25, & \beta &= \beta_o f_{\beta}, & \beta^* &= \beta_o^* f_{\beta}, & \sigma &= 1/2, & \sigma^* &= 1/2, \\ \beta_o &= 9/125, & f_{\beta} &= 1.0, & \beta_o^* &= 9/100, & f_{\beta} &= 1.0, \\ \ell &= k^{1/2} / \omega, \end{aligned} \tag{A.8}$$

Wilcox [90] has illustrated that the model not only performs well for flat boundary layer flows. the major downfall of the standard $k - \omega$ model is that it has a large dependence on the free-stream boundary conditions for ω . In some cases this can lead to inaccurate solution if ω is not appropriately specified at the free-stream boundary.

Menter’s SST model:

Wilcox [91] have shown that the standard $k - \omega$ model processes an inappropriate dependency on the free-stream boundary condition for ω . Wilcox [91] has shown that this free-stream boundary condition can effect the eddy-viscosity. However the effect is less for boundary layer flows (especially for high-Reynolds-number flows) than it is for free-shear flows. Menter introduced cross diffusion in a non-linear manner by multiplying the cross diffusion term with “blending functions” [68]. These functions are zero at the inner edge of a turbulent boundary layer and blend to a unitary value at the outer edge of the layer. Consequently the model behaves like the $k - \varepsilon$ model away from walls and like the $k - \omega$ model in the near-wall region.

Menter proposed the Shear-Stress Transport (SST) model [68], which is implemented in *Code_Saturne* 2.0 and it is used in the present work. The SST model uses a new definition of the eddy-viscosity:

Turbulent kinetic energy

$$\frac{\partial k}{\partial t} + U_j \frac{\partial k}{\partial x_j} = P_k - \beta^* k \omega + \frac{\partial}{\partial x_j} \left[(\nu + \sigma^* \nu_t) \frac{\partial k}{\partial x_j} \right], \quad (\text{A.9})$$

Specific dissipation rate

$$\frac{\partial \omega}{\partial t} + U_j \frac{\partial \omega}{\partial x_j} = \alpha \frac{\omega}{k} P_k - \beta \omega^2 + \frac{\partial}{\partial x_j} \left[(\nu + \sigma \nu_t) \frac{\partial \omega}{\partial x_j} \right] + 2(1 - F_1) \frac{\sigma_{\omega 2}}{\omega} \frac{\partial k}{\partial x_j} \frac{\partial \omega}{\partial x_j}, \quad (\text{A.10})$$

Eddy viscosity

$$SST : \nu_t = \frac{a_1 k}{\max(a_1 \omega; SF_2)}, \quad (\text{A.11})$$

Closure coefficients and auxiliary relations

Let ϕ represent the set of closure constants for the SST model and let ϕ_1 and ϕ_2 represent the constants from the standard $k - \varepsilon$ and $k - \omega$ models respectively.

Set 1, ϕ_1 (*standard $k - \omega$*):

$$\begin{aligned}\beta_1 &= 0.075, & \beta^* &= 0.09, & \sigma_{k1} &= 0.5, \\ \sigma_{\omega 1} &= 0.5, & \kappa &= 0.41, & \alpha_1 &= \beta_2/\beta^* - \sigma_{\omega 1}\kappa^2/\sqrt{\beta^*},\end{aligned}\tag{A.12}$$

Set 2, ϕ_2 (*standard $k - \varepsilon$*):

$$\begin{aligned}\beta_2 &= 0.0828, & \beta^* &= 0.09, & \sigma_{k2} &= 1.0 \text{ (BSL)}, & \sigma_{k2} &= 0.85 \text{ (SST)}, \\ \sigma_{\omega 2} &= 0.85, & \kappa &= 0.41, & \alpha_2 &= \beta_2/\beta^* - \sigma_{\omega 2}\kappa^2/\sqrt{\beta^*},\end{aligned}\tag{A.13}$$

In Menter' models the constants ϕ are calculated using the following blend between the constants ϕ_1 and ϕ_2 :

$$\phi = F_1\phi_1 + (1 - F_1)\phi_2,\tag{A.14}$$

$$F_1 = \tanh\left(\arg_1^4\right),\tag{A.15}$$

and

$$\arg_1 = \min\left[\max\left(\frac{\sqrt{k}}{0.09\omega y}; \frac{500\nu}{y^2\omega}\right) \frac{4\rho\sigma_{\omega 2}k}{CD_{k\omega}y^2}\right],\tag{A.16}$$

Here y is the distance to the nearest surface and $CD_{k\omega}$ is the positive portion of the cross diffusion term, i.e.,

$$CD_{k\omega} = \max\left(2\rho\sigma_{\omega 2}\frac{1}{\omega}\frac{\partial k}{\partial x_j}\frac{\partial \omega}{\partial x_j}; 10^{-20}\right),\tag{A.17}$$

The blending function for the eddy-viscosity relation in the SST model is defined as:

$$F_2 = \tanh \left(arg_2^2 \right), \quad (\text{A.18})$$

where

$$arg_2 = \max \left(2 \frac{\sqrt{k}}{0.09\omega y}; \frac{500\nu}{y^2\omega} \right), \quad (\text{A.19})$$

The $\overline{v^2} - f$ model, version of Durbin

In the $\overline{v^2} - f$ model suggested by Durbin [38] who proposed a surrogate scalar transport equation for a quantity he termed $\overline{v^2}$ and its source term f . Thus, in addition to the k and ε -equations of the $k - \varepsilon$ eddy viscosity model. This enables to account for wall blocking effects as in second moment closures. The main idea is to approximate directly the two-point correlation in the integral equation of the pressure redistribution term by an isotropic exponential function. The non-local character of the redistribution term is preserved by the elliptic nature of the equation.

In modelling of the Reynolds Stress equations Durbin [38] proposed an elliptic relaxation approach to model the pressure-velocity fluctuations term ϕ_{ij} in order to take into account the wall effects in the form of:

$$\phi_{ij} - L^2 \nabla^2 \phi_{ij} = \phi_{ij}^h, \quad (\text{A.20})$$

where ϕ_{ij}^h corresponds to the quasi-homogeneous solution. In the framework of the full Reynolds Stress model. Durbin solves an equation for $f_{ij} = \phi_{ij}/k$ for each ij -component of the tensor. Thus, the total number of equations is increased by six.

In the case of the $\overline{v^2} - f$ model the system of equations for the Reynolds Stress Tensor components is replaced by a transport equation for the value $\overline{v^2}$ and an elliptic equation for a scalar function f related to the energy distribution in the equation for $\overline{v^2}$. The main far-wall-flow is supposed to be isotropic and the $k - \varepsilon$ model can be used. The complete model can be summarised by the following equation set including the Durbin realizability constraint $\mathcal{T} = \min \left[\frac{k}{\varepsilon}, \frac{a}{\sqrt{6}C_\mu S} \right]$, $S = \sqrt{S_{ij}S_{ij}}$, implemented in the definitions of the time and length scales,

$$\frac{\partial k}{\partial t} = P_k - \varepsilon + \frac{\partial}{\partial x_k} \left[(\nu + \nu_t) \frac{\partial k}{\partial x_k} \right], \quad (\text{A.21})$$

$$\frac{\partial \varepsilon}{\partial t} = \frac{C'_{\varepsilon 1} P_k - C_{\varepsilon 2} \varepsilon}{\mathcal{T}} + \frac{\partial}{\partial x_k} \left[\left(\nu + \frac{\nu_t}{\sigma_k} \right) \frac{\partial \varepsilon}{\partial x_k} \right], \quad (\text{A.22})$$

$$\frac{\partial \overline{v^2}}{\partial t} = kf - \frac{\overline{v^2}}{k} \varepsilon + \frac{\partial}{\partial x_k} \left[(\nu + \nu_t) \frac{\partial \overline{v^2}}{\partial x_k} \right], \quad (\text{A.23})$$

$$f - L^2 \frac{\partial^2 f}{\partial x_k^2} = (C_1 - 1) \frac{(2/3 - \overline{v^2}/k)}{\mathcal{T}} + C_2 \frac{\mathcal{P}_k}{k}, \quad (\text{A.24})$$

$$\mathcal{T} = \max \left[\min \left(\frac{k}{\varepsilon}, \frac{ak}{v^2 C_\mu \sqrt{6 S_{ij} S_{ij}}} \right), C_\mathcal{T} \left(\frac{\nu}{\varepsilon} \right)^{1/2} \right], \quad (\text{A.25})$$

$$L = C_L \max \left[\min \left(\frac{k^{3/2}}{\varepsilon}, \frac{k^{3/2}}{v^2 C_\mu \sqrt{6 S_{ij} S_{ij}}} \right), C_\eta \left(\frac{\nu^3}{\varepsilon} \right)^{1/4} \right], \quad (\text{A.26})$$

Eddy viscosity

$$\nu_t = C'_\mu \overline{v^2} \mathcal{T}, \quad (\text{A.27})$$

Closure coefficients and auxiliary relations

It's noted that coefficients C_1 and C_2 originate from the pressure-strain model. Originally, Durbin used the values from the LRR model (1.5 and 0.4, respectively) but subsequently settled for:

$$\begin{aligned} C_\mu &= 0.19, \quad \sigma_k = 1, \quad \sigma_\varepsilon = 1.3, \quad C_1 = 1.4, \quad C_2 = 0.3, \\ C_\mathcal{T} &= 6, \quad C_\eta = 80, \quad C_L = 0.17, \quad C'_{\varepsilon 1} = 1.4 \left[1 + 0.045 \sqrt{\frac{k}{v^2}} \right], \end{aligned} \quad (\text{A.28})$$

The Equation set (A.21)-(A.27) is designed to be integrated up to the wall, using the exact boundary conditions for k and $\overline{v^2}$ (both equal to zero) and $\varepsilon_\omega = 2\nu k/y^2$ at the wall-adjacent node while the wall value of f , i.e. f_ω , is determined from the wall-limiting balance of terms in the $\overline{v^2}$ equation:

$$\left. \frac{\partial \overline{v^2}}{\partial t} \right|_{y \rightarrow 0} = 0 = \underbrace{\frac{k}{\alpha y^2} f}_{\alpha y^2} - \underbrace{\frac{\overline{v^2}}{k} \varepsilon}_{\alpha y^2} + \underbrace{\frac{\partial}{\partial y} \left(\nu_{eff} \frac{\partial \overline{v^2}}{\partial y} \right)}_{\alpha y^2}, \quad (\text{A.29})$$

which results in

$$f_\omega = \frac{-20 \nu^2 \overline{v^2}}{\varepsilon y^4}, \quad (\text{A.30})$$

Successful predictions of a range of flows have been reported, however, the boundary condition for f , Equation A.30, may cause computational instability as the equation is sensitive to near-wall grid clustering: a small unbalance between the numerator and denominator (both varying as y^4 since, in the wall limit $\overline{v^2} \propto y^4$). Thus, the $\overline{v^2} - f$ model does not tolerate very small wall-normal dimensions of the wall-adjacent grid cell. The problem can be avoided by solving the $\overline{v^2}$ and f equations, (A.23) and (A.24), simultaneously.

The $\varphi - f$ model

In order to improve the computational robustness Hanjalić et al. [46] proposed to solve a transport equation for the ratio $\varphi = \overline{v^2}/k$ instead of $\overline{v^2}$, and independently by Laurence et al. [61]. The φ equation can be derived directly from $\overline{v^2}$ and k equations, but an extra 'Cross-diffusion' term, X , appears from direct derivation of the φ equation from the k and $\overline{v^2}$ equations. Equations of φ and f can be summarised as

$$\frac{\partial \varphi}{\partial t} = f - \frac{\varphi}{k} P_k + \frac{\partial}{\partial x_k} \left[\left(\nu + \frac{\nu_t}{\sigma_\varphi} \right) \frac{\partial \varphi}{\partial x_k} \right], \quad (\text{A.31})$$

$$f - L^2 \frac{\partial^2 f}{\partial x_k^2} = \left(C_1 - 1 + C_5^* \frac{P_k}{\varepsilon} \right) \frac{(2/3 - \varphi)}{\mathcal{T}}, \quad (\text{A.32})$$

$$X = \frac{2}{k} \left(\nu + \frac{\nu_t}{\sigma_\varphi} \right) \frac{\partial \varphi}{\partial x_k} \frac{\partial k}{\partial x_k}, \quad (\text{A.33})$$

Closure coefficients and auxiliary relations

$$\begin{aligned} C'_\mu &= 0.22, & C_{\varepsilon 1} &= 1.4 (1 + 0.012/\varphi), & C_1 &= 1.4, & C_{\varepsilon 2} &= 1.9, & C_5^* &= 0.65 \\ \sigma_k &= 1.0, & \sigma_\varepsilon &= 1.3, & \sigma_\varphi &= 1.2, & \sigma_\mathcal{T} &= 6.0, & C_L &= 0.36, & C_\eta &= 85, \end{aligned} \quad (\text{A.34})$$

The $\varphi - f$ model offers two advantages compared with the original $\overline{v^2} - f$ model.

- Instead of ε appearing in the $\overline{v^2}$ equation, which is difficult to model correctly very close to a wall, the φ -equation contains the kinetic energy production P_k , which is much easier to produce accurately if the local turbulent stress and the mean velocity gradient are captured properly.
- Because $\varphi \propto y^2$ as $y \rightarrow 0$, the wall boundary condition for φ reduces to a balance of only two terms, the elliptic relaxation function, f , and the viscous diffusion \mathcal{D}_φ^ν , both with finite values at the wall. In comparison, $P_k \varphi / k$ is negligible as it varies as y^3 .

$$\left. \frac{\partial \varphi}{\partial t} \right|_{y \rightarrow 0} = 0 = \underbrace{f}_{\alpha y^0} - \underbrace{\frac{\varphi}{k} P_k}_{\alpha y^3} + \underbrace{\frac{\partial}{\partial y} \left(\nu_{eff} \frac{\partial \varphi}{\partial y} \right)}_{\alpha y^0}, \quad (\text{A.35})$$

Thus, the wall boundary condition for f becomes:

$$f_\omega = \frac{-2\nu\varphi}{y^2}, \quad (\text{A.36})$$

The new $\varphi - \alpha$ model, version of Billard

Billard [13] combines proposals of Laurence et al. [61] and Manceau and Hanjalić [45]. An elliptic equation is solved for the non-dimensional parameter α (which takes the value 0 at walls and relaxes towards 1 further away) and allows a complete removal of the boundary condition problem. The source term f is defined as a blending between two different forms as follows:

$$f = (1 - \alpha^P) f_w + \alpha^P f_h, \quad (\text{A.37})$$

The functions f_w and f_h are defined, respectively, as the model for f at the wall and away from the wall.

The part of the cross diffusion term associated to the molecular viscosity is defined as

$$\frac{2}{k} \nu \frac{\partial k}{\partial x_j} \frac{\partial \varphi}{\partial x_j} = (1 - \alpha^P) \times 4 \frac{\varphi \varepsilon}{k} + \alpha^P \frac{2}{k} \nu \frac{\partial k}{\partial x_j} \frac{\partial \varphi}{\partial x_j}, \quad (\text{A.38})$$

Equations of the $\varphi - \alpha$ are represented as

$$\frac{\partial k}{\partial t} = P_k - \varepsilon + \frac{\partial}{\partial x_j} \left[\left(\nu + \frac{\nu_t}{\sigma_k} \right) \frac{\partial k}{\partial x_j} \right], \quad (\text{A.39})$$

$$\frac{\partial \varepsilon}{\partial t} = \frac{C'_{\epsilon 1} P_k - C_{\epsilon 2} \varepsilon}{\mathcal{T}} + \frac{\partial}{\partial x_j} \left[\left(\nu + \frac{\nu_t}{\sigma_\varepsilon} \right) \frac{\partial \varepsilon}{\partial x_j} \right], \quad (\text{A.40})$$

$$L^2 \Delta \alpha - \alpha = -1, \quad (\text{A.41})$$

$$\begin{aligned} \frac{\partial \varphi}{\partial t} &= (1 - \alpha^P) f_w + \alpha^P f_h - P_k \frac{\varphi}{k} + \frac{2}{k} \left(\alpha^P \nu + \frac{\nu_t}{\sigma_k} \right) \frac{\partial k}{\partial x_j} \frac{\partial \varphi}{\partial x_j} + \\ &\frac{\partial}{\partial x_j} \left[\left(\nu + \frac{\nu_t}{\sigma_\varphi} \right) \frac{\partial \varphi}{\partial x_j} \right] + \frac{\partial}{\partial x_j} \left[\left(\nu + \frac{\nu_t}{\sigma_\varphi} \right) \frac{\partial \varphi}{\partial x_j} \right], \end{aligned} \quad (\text{A.42})$$

$$f_h = -\frac{1}{T} \left(C_1 - 1 + C_2 \frac{P_k}{\varepsilon} \right) \left(\varphi - \frac{2}{3} \right), \quad (\text{A.43})$$

$$f_w = -\frac{\varphi \varepsilon}{k}, \quad (\text{A.44})$$

$$\mathcal{T} = \max \left(\frac{k}{\varepsilon}, C_T \left(\frac{\nu}{\varepsilon} \right)^{1/2} \right), \quad (\text{A.45})$$

$$L = C_L \max \left(\frac{k^{3/2}}{\varepsilon}, C_T \left(\frac{\nu^3}{\varepsilon} \right)^{1/4} \right), \quad (\text{A.46})$$

$$C'_{\varepsilon 1} = C_{\varepsilon 1} \left(1 + A_1 (1 - \alpha^P) \sqrt{\frac{1}{\varphi}} \right), \quad (\text{A.47})$$

Eddy viscosity

$$\nu_t = C_\mu k \varphi \mathcal{T}, \quad (\text{A.48})$$

Closure coefficients and auxiliary relations

$$\begin{aligned} C_{\varepsilon 1} = 1.44, \quad C_{\varepsilon 2} = 1.83, \quad A_1 = 0.04, \quad C_\mu = 0.22, \quad C_1 = 1.7, \quad C_2 = 1.2, \\ P = 3, \quad \sigma_\varepsilon = 1.22, \quad \sigma_k = 1, \quad \sigma_\varphi = 1, \quad C_L = 0.161, \quad C_\eta = 90, \quad C_T = 0.49 \end{aligned} \quad (\text{A.49})$$

B.2 Stress transport models

In second-order moment closure models the Reynolds-stress-tensor is modelled using the Reynolds-stress equations. The equations of the Reynolds stress equations are:

$$\begin{aligned} \frac{\partial \tau_{ij}}{\partial t} + U_k \frac{\partial \tau_{ij}}{\partial x_k} = -\tau_{ij} \frac{\partial U_j}{\partial x_k} - \tau_{ij} \frac{\partial U_i}{\partial x_j} + 2\nu \frac{\partial u_i}{\partial x_j} \frac{\partial u_j}{\partial x_j} + \overline{u_i \frac{\partial p}{\partial x_j}} + \overline{u_j \frac{\partial p}{\partial x_i}} + \\ \frac{\partial}{\partial x_j} \left[\frac{\nu}{\rho} \frac{\partial \tau_{ij}}{\partial x_j} + \overline{u'_i u'_j} \right], \end{aligned} \quad (\text{A.50})$$

The Reynolds stress equations are a system of six equations, one for each independent component of the Reynolds-stress-tensor. This system of equations also contains

22 new unknowns. The second-order correlations are now the dependent variables and the new unknowns involve third-order correlations as well as correlations involving gradients of the fluctuating velocities and pressure.

Second order closure models close the Reynolds-stress equation by replacing the unknowns with coefficients and algebraic expressions that are based upon mean flow properties. The advantage of Second-order closure models over Eddy-viscosity models is that the Reynolds stress tensor is not treated as an isotropic tensor.

The exact transport equations for the transport of the Reynolds stresses, $\overline{u_i u_j}$, including the buoyancy term which is implemented in *Code_Saturne* 2.0 and which is tested in the present thesis, is expressed as follows:

$$\begin{aligned} \frac{\partial}{\partial t} (\overline{u'_i u'_j}) + \frac{\partial}{\partial x_k} (U_k \overline{u'_i u'_j}) = & -\frac{\partial}{\partial x_j} [\overline{u'_i u'_j} + (\delta_{ij} \overline{u_i} + \delta_{ij} \overline{u_j})] + \frac{\partial}{\partial x_j} \left[\nu_t \frac{\partial}{\partial x_j} (\overline{u'_i u'_j}) \right] - \\ & \left(\overline{u'_i u'_j} \frac{\partial u_j}{\partial x_k} + \overline{u'_i u'_j} \frac{\partial u_i}{\partial x_j} \right) - \beta (g_i \overline{u'_j t'} + g_j \overline{u'_i t'}) + \overline{\left(\frac{\partial u_i}{\partial x_j} + \frac{\partial u_j}{\partial x_i} \right)} - \\ & 2\mu \overline{\frac{\partial u_i}{\partial x_j} \frac{\partial u_i}{\partial x_j}} - 2\rho \Omega_{ij} (\overline{u'_i u'_m} \varepsilon_{ijm} + \overline{u'_i u'_m} \varepsilon_{jim}) + S_{user}, \end{aligned} \quad (\text{A.51})$$

or:

$$\text{Local time derivative} + C_{ij} = D_{T,ij} + D_{L,ij} + P_{ij} + G_{ij} + \phi_{ij} - \varepsilon_{ij} + F_{ij} + S_{user} \quad (\text{A.52})$$

where C_{ij} is the convection term, $D_{T,ij}$ equals the turbulent diffusion, $D_{L,ij}$ stands for the molecular diffusion, P_{ij} is the term for stress strain, G_{ij} equals buoyancy production, ϕ_{ij} is for the pressure strain, ε_{ij} stands for the dissipation and F_{ij} is the production by system rotation. Of these terms, C_{ij} , $D_{L,ij}$, P_{ij} and F_{ij} do not require modelling. $D_{T,ij}$, G_{ij} , ϕ_{ij} and ε_{ij} have to be modelled for closing the equations.

Gibson and Launder's RST model

Gibson and Launder [59] proposed a high-Reynolds-number RST model whose general equation for the Reynolds stress $\overline{u_i u_j}$ is:

$$\frac{\partial (\overline{u'_i u'_j})}{\partial t} + \frac{\partial (U_k \overline{u'_i u'_j})}{\partial x_k} = P_{ij} - \frac{2}{3} \varepsilon \delta_{ij} + \phi_{ij} + \frac{\partial}{\partial x_k} \left[\left(\nu_t + C_s \frac{k}{\varepsilon} \overline{u_i u_j} \right) \frac{\partial \overline{u'_i u'_j}}{\partial x_k} \right], \quad (\text{A.53})$$

P_{ij} is the production of the Reynolds stresses expressed as:

$$P_{ij} = - \left(\overline{u'_i u'_k} \frac{\partial U_j}{\partial x_k} + \overline{u'_j u'_k} \frac{\partial U_i}{\partial x_k} \right), \quad (\text{A.54})$$

where $\frac{2}{3} \varepsilon \delta_{ij}$ represents the dissipation term for high-Reynolds-number flows where it is assumed that local isotropy holds. The diffusion term follows the Generalised Gradient Diffusion Hypothesis (GGDH). The pressure-strain correlation term represents the effective contribution of Gibson and Launder's work [59]. The pressure-strain correlation is expressed as a sum of four terms: an interaction between the fluctuating velocity components themselves, $\phi_{ij,1}$, an interaction between these and the main flow, via a linear relation with the mean velocity gradients, $\phi_{ij,2}$, and two wall reflection terms. The latter are those which were actually proposed by Gibson and Launder [59] as a new contribution since the former, $\phi_{ij,1}$ and $\phi_{ij,2}$, had been already proposed by Launder et al. [60]. The equation for the modelled pressure-strain correlation is:

$$\phi_{ij} = \phi_{ij,1} + \phi_{ij,2} + \phi_{ij,\omega_1} + \phi_{ij,\omega_2}, \quad (\text{A.55})$$

where:

$$\phi_{ij,1} = -C_1 \frac{\varepsilon}{k} \left(\overline{u'_i u'_j} - \frac{2}{3} \delta_{ij} k \right), \quad (\text{A.56})$$

$$\phi_{ij,2} = -C_2 \left(P_{ij} - \frac{2}{3} \delta_{ij} P_k \right), \quad (\text{A.57})$$

$$\phi_{ij,\omega_1} = C'_1 \frac{\varepsilon}{k} \left(\overline{u'_k u'_m} n_k n_m \delta_{ij} - \frac{3}{2} \overline{u'_k u'_i} n_k n_j - \frac{3}{2} \overline{u'_k u'_j} n_k n_i \right), \quad (\text{A.58})$$

$$\phi_{ij,\omega_2} = C'_2 \frac{\varepsilon}{k} \left(\phi_{km,2} n_k n_m \delta_{ij} - \frac{3}{2} \phi_{ik,2} n_k n_i - \frac{3}{2} \phi_{jk,2} n_k n_j \right) F, \quad (\text{A.59})$$

and

$$F = \frac{k^{3/2}}{2.5 y \varepsilon}, \quad (\text{A.60})$$

In the above equation, P_k stands for the production rate of turbulence given by: $P_k = -\overline{u_i u_j} \frac{\partial U_i}{\partial x_j}$, n_m is the unit vector normal to the wall in the m direction and F is the length scale function, y is the normal distance to the wall.

The RST model also requires an equation for the turbulent eddy dissipation rate ε . which can be expressed as:

$$\frac{\partial \varepsilon}{\partial t} + \frac{\partial U_j \varepsilon}{\partial x_j} = \frac{\partial}{\partial x_k} \left[\left(\nu_t + C_\varepsilon \frac{k}{\varepsilon} \overline{u'_i u'_j} \right) \frac{\partial \varepsilon}{\partial x_j} \right] - C_{\varepsilon 1} \frac{\varepsilon}{k} P_k - C_{\varepsilon 2} \frac{\varepsilon^2}{k}, \quad (\text{A.61})$$

Closure coefficients and auxiliary relations

$$\begin{aligned} C_1 &= 1.8, & C_2 &= 0.6, & C'_1 &= 0.5, & C'_2 &= 0.3, & C_s &= 0.22, \\ C_\varepsilon &= 0.18, & C_{\varepsilon 1} &= 1.44, & C_{\varepsilon 2} &= 1.92, \end{aligned} \quad (\text{A.62})$$

The SSG RST model

The SSG Reynolds stress transport model is also a high-Reynolds-number model, developed by Speziale et al. [81]. Its general equation form for the Reynolds stresses $\overline{u'_i u'_j}$ and the turbulent eddy dissipation rate ε are the same of those presented for the GL model, Equations A.53 and A.61. The main difference between these two models lies in the pressure strain correlation expression. Also starting from the Poisson equation for the instantaneous pressure field, Speziale et al. [81] developed a general solution, subjected to physical constrains, for the pressure strain correlation which resulted in a non-linear formulation for the latter, where it varies quadratically with the anisotropy tensor defined by $b_{ij} = \frac{\overline{u'_i u'_j} - \frac{2}{3} k \delta_{ij}}{2k}$. The resulting expression for the pressure strain correlation ϕ_{ij} is thus:

$$\begin{aligned} \phi_{ij} &= - \left(C_1 + C_1^* \frac{\rho}{\varepsilon} \right) b_{ij} + C_2 \epsilon \left(b_{ik} b_{kj} - \frac{1}{3} b_{mn} b_{mn} \delta_{ij} \right) + \left(C_3 - C_3^* \sqrt{A} \right) k S_{ij} + \\ &C_4 k \left(b_{ik} S_{jk} + b_{jk} S_{ik} - \frac{2}{3} b_{mn} S_{mn} \delta_{ij} \right) + C_5 k (b_{ik} W_{jk} + b_{jk} W_{ik}), \end{aligned} \quad (\text{A.63})$$

where $A = b_{ij} b_{ij}$ is the stress invariant, $S_{ij} = \frac{1}{2} \left(\frac{\partial U_i}{\partial x_j} + \frac{\partial U_j}{\partial x_i} \right)$ and $W_{ij} = \frac{1}{2} \left(\frac{\partial U_i}{\partial x_j} - \frac{\partial U_j}{\partial x_i} \right)$ are the mean strain and vorticity tensors.

In Equation A.63, the term: $-(C_1 + C_1^* \frac{\varphi}{\varepsilon}) b_{ij}$ is equivalent to the interaction between the fluctuating velocity components themselves, $\phi_{ij,1}$ used in the GL model in section (3.3.2). The second term $C_2 \varepsilon (b_{ik} b_{kj} - \frac{1}{3} b_{mn} b_{mn} \delta_{ij})$ contains the quadratically non-linear terms in the anisotropy tensor b_{ij} . The term $(C_3 - C_3^* \sqrt{A}) k S_{ij}$ is linearly dependent on the mean strain rate tensor, although its coefficient still depends on the anisotropy tensor. The term $C_4 k (b_{ik} S_{jk} + b_{jk} S_{ik} - \frac{2}{3} b_{mn} S_{mn} \delta_{ij}) + C_5 k (b_{ik} W_{jk} + b_{jk} W_{ik})$ define the dependence of the pressure-strain correlation on the interaction between the anisotropy tensor and the mean strain and vorticity tensors, respectively. There is no wall reflection term.

Closure coefficients and auxiliary relations

$$\begin{aligned} C_1 &= 3.4, & C_1^* &= 1.8, & C_2 &= 4.2, & C_3 &= 0.8, & C_3^* &= 1.3, & C_4 &= 1.25, \\ C_5 &= 0.4, & C_s &= 0.22, & C_\varepsilon &= 0.18, & C_{\varepsilon 1} &= 1.44, & C_{\varepsilon 2} &= 1.83, \end{aligned} \quad (\text{A.64})$$

Appendix C

Numerical methods

C.1 Finite Volume Method (FVM)

Code_Saturne 2.0 is based on the finite volume method. This method relies on:

- Dividing the domain into control volumes.
- Formal integration of the governing equation of fluid flow over each control volume in the solution domain.
- Discretization involves the substitution of a variety of finite-differences-type of approximations for the terms in the integrated equation, representing flow processes such as convection, diffusion and sources. This converts integral equations into a system of algebraic equations.
- Solution of the algebraic equations by an iterative method.

If one considers a general variable ϕ , the conservative form of all fluid flow equations, including equations for scalar quantities such as temperature etc., can usefully be written in the following form:

$$\frac{\partial (\rho\phi)}{\partial t} + \text{div} (\rho\phi\mathbf{u}) = \text{div} (\Gamma \underline{\text{grad}}\phi) + S_\phi, \quad (\text{A.1})$$

where ϕ represents the scalar being solved for, and the source term can be decomposed as:

$$S_\phi = S_i(f, \varphi)\phi + S_e, \quad (\text{A.2})$$

where f represents the physical properties (ρ, Γ, \dots) , φ represents the variable of the problem $(\underline{u}, \mu_t, k, \varepsilon, \dots)$, S_i is the linear part of the source terms and S_e include all other source terms.

Equation (A.1) highlights the various transport processes affecting variable ϕ : the rate of change term and the convective term on the left hand side and the diffusive term (Γ = diffusivity coefficient) and the source term respectively on the right hand side. The key step of the finite volume method is the integration of Equation (A.1) over a three-dimensional control volume CV yielding:

$$\int_{\Omega} \frac{\partial (\rho\phi)}{\partial t} d\Omega + \int_{\Omega} \text{div} (\rho\phi\underline{u}) d\Omega = \int_{\Omega} \text{div} (\Gamma \underline{\text{grad}}\phi) d\Omega + \int_{\Omega} S_{\phi} d\Omega, \quad (\text{A.3})$$

The volume integrals in the second term on the left hand side, the convective term, and the first term on the right hand side, the diffusive term, are re-written as integrals over the entire bounding surface of the control volume by using the Gauss divergence theorem. For a vector \underline{a} this theorem states:

$$\int_{\Omega} \text{div} \underline{a} d\Omega = \int_A \underline{n} \cdot \underline{a} dA, \quad (\text{A.4})$$

Applying Gauss divergence theorem, Equation (A.3) can be written as follows:

$$\frac{\partial}{\partial t} \left(\int_{\Omega} \rho\phi d\Omega \right) + \int_A \underline{n} \cdot (\rho\phi\underline{u}) dA = \int_A \underline{n} \cdot (\Gamma \underline{\text{grad}}\phi) dA + \int_{\Omega} S_{\phi} d\Omega, \quad (\text{A.5})$$

The order of integration and differentiation has been changed in the first term on the left hand side of Equation (A.5) to illustrate the physical meaning. This term signifies the rate of change of the total amount of fluid variable ϕ in the control volume. The product $\underline{n} \cdot (\rho\phi\underline{u})$ represents the flux component of variable ϕ due to fluid flow along the outward normal vector \underline{n} , so the second term on the left hand side of Equation (A.5), the convection term, is therefore the net rate of change of fluid variable ϕ of the fluid element due to convection.

In time dependent problems, it is also necessary to integrate with respect to time t over a small interval $t + \Delta t$ from, say, t until Δt . This yields the most general integrated form of the transport equation:

$$\int_{\Delta t} \frac{\partial}{\partial t} \left(\int_{\Omega} \rho \phi d\Omega \right) dt + \int_{\Delta t} \int_A \underline{n} \cdot (\rho \phi \underline{u}) dA dt = \int_{\Delta t} \int_A \underline{n} \cdot (\Gamma \underline{grad} \phi) dA dt + \int_{\Delta t} \int_{\Omega} S_{\phi} d\Omega dt, \quad (\text{A.6})$$

C.2 Space discretization in *Code_Saturne 2.0*

Discretization in space is achieved using the above finite volume approach, with a co-located storage arrangement of all variables.

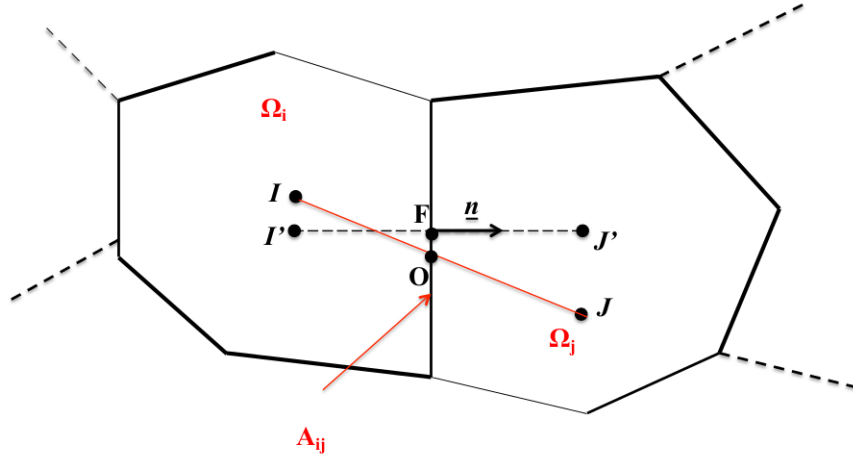


Figure C.1: Notation for the spatial discretization.

In Figure (C.1), I denotes the cell centre. J is the centre of the neighbouring cell. I' and J' are the projection points of the cell centres onto the face normal vector. O is the point where the line that connects the two cell centres, crosses the face between them. Ω_i and Ω_j are the volumes of cells I and J respectively. A_{ij} is the area of the face between the cell nodes I and J .

After integrating each term of Equation A.1, one obtains the finite volume discretization.

- Time derivative:

$$\rho \frac{\partial}{\partial t} \int_{\Omega_i} \phi_i d\Omega = \rho \frac{\partial}{\partial t} (\phi_i \Omega_i), \quad (\text{A.7})$$

where ϕ_i is the value of ϕ at the cell centre I .

- Convection term:

$$\int_{\Omega} \text{div}((\phi \rho \underline{u})) d\Omega = \int_{A_{ij}} \phi \rho \underline{u} \cdot \underline{n} dA = \sum_{j \in N(i)} \phi_{ij} (\rho \underline{u} \cdot \underline{n})_{ij} A_{ij}, \quad (\text{A.8})$$

where ϕ_{ij} is the value of ϕ at the face centre, interpolated from the cell centres. $N(i)$ are the neighbouring cells of i .

- Diffusion term:

$$\int_{\Omega} \text{div}(\Gamma \underline{\text{grad}} \phi) d\Omega = \int_{A_{ij}} (\Gamma \underline{\text{grad}} \phi) \cdot \underline{n} dA = \sum_{j \in N(i)} (\Gamma \underline{\text{grad}} \phi)_{ij} \cdot \underline{n} A_{ij}, \quad (\text{A.9})$$

ϕ_{ij} and $\underline{\text{grad}} \phi_{ij}$ are needed (at the face) so it needs to be interpolated. Three different options are available in *Code_Saturne 2.0*. They are presented in the following section.

C.2.1 Convection schemes

In *Code_Saturne 2.0* the convection can be calculated either by using an upwind differencing scheme (UDS), a central differencing scheme (CDS) or a second order linear upwind scheme (SOLU). The code has also a slope test based on the product of the gradients at the cell centres to dynamically switch from CDS to UDS. These are detailed as:

- **First order upwind scheme (UDS)**

$$\phi_{ij} = \begin{cases} \phi_I, & \text{if } (\underline{u} \cdot \underline{n})_F > 0 \quad (\text{positive flux}) \\ \phi_J, & \text{if } (\underline{u} \cdot \underline{n})_F < 0 \quad (\text{negative flux}) \end{cases} \quad (\text{A.10})$$

This scheme is robust and stable, but introduces additional numerical diffusion which can become large if the grid is coarse and dramatic in LES.

- **Second order central difference scheme (CDS)**

For a centred scheme, the value at the face can be computed as:

$$\phi_{ij} = \alpha_{ij}\phi_I + (1 - \alpha_{ij})\phi_J + \frac{1}{2} \left[(\underline{\text{grad}} f)_I + (\underline{\text{grad}} f)_J \right] \cdot \underline{OF}, \quad (\text{A.11})$$

with: $\alpha_{ij} = \frac{(FJ' \cdot \underline{n})}{(I'J' \cdot \underline{n})}$

The last term in Equation (A.11) is added for non-orthogonal grids, where the centre of the face does not lie at the midpoint between the cell centres (Figure C.1).

- **Second order linear upwind scheme (SOLU)**

$$\phi_{ij} = \begin{cases} \phi_I + \underline{IF} \cdot (\underline{\text{grad}} f)_I, & \text{if the flux is positive} \\ \phi_J + \underline{JF} \cdot (\underline{\text{grad}} f)_J, & \text{if the flux is negative} \end{cases} \quad (\text{A.12})$$

When using a centred scheme, a “slope test” (based on the gradient of the variable) is available in order to stabilise the calculation, by introducing non-linearities in the convection operator it allows to switch from the centred or SOLU scheme to the first order upwind scheme without blending. In the present thesis the slope test is activated.

C.2.2 Diffusion terms

The diffusion term on the right hand side of Equation (A.9) is computed as:

$$\sum_{j \in N(i)} \Gamma (\underline{\text{grad}} \phi)_{ij} \cdot \underline{n} dA = \sum_{j \in N(i)} \Gamma \frac{\phi_{I'} - \phi_{J'}}{I'J'} \cdot \underline{n} A_{ij}, \quad (\text{A.13})$$

The values of $\phi_{I'}$ and $\phi_{J'}$ can be computed by using the gradient at the cell centre:

$$\phi_{I'} = \phi_I + (\underline{\text{grad}} \phi)_I \cdot \underline{II'}, \quad (\text{A.14})$$

C.2.3 Gradient reconstruction

For some of the approximations above (and in assembling source terms for some transport equations), one needs values of the gradient of variables at the cell centres. As mentioned above in *Code_Saturne 2.0*, two methods are available:

- Iterative reconstruction of the non-orthogonalities
- Least squares method based on the first neighbouring cells (those that share a face)

C.2.3.1 Standard iterative method in *Code_Saturne* 2.0

The calculation of the gradients is achieved by an iterative solver (see Muzaferija and Gosman [71]) in which the gradient is expressed as:

$$\left(\underline{grad} \phi\right)_I = \frac{1}{\Omega} \int_{\Omega} \left(\underline{grad} \phi\right) d\Omega = \frac{1}{\Omega} \sum_{j \in N(i)} \int_A \phi \underline{n} dA, \quad (\text{A.15})$$

The surface integral can be approximated using the midpoint rule so that it becomes:

$$\left(\underline{grad} \phi\right)_I = \frac{1}{\Omega} \sum_{j \in N(i)} \phi_F A_{ij} \cdot \underline{n}, \quad (\text{A.16})$$

To obtain the value of ϕ_F , a Taylor series expansion can be applied to obtain:

$$\phi_F = \phi_o + \underline{OF} \left(\underline{grad} \phi\right)_o + \mathcal{O} \left(\| \underline{OF} \|^2\right), \quad (\text{A.17})$$

The value of ϕ_o can be obtained by a linear interpolation and the gradient at the same point, $\left(\underline{grad} \phi\right)_o$, from an average between the values of $\left(\underline{grad} \phi\right)_I$ and $\left(\underline{grad} \phi\right)_J$. Finally, the system to solve can be written as:

$$\begin{aligned} \left(\underline{grad} \phi\right)_I &= \frac{1}{\Omega} \sum_{j \in N(i)} [\alpha_{ij} \phi_I + (1 - \alpha_{ij}) \phi_J + \\ &\frac{1}{2} \underline{OF} \left(\left(\underline{grad} \phi\right)_I + \left(\underline{grad} \phi\right)_J \right)] A_{ij} \cdot \underline{n}, \end{aligned} \quad (\text{A.18})$$

In the latter equation, $\left(\underline{grad} \phi\right)_o$ has been evaluated as $\frac{1}{2} \left(\underline{grad} \phi\right)_I + \frac{1}{2} \left(\underline{grad} \phi\right)_J$, this is sufficient to obtain a second order approximation for ϕ_F . Moreover, numerical experiments carried out on complex industrial cases indicated that this approximation seemed to provide more robustness than using strict linear interpolation to approximate $\left(\underline{grad} \phi\right)_o$.

C.2.3.2 Least squares method

Solving Equation (A.18) remains costly. A more direct method has therefore also been implemented, based on the least squares approach described in Muzaferija and Gosman [71].

Given a data $\{(x_1, y_1) \dots, (x_N, y_N)\}$, one may define the error associated to saying $y = a.x + b$ by:

$$E(a, b) = \sum_{n=1}^N (y_n - (ax_n + b))^2, \quad (\text{A.19})$$

The goal is to find values a and b that minimise the error.

Within the present code, the error, Equation (A.19), is expressed in *Code_Saturne 2.0* as:

$$E_I^\phi(\underline{grad}\phi, \underline{grad}\phi) = \sum_{j \in N(i)}^N \frac{1}{\|\underline{IJ}\|^2} \left(\phi_J - \left(\phi_I + (\underline{grad}\phi)_I \cdot \underline{IJ} \right) \right)^2, \quad (\text{A.20})$$

Assuming $\|\underline{IJ}\| \neq 0$, the aim is to determine the value for $(\underline{grad}\phi)_I$ that minimises the associated error $E_I^\phi(\underline{grad}\phi, \underline{grad}\phi)$. If, for a given cell I , there exist at least three faces for which the related vectors \underline{IJ} are linearly independent, the minimisation of Equation (A.20) has a unique solution.

To illustrate the method, consider system (A.20) on a two-dimensional triangular cell I . Neighbouring cells are denoted J , K and L . One also defines the unit vector $\underline{m}_{IP} = \frac{1}{\|\underline{IP}\|} \underline{IP}$ and the scalar quantity $g_P = \frac{\phi_P - \phi_I}{\underline{IP}}$, with P standing for J , K and L cell centres. Considering these notations, the minimum error reaches zero under the following condition:

$$g_J(\underline{m}_{IK} \times \underline{m}_{IL}) + g_K(\underline{m}_{IL} \times \underline{m}_{IJ}) + g_L(\underline{m}_{IJ} \times \underline{m}_{IK}) = 0, \quad (\text{A.21})$$

C.3 Time discretization

Code_Saturne 2.0 can solve flows in both steady and unsteady modes. It uses a theta (θ) scheme for the time discretization. All equations are solved sequentially, in a segregated fashion. Given a time step $\Delta t = t_{n+1} - t_n$ integration of Equation (A.6) leads to:

$$\begin{aligned}
& \Omega \frac{\rho}{\Delta t} (\phi^{n+1} - \phi^n) + \theta \left[\text{div} \left((\rho \underline{u}) \phi^{n+1} \right) - \text{div} \left(\Gamma \underline{\text{grad}} \phi^{n+1} \right) \right] = \\
& - (1 - \theta) \left[\text{div} \left((\rho \underline{u}) \phi^{n+1} \right) - \text{div} \left(\Gamma \underline{\text{grad}} \phi^{n+1} \right) \right] + \\
& \Omega \left[S_i(f, \varphi^n) (\theta \phi^{n+1} + (1 - \theta) \phi^n) + [S_e(f, \varphi)]^{n+\theta} \right], \tag{A.22}
\end{aligned}$$

The code allows two options for the constant θ :

$$\begin{cases} \theta = 1, & \text{for an implicit first order Euler scheme} \\ \theta = 1/2, & \text{for a second order Crank - Nicholson scheme} \end{cases}$$

The system (A.22) is solved in an iterative and incremental manner. Considering k as the index of the sub-iteration, the increments of a variable ϕ are presented as:

$$\begin{cases} \Delta \phi^{n+1,k+1} = \phi^{n+1,k+1} - \phi^{n+1,k}, \\ \Delta \phi^{n+1,k} = \phi^{n+1,k} - \phi^{n+1,0}, \end{cases} \tag{A.23}$$

with the value at the previous time step is $\phi^{n+1,0} = \phi^n$.

C.4 Pressure-velocity coupling (pressure correction)

Code_Saturne 2.0 achieves time-stepping and velocity-pressure coupling via a fractional step scheme that can be associated with the SIMPLEC method [87]. The solution algorithm consists of a prediction-correction method.

In the first step, the momentum equation is solved using an explicit pressure gradient from the previous time step. In the description below, time step n is considered, of size Δt , extending from $t = t^{(n)}$ to $t = t^{(n+1)}$, with $\phi^{(n)}$ denoting the value of $\phi(t)$ at time level $t^{(n)}$. $\underline{Q}^{(n)} = \rho \underline{u}^{(n)}$ and $P^{(n)}$ are the momentum and pressure at time level n respectively. The density ρ can be a function of scalars like temperature ($\rho^{(n)} = \mathcal{F}(T^{(n)})$).

The system to solve at the first step of the method is:

$$\Omega \frac{\underline{Q}^* - \underline{Q}^{(n)}}{\Delta t} + \text{div} \left(\underline{u}^* \underline{Q}^{(n)} - \mu \text{grad} \underline{u}^* \right) = -\underline{\text{grad}} P^{(n)} + \Omega S_\phi^{(n)}, \tag{A.24}$$

where S includes all source terms that can be made implicit or explicit, i.e. $S = A + B \cdot \underline{u}$.

After this prediction step, a new velocity field is obtained (denoted by \underline{u}^*),

The second step consists of correcting the pressure gradient and velocity fields in order to satisfy the continuity and momentum equations. This is done by using the momentum equation (with convection and diffusion variations neglected) to link pressure corrections to velocity ones, and requiring that the corrected velocity field satisfy the continuity equation. The system is therefore:

$$\begin{cases} \underline{Q}^{**} - \underline{Q}^* = -\Delta t \underline{grad} (P^{**} - P^{(n)}), \\ \text{div} (\underline{Q}^{**}) = 0 \end{cases} \quad (\text{A.25})$$

One considers $\Delta P = P^{**} - P^{(n)} = P^{**} - P^*$, and combining Equations (A.25) leads to a Poisson equation for the pressure update, which can be written as:

$$\text{div} [\Delta t \underline{grad} (P^{**} - P^*)] = \text{div} (\underline{Q}^*), \quad (\text{A.26})$$

Once the updated pressure (P^{**}), has been obtained, the velocity field is corrected, via the first expression in Equation (A.25). After the above procedure, the resolution of turbulent variables is done according to their time scheme.

The third step is to resolve scalar equations (such as temperature T in the present thesis). Following the same approach as for the velocity, one gets:

$$\Omega \rho^{(n)} \frac{T^{(n+1)} - T^*}{\Delta t} + \text{div} (T^{(n+1)} \underline{Q}^{**} - \Gamma \underline{grad} T^{(n+1)}) = \Omega S'_\phi{}^{(n+1)}, \quad (\text{A.27})$$

with $T^* = T^{(n)}$, and the source term $S'_\phi = A + B.T$.

Once this step has been completed, the other physical properties of the fluid may also be updated and the whole process can then start again.

Rhie & Chow interpolation [77] is used when evaluating fluxes in the pressure correction equation in order to avoid oscillations that can otherwise occur.

C.5 Linear system solution algorithm

The full flow solution algorithm comprises a large iterative loop:

- Calculate the physical properties (ρ , ν_t ...)
- Calculate predicted velocities (in a segregate fashion)
- Compute the updated pressure equation

- Correct velocities to ensure mass conservation
- Calculate turbulent and other scalar variables (in a segregate fashion)
- Begin next iteration.

The default treatment is to use the Jacobi method for convected quantities, and algebraic multigrid method for pressure (with a conjugate gradient). These methods are detailed in the book of Ferziger and Peric [40].

C.6 Boundary Conditions

Two major kinds of boundary conditions are:

- Dirichlet boundary conditions: The value of the variable is fixed at the boundary face.
- Neumann boundary condition: The normal gradient of the variable at the boundary face is fixed.

In order to solve the flow field, boundary conditions need to be applied for each variable. In terms of the discretized equations, quantities on boundaries that need to be evaluated include:

- The convective term, Equation (A.8), a boundary value is required for the term $(\rho \underline{u}^{(n)} \cdot \underline{n}) \phi$;
- The diffusion term, Equation (A.9), a boundary value is necessary for the term $\Gamma (\underline{grad} \phi \cdot \underline{n})$;
- The source term, Equation (A.6), if this depends on $\underline{grad} \phi$, a boundary value is required when computing the gradient at cell centres;
- The pressure gradient term $\underline{grad} (P^{**} - P^{(n)}) \cdot \underline{n}$ in Equation (A.25).
- Boundary values of the terms $(\Delta T \underline{grad} \Delta P \cdot \underline{n})$ and $((\underline{Q}^* \cdot \underline{n}))$ in the Poisson Equation (A.26);

The boundary treatment of the terms mentioned above is detailed hereafter for inlets, outlets, walls and symmetry conditions.

C.6.1 Inlet

At an inlet boundary, a Dirichlet condition is prescribed for all transported variables (velocity, scalars, turbulent variables ...). The boundary conditions for discrete terms in Equation (A.6) are built under the following assumptions:

- The inlet boundary value for the convection flux, $(\rho \underline{u}^{(n)} \cdot \underline{n}) \phi$, is $(\rho \underline{u}_{inlet}^{(n)} \cdot \underline{n}) \phi_{inlet}^{n+1}$.
- For diffusion terms, the inlet boundary value for the flux is calculated as:

$$(\underline{grad} \phi \cdot \underline{n})_{inlet} = \Gamma \frac{\phi_{inlet}^{(n+1)} - \phi_{I'}^*}{\underline{I'} \underline{F} \cdot \underline{n}}, \quad (\text{A.28})$$

- For source terms which require the computation of the gradient of a variable ϕ , the value $\phi_{inlet}^{(n+1)}$ is used as a boundary face value.

In order to compute the pressure gradient, a homogeneous Neumann condition (zero flux) is imposed although an extrapolation from interior nodes is possible.

When solving the Poisson Equation (A.26), the term $\Delta t \underline{grad} \Delta P \cdot \underline{n}$ is set to zero on the boundary, while the boundary value of the term $\rho \underline{u}^* \cdot \underline{n}$ is computed as $\rho_{inlet}^{(n+1)} \underline{u}_{inlet}^{(n+1)} \cdot \underline{n}$. When updating the momentum at cell centres, via Equation (A.25), the required pressure gradient is extrapolated (first order approximation in space) from the cell value of ΔP_I taking into account the assumption $\Delta t \underline{grad} \Delta P \cdot \underline{n} = 0$ on the boundary.

C.6.2 Outlet

At an outlet, a homogeneous Newman condition is imposed on the velocity, scalars and turbulent variables. Dirichlet conditions are applied to pressure, $P_{outlet}^{(n+1)}$. The boundary values for discrete terms in Equation (A.6) are set as:

- The boundary value for the convective flux $(\rho \underline{u}^{(n)} \cdot \underline{n})_{outlet} \phi^*$ is prescribed, using the homogeneous condition for ϕ , as $(\rho \underline{u}^{(n)} \cdot \underline{n})_{outlet} \phi_{I'}^*$.
- The boundary values for the diffusion fluxes $(\Gamma (\underline{grad} \phi) \cdot \underline{n})$ are set to zero.
- In source terms a first order approximation is used to set boundary values of $\phi = \phi_{I'}$. The Dirichlet condition for pressure provides the boundary value used for the computation of the pressure gradient.

The Dirichlet condition is used to prescribe the term ΔP in the Poisson Equation (A.26). In the momentum correction Equation (A.25), the boundary value for ΔP is set to zero.

C.6.3 Walls

For both walls and symmetries the following assumptions are made:

- Zero mass flow rate normal to walls and symmetry planes.
- A Dirichlet condition is set for the tangential velocity and scalars (in case of fixed values) at the walls and a homogeneous Neumann condition at symmetry planes.
- Pressure gradient normal to the face is set to zero, although it can also be computed via an explicit extrapolation of the value at the boundary cell.
- The boundary value for the convective flux in Equation (A.6) is set to zero.
- For diffusive fluxes in Equation (A.6), if a Neumann condition applies to the variable ϕ , this is used to evaluate the boundary value for $\Gamma(\underline{grad} \phi_{\omega} \cdot \underline{n})$. If a Dirichlet condition applies, the boundary value is then computed in a similar way as for inlets (Equation (A.28)).
- When computing gradients, for which a value of ϕ is required at the boundary, the treatment again depends on the boundary condition applied to ϕ . If a homogeneous Neumann condition is imposed, the boundary value is extrapolated from the boundary cell centre value.
- For the pressure gradient calculation, if the flux of the variable at the face is prescribed, the boundary value is:

$$\phi_{wall} = \phi_{I'} + \underline{I'F}(\underline{grad} \phi \cdot \underline{n}), \quad (\text{A.29})$$

To solve the Poisson Equation (A.26), the boundary values of $\Delta t \underline{grad} \Delta P \cdot \underline{n}$ and $\rho \underline{u}^* \cdot \underline{n}$ are set to zero. For the momentum correction Equation (A.25), the boundary value for ΔP is obtained from the adjacent cell centres values assuming that: $\Delta t \underline{grad} \Delta P \cdot \underline{n} = 0$.

For turbulent flows, the boundary conditions at the walls are detailed in sections 4.3.1 and 4.3.2.

Appendix D

Grid sensitivity tests

Seven different grids have been used to explore grid sensitivity and decide upon an optimal grid resolution for the computations using high-Re models and the standard “two-velocity-scale wall function”. These include uniform and non-uniform meshes, varying both the interior mesh sizes and the near-wall cell sizes, giving different values of the dimensionless near-wall node distance y^+ . The grids are shown in Figure A.1 and their parameters are summarised in Table (A.1).

	Grid 1 (a)	Grid 2 (b)	Grid 3 (c)	Grid 4 (d)	Grid 5 (e)	Grid 6 (f)	Grid 7 (g)
Density	80×20	80×20	80×22	100×22	50×50	80×20	80×40
Y	0.004	0.007	0.1	0.002	0.002	0.002	0.002
Y^+ [min, max]	[3, 11]	[2, 8]	[3, 8]	[3, 7.5]	[0.5, 25]	[0.5, 11]	[0.5, 11.5]

Table A.1: Parameters of computational grids used for 2-D grid sensitivity tests.

Profiles of mean temperature, vertical velocity, rms fluctuating velocity at three heights across the cavity, and local Nusselt number distribution, are presented in Figures A.2 to A.5, for three heights inside the vertical cavity. Results obtained using the seven grids mentioned earlier, are compared with experimental data of Betts and Bokhari [11]. Comparisons show that thermal and dynamic results are dependent on grid refinement. The uniform mesh (Grid 1) 80×20 resolution is considered sufficient to solve the problem for high-Reynolds-number models. At this resolution the value of dimensionless distance from the wall, y^+ , to the first inside node next to the wall is around 10 (See Figure A.6). However, the rest of the grids (Grids 2 to 7) show discrepancies comparing with experimental data and therefore they are not used in the present thesis.

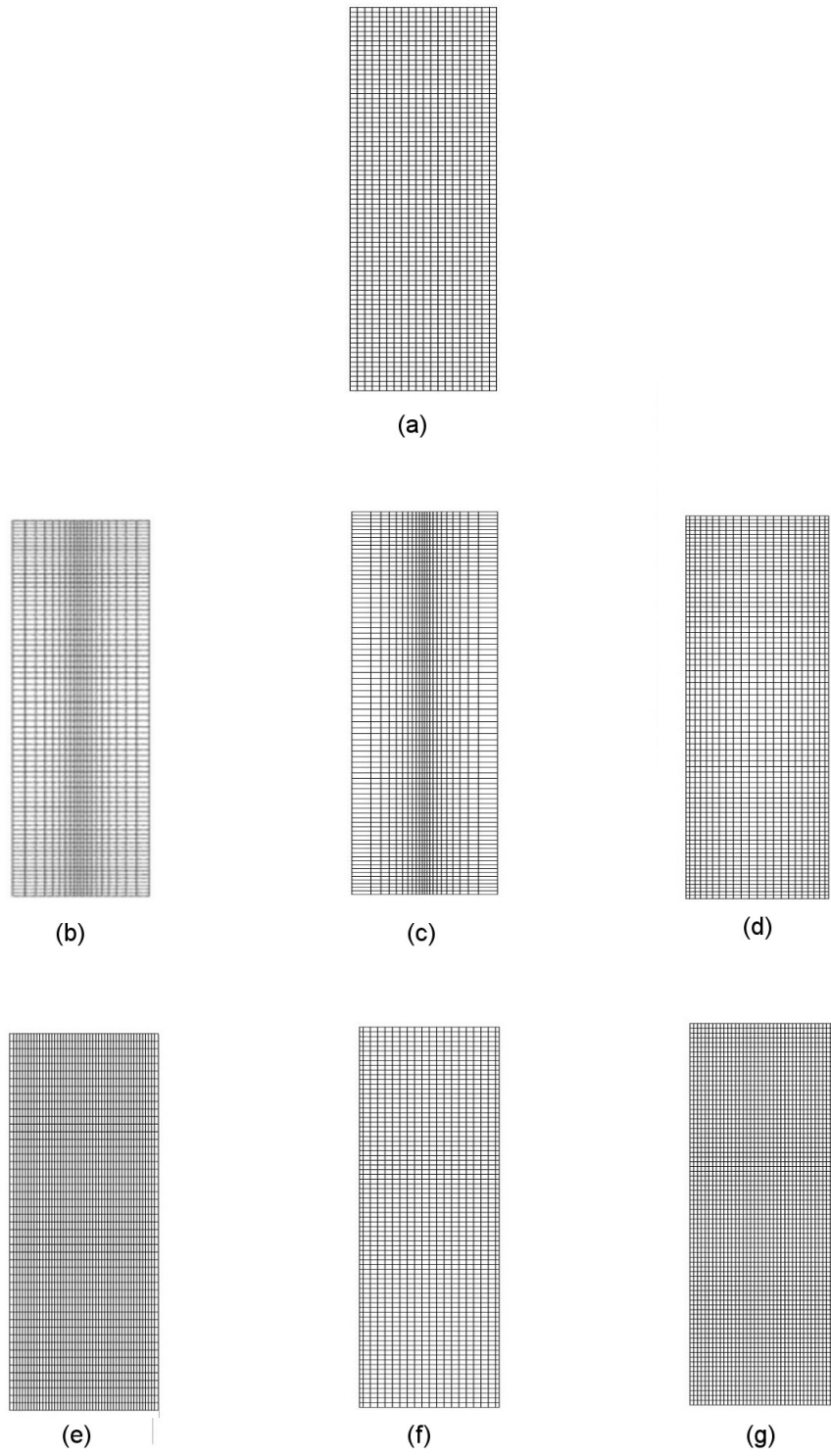


Figure A.1: 2-D computational meshes used for grid sensitivity tests.

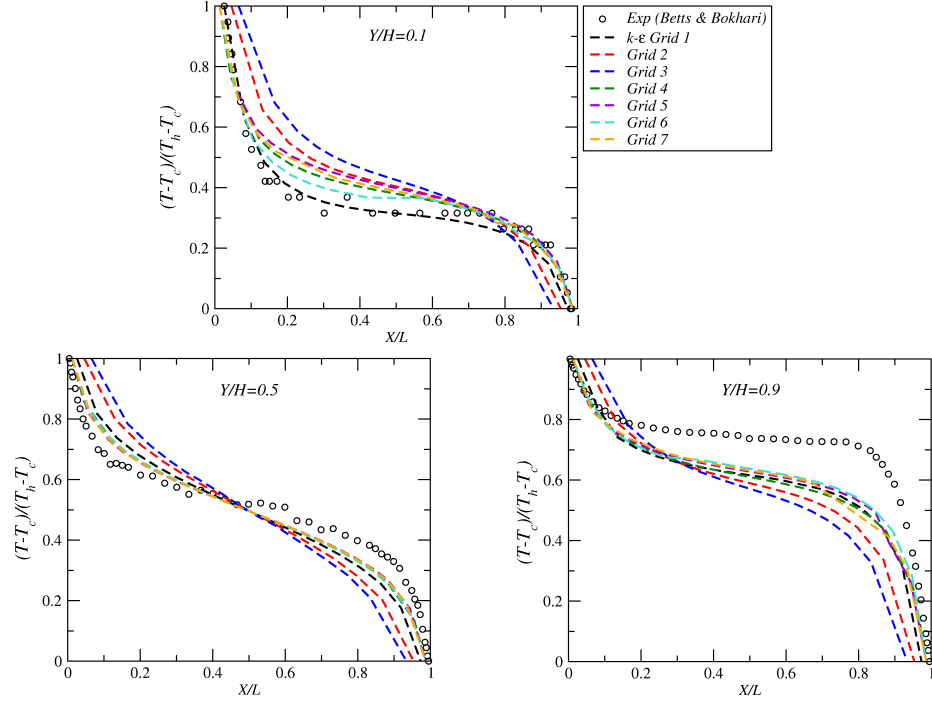


Figure A.2: Mean temperature profiles at three heights inside the vertical cavity. Comparison between different 2-D computational meshes.

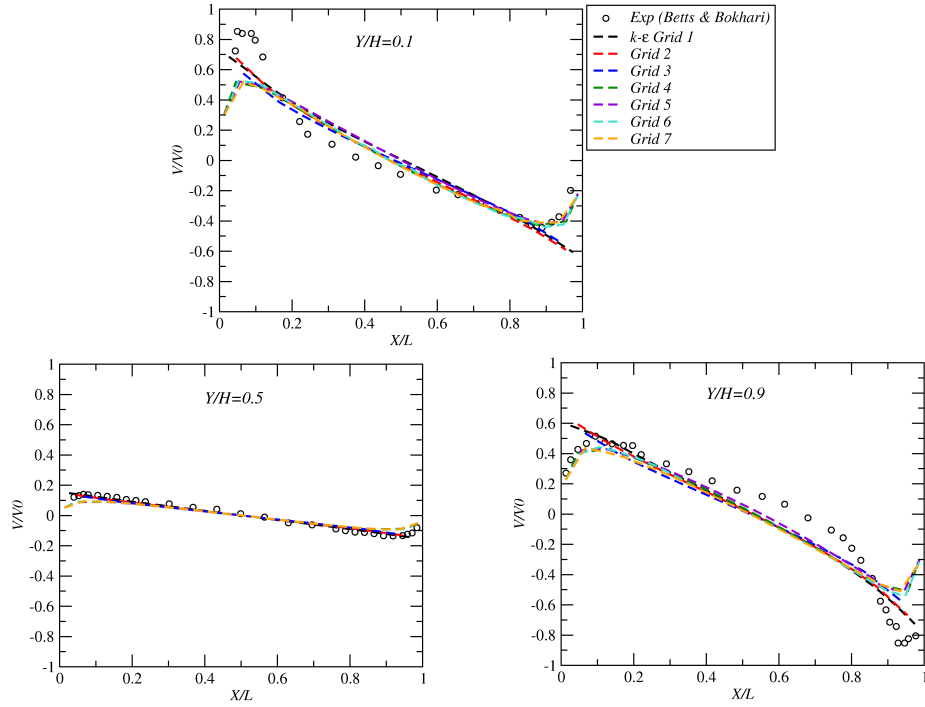


Figure A.3: Mean velocity profiles at different heights inside the vertical cavity. Comparison between different 2-D computational meshes.

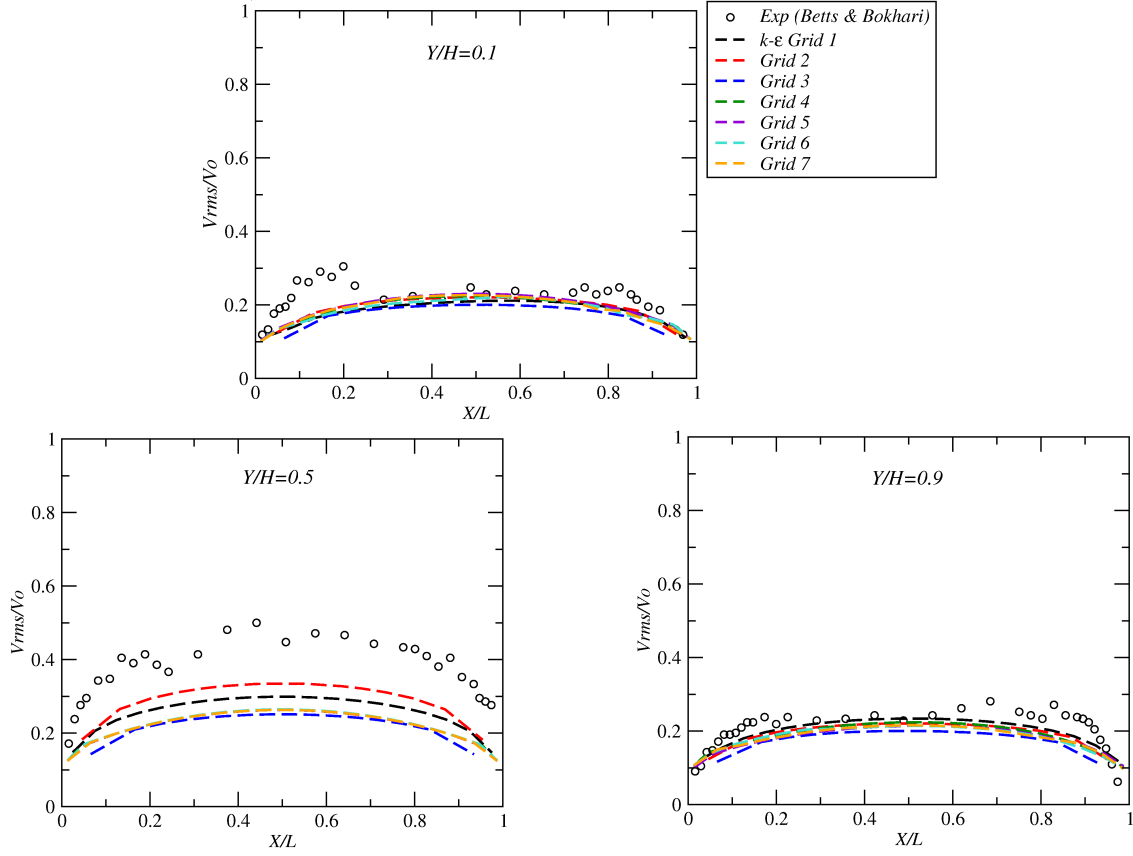


Figure A.4: Rms velocity fluctuation profiles at different heights inside the vertical cavity. Comparison between different 2-D computational meshes.

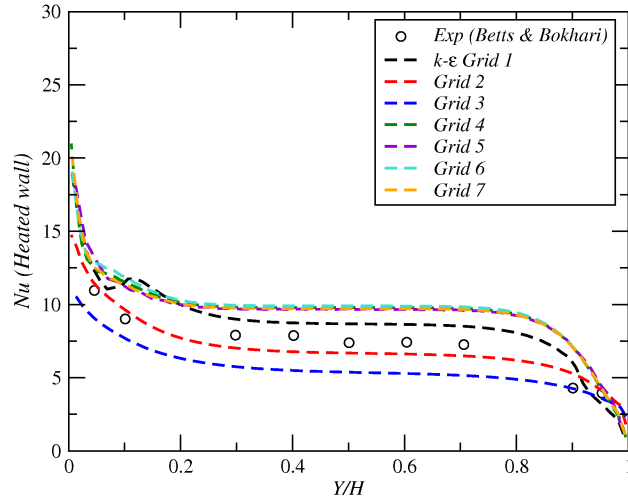


Figure A.5: Local Nusselt number distribution along heated wall of the vertical cavity. Comparison between different 2-D computational meshes.

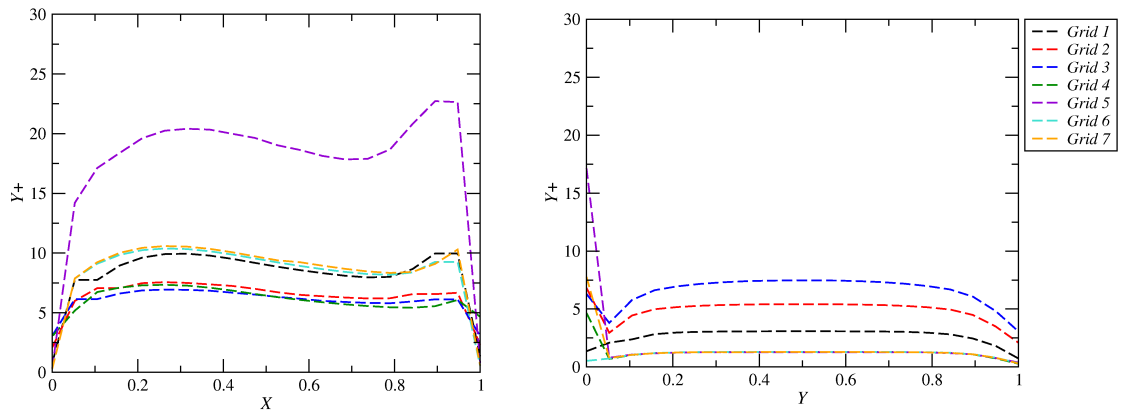


Figure A.6: Dimensionless distance (y^+) distribution along horizontal and vertical walls of the the tall cavity. Comparison between different 2-D computational meshes.